1999 REVIEW OF SUPERCONDUCTING DIPOLE AND QUADRUPOLE MAGNETS FOR PARTICLE ACCELERATORS

Arnaud Devred
(Arnaud.Devred@cea.fr)

Commissariat à l'Energie Atomique de Saclay (CEA/Saclay)
DSM/DAPNIA/STCM
F–91191 GIF-SUR-YVETTE CEDEX
FRANCE

and

LHC/MMS
CERN, Laboratoire Européen pour la Physique des Particles
CH–1211 GENEVE 23
SUISSE

ABSTRACT

The quest for elementary particles has promoted the development of particle accelerators producing beams of increasingly higher energies. In a synchrotron-type accelerator, the particle energy is directly proportional to the product of the machine's radius times the bending magnets' field strength. Present proton experiments at the TeV scale require facilities with circumferences ranging from a few to tens of kilometers and relying on a large number (several hundreds to several thousands) of high field dipole magnets and high field gradient quadrupole magnets. These electro-magnets use high current density, low critical temperature superconducting cables and are cooled down at liquid helium temperature. They are among the most costly and the most challenging components of the machine.

After explaining what are the various types of accelerator magnets and why they are needed (section 1), we present a brief history of large superconducting particle accelerators, and we detail ongoing superconducting accelerator magnet R&D programs around the world (section 2). Then, we review the superconducting materials that are available at industrial scale (chiefly, NbTi and Nb_3Sn), and we describe the manufacturing of NbTi wires and cables (section 3). We also present the difficulties of processing and insulating Nb_3Sn conductors, which, so far, have limited the use of this material in spite of its superior performances. We continue by presenting the complex formalism used to represent two-dimensional fields (section 4), and we discuss the two-dimensional current distributions that are the most appropriate for generating pure dipole and pure quadrupole fields (section 5). We explain how these ideal distributions can be approximated by so-called $\cos\theta$ and $\cos 2\theta$ coil designs and we describe the difficulties of realizing coil ends. Next, we present the mechanical design concepts that have been developed to restrain magnet coils and to ensure proper conductor positioning (section 6). We also show how these concepts have evolved in time to accommodate higher and higher Lorentz forces. We follow by presenting the complex formalism used to describe magnetic measurement systems based on rotating pick-up coil arrays (section 7), and we summarize the various sources of field errors (section 8). Finally, after describing the cooling schemes that have been implemented in large superconducting particle accelerators (section 9), we discuss issues related to quench performance (section 10) and to quench protection (section 11).

FOREWORD

This review is a work in progress and is the fourth version of a paper initially prepared for the Wiley Encyclopedia of Electrical and Electronics Engineering. The references of the first three versions are

• A. Devred, "Superconducting magnets for particle accelerators and storage rings." In J.G. Webster (ed.), *Wiley Encyclopedia of Electrical and Electronics Engineering*, New York, NY: John Wiley & Sons, Vol. 20, pp. 743–762, 1999.

• A. Devred, "Review of superconducting storage-ring dipole and quadrupole magnets." In S. Turner (ed.), *Proc. of the CERN Accelerator School on Measurement and Alignment of Accelerator and Detector Magnets*, CERN 98–05, Geneva, Switzerland: CERN, pp. 43–78, 1998.

• A. Devred, "Review of superconducting dipole and quadrupole magnets for particle accelerators," DAPNIA/STCM Preprint 98–07, August 1998.

Compared to the last version, the main additions are: a more detailed description of the magnet systems for large particle accelerators (section 1), a status report on LHC magnets and a review of ongoing accelerator magnet R&D programs around the world (section 2), and more thorough presentations of the complex formalism used for magnetic field and magnetic flux computations (sections 4 and 7).

These additions rely extensively on the material assembled for a series of lectures taught at the US Particle Accelerator School at Argonne National Laboratory, sponsored by the University of Chicago, June 14–25, 1999. A compilation of the viewgraphs used during these lectures can be found in

• A. Devred, "Argonne Lectures on Particle Accelerator Magnets," DAPNIA/STCM Preprint 99–05, Volumes A, B, and C, September 1999.

Comments and suggestions are welcome.

CONTENTS

1	**MAGNET SYSTEMS FOR LARGE PARTICLE ACCELERATORS**	**1**
1.1	On the Need of High Energy Accelerators	1
1.2	Accelerator Chains	1
1.2.1	Linear and Circular Accelerators	1
1.2.2	Example: CERN Accelerator Complex	1
1.3	Synchrotron-Type Accelerators	4
1.3.1	Accelerator Main Ring	4
1.3.2	Charged Particle Acceleration	5
1.3.3	Charged Particle Guiding and Focusing	6
1.3.4	Beam Energy Versus Bending Radius	7
1.4	Layout of Large Circular Accelerators	7
1.4.1	Magnet Classification	7
1.4.2	Arc Magnets	8
1.4.3	Insertion and Final Focusing Magnets	8
1.4.4	Detector Magnets	8
1.4.5	Example: LHC at CERN	9
1.4.5.1	Layout	9
1.4.5.2	LHC Arcs	10
1.4.5.3	LHC Insertion Regions	10
1.4.5.4	LHC Experiments	11
1.5	Dipole and Quadrupole Magnets	14
1.5.1	Coordinate System Definitions	14
1.5.2	Normal Dipole Magnet	15
1.5.3	Normal Quadrupole Magnet	16
2	**SUPERCONDUCTIVITY APPLIED TO PARTICLE ACCELERATOR MAGNETS**	**19**
2.1	Why Superconductivy?	19
2.2	Review of Large Superconducting Particle Accelerators	20
2.2.1	Tevatron	20
2.2.2	HERA	21
2.2.3	UNK	21
2.2.4	SSC	22
2.2.5	RHIC	23

2.2.6 LHC 23
2.2.6.1 Overview, Cost and Funding 23
2.2.6.2 Sharing of the Work on Superconducting Magnet Development 25
2.2.6.3 Status of Cable and Magnet Programs 25
2.3 Prominent Features of Superconducting Accelerator Magnets 27
2.4 Superconducting Accelerator Magnet R&D 29
2.4.1 State of the Art in NbTi Dipole Magnets at 1.8 K 29
2.4.1.1 Overview 29
2.4.1.2 LHC Dipole Magnet Models 29
2.4.1.3 LBNL Dipole Magnet Model D19 32
2.4.1.4 Dipole Magnet for the CERN Cable Test Facility 32
2.4.2 State of the Art in Nb_3Sn Dipole Magnets 33
2.4.2.1 Overview 33
2.4.2.2 Twente University Dipole Magnet Model MSUT 33
2.4.2.3 LBNL Dipole Magnet Model D20 33
2.4.3 Ongoing R&D Programs 34

3 CONDUCTOR AND CONDUCTOR INSULATION FOR PARTICLE ACCELERATOR MAGNETS 37
3.1 Review of Superconducting Materials 37
3.1.1 Niobium-Titanium Alloy 37
3.1.2 Nb_3Sn Compound 38
3.1.3 High Temperature Superconductors 38
3.2 Superconducting Multifilamentary Composites 38
3.3 Transition of Multifilamentary Wires 39
3.3.1 Voltage-Current Curve 39
3.3.2 Critical Current 39
3.3.3 N-Value 41
3.4 NbTi Wires 42
3.4.1 Processing 42
3.4.2 Design and Manufacturing Issues 43
3.4.3 Critical Surface Parametrization 45
3.5 Nb_3Sn Wires 45
3.5.1 Processing 45
3.5.2 Critical Surface Parametrization 46
3.6 Rutherford-Type Cable 47
3.7 Cable Insulation 50
3.7.1 Insulation Requirements 50

3.7.2 Insulation of NbTi Cables 50
3.7.3 Insulation of Nb_3Sn Cables 51

4 COMPLEX FORMALISM FOR TWO-DIMENSIONAL FIELDS 53
4.1 Conductor Model And Problem Symmetry 53
4.2 Properties Derived From Biot and Savart's Law 53
4.3 Properties Derived From Maxwell-Gauss' Equation 54
4.4 Properties Derived From Maxwell-AmpEre's Equation 54
4.5 Complex Magnetic Flux Density Outside the Conductors 55
4.6 Complex Magnetic Flux Density Inside the Conductors 56
4.7 Integral Formulae for computing Two-Dimensional Magnetic Flux densities 57
4.7.1 Conductor Model And Notations 57
4.7.2 Properties Derived From Cauchy's Integral Formulae 57
4.7.3 Practical Formulae For Magnetic Flux Density Computation 58
4.7.4 Example: Cylindrical Conductor With Circular Cross-Section 59
4.8 Multipole Expansion For Two-Dimensional Fields 61
4.8.1 Power Series Expansion 61
4.8.2 Interpretation of Power Series Expansion Coefficients 62
4.8.2.1 Coefficients of Order n = 1 62
4.8.2.2 Coefficients of Order n = 2 63
4.8.2.3 Coefficients of Order n 63
4.8.3 Reference Radius 64
4.8.4 Coordinate System Transformations 64
4.8.4.1 Translation 64
4.8.4.2 Rotation 66
4.8.4.3 Change of x-axis Orientation 67
4.8.4.4 Change of y-axis Orientation 68
4.9 Magnetic Flux Densities Produced By Simple Current Distributions 70
4.9.1 Single Current Line in Free Space 70
4.9.1.1 At the Origin of the Coordinate System 70
4.9.1.2 Outside the Origin of the Coordinate System 70
4.9.1.3 Power Series Expansion 71
4.9.2 Single Current Line Within a Circular Iron Yoke 72
4.9.3 Quadruplet of Current Lines with Dipole Symmetry 73
4.9.4 Octuplet of Current Lines with Quadrupole Symmetry 75
4.9.5 $\mathrm{Cos}p\theta$ and $\mathrm{Sin}p\theta$ Current Sheets 75
4.9.6 Cylindrical Current Shells 76

4.9.7 Cylindrical Current Shells Within a Circular Iron Yoke 78
4.9.8 Cylindrical Current Shell Assemblies with Multiple Layers 79
4.9.9 Cylindrical Current Shells with Angular Wedges 80

5 MAGNETIC DESIGN OF PARTICLE ACCELERATOR MAGNETS 83
5.1 Two-Dimensional Geometry 83
5.1.1 Symmetry Considerations 83
5.1.2 Current Shell Approximations 83
5.1.3 Iron Yoke Contribution 84
5.1.4 Computing Transport Current Field 85
5.1.5 Operating Current Margin 87
5.1.6 Conductor Grading 88
5.1.7 Limits of Cosθ Coil Design 89
5.2 Coil End Design 90
5.3 Sagitta 90

6 MECHANICAL DESIGN OF PARTICLE ACCELERATOR MAGNETS 93
6.1 Support Against the Lorentz Force 93
6.1.1 Components of the Lorentz Force 93
6.1.2 Stability Against Mechanical Disturbances 93
6.1.3 Conceptual Design 93
6.2 Azimuthal Pre-Compression 94
6.2.1 Preventing Collar Pole Unloading 94
6.2.2 Pre-Compression Requirements 94
6.2.3 Choice of Collar Material 95
6.3 Radial Support 96
6.3.1 Limiting Radial Deflections 96
6.3.2 Seeking Yoke Support 96
6.3.3 Mechanical Design with Fully Mated Yoke Assembly 97
6.3.4 Mechanical Design with Yoke Midplane Gap at Room Temperature 97
6.3.5 RHIC Magnets 99
6.4 End Support 100

7 COMPLEX FORMALISM FOR PICK-UP COILS ROTATING IN A TWO DIMENSIONAL FIELD 101
7.1 Conductor Model and Notations 101
7.2 Complex potential 101

7.2.1 Vector Potential 101
7.2.2 Scalar Potential 102
7.2.3 Complex Potential Definition 102
7.2.4 Relationship Between Complex Potential and Complex Magnetic Flux Density 103
7.2.5 Power Series Expansion of Complex Potential 103
7.3 Magnetic Flux Trough a Surface 104
7.4 Magnetic Flux Picked-Up by a Rotating Coil 106
7.5 Voltage Induced in a Rotating Pick-Up Coil 107
7.6 Magnetic Flux Picked-Up by a Rotating Coil Array 108
7.7 Effective Voltage Readout from a Rotating Pick-Up Coil Array 108
7.8 Examples of Rotating Pick-Up Coils and Pick-Up Coil Arrays 109
7.8.1 Notations 109
7.8.2 Radial coils 110
7.8.2.1 Definition 110
7.8.2.2 Sensitivity Factors 110
7.8.2.3 Magnetic Flux and Induced Voltages 111
7.8.2.4 Case of a Radial Pick-Up Coil with a Thick Winding 111
7.8.2.5 Case of an Imperfect Radial Pick-Up Coil 116
7.8.3 Tangential Coils 118
7.8.3.1 Definition 118
7.8.3.2 Sensitivity Factors 119
7.8.3.3 Magnetic Flux and Induced Voltages 119
7.8.3.4 Case of a Tangential Pick-Up Coil With a Thick Winding 120
7.8.3.5 Case of an Imperfect Tangential Pick-Up Coil 123
7.8.4 Morgan Coil Arrays 124
7.8.4.1 Dipole Coils 124
7.8.4.2 Quadrupole Coil Array 125
7.8.4.3 2P-Pole Coil Array 126
7.9 Effects of Imperfections in Pick-Up Coil Rotation 128
7.9.1 Notations 128
7.9.2 Effects of Transverse Displacements of Rotation Axis 128
7.9.2.1 Basic Equations 128
7.9.2.2 Case of a Transverse Displacement in a Pure Dipole Field 129
7.9.2.3 Case of a Transverse Displacement in a Pure Quadrupole Field 129
7.9.2.4 Case of a Periodic Transverse Displacement in a Pure Quadrupole Field 130
7.9.2.5 Case of a Translation in a Pure Quadrupole Field 131
7.9.2.6 Case of a Cos(pθ) Displacement in a Pure Quadrupole Field 132
7.9.2.7 Case of a Sin(pθ) Displacement in a Pure Quadrupole Field 133

7.9.2.8 Case of a Transverse Displacement in a Pure 2n-Pole Field 133
7.9.3 Effects of Angular Shifts Between Angle Encoder and Coil 134
7.9.3.1 Basic Equations 134
7.9.3.2 Case of a Pure 2n-Pole Field 135
7.9.3.3 Approximation for Small Angular Shifts 135
7.9.3.4 Approximation for Small, Periodic Angular Shifts 135
7.9.3.5 Case of Small Angular Shifts in $Cos(p\theta_m)$ 137
7.9.3.6 Case of Small Angular Shifts in $Sin(p\theta_m)$ 138
7.9.4 Origins of Spurious Quadrupole Fields in a Pure Dipole Field Measured with a Rotating Pick-Up Coil 139
7.9.5 Origins of Spurious Sextupole Fields in a Pure Quadrupole Field Measured with a Rotating Pick-Up Coil 139

8 FIELD QUALITY OF PARTICLE ACCELERATOR MAGNETS 141
8.1 Multipole Expansion 141
8.2 Field Quality Requirements 141
8.3 Field Quality Measurements 142
8.3.1 Magnetic Measurement Systems 142
8.3.2 Field Errors Classification 142
8.4 Geometric Errors 143
8.4.1 Types of Geometric Errors 143
8.4.2 Effects of Azimuthal Coil Size Mismatch 143
8.5 Iron Saturation 144
8.6 Superconductor Magnetization 145
8.6.1 Critical State Model 145
8.6.2 Effects of Superconductor Magnetization 145
8.6.3 Time Decay 146
8.7 Coupling Currents 146
8.8 Longitudinal Periodicity 148

9 PARTICLE ACCELERATOR MAGNET COOLING 149
9.1 Superconductor Critical Temperature 149
9.2 Magnet Critical Temperature at a Given Current 149
9.3 Temperature and Enthalpy Margins 150
9.4 Effects of Beam Losses 151
9.5 Helium Cooling 152
9.6 Saturated Helium I Versus Supercritical Helium 153
9.7 Helium-I Cryogenic Systems 154

9.8 Superfluid Helium 154
9.9 Helium-II Cryogenic systems 155
9.10 Magnet Cryostat 156

10 QUENCH PERFORMANCE OF PARTICLE ACCELERATOR MAGNETS 157
10.1 What is a Quench? 157
10.2 Magnet Training and Quench Plateau 157
10.3 Accuracy of Short Sample Current Limit Estimations 159
10.4 Quench Origins 160
10.5 Discriminating Between Conductor-Limited and Mechanically-Induced Quenches 161
10.6 Mechanical Training 162
10.7 Quench Performance as a Function of Ramp Rate 162
10.8 Specification on Quench Performance 165

11 QUENCH PROTECTION OF PARTICLE ACCELERATOR MAGNETS 167
11.1 The Effects of a Quench 167
11.1.1 Conductor Heating 167
11.1.2 Maximum Temperature Requirement 167
11.1.3 Protecting a Quenching Magnet 168
11.2 Hot Spot Temperature 168
11.2.1 Estimating Hot Spot Temperature 168
11.2.2 Limiting Hot Spot Temperature 169
11.3 Quench Detection 169
11.4 Protection of a Single Magnet 170
11.4.1 Current Discharge 170
11.4.2 Maximum Voltage to Ground 170
11.4.3 Quench Protection Heaters 171
11.5 Protection of a Magnet String 171

12 CONCLUSION AND PERSPECTIVES 175

ACKNOWLEDGMENTS 176

REFERENCES 177

NOMENCLATURE

ROMAN LETTERS

$\mathbf{a} = R\,e^{i\alpha}$	Position in the complex plane of a generic current line.
$\mathbf{a}^*$	Complex conjugate of **a**.
A_1	Skew dipole field coefficient (T).
$\mathbf{A_1}, \mathbf{A_2}, \mathbf{A_3}, \mathbf{A_4}$	Positions in the complex plane of the four corners of a given turn of a magnet coil assembly.
$A_1^s,\ A_2^s,\ A_3^s$	Spurious skew dipole, quadrupole and sextupole field coefficients produced by imperfections in pick-up coil rotation (T).
a_2	Skew quadrupole coefficient (dimensionless).
A_2	Skew quadrupole field coefficient (T).
a_3	Skew sextupole coefficient (dimensionless).
A_3	Skew sextupole field coefficient (T).
$\mathbf{a_j}$	Positions in the complex plane of the current lines used for the computation of the transport-current field produced by a given turn of a magnet coil assembly wound from a Rutherford-type cable.
$\mathbf{a}_j^*$	Complex conjugate of $\mathbf{a_j}$.
$\mathbf{a_m} = R_y^2 / \mathbf{a}^*$	Position in the complex plane of the mirror image of a current line located within an iron yoke.
$\overrightarrow{A_M}$	Vector potential at M.
$A_{M,z}$	z-components of $\overrightarrow{A_M}$.
a_n	Skew $2n$-pole coefficient (dimensionless).
A_n	Skew $2n$-pole field coefficient (T).
A_n'	Transformed skew $2n$-pole field coefficient after a change of reference radius or a change of coordinate system (T).
A_n^{line}	Skew $2n$-pole field coefficient produced by a current line alone in free space (T).
A_n^{tot}	Resulting skew $2n$-pole field coefficient produced by a current line located within an iron yoke (T).
A_n^{yoke}	Contribution of the iron yoke to the skew $2n$-pole field coefficient (T).
A_p	Skew $2p$-pole field coefficient (T).

A^{s}_{p-n}, A^{s}_{p-1}, A^{s}_{p}, A^{s}_{p+1}, A^{s}_{p+n}	Spurious skew multipole field coefficients produced by imperfections in pick-up coil rotation.
B	Modulus of $\vec{B}$ (T).
$\vec{B}$	Magnetic flux density vector.
$\mathbf{B(s)}$	Complex magnetic flux density.
$\mathbf{[B(s)]^*}$	Complex conjugate of **B(s)**.
$\mathbf{B'}$	Image of **B** in a coordinate system transformation.
$\mathbf{(B')^*}$	Complex conjugate of **B'**.
$\mathbf{B^{(n)}(s)}$	n-th derivative of **B** with respect to **s**.
$\mathbf{B^{yoke}}$	Contribution of the iron yoke to the complex magnetic flux density.
B_1	Dipole field strength or normal dipole field coefficient (T).
B^{s}_{1}, B^{s}_{2}, B^{s}_{3}	Spurious normal dipole, quadrupole and sextupole field coefficients produced by imperfections in pick-up coil rotation (T).
b_2	Normal quadrupole coefficient (dimensionless).
B_2	Normal quadrupole field coefficient (T).
B_{2k+1}	Allowed multipole field coefficients for a current distribution with a dipole symmetry (T).
b_3	Normal sextupole coefficient (dimensionless).
B_3	Normal sextupole field coefficient (T).
B_{4k+2}	Allowed multipole field coefficients for a current distribution with a quadrupole symmetry (T).
B_5	Normal decapole field coefficient (T).
B_6	Normal dodecapole field coefficient (T).
B_7	Normal 14-pole field coefficient (T).
B_9	Normal 18-pole field coefficient (T).
B_{10}	Normal 20-pole field coefficient (T).
B_{11}	Normal 22-pole field coefficient (T).
B_{14}	Normal 28-pole field coefficient (T).
$B_{C2}(T)$	Upper critical magnetic flux density at T (T).
B_{C20}	Upper critical magnetic flux density at $T = 0$ K (T).
B_{C20m}	Upper critical magnetic flux density at $T = 0$ K and $\varepsilon = 0$ (T).
$\mathbf{B_E(s)} = B_y + i\,B_x$	Complex magnetic flux density outside conductors.
$\mathbf{B_I(s)} = B_y + i\,B_x - \frac{\mu_0 J_0}{2}\,\mathbf{s^*}$	Complex magnetic flux density inside conductors.
$\overrightarrow{B_M}$	Magnetic flux density vector at M.

$B_{M,x}$, $B_{M,y}$, $B_{M,z}$	x-, y- and z-components of $\overrightarrow{B_M}$.
b_n	Normal $2n$-pole coefficient (dimensionless).
B_n	Normal $2n$-pole field coefficient (T).
$B_n^{'}$	Transformed normal $2n$-pole field coefficient after a change of reference radius or a change of coordinate system (T).
B_n^{line}	Normal $2n$-pole field coefficient produced by a current line alone in free space (T).
B_n^{shell}	Normal $2n$-pole field coefficient produced by a current shell alone in free space (T).
B_n^{tot}	Resulting normal $2n$-pole field coefficient produced by a current line located within an iron yoke (T).
B_n^{yoke}	Contribution of the iron yoke to the normal $2n$-pole field coefficient (T).
B_p	Normal $2p$-pole field coefficient (T).
B_{peak}	Peak magnetic flux density on a magnet coil (T).
B^s_{p-n}, B^s_{p-1}, B^s_p, B^s_{p+1}, B^s_{p+n}	Spurious normal multipole field coefficients produced by imperfections in pick-up coil rotation.
B_x, B_y, B_z	x-, y- and z-components of $\vec{B}$.
c	Complex integration constant.
$C_{cond}(T)$	Specific heat per unit volume of conductor (J/m^3).
c_D	Complex constant appearing in the magnetic flux picked-up by a rotating coil affected by transverse displacements of rotation axis.
$C^p_{n-1} = \frac{(n-1)!}{p!(n-p-1)!}$	
$C^p_n = \frac{n!}{p!(n-p)!}$	
cos( )	cosine function.
cot( )	cotangent function.
coth( )	hyperbolic cotangent function.
c_ϑ	Real constant appearing in the magnetic flux picked-up by a rotating coil affected by angular shifts.
$D(\varepsilon) = D_{Nb_3Sn}\,(1-\beta\,\lvert\varepsilon\rvert^{1.7})^{1/2}$	Strain-dependent function appearing in the parametrization of the critical surface of Nb_3Sn.
$\mathbf{D}(\theta)$	Transverse displacement in the complex plane of the rotation axis of a pick-up coil.

$\mathbf{D_{-4}}$, $\mathbf{D_{-1}}$, $\mathbf{D_0}$, $\mathbf{D_2}$	Complex coefficients of order (–4), (–1), 0 and 2 in the Fourier expansion of $\mathbf{D}(\theta)$.
$\mathbf{D}^*_{-4}$	Complex conjugate of $\mathbf{D_{-4}}$.
$\mathbf{D_{max}}$	Maximum amplitude of transverse displacements in $\cos(p\theta)$ or $\sin(p\theta)$.
$\mathbf{D}^*_{\mathbf{max}}$	Complex conjugate of $\mathbf{D_{max}}$.
D_{Nb_3Sn}	Fitting parameter appearing in the parametrization of the critical surface of Nb_3Sn ($AT^{1/2}mm^{-2}$).
D_{NbTi}	Fitting parameter appearing in the parametrization of the critical surface of NbTi (T).
$\mathbf{D_{-p-1}}$, , $\mathbf{D_{-p}}$, $\mathbf{D_{p-1}}$, $\mathbf{D_p}$	Complex coefficients of the Fourier expansion of $\mathbf{D}(\theta)$.
$\mathbf{D}^*_{\mathbf{-p-1}}$, $\mathbf{D}^*_{\mathbf{-p}}$	Complex conjugate of $\mathbf{D_{-p-1}}$ and $\mathbf{D_{-p}}$.
d_{wire}	Wire diameter (m).
da	Elementary variation of **a**.
$\overrightarrow{dl}$	Arc element vector.
dR	Elementary variation of R (m).
$\mathbf{ds} = dx + i\,dy$	Elementary variation of **s**.
$\overrightarrow{dS}$	Surface element vector.
dV_G	Elementary volume in the vicinity of G.
dx, dy	Elementary variations of x and y (m).
$d\alpha$	Elementary variation of α (rad).
$d\theta$	Elementary variation of θ (rad).
$e^{()}$	Exponential function.
$\vec{E}$	Electric field vector.
$E(\Gamma_{cond})$	Exterior of Γ_{cond}.
$\overline{E(\Gamma_{cond})} = E(\Gamma_{cond}) \cup \Gamma_{cond}$	
$E(\Gamma_R)$	Exterior of Γ_R.
$E_C = 0.1\ \mu V/cm$	Electric field criterion for the determination of the critical current of a superconducting multifilamentary composite wire.
E_{coil}	Coil Young's modulus (in the azimuthal direction; MPa).
E_{super}	Apparent electric field in the superconductor of a multifilamentary composite wire switching to the normal resistive state (V/m).
$\overrightarrow{F_C} = q\ \vec{E}$	Coulomb's force vector.
$\overrightarrow{F_L} = q\ \overrightarrow{v_q} \times \vec{B}$	Lorentz' force vector.
$f(I)$	Given function of I.

$f(B,T_0)$	Given function of B and T_0.
$f_{\text{quad}} \approx \frac{1}{\sqrt{\kappa_g}} \cot\left(\sqrt{\kappa_g}\, l_{\text{quad}}\right)$	Normal quadrupole magnet focusing length (m).
$f'_{\text{quad}} \approx \frac{-1}{\sqrt{\kappa_g}} \coth\left(\sqrt{\kappa_g}\, l_{\text{quad}}\right)$	Normal quadrupole magnet defocusing length (m).
g	Quadrupole field gradient (T/m).
G	A given point within a conductor.
G_p	Gain of the channel of the electronic card channel to which is connected the p-th coil of a rotating pick-up coil array (dimensionless).
$\vec{H}$	Magnetic field vector.
h_{rad}	Height of the winding groove of a radial pick-up coil with a thick winding (m).
h_{tan}	Height of the winding groove of a tangential pick-up coil with a thick winding (m).
i	Pure imaginary number of modulus 1.
I	Current intensity (A).
$\mathrm{I}(\Gamma_{\text{cond}})$	Interior of Γ_{cond}.
$\overline{\mathrm{I}(\Gamma_{\text{cond}})} = \mathrm{I}(\Gamma_{\text{cond}}) \cup \Gamma_{\text{cond}}$	
$\mathrm{I}(\Gamma_R)$	Interior of Γ_R.
$I_0 = \pi R^2 J_0$	Current intensity in a cylindrical conductor of radius R (A)
I_C	Critical current (A).
I_{C1}	Critical current determined according to the electric field criterion (A).
I_{C2}	Critical current determined according to the resistivity criterion (A).
I_f	Pre-cycle flattop current (A).
$I_m = \frac{\mu - 1}{\mu + 1} I$	Intensity of the mirror image of a current line located within an iron yoke.
I_{mag}	Magnet current (A).
$I_n^{\tan}$	Imaginary part of the sensitivity factor of order n of a tangential pick-up coil (m^2).
I_{op}	Operating current (A).
I_q	Quench current (A).
$I_{qm}(T_0)$	Maximum quench current of a magnet at T_0 (K).
$I_{ss}(T_0)$	Short sample current limit of a magnet at T_0 (K).
I_{wire}	Current supplied to a wire (A).

$\mathrm{Im}(\ )$	Imaginary part function.
j	integer.
j_{sheet}	Linear current density of a current sheet (A/m).
J	Current density (A/m^2).
$\vec{\mathrm{J}}$	Current density vector.
J_0	A given current density value (A/m^2).
J_1^{rad}	Real part of the sensitivity factor of order 1 of an ideal radial pick-up coil (m^2).
J_{C}	Critical current density (A/m^2).
J_{Cref}	Critical current density of a NbTi wire at 4.2 K and 5 T (A/m^2).
$\overrightarrow{\mathrm{J_G}}$	Current density vector at G.
$J_{\mathrm{G},z}(x,y)$	z-component of $\overrightarrow{\mathrm{J_G}}$.
J_{in}	Current density in the innermost layer of a multiple layer coil assembly (A/m^2).
$J_{\mathrm{m}}(x,y) = \frac{\mu-1}{\mu+1}\frac{R_{\mathrm{o}}^2 R_{\mathrm{i}}^2}{R_{\mathrm{y}}^4} J$	Current density of the mirror image of a cylindrical current shell located within an iron yoke (A/m^2).
$J_{\mathrm{n}}^{\mathrm{dip}}$	Real part of the sensitivity factor of order n of a dipole pick-up coil (m^2).
$J_{\mathrm{n-1}}^{\mathrm{rad}}$, $J_{\mathrm{n}}^{\mathrm{rad}}$	Real parts of the sensitivity factors of order (n-1) and n of an ideal radial pick-up coil (m^2).
J_{out}	Current density in the outermost layer of a multiple layer coil assembly (A/m^2).
$J_{\mathrm{z}}(x,y)$	z-component of $\vec{\mathrm{J}}$.
k	Integer.
$\mathbf{K_1}$, $\mathbf{K_2}$, $\mathbf{K_3}$	Sensitivity factors of order 1, 2 and 3 of a rotating pick-up coil.
$\mathbf{K_1^*}$, $\mathbf{K_2^*}$	Complex conjugate of $\mathbf{K_1}$ and $\mathbf{K_2}$.
$\mathbf{K_1^{rad}}$	Sensitivity factor of order 1 of a radial coil.
$\mathbf{K_n}$	Sensitivity factor of order n of a rotating pick-up coil.
$\mathbf{K_n^*}$	Complex conjugate of $\mathbf{K_n}$.
$\mathbf{K_n^{2P\text{-}pole}}$	Resulting sensitivity factor of order n of a Morgan $2P$-pole coil array.
$\mathbf{K_n^{array}}$	Resulting sensitivity factor of order n of a rotating pick-up coil array.

$\mathbf{K_n^{C_p}}$	Sensitivity factor of order n of the p-th coil of a rotating pick-up coil array.
$\mathbf{K_n^{dip}}$	Sensitivity factor of order n of a dipole pick-up coil.
$\mathbf{K_n^{out}}$	Effective sensitivity factor of order n of a rotating pick-up coil array connected to a multiple channel electronic card.
$\mathbf{K_n^{Q_1}}$, $\mathbf{K_n^{Q_2}}$	Sensitivity factors of order n of the elementary tangential coils making up a quadrupole pick-up coil array.
$\mathbf{K_n^{quad}}$	Resulting sensitivity factor of order n of a quadrupole pick-up coil array.
$\mathbf{K_n^{rad}}$	Sensitivity factor of order n of a radial pick-up coil.
$\mathbf{K_n^{T_1}}$, $\mathbf{K_n^{T_p}}$	Sensitivity factors of order n of the elementary tangential coils making up a $2P$-pole pick-up coil array.
$\mathbf{K_n^{tan}}$	Sensitivity factor of order n of a tangential pick-up coil.
$\mathbf{K_{p-n}}$, $\mathbf{K_{p-1}}$, $\mathbf{K_p}$, $\mathbf{K_{p+1}}$, $\mathbf{K_{p+n}}$	Sensitivity factors of order $(p\text{-}n)$, $(p\text{-}1)$, p, $(p+1)$ and $(p+n)$ of a rotating pick-up coil.
L	A given length value (m).
l_{dip}	Magnetic length of a dipole magnet (m).
L_{mag}	Total inductance of a magnet (H).
$L_{pick\text{-}up}$	Length of a rotating pick-up coil (m).
l_{quad}	Magnetic length of a quadrupole magnet (m).
L_{rad}	Length of a radial pick-up coil (m).
L_{tan}	Length of a tangential pick-up coil (m).
L_{wire}	Wire length (m).
ln( )	Natural logarithm function.
M	A given point of space.
M_1	Point of coordinates $(x_1, y_1, 0)$ at one extremity of Γ.
M_1^{dip}	Point of coordinates $(-R, 0, 0)$ at one extremity of Γ_{dip}.
M_1^{rad}	Point of coordinates $(R_1^{rad}, 0, 0)$ at one extremity of Γ_{rad}.
M_1^{tan}	Point of coordinates $(R_{tan}\cos\delta/2, R_{tan}\sin\delta/2, 0)$ at one extremity of Γ_{tan}.
M_2	Point of coordinates $(x_2, y_2, 0)$ at the extremity of Γ opposite to M_1.
M_2^{dip}	Point of coordinates $(R, 0, 0)$ at the extremity of Γ_{dip} opposite to M_1^{dip}.

M_2^{rad}	Point of coordinates (R_2^{rad},0,0) at the extremity of Γ_{rad} opposite to M_1^{rad}.
M_2^{tan}	Point of coordinates ($R_{tan}\cos\delta/2$,$-R_{tan}\sin\delta/2$,0) at the extremity of Γ_{tan} opposite to M_1^{tan}.
M_3	Point of coordinates (x_2, y_2,$L_{pick\text{-}up}$).
M_4	Point of coordinates (x_1, y_1,$L_{pick\text{-}up}$).
$m_i(T_0)=1-I_{op}/I_{qm}(T_0)$	Operating current margin of a superconducting magnet at T_0 (dimensionless).
n	Integer.
N	Resistive transition index (dimensionless) or a given integer value.
N_{cable}	Number of cable strands.
N_l	Number of current lines in the current line model used for the computation of the transport-current field produced by a given turn of a magnet coil assembly wound from a Rutherford-type cable.
$N_{pick\text{-}up}$	Number of turns of a rotating pick-up coil.
N_{rad}	Number of turns of a radial pick-up coil.
N_{tan}	Number of turns of a tangential pick-up coil.
O	A given point of the design orbit of an accelerator ring.
O'	Image of O in a coordinate system transformation.
p	Integer.
P	A given integer.
p_{cable}	Rutherford-type cable pitch length (m).
q	Particle charge (Cb).
Q_1, Q_2	Tangential coils making up a quadrupole pick-up coil array.
q_e	Particle charge in units of electron charge (dimensionless).
R	Modulus of **a** or a given radius value (m).
R_1^{rad}	Radius of M_1^{rad} (m).
R_2^{rad}	Radius of M_2^{rad} (m).
$R_a^{rad}=\left(R_i^{rad}+R_o^{rad}\right)/2$	
$R_a^{tan}=\left(R_i^{tan}+R_o^{tan}\right)/2$	
R_b	Resistance of the bypass elements used in the protection of a string of superconducting magnets (Ω).

R_c^{rad}	Distance between the central axis of a radial pick-up coil and the z-axis (m).
R_c^{tan}	Distance between the central axis of a tangential pick-up coil and the z-axis (m).
R_{collar}	Collar outer radius (m).
R_{ext}	External resistance used for the quench protection of a superconducting magnet (Ω).
R_i	Inner radius of a cylindrical current shell or of a magnet coil assembly (m).
R_i^{in}	Inner radius of the innermost cylindrical current shell in a multiple-layer current shell assembly (m).
R_i^{out}	Inner radius of the outermost cylindrical current shell in a multiple-layer current shell assembly (m).
R_i^{rad}	Distance between the bottom of the winding groove and the central axis of a radial pick-up coil with a thick winding (m).
R_i^{tan}	Distance between the bottom of the winding groove and the central axis of a tangential pick-up coil with a thick winding (m).
$R_{im} = R_y^2/R_o$	Inner radius of the mirror image of a cylindrical current shell located within an iron yoke (m).
R_o	Outer radius of a cylindrical current shell (m).
R_o^{in}	Outer radius of the innermost cylindrical current shell in a multiple-layer current shell assembly (m).
R_o^{out}	Outer radius of the outermost cylindrical current shell in a multiple-layer current shell assembly (m).
R_o^{rad}	Distance between the top of the winding groove and the central axis of a radial pick-up coil with a thick winding (m).
R_o^{tan}	Distance between the top of the winding groove and the central axis of a tangential pick-up coil with a thick winding (m).
$R_{om} = R_y^2/R_i$	Outer radius of the mirror image of a cylindrical current shell located within an iron yoke (m).
$R_q(t)$	Resistance of a quenching magnet (Ω).

$r_{\text{rad}} = \left(R_{\text{o}}^{\text{rad}} - R_{\text{i}}^{\text{rad}}\right)/2$	
R_{ref}	Reference radius for the power series expansion of **B** around the complex plane origin (m).
R'_{ref}	Transformed reference radius for the power series expansion of **B** around the complex plane origin (m).
$r_{\text{tan}} = \left(R_{\text{o}}^{\text{tan}} - R_{\text{i}}^{\text{tan}}\right)/2$	
R_{tan}	Radius of M_1^{tan} and M_2^{tan} (m).
R_{y}	Iron yoke inner radius (m).
Re( )	Real part function.
$\mathbf{s} = x + \text{i}\,y$	Complex variable.
s*	Complex conjugate of **s**.
s'	Image of **s** in a coordinate system transformation.
(s')*	Complex conjugate of **s'**.
$S(\Gamma_{\text{i}})$	Disk of center, O, and radius, R_{i}, located in the $(O, \vec{x}, \vec{y})$ plane.
$\mathbf{s_1} = x_1 + \text{i}\,y_1$	Position in the complex plane of M_1.
$\mathbf{s_{1,0}}$	Position of M_1 at $\theta = 0$.
$\mathbf{s_2} = x_2 + \text{i}\,y_2$	Position in the complex plane of M_2.
$\mathbf{s_{2,0}}$	Position of M_2 at $\theta = 0$.
S_{cond}	Cross-sectional area of a conductor (m^2).
S_{wire}	Cross-sectional area of a wire (m^2).
sin( )	Sine function.
t	Time (s).
t_0	Start time of the integration of the voltage readout from a rotating pick-up coil (s).
T	Temperature (K).
T_0	A given temperature value (K).
T_1, T_2, T_p	Tangential coils making up a $2P$-pole pick-up coil array.
$T_C(B)$	Critical temperature at B (K).
T_{C0}	Critical temperature at $B = 0$ T (K).
T_{C0m}	Critical temperature at $B = 0$ T and $\varepsilon = 0$ (K).
$t_{\text{cable,m}}$	Rutherford-type cable mid-thickness (m).
$T_{CI}(I)$	Magnet critical temperature at current I (K).
T_{max}	Hot spot temperature (K).
T_{op}	Operating temperature (K).
t_{quench}	Start time of a superconducting magnet quench (s).
T_{quench}	Magnet coil temperature at t_{quench} (K).

$U_{out}(t)$	Integral of V_{out} between t_0 and t (V).
$U_{pick\text{-}up}(t)$	Integral of $V_{pick\text{-}up}$ between t_0 and t (V).
$U_{rad}(t)$	Integral of V_{rad} between t_0 and t (V).
$U_{tan}(t)$	Integral of V_{tan} between t_0 and t (V).
$V(\Sigma_{cond})$	Volume inside Σ_{cond}.
$V_C = E_C L_{wire}$	Voltage across a superconducting multifilamentary composite wire sample corresponding to an apparent electric field E_C in the superconductor (V).
V_{mag}	Total voltage across a magnet (V).
$V_{out}(t)$	Effective voltage readout at the output of a multi-channel electronic card to which is connected a rotating pick-up coil array (V).
V_p	Voltage induced in the p-th coil of a rotating pick-up coil array (V).
$V_{pick\text{-}up}(t)$	Voltage induced in a rotating pick-up coil (V).
$\overrightarrow{v_q}$	Velocity vector of a particle of charge q.
$V_{rad}(t)$	Voltage induced in a radial pick-up coil (V).
$V_{tan}(t)$	Voltage induced in a tangential pick-up coil (V).
V_{wire}	Voltage across a wire sample (V).
W(s)	Complex potential.
w_{cable}	Rutherford-type cable width (m).
x	abscissa (m).
$\vec{x}$	Unit vector of a rectangular coordinate system associated with O and defining the horizontal direction.
$\vec{X}$	Unit vector of a rectangular coordinate system such that $(\Omega, \vec{X}, \vec{Z})$ defines the plane of the design orbit of an accelerator ring.
$\vec{x'}$	Image of $\vec{x}$ in a coordinate system transformation.
x_1, y_1	x- and y- coordinates of M_1.
x_2, y_2	x- and y- coordinates of M_2.
y	Ordinate (m).
$\vec{y}$	Unit vector of a rectangular coordinate system associated with O and defining the vertical direction.
$\vec{Y}$	Unit vector of a rectangular coordinate system associated with Ω, perpendicular to the plane of the design orbit of an accelerator ring.
$\vec{y'}$	Image of $\vec{y}$ in a coordinate system transformation.

Y_{n-1}^{rad}, Y_n^{rad}	Parameters appearing in the sensitivity factors of order (n-1) and n of an imperfect radial pick-up coil (m^2).
z	z-coordinate (m).
$\vec{z}$	Unit vector of a rectangular coordinate system associated with O and corresponding to the main direction of particle motion.
$\vec{Z}$	Unit vector of a rectangular coordinate system such that $(\Omega, \vec{X}, \vec{Z})$ defines the plane of the design orbit of an accelerator ring.

GREEK LETTERS

α	Argument of **a** (rad).
α_0	Pole angle of a cylindrical current shell (rad).
α_0^{in}	Pole angle of the innermost cylindrical current shell in a multiple-layer current shell assembly (rad).
α_0^{out}	Pole angle of the outermost cylindrical current shell in a multiple-layer current shell assembly (rad).
α_1, α_2	Wedge angles in a cylindrical current shell (rad).
α_{coil}, α_{collar}, α_{yoke}	Integrated thermal expansion coefficients between liquid helium temperature and room temperature of a coil assembly (in the azimuthal direction), collar material, and yoke material (m/m).
β	Fitting parameter appearing in the parametrization of the critical surface of Nb_3Sn (dimensionless).
β_1, β_2, β_3	Fitting parameters appearing in the parametrization of the critical surface of NbTi (dimensionless).
Γ	Arc located in the plane of equation (z = 0) and extending between the points M_1 and M_2.
Γ_{cond}	Arc at the intersection of Σ_{cond} with the $(O, \vec{x}, \vec{y})$ plane.
Γ_{dip}	Arc located in the plane of equation (z = 0) and extending between the points M_1^{dip} and M_2^{dip}.
Γ_i	Circle of center, O, and radius, R_i, located in the $(O, \vec{x}, \vec{y})$ plane.
Γ_R	Circle of center, O, and radius, R, located in the $(O, \vec{x}, \vec{y})$ plane.

Γ_{rad}	Arc located in the plane of equation ($z = 0$) and extending between the points M_1^{rad} and M_2^{rad}.
Γ_{tan}	Arc located in the plane of equation ($z = 0$) and extending between the points M_1^{tan} and M_2^{tan}.
δ_{rad}	Misalignment of an imperfect radial pick-up coil (rad).
δ_{tan}	Opening angle of a tangential pick-up coil (rad).
ΔH_{op}	Operating enthalpy margin (J/m^3).
Δr_{cd}	Thermal shrinkage differential between collar outer radius and yoke inner radius during magnet cooldown (m).
ΔT	A given temperature increase (K).
ΔT_0	A given increase in T_0 (K).
ΔT_{op}	Operating temperature margin (K).
$\Delta T_{qm}(I)$	Minimum temperature increase likely to initiate a quench in a superconducting magnet supplied by a current I (K).
Δh_{rad}	Deformation in the width of an imperfect radial pick-up coil (m).
Δx, Δy	Displacements along the x- and y-axes.
$\Delta\theta$	A given angle variation (rad).
$\Delta\sigma_{cd}$	Loss in magnet coil azimuthal pre-compression during cooldown (MPa).
ε	Strain (dimensionless).
ε_{GeV}	Charged particle energy in giga electron-volts.
ζ	Sign identifier.
ζ_p	Polarity of the p-th coil of a rotating pick-up coil array.
θ	Azimuth reckoned in the $(O, \vec{x}, \vec{y})$ plane with respect to a zero mark or the x-axis (rad).
θ_0	Rotating pick-up coil angle at t_0 (rad).
θ_m	Angle measured by the angle encoder attached to a rotating pick-up coil (rad).
$\kappa_g \approx 0.3\, q_e\, g/\varepsilon_{GeV}$	Normalized gradient of a quadrupole magnet $(rad/m)^2$.
K_{cable}	Overall compaction factor of a Rutherford-type cable (dimensionless).
λ_{wire}	Copper-to-superconductor or copper-to-non-copper ratio of a superconducting multifilamentary composite wire (dimensionless).
μ	Relative magnetic permeability of iron yoke (dimensionless).
$\mu_0 = 4\pi 10^{-7}$ H/m	Magnetic permeability of vacuum.

$\xi_{dip} \approx \frac{l_{dip}^2}{8\chi}$	Horizontal sagitta of an arc dipole magnet for a large accelerator ring (m).
$\pi = 3.14159265358979323846264 3$	
$\rho_C = 10^{-14}\ \Omega m$	Resistivity criterion for the determination of the critical current of a superconducting multifilamentary composite wire.
ρ_{cond}	Overall conductor resistivity in the normal state (Ωm).
ρ_{super}	Apparent resistivity of the superconductor in a multifilamentary composite wire switching to the normal resistive state (Ωm).
$\Sigma(\Gamma)$	Surface generated by translation of the arc Γ between the plane of equation ($z = 0$) and the plane of equation ($z = L$).
$\Sigma(\Gamma_{dip})$	Surface generated by translation of the arc Γ_{dip} between the plane of equation ($z = 0$) and the plane of equation ($z = L_{dip}$).
$\Sigma(\Gamma_{rad})$	Surface generated by translation of the arc Γ_{rad} between the plane of equation ($z = 0$) and the plane of equation ($z = L_{rad}$).
$\Sigma(\Gamma_{tan})$	Surface generated by translation of the arc Γ_{tan} between the plane of equation ($z = 0$) and the plane of equation ($z = L_{tan}$).
Σ_{cond}	Surface of a conductor (or of an ensemble of conductors).
$\phi_{array}(\theta)$	Total magnetic flux picked-up by a rotating coil array (Wb).
$\phi_{dip} \approx l_{dip}/\chi$	Angular deflection of a charged particle trajectory in a dipole magnet of length l_{dip} (rad).
$\phi_{out}(\theta)$	Effective magnetic flux picked-up by a rotating coil array connected to a multi-channel electronic card (Wb).
$\phi_{rad}(\theta)$	Magnetic flux picked-up by a radial coil (Wb).
ϕ_p	Magnetic flux picked-up by the p-th coil of a rotating coil array (Wb).
$\phi_{pick\text{-}up}(\theta)$	Magnetic flux picked-up by a rotating coil (Wb).
$\phi_{tan}(\theta)$	Magnetic flux picked-up by a tangential coil (Wb).
$\phi_{\Sigma(\Gamma)} = -L\ \mathrm{Re}[\mathbf{W}(\mathbf{s_2}) - \mathbf{W}(\mathbf{s_1})]$	Magnetic flux through the surface $\Sigma(\Gamma)$ (Wb).
$\chi \approx \frac{\varepsilon_{GeV}}{0.3\ q_e\ B}$	Bending radius of a charged particle trajectory in an uniform magnetic flux density (m).

ψ_{cable}	Pitch angle of a Rutherford-type cable (rad).
ψ_{M}	Scalar potential at M.
ω	Pick-up coil angular velocity around its rotation axis (rad/s).
Ω	Origin of a coordinate system associated with the design and planar orbit of an accelerator ring.
$\vartheta(\theta_{\text{m}}) = \theta - \theta_{\text{m}}$	Angular shift between between angle encoder and rotating pick-up coil (rad).
ϑ_{-5}, ϑ_{-3}, ϑ_{1}	Complex coefficients of order (–5), (–3) and 1 in the Fourier expansion of $\vartheta(\theta_{\text{m}})$.
ϑ^{*}_{-5}, ϑ^{*}_{-3}	Complex conjugates of ϑ_{-5} and ϑ_{-3}.
ϑ_{max}	Maximum amplitude of small angular shifts in $\cos(p\theta_{\text{m}})$ or $\sin(p\theta_{\text{m}})$.
ϑ_{-n-p}, ϑ_{-n}, ϑ_{-p}, ϑ_{p-n}, ϑ_{p}	Complex coefficients of the Fourier expansion of $\vartheta(\theta_{\text{m}})$.
ϑ^{*}_{-n-p}, ϑ^{*}_{-p}	Complex conjugate of ϑ_{-n-p} and ϑ_{-p}.

MATHEMATICAL SYMBOLS

$\in$	Belongs to.
$\notin$	Does not belong to.
$\cup$	Reunion of two ensembles.
!	Factorial.
x	Vectorial product.
$\vec{\nabla}() = \frac{\partial()}{\partial x}\vec{\text{x}} + \frac{\partial()}{\partial y}\vec{\text{y}} + \frac{\partial()}{\partial z}\vec{\text{z}}$	Vectorial operator.

1 MAGNET SYSTEMS FOR LARGE PARTICLE ACCELERATORS

1.1 ON THE NEED OF HIGH ENERGY ACCELERATORS

The main activity in nuclear and high-energy physics is the study of the internal structures of charged particles. The research is carried out by smashing particles into pieces and by analyzing the nature and characteristics of the pieces. The particles are broken by accelerating them to high momenta and either by blasting them against a fixed target or by colliding them among themselves. To achieve high event rates, the particles are bunched together and the bunches are formatted into high intensity beams, which are strongly focused near the targets or collision points. The more elementary the particles, the higher the energy needed to smash them. Experiments at the proton scale require beam energies of the order of 1 TeV or more (1 TeV $\approx$ 1.6 10^{-7} J) [1].

1.2 ACCELERATOR CHAINS

1.2.1 LINEAR AND CIRCULAR ACCELERATORS

There are two main types of particle accelerators: (1) linear accelerators, referred to as *linacs*, and (2) circular accelerators. In a linac, the charged particles travel along a mostly straight trajectory and go successively through a large number of accelerating stations. In a circular accelerator, the beam is circulated many times around a closed orbit. A circular accelerator only relies on a few accelerating stations, through which the charged particles go at every turn, but it requires a large number of guiding elements, which are distributed over the accelerator arcs. The most powerful machines are made up of several stages, which progressively raise the beam energy. Each stage is a fully-fledged accelerator, which can be of either type.

1.2.2 EXAMPLE: CERN ACCELERATOR COMPLEX

As an illustration, Figure 1 shows an aerial view of the accelerator chain presently running at the European Laboratory for Particle Physics (CERN). The CERN complex, located at the French/Swiss border near Geneva, Switzerland, includes several linear accelerators and four circular machines: (1) the Proton Synchrotron Booster (PSB), (2) the Proton Synchrotron (PS), (3) the Super Proton Synchrotron (SPS), and (4) the Large Electron Positron (LEP) collider.

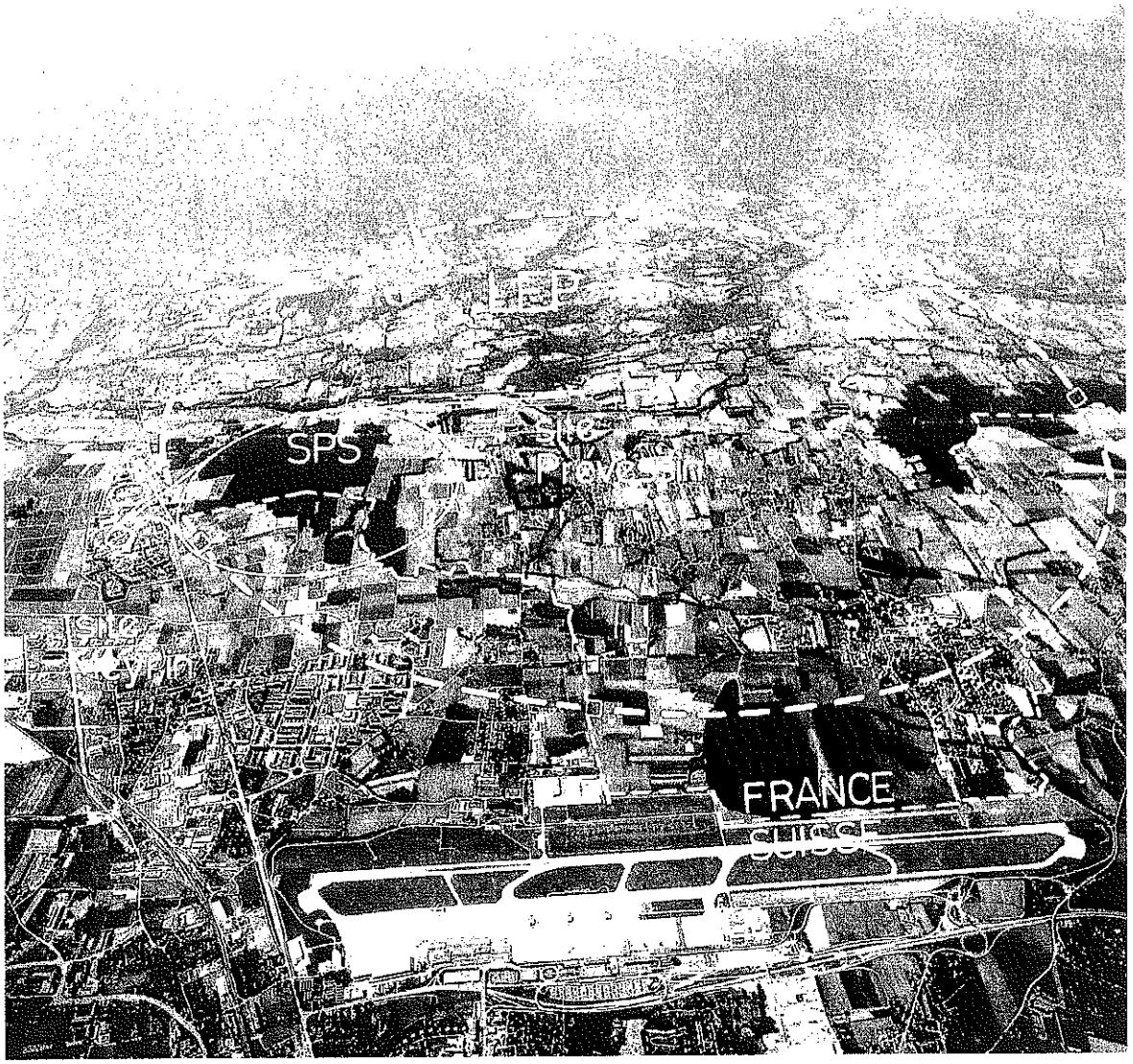

Figure 1. Aerial view of the site of the CERN accelerator complex. The scale is given by Geneva airport, which is visible at the bottom of the photograph.

The Proton Synchrotron Booster has a 50 m diameter and can accelerate protons up to 1 GeV (1 GeV $\approx$ 1.6 10^{-10} J). The Proton Synchrotron has a 200-m diameter. It was commissioned in November 1959 and can accelerate protons up to 26 GeV. The Super Proton Synchrotron has a circumference of 6.9 km and is installed in an underground tunnel at a depth varying from 25 to 65 m. It was commissioned in September 1976 and can raise proton energy up to 450 GeV. The largest ring of the CERN complex is the LEP collider, with a 27-km circumference [2]. It is installed in an underground tunnel at a depth varying from 50 to 150 m. It was commissioned in July 1989 and is operated as an electron/positron collider with energy of the order of 100 GeV per beam.

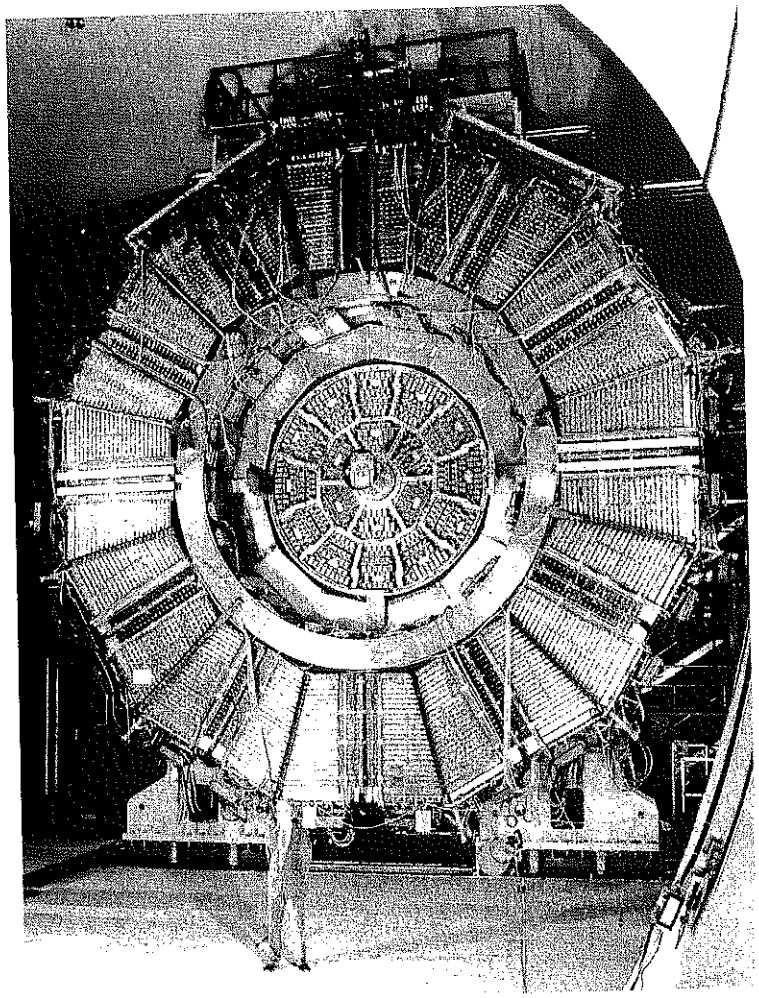

Figure 2. View of the ALEPH experiment implemented around one of the interaction points of the LEP collider at CERN. At the foreground is Jack Steinberger, Nobel Laureate in Physics, 1988 (with Leon Lederman and Melvin Schwartz), for the discovery of the muon neutrino.

The electron and positron beams of LEP are designed to collide at four interaction points surrounded by four physics experiments: ALEPH, DELPHI (which stands for DEtector with Lepton, Photon and Hadron Identification), L3, and OPAL (which stands for Omni-Purpose Apparatus at LEP). Figure 2 shows a view of the ALEPH experiment, which includes a large superconducting solenoid, embedded in the detector array. This solenoid was designed and built at Commissariat à l'Energie Atomique de Saclay (CEA/Saclay), near Paris, France [3]. It is 7 m long, has an inner bore of about 5 m, and produces a central field of 1.5 T. The stored energy is of the order of 140 MJ.

In December 1994, CERN has approved the construction in the LEP tunnel of the Large Hadron Collider (LHC). LHC will be a proton/proton collider with a maximum energy of 7 TeV per beam that will use the PSB, PS and SPS as injector chain [4]. Salient LHC parameters are summarized in Table 1 and detailed descriptions of the machine and of the planned high energy physics experiments are given in section 1.4.5. Commissioning is scheduled for 2005.

Table 1. Salient parameters of the Large Hadron Collider (LHC) at CERN [4].

	Injection	Storage/Collision
Layout		
Total circumference (m)	26658.883	
Number of arcs	8	
Bending radius (m)	2784.36	
Number of insertion regions	8	
Insertion region length (m)	528	
Number of interaction points	4	
Beam energy (GeV)	450	7000
Arc magnet lattice		
Number of cells per arc	23	
Cell length (m)	106.92	
Number of twin-aperture dipole magnets per cell	6	
Number of twin-aperture quadrupole magnets per cell	2	
Twin-aperture arc dipole magnet		
Total number	1232	
Magnetic length (m)	14.200	
Dipole field strength (T)	0.539	8.386
Twin-aperture arc quadrupole magnet		
Total number	386	
Magnetic length (m)	3.10	
Quadrupole field gradient (T/m)	14.5	223

1.3 SYNCHROTRON-TYPE ACCELERATORS

1.3.1 ACCELERATOR MAIN RING

In this review, we only consider accelerator chains whose last stage is a closed-orbit ring, referred to as *main ring*, and we limit ourselves to the study of the guiding elements distributed over the main ring arcs.

In the largest machines, the main ring is usually installed in an underground tunnel and, as we have seen for LEP at CERN, its circumference can exceed 10 kilometers.

Such a ring is operated in three phases: (1) *injection*, during which the beam, which has been prepared in various pre-accelerators, is injected at low energy, (2) *acceleration*, during which the beam is accelerated to nominal energy and (3) *storage*, during which the beam is circulated at nominal energy for as long as possible and is made available for physics experiments.

As mentioned in section 1.1, there are two types of experiments: (1) *fixed-target* experiments, for which the beam is extracted from the main ring to be blasted against a fixed target, and (2) *colliding-beam* experiments, for which two counter-rotating beams are blasted at each other. The breakage products are analyzed in large detector arrays surrounding the targets or collision points.

The main ring of an accelerator chain works as a synchrotron-type accelerator where the beam is circulated on a closed orbit, which remains the same throughout injection, acceleration and storage [5], [6]. It includes a small series of accelerating elements, located in one ring section, and through which the charged particles go at every turn. It also includes a large number of guiding elements, which are distributed over the ring arcs, and which are used to circulate and control the beam around its design orbit.

1.3.2 CHARGED PARTICLE ACCELERATION

Charged particles are accelerated by means of electric fields. The force, $\vec{F}_C$, exerted by an electric field, $\vec{E}$, on a charge, q, is given by Coulomb's law

$$\vec{F}_C = q\,\vec{E} \tag{1}$$

Such a force results in acceleration parallel to $\vec{E}$.

In most particle accelerators, the accelerating stations are made up of Radio Frequencies (RF) cavities, which can be either normal conducting or superconducting [7].

Figure 3 shows a set of superconducting RF cavity modules installed in the LEP tunnel at CERN [8]. The 12.5-m-long modules include four cavities made up of four half-wavelength, quasi-spherical cells. The cavities are operated at a frequency of 352.209 MHz and a nominal average electric field of 6 MV/m. LEP uses 272 superconducting cavities, providing a total RF voltage of about 2800 MV, and corresponding to an active length of 462 m.

It should be noted that average electric fields of 25 MV/m are now routinely achieved in 9-cell, 1.3 GHz superconducting RF cavities developed as part of the R&D efforts for the Tera Electron volts Superconducting Linear Accelerator (TESLA) [9]. TESLA is an electron/positron linear collider, with energy of 500 GeV per beam, under consideration at the Deutsches Elektronen SYnchrotron (DESY) laboratory, near Hamburg, Germany [10].

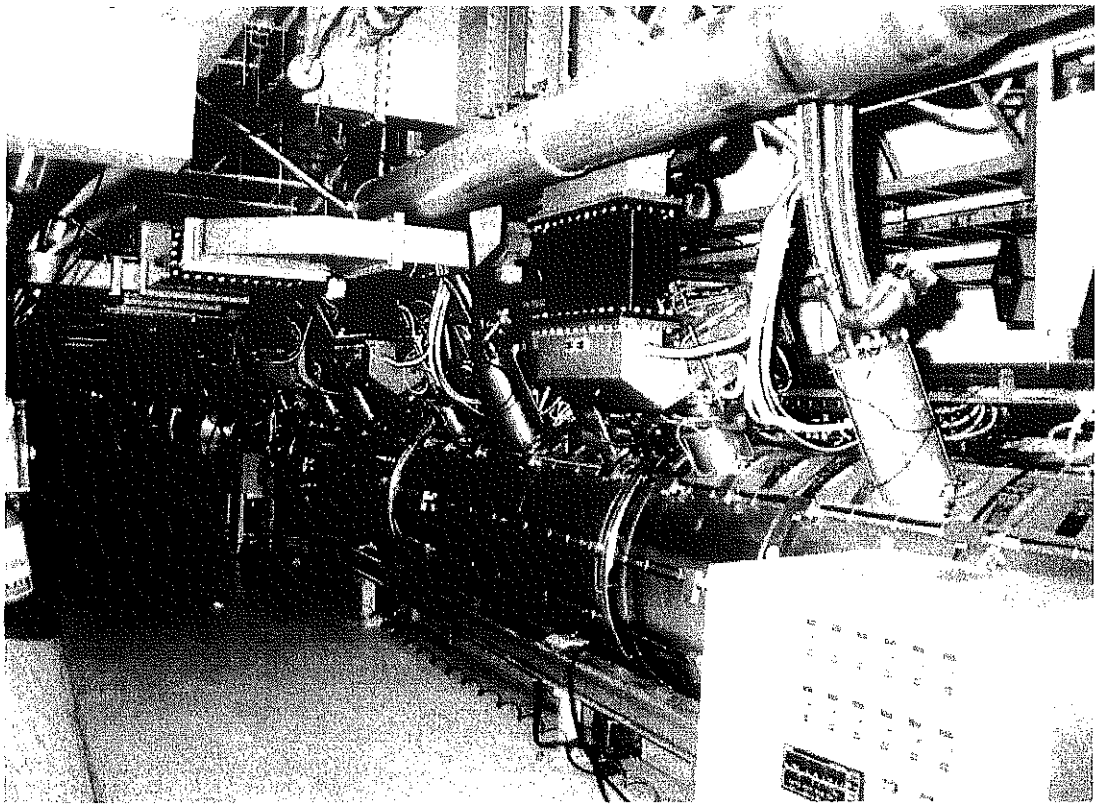

Figure 3. View of a set of superconducting RF cavity modules used in the LEP collider at CERN.

1.3.3 CHARGED PARTICLE GUIDING AND FOCUSING

Beams of charged particles are guided and focused by means of magnetic flux densities. The force, $\overrightarrow{F_L}$, exerted by a magnetic flux density, $\vec{B}$, on a charge, q, traveling at a velocity, $\overrightarrow{v_q}$, is given by Lorentz' law

$$\overrightarrow{F_L} = q\ \overrightarrow{v_q} \times \vec{B} \tag{2}$$

Such a force is perpendicular to the directions of $\overrightarrow{v_q}$ and $\vec{B}$ and its only action is to bend the particle trajectory.

If $\overrightarrow{v_q}$ and $\vec{B}$ are perpendicular, the particle is deviated on an arc of a circle, tangent to $\overrightarrow{v_q}$ and perpendicular to $\vec{B}$, and of radius of curvature, χ, which can be estimated as

$$\chi \approx \frac{\mathcal{E}_{GeV}}{0.3\ q_e B} \tag{3}$$

Here, χ is in meters, B is the amplitude of $\vec{B}$ in teslas, q_e is the particle charge in units of electron charge, and $\mathcal{E}_{GeV}$ is the particle energy in giga electron volts (GeV). Equation (3) shows that, to maintain a constant radius of curvature as the particle is accelerated, B must be ramped up linearly with $\mathcal{E}_{GeV}$.

Table 2. Bending radius versus bending magnetic flux density for a 10-TeV, synchrotron-type, proton accelerator.

	B (T)	χ (km)	Circumference (km)
Low Field	2	16.7	105
Medium Field	6	5.6	35
High Field	10	3.3	21

1.3.4 BEAM ENERGY VERSUS BENDING RADIUS

Let us use Eq. (3) to dimension a 10 TeV proton accelerator, choosing successively for B, a low value of 2 T, an intermediate value of 6 T, and a high value of 10 T. The results are presented in Table 2.

The bending radii and ring circumferences computed in Table 2 show that, when designing a large synchrotron-type accelerator, a trade-off must be found between, on one hand, the availability of land and the tunneling costs, and, on the other hand, the feasibility and costs of the electromagnets.

For LHC at CERN, the radius of curvature of the existing LEP tunnel limits the χ-value. In the present (1999) design, χ is worth 2784.32 m and the magnetic flux density of the bending magnets in the storage/collision phase is set to 8.386 T (see Table 1). It follows from Eq. (3) that the maximum proton energy is 7000 GeV.

1.4 LAYOUT OF LARGE CIRCULAR ACCELERATORS

1.4.1 MAGNET CLASSIFICATION

The main ring of an accelerator chain is usually made up of several *bending arcs* separated by quasi-straight *insertion regions*. The bending arcs have all the same radius of curvature and are designed to provide an integrated bending angle of (2π). The insertion regions house the accelerating stations and the beam injection and extraction lines. In the case of a collider ring, the two counter-rotating beams are designed to cross at the middle of at least one of the insertion regions. The insertion region middle points where the beams cross are referred to as *interaction points* and the space around them is available for physics experiments.

The electromagnets found around an accelerator main ring can be classified into three categories: (1) a large number of *arc magnets*, distributed over the ring arcs, (2) a limited number of *insertion and final focusing magnets*, used to handle the beams in the insertion regions and near the targets or collision points, and (3) large *detector magnets* implemented in the physics experiments.

1.4.2 ARC MAGNETS

The magnets distributed over the ring arcs have two main functions: (1) bending of the beam around a closed and constant orbit, and (2) focusing of the beam to achieve a proper size and intensity. In large machines, the bending and focusing functions are separated: the former is provided by dipole magnets whereas the latter is provided by pairs of focusing/defocusing quadrupole magnets (see section 1.5.3). These magnets are arranged around the arcs in a regular lattice of cells, made up of a focusing quadrupole, a string of bending dipoles, a defocusing quadrupole and another string of bending dipoles [11]. Several correction magnets are also implemented within each cell to allow better control of the beam optics. Due to their large number, the arc magnets are usually mass-produced in industry.

1.4.3 INSERTION AND FINAL FOCUSING MAGNETS

In addition to the arc magnets, an accelerator main ring includes a number of special magnets. Among them are magnets used to transport the beam from the injector chain to the main ring and sets of strongly focusing quadrupole magnets located near the targets or collision points. The design and fabrication of the insertion and final focusing magnets are very similar to those of the arc dipole and quadrupole magnets, except that they are produced in limited series and that they have to be customized to their crowded environment. In some cases, the final focusing quadrupole magnets are inserted at the extremities of the detector array and must be designed to sustain the stray field of the detector magnet [12].

1.4.4 DETECTOR MAGNETS

The physics experiments surrounding the targets or collision points usually rely on large magnet systems, which are embedded in the detector, array [13]. The magnet system is based either on a solenoid or on a toroid (or on a combination of both). The magnet structure must be minimized to save space and to reduce interactions with the particles. Furthermore, once buried in the detector array, the magnet system is no longer accessible for repair and maintenance and, therefore, must be engineered to operate safely and reliably. The technology of detector magnets is very different from that of accelerator magnets and is not discussed in this review.

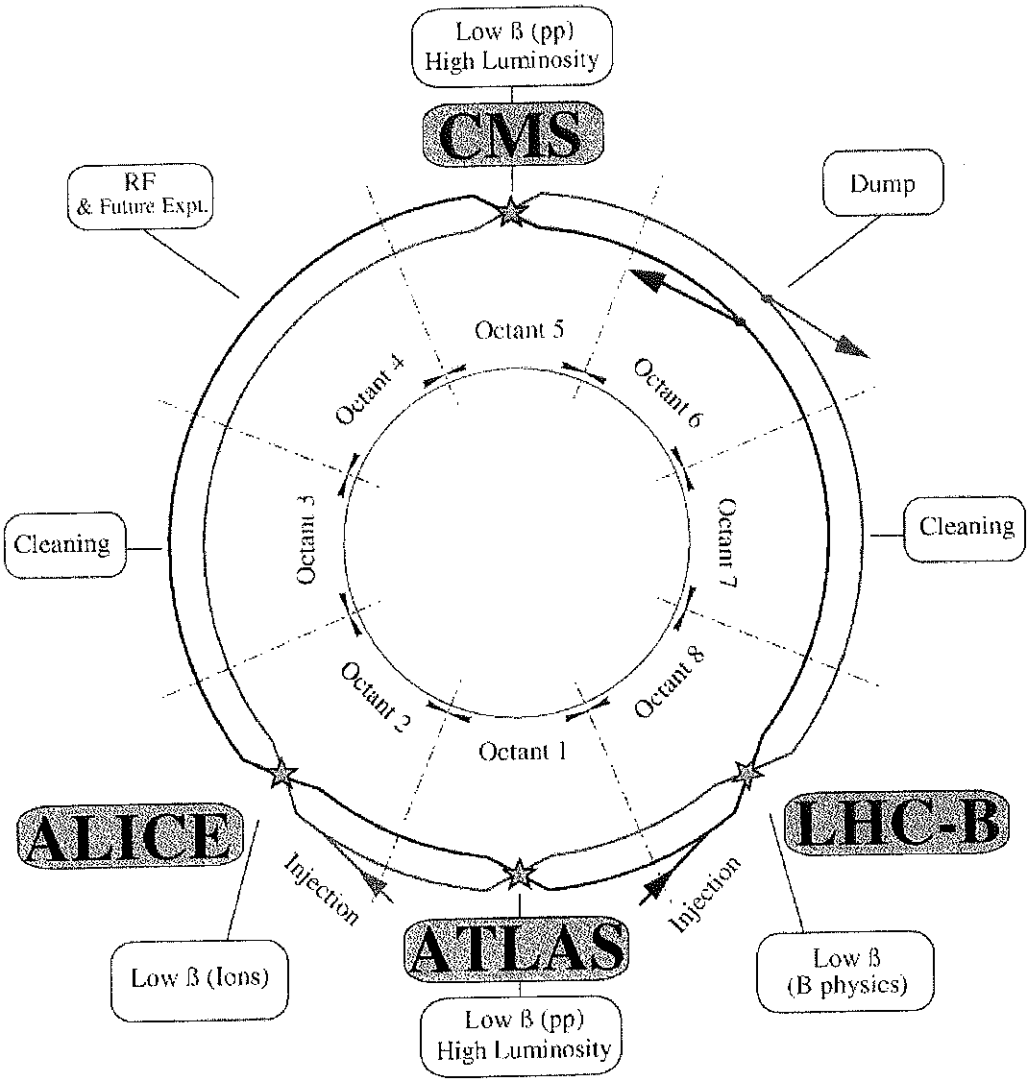

Figure 4. Schematic layout of the Large Hadron Collider (LHC) at CERN.

1.4.5 EXAMPLE: LHC AT CERN

1.4.5.1 Layout

As an illustration, Figure 4 shows the layout of LHC at CERN [4]. The LHC ring is divided into 8 bending arcs separated by 8 insertion regions. The ring circumference is 26658.883 m and each insertion region is about 528 m long (see Table 1). The two counter-rotating proton beams are circulated around the eight arcs and cross at the middle of four of the insertion regions. The accelerating stations are located in one of the insertion regions where the beams do not cross. They are made up of eight, single-cell, RF cavities per beam, operated at a frequency of the order of 400.8 MHz and a maximum average electric field of 5 MV/m. The total RF voltage is 16 MV per beam.

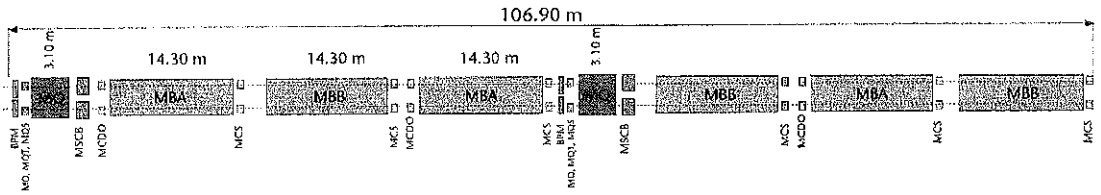

Figure 5. Cell of the proposed magnet lattice for the LHC arcs at CERN.

1.4.5.2 LHC Arcs

The 8 bending arcs of LHC have identical magnet lattices. They include 23 cells, which, as represented in Figure 5, are made up of 6 superconducting dipole magnets, 1 focusing and 1 defocusing quadrupole magnet, both superconducting, and several corrector magnets. The arc dipole and quadrupole magnets have two apertures, housing pipes for the two counter-rotating proton beams. Such magnets are referred to as *twin-aperture* magnets. The arc dipole magnets are 14.2 m long and are designed to produce a magnetic flux density of 8.386 T during the storage/collision phase. The arc quadrupole magnets are 3.1 m long and are designed to operate with a maximum field gradient of 223 T/m. The inner bore diameter of the coil assemblies is 56 mm, and the distance between the central axes of the two apertures is 194 mm for both magnet types. The cell length is of the order of 106.9 m.

1.4.5.3 LHC Insertion Regions

In the four insertion regions where the two beams cross, two sets of special magnets are required: (1) dipole magnets, to bring the beams together on one side of the collision points and to separate them on the other side, and (2) quadrupole magnets, to ensure final focusing on both sides of the collision points.

As illustrated in Figure 6, which shows the proposed magnet lattice on the right hand-side of one of the four LHC collision points, the final focusing is provided by so-called *inner triplets*, and the beam separation is performed in two stages. The inner triplets are made up of four, superconducting, high-field-gradient quadrupole magnets, powered by a common power supply [14]. These magnets, with lattice designation Q1, Q2a, Q2b and Q3, have one, large aperture, with a 70-mm inner bore diameter, and accommodate the two beams within a single pipe.

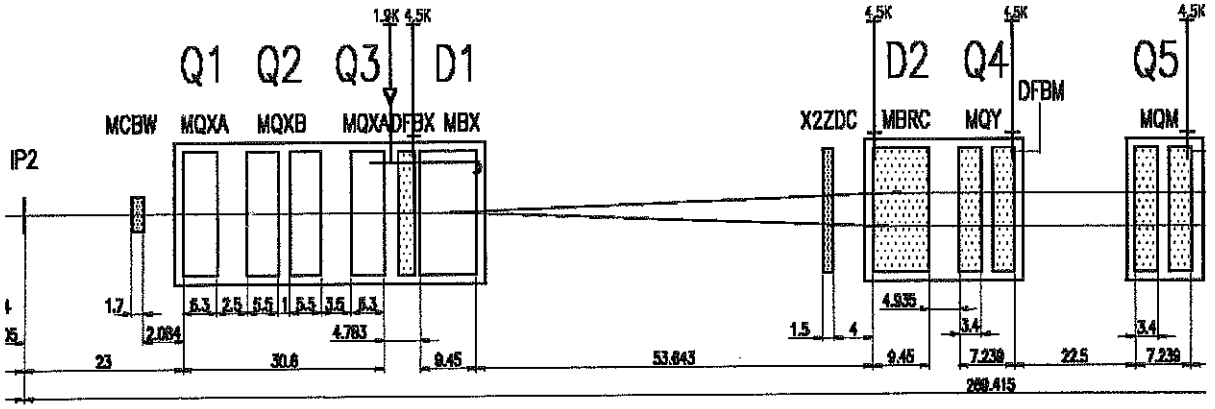

Figure 6. Proposed magnet lattice for the right-hand side of the #2 Interaction Point of LHC at CERN.

The two stages of beam separation are: (1) a low-field, single-aperture dipole magnet, with lattice designation D1, handling the beams exiting from the inner triplet into a single, large beam pipe, and (2) a low-field, twin-aperture dipole magnet, with lattice designation D2, located somewhat further away from the collision point and handling the beams exiting from D1 into two separate beam pipes. The D1 magnets are either superconducting or normal resistive, depending on the insertion regions and the amount of beam losses near the collision point. The D2 magnets are all superconducting, and the distance between the central axes of their two apertures is 188 mm.

Furthermore, additional superconducting dipole magnets are required in the insertion region where the accelerating stations are located. These magnets, with lattice designation D3a, D3b, D4a and D4b, are used to increase the beam separation from 194 mm to 420 mm at one end of the stations and to bring it back to 194 mm at the other end, so that dedicated RF cavity modules can be installed on each of the beam lines.

The magnetic lengths of the superconducting D1, D2, D3 and D4 magnets is 9.45 m and the inner bore diameter of the coil assemblies is 80 mm.

1.4.5.4 LHC Experiments

At present (1999), two high-energy physics experiments are being developed for LHC: (1) ATLAS (which stands for Air core Toroid for Large Acceptance Spectrometer or A Toroidal LHC ApparatuS), and (2) CMS (which stands for Compact Muon Solenoid). Both experiments rely on large magnet systems, which are embedded in the detector array. Salient parameters of these magnets, which are engineered at various laboratories around the world under CERN supervision, are summarized in Table 3.

Table 3. Salient parameters of superconducting magnets for LHC experiments at CERN.

Experiment Magnet Name Reference	ATLAS Barrel Toroid [15]	ATLAS End Cap Toroids [19]	ATLAS Central Solenoid [16]	CMS Solenoid [21]
Developer	CEA/Saclay & INFN/Milan	RAL	KEK	CEA/Saclay & INFN/Genoa
Number of coils	8	2 x 8	1	1
Length (m)	25.3	5	5.3	12.5
Inner diameter (m)	9.4	1.65	2.468	6.320
Outer diameter (m)	20.1	10.7	2.63	6.944
Operating Current (kA)	20.5	20.0	7.6	19.5
Central field (T)			2.0	4.0
Maximum field on coil (T)	3.9	4.13	2.6	4.6
Stored energy (MJ)	1080	2 x 250	39	2670

As shown in Figure 7, the magnet system for ATLAS is made up of four superconducting elements [15]: (1) a Central Solenoid (CS), located at the detector heart and providing a 2.0-T axial magnetic flux density, (2) a Barrel Toroid (BT), located around the central solenoid, and (3) two End-Caps Toroids (ECT), inserted at both ends of the Barrel Toroid and lined up with the Central Solenoid.

The Central Solenoid is engineered at KEK, High Energy Accelerator Research Organization, in Tsukuba, Japan [16]. It is 5.3 m long with a 2.3 m warm bore inner diameter. The stored energy is 39 MJ and the peak magnetic flux density on the conductor is 2.6 T. The Barrel Toroid was initially designed at CEA/Saclay [17], and is now developed by a collaboration including CEA/Saclay and the Istituto Nazionale di Fisica Nucleare, Sezione di Milano (INFN/Milan), in Italy [18]. It is made up of 8 racetrack-type coils, which are 25.3 m long. The Barrel Toroid inner diameter is 9.4 m and its outer diameter is 20.1 m. The total (8 coils) stored energy is 1.1 GJ and the peak magnetic flux density on the conductor is 3.9 T. The two End-Cap Toroids are also made up of 8 racetrack-type coils, which are 5 m long. The End-Cap Toroids' inner radii are 1.65 m and their outer radii are 10.7 m. The stored energy is 250 MJ per toroid and the peak magnetic flux density on the conductor is 4.13 T. The End-Cap Toroids are engineered at Rutherford Appleton Laboratory (RAL) in the United Kingdom [19]. The overall length of the ATLAS experiment is 44 m, while its overall diameter is 22 m.

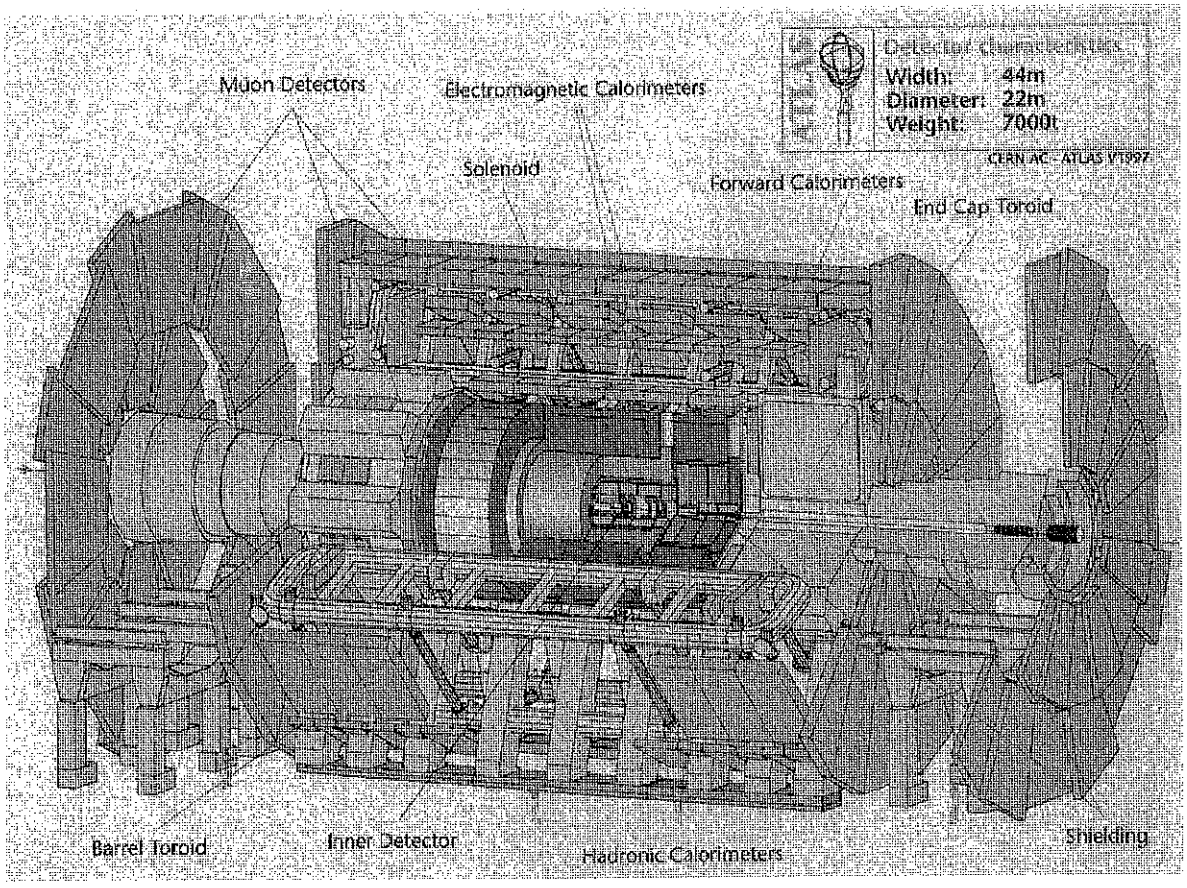

Figure 7. Artist view of the proposed ATLAS experiment for LHC at CERN.

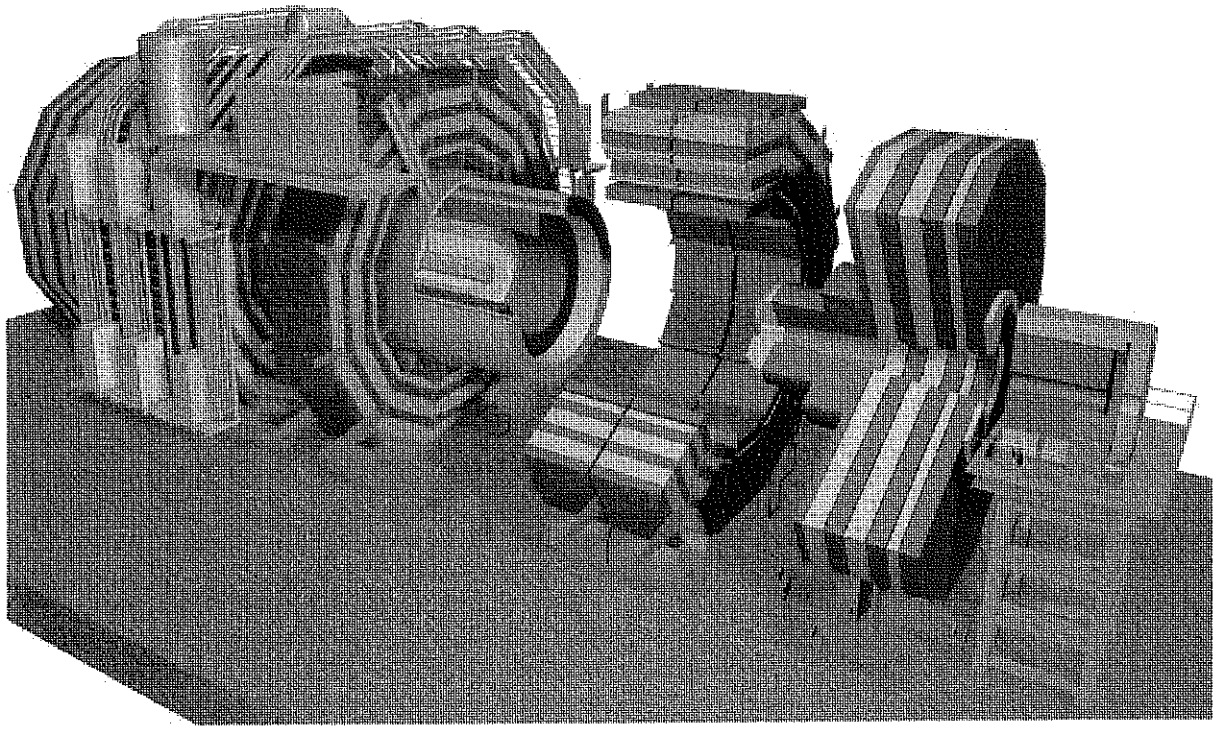

Figure 8. Artist view of the magnetic system for the proposed CMS experiment at CERN showing the superconducting solenoid at the heart of its iron yoke.

As illustrated in Figure 8, the magnetic system for the CMS detector is made up of a large superconducting solenoid surrounded by an iron yoke. The superconducting solenoid is 12.5 m long with a 5.9 m free bore inner diameter. It produces an axial magnetic flux density of 4.0 T. The stored energy is 2.7 GJ and the peak magnetic flux density on the conductor is 4.6 T. Similarly to the ATLAS Barrel Toroid, the CMS solenoid was initially designed at CEA/Saclay [20], and is now developed by a collaboration including CEA/Saclay and INFN/Genoa [21]. The iron yoke surrounding the solenoid is divided into three parts: (1) a barrel yoke, weighing 6000 metric tons, and (2) two end-cap disks, weighing 2000 metric tons each. The total weight of the CMS experiment is estimated at about 14500 metric tons.

1.5 DIPOLE AND QUADRUPOLE MAGNETS

1.5.1 COORDINATE SYSTEM DEFINITIONS

Let $(\Omega, \vec{X}, \vec{Y}, \vec{Z})$ designate a rectangular coordinate system, and let us consider an accelerator ring whose design orbit is planar and is located in the $(\Omega, \vec{X}, \vec{Z})$, as represented in Figure 9. Furthermore, let O be a given point of the design orbit, and let $(O, \vec{x}, \vec{y}, \vec{z})$ designate a rectangular coordinate system associated with O, such that $\vec{y}$ and $\vec{Y}$ are one and the same and $\vec{z}$ is tangent to the design orbit at O. Throughout the paper, the x-axis defines the horizontal direction, the y-axis defines the vertical direction, and the z-axis corresponds to the main direction of particle motion.

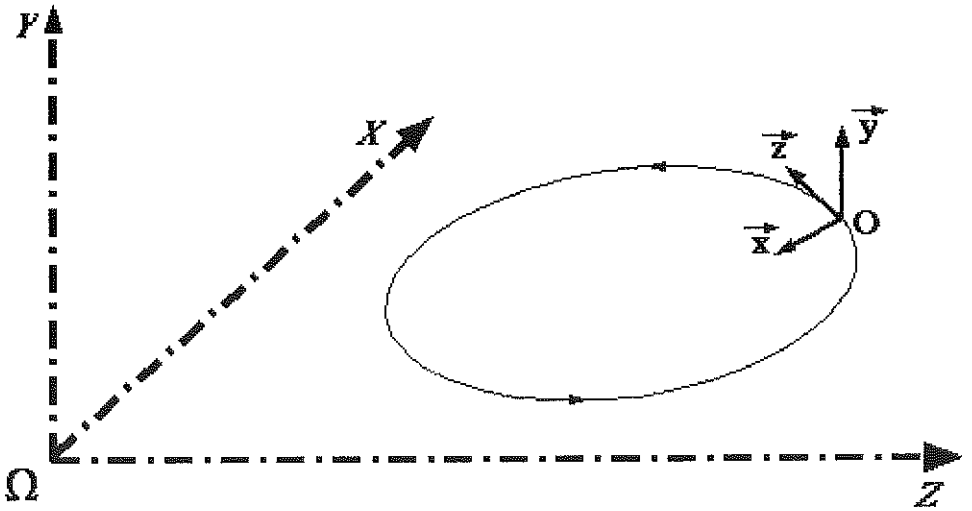

Figure 9. Coordinate systems associated with the design orbit of an accelerator ring.

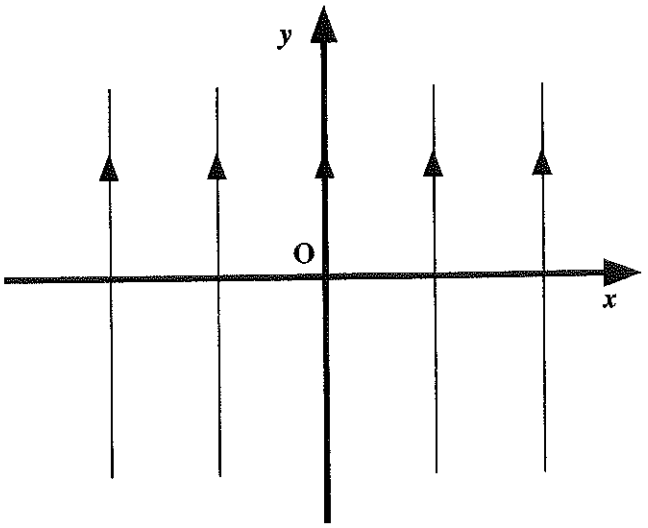

Figure 10. Ideal normal dipole magnet field lines.

1.5.2 NORMAL DIPOLE MAGNET

An ideal normal dipole magnet whose center is positioned at O is a magnet, which, within its aperture, produces an uniform magnetic flux density parallel to the y-axis and such that

$$B_x = 0 \qquad B_y = B_1 \qquad \text{and} \qquad B_z = 0 \tag{4}$$

where B_x, B_y and B_z are the x-, y- and z-components of the magnetic flux density, and B_1 is a constant referred to as the *dipole field strength* (in teslas). As represented in Figure 10, the field lines of an ideal normal dipole magnet are straight lines parallel to the y-axis.

A charged particle traveling along the direction of the z-axis through the aperture of a normal dipole magnet of length, l_{dip}, describes an arc of circle parallel to the horizontal $(\vec{x},\vec{z})$ plane. The angular deflection, ϕ_{dip}, of the particle trajectory can be estimated as

$$\phi_{dip} \approx \frac{0.3\, q_e\, B_1\, l_{dip}}{\varepsilon_{GeV}} = \frac{l_{dip}}{\chi} \tag{5}$$

Here, ϕ_{dip} is in radians, l_{dip} and χ are in meters, q_e is in units of electron charge, B_1 is in teslas, and ε_{GeV} is in GeV.

The effect of a dipole magnet on a beam of charged particles can be compared to the effect of a prism on a light ray.

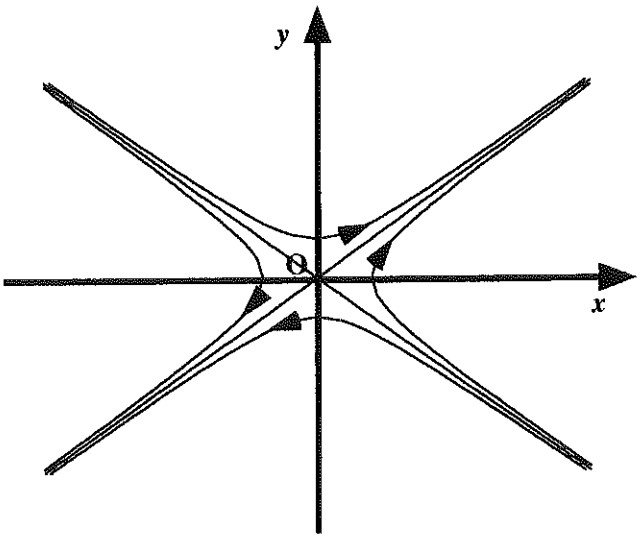

Figure 11. Ideal normal quadrupole magnet field lines.

For the storage/collision phase of LHC at CERN, we have (see Table 1): B_1 = 8.386 T, l_{dip} = 14.2 m, and $\varepsilon_{GeV} \approx 7000$. It follows from Eq. (5) that a single arc dipole magnet bends the proton trajectory by an angle $\phi_{dip} \approx 5.2$ mrad. Hence, a full (2π) rotation requires a total of 1232 arc dipole magnets.

1.5.3 NORMAL QUADRUPOLE MAGNET

An ideal normal quadrupole magnet whose center is positioned at O is a magnet, which, within its aperture, produces a two-dimensional magnetic flux density parallel to the $(\vec{x}, \vec{y})$ plane and such that

$$B_x = g\,y \qquad B_y = g\,x \qquad \text{and} \qquad B_z = 0 \tag{6}$$

where g is a constant referred to as the *quadrupole field gradient* (in teslas per meter). The field lines of an ideal normal quadrupole magnet are hyperbolae of center O whose asymptotes are the first and second bisectors (see Figure 11).

As illustrated in Figure 12(a) and Figure 12(b), a beam of positively charged particles traveling along the direction of the z-axis through the aperture of an ideal normal quadrupole magnet is horizontally focused and vertically defocused when g is positive. Conversely, the beam is vertically focused and horizontally defocused when g is negative. In reference to its action along the x-axis (on a beam of positively charged particles traveling in the positive z-direction), a magnet with a positive gradient is called a *focusing* quadrupole magnet, while a magnet with a negative gradient is called a *defocusing* quadrupole magnet. To obtain a net focusing effect along both x- and y-axes, focusing and defocusing quadrupole magnets must be alternated in the magnet lattice [5].

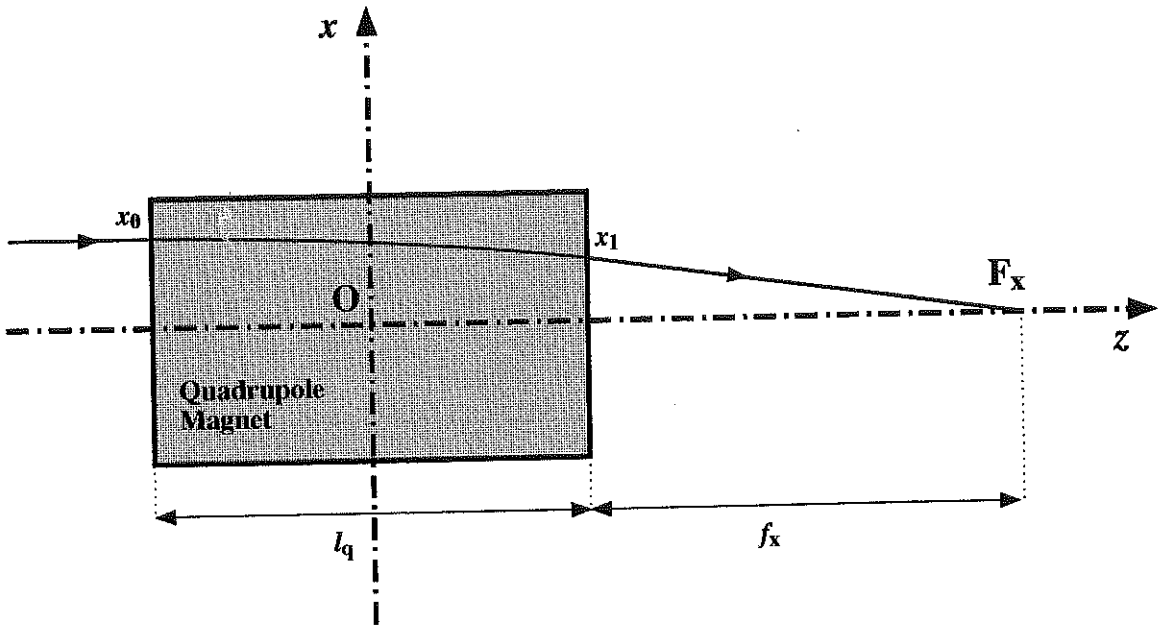

Figure 12(a). Horizontal focusing of positively charged particles circulating through the aperture of an ideal normal quadrupole magnet with a positive gradient.

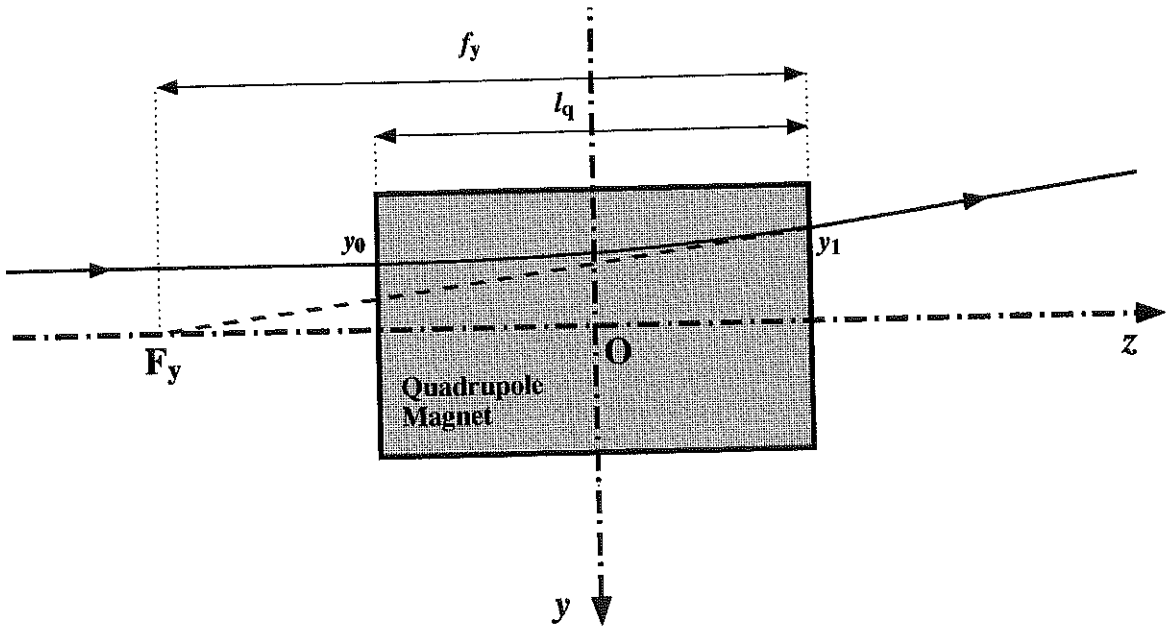

Figure 12(b). Vertical defocusing of positively charged particles circulating through the aperture of an ideal normal quadrupole magnet with a positive gradient.

The effects of focusing/defocusing quadrupole magnets on a beam of charged particles are similar to those of convex/concave lenses on a light ray. By analogy, the focusing effect of a normal quadrupole magnet of length, l_{quad}, can be characterized by the *focal length*, f_{quad}, given by

$$f_{\text{quad}} \approx \frac{1}{\sqrt{\kappa_{\text{g}}}} \cot\left(\sqrt{\kappa_{\text{g}}}\, l_{\text{quad}}\right) \tag{7}$$

while the defocusing effect, can be characterized by the focal length, f'_{quad}, given by

$$f'_{\text{quad}} \approx \frac{-1}{\sqrt{\kappa_{\text{g}}}} \coth\left(\sqrt{\kappa_{\text{g}}}\, l_{\text{quad}}\right) \tag{8}$$

In Eqs. (7) and (8), f_{quad} and f'_{quad} are taken from the magnet end where the beam exits [see Figure 12(a) and Figure 12(b)], and κ_{g} is the *normalized gradient*, defined as

$$\kappa_{\text{g}} \approx \frac{0.3\, q_{\text{e}}\, g}{\varepsilon_{\text{GeV}}} \tag{9}$$

Here, κ_{g} is in $(\text{rad/m})^2$, q_{e} is in units of electron charge, g is in teslas per meter, and ε_{GeV} is in GeV.

Equations (7) and (8) show that in order to keep the focal lengths constant during the acceleration phase, κ_{g} must be kept constant, and Eq. (9) shows that in order to keep κ_{g} constant, g must be raised in proportion to beam energy. As a result, during the acceleration phase, the arc dipole and quadrupole magnets are ramped up together so as to ensure that the bending dipole field strength and the focusing/defocusing quadrupole field gradients track the beam energy.

For the storage/collision phase of the LHC at CERN, we have (see Table 1): g = 223 T/m, l_{quad} = 3.1 m, and $\varepsilon_{\text{GeV}} \approx$ 7000 GeV. It follows from Eq. (9) that: $\kappa_{\text{g}} \approx$ 0.01 $(\text{rad/m})^2$, while Eq. (7) yields: $f_{\text{quad}} \approx$ 32.7 m, and Eq. (8) yields: $f'_{\text{quad}} \approx -$ 34.8 m. The LHC arcs count a total number of 386 quadrupole magnets.

2 SUPERCONDUCTIVITY APPLIED TO PARTICLE ACCELERATOR MAGNETS

2.1 WHY SUPERCONDUCTIVY?

Throughout the years, the quest for elementary particles has promoted the development of accelerator systems producing beams of increasingly higher energies. Equation (3) shows that, for a synchrotron, the particle energy is directly related to the product (χB). Hence, to reach higher energies, one must increase either the bending radius or the strength of the arc dipole magnets (or both). Increasing the bending radius means a longer tunnel. Increasing the magnetic flux density of the arc dipole magnets above 2 T leads to the use of superconducting magnets (see below). The trade-off between tunneling costs, magnet development costs and accelerator operating costs is, since the late 1970's, in favor of using superconducting magnets generating the highest possible fields and field gradients [11].

Superconductivity is a unique property exhibited by some materials at low temperatures where the resistivity drops to zero. As a result, materials in the superconducting state can transport current without power dissipation by the Joule effect. This offers at least two advantages for large magnet systems such as those needed in accelerator main rings: (1) a significant reduction in electrical power consumption and (2) the possibility of relying on much higher overall current densities in magnet coils.

There are, however, at least three drawbacks in using superconducting magnets: (1) to reach the superconducting state, the magnets must be cooled down and maintained at low temperatures, which requires large cryogenic systems (see section on magnet cooling), (2) it can happen that an energized magnet, initially in the superconducting state, abruptly and irreversibly switches back to the normal resistive state in a phenomenon referred to as a *quench* (see section on quench performance), and (3) superconductors generate magnetization effects which result in field distortions that have to be corrected (see section on field quality).

The occurrence of a quench causes an instantaneous beam loss and requires that all or part of the magnet ring be rapidly ramped down to limit conductor heating and possible damage in the quenching magnet (see section on quench protection). Once the quenching magnet is discharged, it can be cooled down again and restored into the superconducting state, and the machine operations resume. Hence, a quench is seldom fatal but it is always a serious disturbance. All must be done to prevent it from happening and all cautions must be taken to ensure the safety of the installation when it does happen.

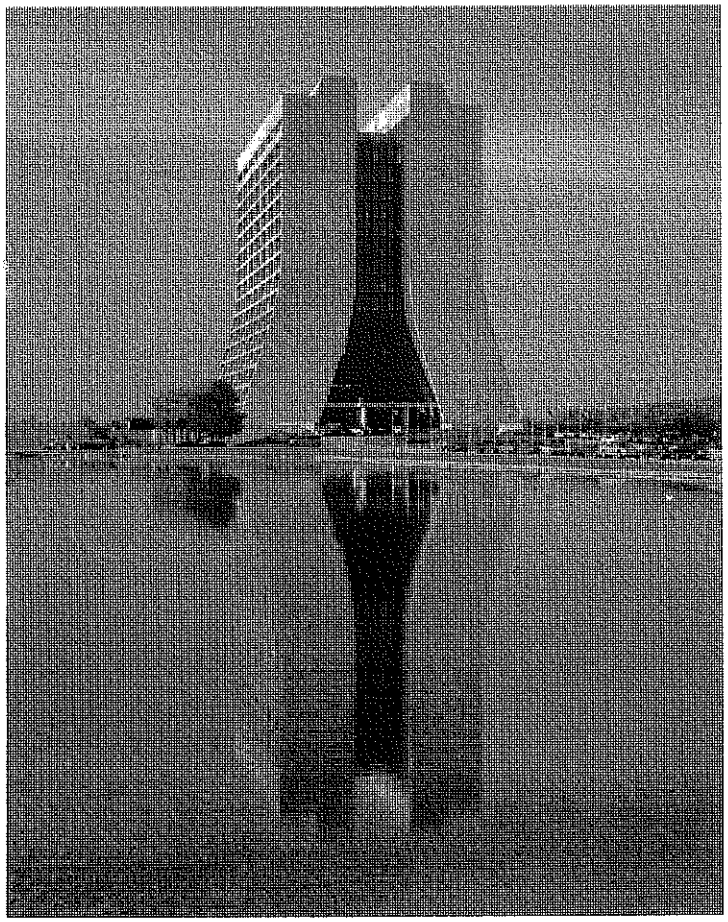

Figure 13. View of the Fermilab High Rise, modeled after the Gothic cathedral of Beauvais, France.

2.2 REVIEW OF LARGE SUPERCONDUCTING PARTICLE ACCELERATORS

2.2.1 TEVATRON

The first large-scale application of superconductivity was the Tevatron, a proton synchrotron with a circumference of 6.3 km built at Fermi National Accelerator Laboratory (FNAL, also referred to as Fermilab) near Chicago, Illinois and commissioned in 1983 [22]. The Tevatron now operates as a proton/antiproton collider with a maximum energy of 900 GeV per beam. It relies on about 1000 superconducting dipole and quadrupole magnets, with a maximum operating magnetic flux density of 4 T in the arc dipole magnets [23]–[27].

Figure 13 shows a view of the *High Rise*, an emblematic landmark of Fermilab. The High Rise, which is 239 feet tall (≈ 72.8 m), serves as an office building and was designed by Robert R. Wilson, Fermilab's first Director from 1967 to 1978, after the Gothic cathedral in Beauvais, France. Fermilab is also famous for its prairie restoration program and its thriving buffalo herd, as well as for Chez Leon, a popular hangout among gourmet physicists at the Users' Center, every Wednesday at lunch and every Thursday at dinner. (Chez Leon is named after Leon M. Lederman, Fermilab's second Director from 1978 to 1989.)

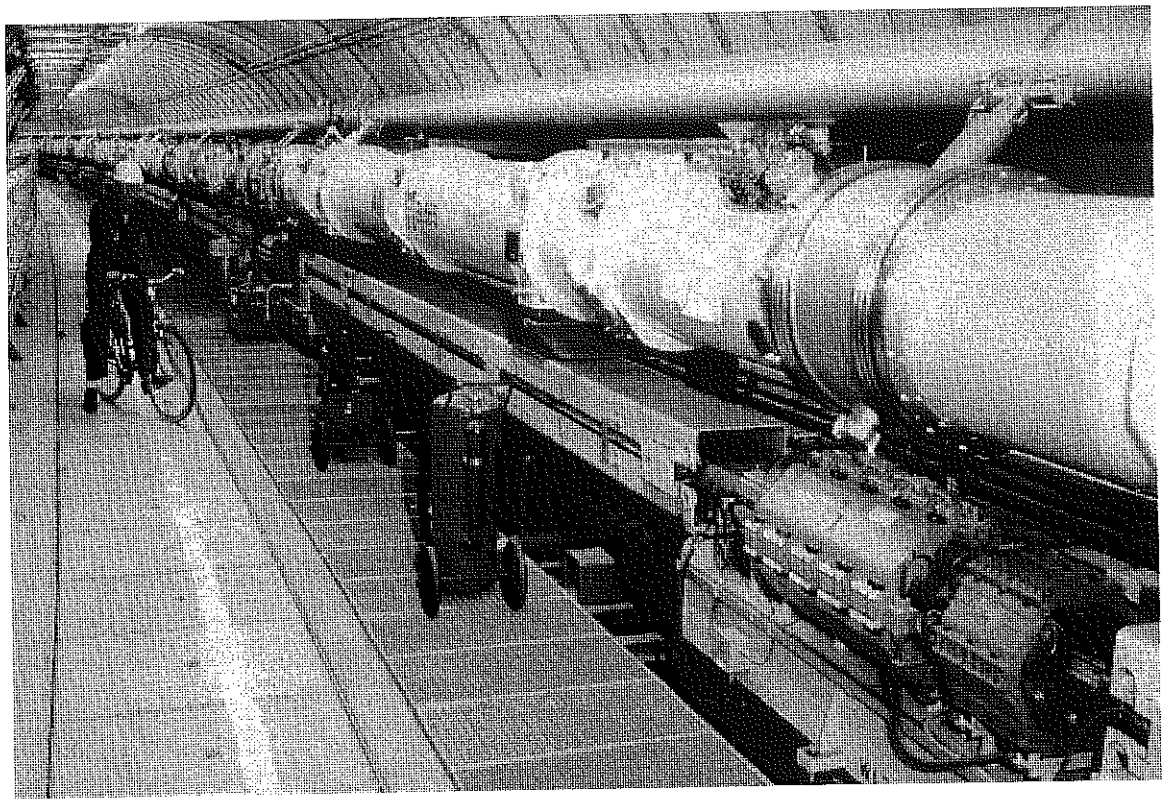

Figure 14. View of the HERA tunnel at DESY, showing the superconducting proton ring on top of the conventional electron ring.

2.2.2 HERA

The second, large particle accelerator to rely massively on superconducting magnet technology was HERA (Hadron Elektron Ring Anlage) built at DESY (Deutsches Elektronen–SYnchrotron) laboratory near Hamburg, Germany and commissioned in 1990 [28]. HERA is an electron/proton collider with a circumference of 6.3 km. As illustrated in Figure 14, it includes two large rings positioned on top of each other: (1) an electron ring, relying on conventional magnets (maximum energy: 30 GeV) and (2) a proton ring, relying on superconducting magnets (maximum energy: 820 GeV). The superconducting arc dipole magnets of the proton ring were developed at DESY and have a maximum operating magnetic flux density of 4.7 T [29]–[31]. The superconducting arc quadrupole magnets were developed at CEA/Saclay [32], [33].

2.2.3 UNK

Since the early 1980's, the Institute for High Energy Physics (IHEP) located in Protvino, near Moscow, Russia is working on a project of proton accelerator named UNK (Uskoritelno-Nakopitelniy Komplex). The circumference of the main ring is 21 km for a maximum energy of 3 TeV in a fixed target mode [34]. The maximum operating magnetic

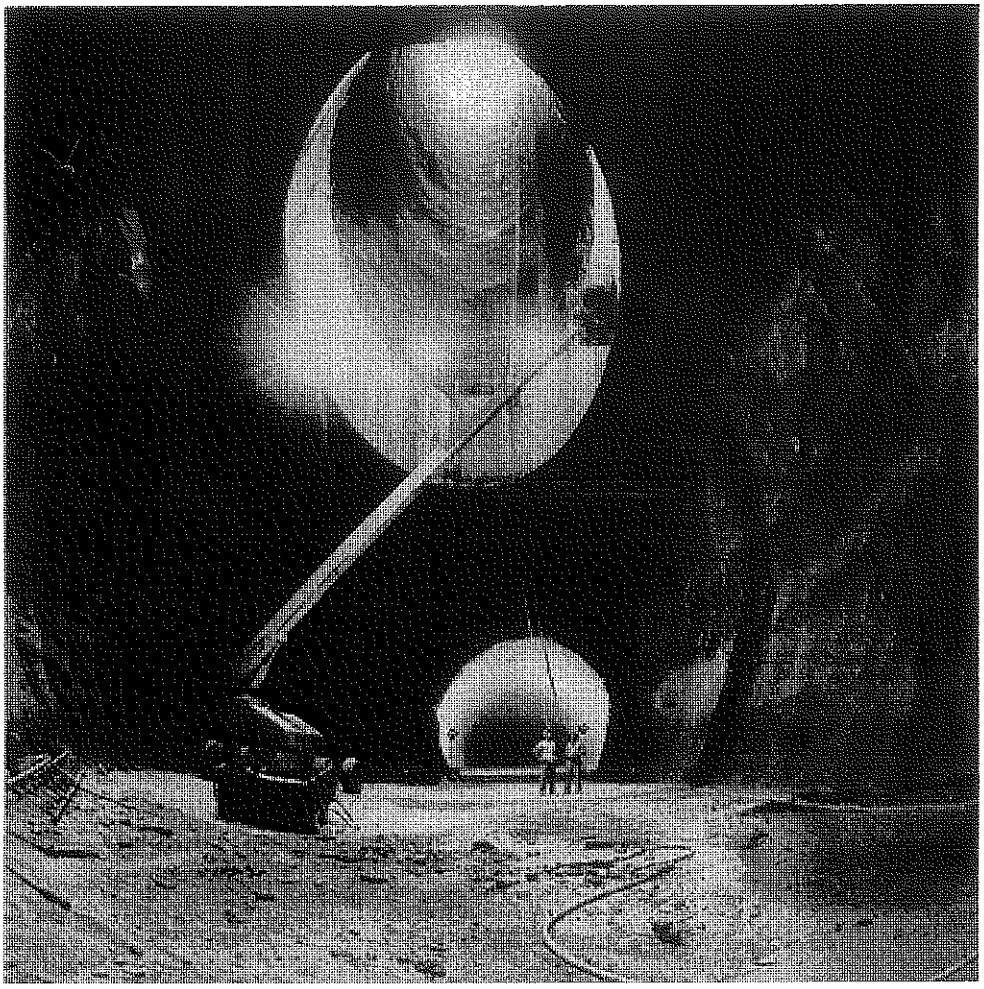

Figure 15. View of what was to become the main delivery shaft for the SSC tunnel; now a hole in the ground, in the countryside, near Waxahachie, TX.

flux density of the arc dipole magnets is 5 T [35]. A number of superconducting dipole and quadrupole magnet prototypes have been built and cold-tested and the tunnel is almost completed, but, given the present (1999) economical situation in Russia, the future of the machine is undecided.

2.2.4 SSC

In the mid 1980's, the USA started the Superconducting Super Collider (SSC) project, a giant proton/proton collider with a maximum energy of 20 TeV per beam [36]. The last stage of the SSC complex would have been made up of two identical rings of superconducting magnets installed on top of each other in a tunnel with a circumference of 87 km. The maximum operating magnetic flux density of the arc dipole magnets was 6.8 T. The project was eventually cancelled in October 1993 by decision of the United States Congress, after 12 miles of tunnel had been dug South of Dallas, Texas, and a successful superconducting magnet R&D program had been carried out [37]–[44].

Figure 15 shows a view of what was to become the main delivery shaft for the SSC tunnel, and of what is now a hole in the ground abandonned in the countryside, near the picturesque town of Waxahachie, Texas.

2.2.5 RHIC

Brookhaven National Laboratory (BNL), located on Long Island, New York, has completed in 1999 the construction on its site of the Relativistic Heavy Ion Collider (RHIC). RHIC is designed to collide beams of nuclei as heavy as gold at energies between 7 and 100 GeV per beam and per unit of atomic mass [45]. It is made up of two separate, but nearly identical rings of superconducting magnets, with a circumference of 2.4 miles (3.8 km). The beams circulated in the two rings cross at six points. Four of the six collision points are surrounded by physics experiments: two large ones, referred to as PHENIX and STAR (which stands for Solenoid Tracker At Rhic), and two smaller ones, referred to as PHOBOS and BRAHMS (which stands for Broad RAnge Hadron Magnetic Spectrometers).

The superconducting dipole and quadrupole magnets for the RHIC arcs were developed at BNL and were manufactured from so-called *built-to-print packages* by Northrop Grumman Corporation [46]–[48]. All insertion and special magnets were built at BNL [49], [50]. The strands for the superconducing cables used in the RHIC magnets were produced by Oxford Superconducting Technology and the cabling operation was performed by New England Electric Wire Corporation [51]. The maximum operating magnetic flux density of the arc dipole magnets is 3.4 T.

Commissioning of RHIC is underway.

2.2.6 LHC

2.2.6.1 Overview, Cost and Funding

As already mentioned in section 1.2.2, in December 1994, the European Laboratory for Particle Physics (CERN) has approved the construction of the Large Hadron Collider (LHC) in its existing 27-km-circumference tunnel located at the Swiss/French border, near Geneva, Switzerland. LHC will be a proton/proton collider with a maximum energy of 7 TeV per beam [4], [52].

The cost of the LHC machine (not including the ATLAS and CMS detectors) is estimated at about CHF 2,615,000,000 (1999 prices). It is funded through the CERN budget, provided by its 19 member states, plus seven special contributions. Two of the special contributions come from member states: France and Switzerland, and are supposed to

compensate for the economical advantages these two countries may draw from hosting CERN on their territory, and the remaining five come from non-member states: Canada, India, Japan, the Russian Federation and the USA, and are supposed to buy them rights for future usage of the CERN facilities when participating to LHC experiments.

The French special contribution is evaluated at CHF 64,500,000, and consists mainly in 204-man-year of work at French National Laboratories. The 204-man-year are divided up into four sectors of activities: (1) 75 are dedicated to support the development and the industrialization of the arc quadrupole magnet cold masses at CEA/Saclay, (2) 61 are dedicated to support the development and the industrialization of the cryostats for the so-called *short straight sections* (which, among other, house the arc quadrupole magnets) at the Institut National de Physique Nucléaire et de Physique des Particules (IN2P3), (3) 33 are dedicated to support instrumentation-related activities at IN2P3, and (4) 35 are dedicated to support cryogenics-related activities at CEA/Grenoble.

Switzerland is contributing CHF 25,000,000 *in kind*. The bulk of this contribution involves the civil engineering work needed to build new underground transfer lines from the SPS to the LHC.

Canada is contributing CA$ 30,000,000, divided up into CA$ 11,000,000 to fund LHC-related activities at the TRI-University Meson Facility (TRIUMF), and CA$ 19,000,000 to be spend on Canadian goods. TRIUMF, which is located on the campus of the University of British Columbia, near Vancouver, is working on upgrades of the PS and PSB injectors.

The Indian contribution will total US$ 25,000,000 over a 10-year period, while Japan, with JP¥ 13,850,000,000 (≈ CHF 160,000,000), is the second largest contributor after the USA. The detail of the Japanese contribution is quite complex, but it includes money to fund LHC-related activities at KEK and money to be spent on Japanese goods.

The Russian Federation has agreed to deliver, over a 10-year period, raw materials and manufactured goods for an estimated value of CHF 100,000,000. This includes, in particular, conventional dipole and quadrupole magnets for the SPS-LHC transfer lines, which are already being shipped to CERN on a regular basis.

Finally, the largest special contribution is coming from the USA, with a total of US$ 200,000,000. This contribution is divided up into US$ 110,000,000 to fund LHC-related activities at US National Laboratories (mainly, BNL, Fermilab and LBNL), and US$ 90,000,000 to be spent on US goods (such as Nb and NbTi alloy, whose only suppliers are American). In addition, the USA are also actively funding the ATLAS and CMS detectors.

2.2.6.2 Sharing of the Work on Superconducting Magnet Development

As described in section 1.4.5, the two counter-rotating proton beams of LHC are accelerated in a single ring, whose arcs are made up of twin-aperture superconducting magnets, housing two beam pipes within a same mechanical structure. The LHC arcs require a total number of 1232 dipole magnets and 386 quadrupole magnets.

The arc dipole magnets are developed by CERN and have a maximum operating magnetic flux density of 8.386 T [53]–[56]. They rely on two-layer coil assemblies with an inner diameter of 56 mm. The two coil layers are wound from different cables, which are referred to as *inner* and *outer* cables.

The arc quadrupole magnets are developed at CEA/Saclay, and have a maximum operating field gradient of 223 T/m [57]–[59]. They also rely on two-layer coil assemblies with an inner diameter of 56 mm, but the two coil layers are wound from the same cable, and this cable is the same as the dipole magnet outer cable.

Furthermore, the two LHC beams are designed to collide at four interaction points, surrounded, on both sides, by inner triplets, made up of four, single-aperture quadrupole magnets, with lattice designation Q1, Q2a, Q2b and Q3 (see section 1.4.5.3). Eight magnets of each type (one on each side of each interaction point) are required. The coil aperture is 70 mm for all 32 magnets and the nominal field gradient is 205 T/m. The 16 Q2a and Q2b cold masses will be provided by the USA, while the 16 Q1 and Q3 cold masses will be provided by Japan, as part of the special contributions of these two countries to the LHC machine. The US magnets are developed at FNAL [60]. They rely on a two-layer coil design and use cables made from leftover SSC strands. The Japanese magnets are developed at KEK [61], and rely on a four-layer coil design originally conceived at CERN [62].

Also part of the US contribution to LHC is the supply of 20 superconducting, beam-separation dipole magnets, with lattice designation D1, D2, D3a, D3b, D4a and D4b. These single- and twin-aperture cold masses are developed at BNL, and are based on the existing dipole magnet design for the RHIC arcs [63]. The inner diameter of the coil assemblies is 80 mm and the nominal dipole field ranges from 2.75 T to 3.8 T, depending on the magnet type and on its location. The BNL magnets also use cables made from leftover SSC strands.

2.2.6.3 Status of Cable and Magnet Programs

Regarding cables, two contracts for the supply of 26 metric tons of Nb and 470 metric tons of NbTi alloy, and five contracts for the production of 2370 km of inner cable and 4600 km of outer cable were signed during the second semester of 1998. The Nb and

NbTi contracts were awarded to Oremet Wha Chang, in the USA. The cable production is divided into lots corresponding to the quantity of inner and outer cables needed to manufacture one octant of arc dipole and quadrupole magnets. It is shared among 5 different manufacturers: (1) Alstom, in France, responsible for 5 octants of inner cable and 3 octants of outer cable, (2) Europa Metalli, in Italy, responsible for 3 octants of outer cable, (3) Furukawa Electric Company, in Japan, responsible for 1 octant of outer cable, (4) Intermagnetics General Corporation (IGC), in the USA, responsible for 1 octant of outer cable, and (5) Vacuumschmelze in Germany, responsible for 3 octants of inner cable. The cabling of the Europa Metalli and Vacuumschmelze strands is sub-contracted to Brugg, in Switzerland, the cabling of the IGC strands is sub-contracted to New England Electric Wire Corporation, in the USA, while Alstom and Furakawa take care, in house, of their own cabling. It is foreseen to perform critical current measurements on at least 60 000 wire short samples and on about 4000 cable short samples. The wire tests and 25% of the cable tests will be done at CERN while the remaining cable tests will be done at BNL. The Oremet Wah Chang and IGC contracts and the BNL cable tests are part of the US contribution to LHC, while the Furukawa contract is covered by the Japanese contribution.

Regarding the arc dipole magnets, a series of six 14-m-long, 56-mm-twin aperture prototypes is presently being built. The collared-coil assemblies of these prototypes are manufactured under contract with CERN by Ansaldo Energia, in Italy, Noell, in Germany, and a French consortium made up of Jeumont Industries and Alstom. They are then shipped to CERN for integration into cold masses and cold tests. The cold tests of these prototypes should be completed by the end of 2000. In the meantime, each of the three aforementioned companies was awarded, in November 1999, a contract for the production of 30 arc dipole magnet cold masses. The final contracts for the mass-production of the arc dipole magnets are expected to be adjudicated in 2001, after reception and evaluation at CERN of in between 20 to 30 dipole magnet cold masses (out of the 90 that are in order). Note that all arc dipole magnets will be cold tested at CERN prior to installation in the tunnel.

Regarding the arc quadrupole magnets, CEA/Saclay is completing the manufacturing of a series of three 3-m-long, 56-mm-twin aperture prototypes, which will be cold-tested at CEA/Saclay and at CERN in the oncoming 6 months. The contracts for the mass-production of the arc quadrupole magnets will be awarded in March 2000. As for the arc dipole magnets, all arc quadrupole magnets will be cold tested at CERN prior to tunnel installation.

Regarding the final focusing quadrupole magnets, Fermilab is completing a short magnet model program, and is planning to build 2 full-length prototypes before starting production. All Q2a and Q2b cold masses will be built and cold tested at Fermilab. In the meantime, KEK is also completing a short magnet model program and has awarded a contract

to Toshiba Corporation to build 1 full-length prototype and produce the Q1 and Q3 cold masses. All Japanese cold masses will be cold-tested at KEK.

Finally, regarding the beam-separation dipole magnets, BNL is presently building two 3-m-long models that will be evaluated before starting production of the 20 units (plus one spare of each magnet type). All cold masses will be built and cold-tested at BNL.

Commissioning of the LHC machine is scheduled for 2005.

2.3 PROMINENT FEATURES OF SUPERCONDUCTING ACCELERATOR MAGNETS

Selected parameters of the major superconducting particle accelerators described in the previous section are summarized in Table 4, while Figure 16 presents cross-sectional views of the Tevatron, HERA, SSC, RHIC and LHC arc dipole magnets in their cryostats [64].

Table 4. Selected parameters of major superconducting particle accelerators.

Laboratory Machine Name	FNAL Tevatron	DESY HERA	IHEP UNK	SSCL SSC	BNL RHIC	CERN LHC
Circumference (km)	6.3	6.3	21	87	3.8	27
Particle type	$p\bar{p}$	ep	pp	pp	heavy ions	pp
Energy/beam (TeV)	0.9	0.82	3	20	up to 0.1[a]	7
Arc Dipole Magnets						
Number	774	416	2168	7944	264	1232[b]
Aperture (mm)	76.2	75	70	50	80	56
Magnetic length (m)	6.1	8.8	5.8	15	9.7	14.2
Field (T)	4	4.68	5.0	6.79	3.4	8.36
Arc Quadrupole Magnets						
Number	216	256	322	1696	276	386[b]
Aperture (mm)	88.9	75	70	50	80	56
Magnetic length[c] (m)	1.7	1.9	3.0	5.7	1.1	3.1
Gradient (T/m)	76	91.2	97	194	71	223
Commissioning	1983	1990	undecided	cancelled	underway	2005

a) Per unit of atomic mass.
b) Twin-aperture magnets.
c) Quadrupoles come in several lengths.

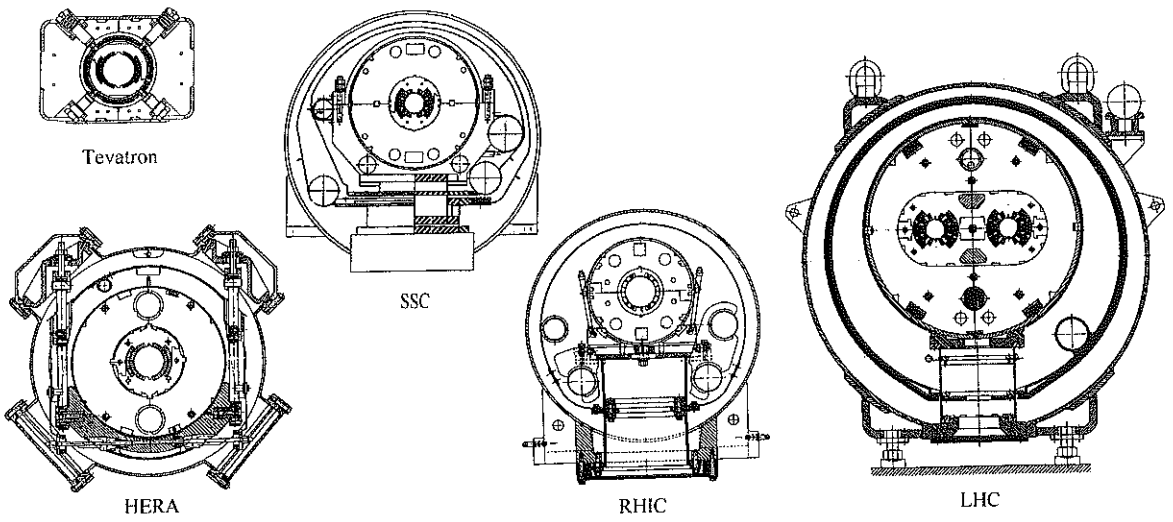

Figure 16. Cross-sectional views of superconducting dipole magnets for large particle accelerators [64].

The magnets rely on similar design principles, which are detailed in the oncoming sections. The field is produced by saddle shape coils that, in their long straight sections, approximate $\cos\theta$ conductor distributions for dipole magnets and $\cos 2\theta$ conductor distributions for quadrupole magnets. The coils are wound from Rutherford-type cables made up of NbTi multifilamentary strands and are usually restrained by means of laminated collars. The collared-coil assembly is placed within an iron yoke providing a return path for the magnetic flux.

In the case of the Tevatron, the collared-coil assembly is cold while the iron yoke is warm. Starting with HERA, the iron yoke is included in the magnet cryostat and an outer shell delimiting the region of helium circulation completes the cold mass. In the case of LHC, the cold mass includes two collared-coil assemblies within a common iron yoke.

Tevatron, HERA, UNK, SSC and RHIC magnets are cooled by boiling helium at 1 atmosphere (4.2 K) or supercritical helium at 3 to 5 atmosphere (between 4.5 and 5 K), while LHC magnets are cooled by superfluid helium at 1.9 K. The particle beams are circulated within a vacuum chamber inserted into the magnet coil apertures. The vacuum chamber, usually referred to as *beam pipe*, is cooled by the helium bathing the magnet coil.

2.4 SUPERCONDUCTING ACCELERATOR MAGNET R&D

2.4.1 STATE OF THE ART IN NBTI DIPOLE MAGNETS AT 1.8 K

2.4.1.1 Overview

As explained in section 3.1.1, the most commonly used superconducting material is an alloy of niobium and titanium (NbTi). NbTi has an upper critical field, B_{C2}, of the order of 10.7 T at 4.2 K and 13.6 T at 1.8 K.

A history of the development of high field accelerator magnets up to 1988 can be found in Ref. [65]. At the time, the record holder was a NbTi dipole magnet model built at KEK, which was completed in 1985 and which reached 9.3 T on its first quench at 1.8 K [66].

Over the last 10 years, at least six fully-fledged dipole magnets, relying on NbTi cables operated at a nominal temperature of 1.8 K, have reached the 10-T landmark. In addition, since 1997, at least 8 versions of LHC dipole magnet models built or re-built at the CERN Coil Test Facility (CTF) have also been trained up to 10 T [67]. The 10-T dipole magnet models all use two-layer, $\cos\theta$ coils wound from Rutherford-type cables, and rely on design concepts similar to those outlined in the previous section. Salient parameters of some of these magnets are summarized in Table 5.

2.4.1.2 LHC Dipole Magnet Models

The majority of the dipole magnet models having reached 10 T was built in the framework of the LHC R&D program. Let us single out four of them, referred to as MTAJS, MTACERN, MFISC and MSA4KEK, which, for various reasons, have marked this program.

MTAJS is a 1-m-long, twin-aperture model, with coil assembly inner diameters of 50 mm and a distance between aperture axes of 180 mm. It was built, under contract with CERN, by Jeumont-Schneider Industrie, in France [68], and was cold tested at CERN. MTAJS exhibited its first quench at 7.6 T, and, after a large number of training quenches (> 70), distributed over three test campaigns separated by two thermal cycles to room temperature, was the first dipole magnet to reach 10 T in September 1991 [69].

MTACERN is another 1-m-long, twin-aperture model, with coil assembly inner diameters of 50 mm, but a distance between aperture axes of 200 mm. It was assembled and cold tested at CERN, following the recommendations of the 1991 External Review Committee of the LHC project [70].

Table 5. Salient features of selected NbTi dipole magnet models having reached 10 T at 1.8 K nominal.

Name References	MTAJS [68], [69]	D19 [80]	MTACERN [70], [71]	MFISC [72]–[74]	MSA4KEK [75]	MFRESCA [83]
Manufacturer	CERN/ Jeumont	LBNL	CERN	CERN	KEK/ Toshiba	CERN/ Holec
Year of completion	1991	1992	1993	1995	1995	1999
Type	Twin	Single	Twin	Twin	Single	Single
Dist. between Axes (mm)	180	n/a	200	200	n/a	n/a
Yoke Outer Diameter (mm)	540	330	580	600	520	708
Coil Inner Diameter (mm)	50	50	50	56	50	88
Number of Coil Layers	2	2	2	2	2	2
Conductor Area (mm^2)						
Inner Layer	17x2.28	12.34x1.457	17x2.28	16.7x1.965	15x2.489	16.7x1.965
Outer Layer	17x1.475	11.68x1.157	17x1.475	16.7x1.560	15x1.327	16.7x1.560
Design Parameters @10 T						
Current (A)	14800	9570	14800	14370	12720	13600
Peak Field on Coil (T)	10.2	10.6	10.2	10.3	10.2	10.4
Lorentz Force[a] (kN/m)						
Horizontal	2276	2331	2276	2120	2140	3630
Vertical	−1210	−887	−1210	−1030	−1155	−2730
Stored Energy (kJ/m)	684[b]	250	684[b]	760[b]	310	695
Test Results						
Field at 1st Quench[c] (T)	7.6	9.4[d]	9.02	8.9	7.85	8.46
Numb. Quenches to 10 T	>70	9[d]	≈40	3	13	6
Max. Quench Field[c] (T)	≈10	10.06	10.5	10.53	10.3	10.09

a) Integrated over coil assembly top right quadrant.
b) For both apertures.
c) On magnet axis.
d) The magnet was first trained at 4.35 K nominal.

MTACERN had its first quench at 9.02 T and, after of the order of 40 training quenches, distributed over 2 test campaigns separated by one thermal cycle to room temperature, reached a maximum magnetic flux density of 10.5 T in March 1993 [53], [71]. (Note that the quench plots presented in Refs. [53] and [71] do not show all the quenches.)

MFISC, shown in Figure 17(a), is also a 1-m-long, twin-aperture model, but with coil assembly inner diameters of 56 mm and a distance between aperture axes of 200 mm. It was designed in collaboration with the Helsinki University of Technology, in Finland [72], but was built and cold tested at CERN [73], [74].

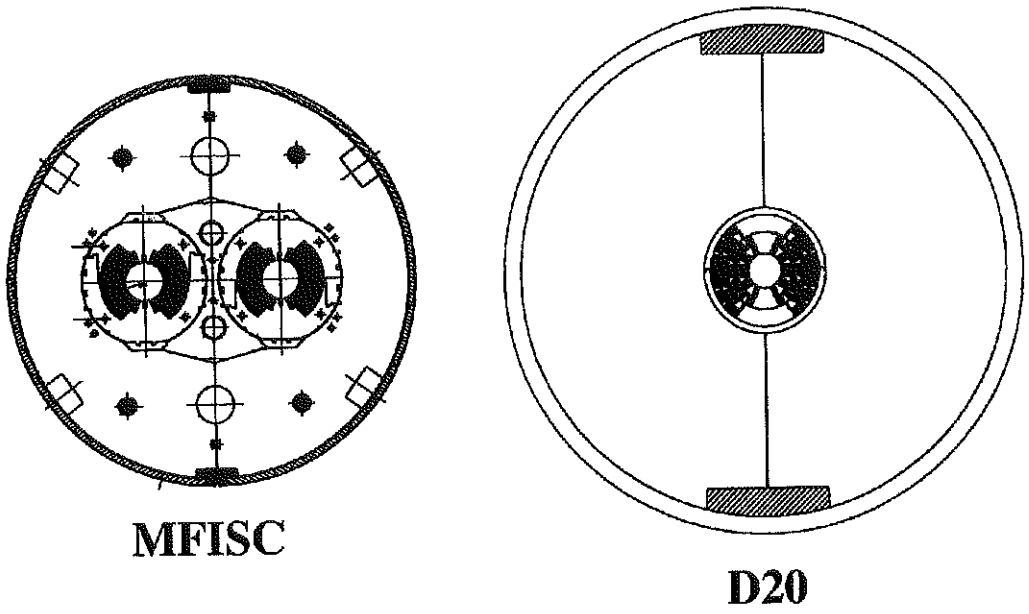

Figure 17. Examples of short R&D dipole magnet models: (a) 56-mm-twin-aperture dipole magnet model MFISC, which relies on NbTi cables and which has reached a maximum magnetic flux density of 10.53 T at 1.77 K, and (b) 50-mm-single-aperture dipole magnet model D20, which relies on Nb_3Sn cables and which has reached a record magnetic flux density of 13.5 T at 1.8 K.

MFISC exhibited its first quench at 8.9 T, crossed the 10-T threshold on its third quench, and reached its estimated short sample limit of 10.4 T at 1.9 K on its fifth quench in July 1995. The magnet was then warmed up to room temperature and cooled down again two weeks later. At the beginning of the second test campaign, the magnet exhibited two re-training quenches at 10.04 T and 10.2 T, before reaching again its short sample limit on the third quench. The magnet was then warmed up and left on the side until November 1996, when it was re-tested for the third time. The third test campaign was equally successful, with two re-training quenches at 10.09 T and 10.27 T, before, again reaching close to the short sample limit on the third quench. As of today, MFISC can be considered as the most successful NbTi dipole magnet, with a record magnetic flux density of 10.53 T at 1.77 K. It would definitely have been worth to pursue this very promising program by building, at least, another dipole magnet model of the same design.

MSA4KEK is a 1-m-long, 50-mm-single-aperture model that was built under contract with KEK, by Toshiba Corporation, in Japan and cold tested at KEK [75]. It exhibited its first quench at 7.85 T, crossed the 10-T threshold on its 13^{th} quench and, after a few more quenches, reached a maximum magnetic flux density of 10.3 T in February 1995. The magnet was then thermal cycled to room temperature, and, during the second test campaign, took about 10 re-training quenches to restore a magnetic flux density of 10.15 T.

Furthermore, and as already mentioned, CERN has now been operating for several years a Coil Test Facility. This facility is used to assemble, disassemble and re-assemble short dipole magnet models with a fast turnaround. This allows for quick fixing of problems identified during magnet cold testing and for experimenting at low costs various variations in design features. Up to now, more than 20 different magnet models have been built and re-built, some of them several times, and the results of this program are described in numerous papers [76]–[79]. Among them, at least 8 versions of 5 magnet models (referred to as MBSMS3 version 4 and 5, MBSMS15 version 1, MBSMS17 version 1, 2 and 4, MBSMS18 version 1, and MBSMS19 version 4) have reached 10 T, usually after a rather long training sequence (from 10 to 25 quenches). The highest magnetic flux density achieved is 10.14 T (on magnet model MBSMS3 version 5).

2.4.1.3 LBNL Dipole Magnet Model D19

On the side of the SSC magnet R&D program, Lawrence Berkeley National Laboratory (LBNL), located in the San Francisco bay area, has built and cold tested in 1992 a 1-m-long, 50-mm-single-aperture dipole magnet model referred to as D19 [80]. D19 was first tested at a nominal temperature of 4.35 K, where it reached its estimated short sample limit of 7.6 T on the second quench. After of the order of 15 quenches at 4.35 K, distributed over three test campaigns separated by two thermal cycles to room temperature, the magnet was cooled down to a nominal temperature of 1.8 K. The first 1.8-K quench was at 9.4 T. The magnet crossed the 10-T threshold on its 9^{th} quench at 1.8 K, and reached an estimated magnetic flux density of 10.06 T on its 11^{th} quench (which took place on April 1, 1992).

It is worth mentioning that this two-layer coil magnet model was later disassembled, and that its innermost coil layer, wound from a NbTi cable, was removed and replaced by a coil layer of the same geometry, but wound from a Nb_3Sn cable [81]. The magnet model was then re-built using the hybrid Nb_3Sn-NbTi coil assembly, but the quench performance was not as good as that of the original, all-NbTi model [82].

2.4.1.4 Dipole Magnet for the CERN Cable Test Facility

CERN has recently developed a 1.7-m-long, 88-mm-single-aperture dipole magnet to provide a background magnetic flux density for its cable test facility [83]. This magnet, referred to as MFRESCA, was built under contract by Holec Machine Apparaten (HMA) Power Systems, in the Netherlands, and was cold tested at CERN. It exhibited its first quench at 8.46 T and reached 10.09 T on its 6^{th} quench. It is now routinely excited up to 9.6 T without problem [84].

2.4.2 State of the Art in Nb_3Sn Dipole Magnets

2.4.2.1 Overview

As explained in section 3.1.2, besides NbTi, the only other superconducting material that is available at industrial scale is an intermetallic compound of niobium and tin, with the stoichiometry Nb_3Sn. Nb_3Sn has a higher critical temperature and a higher upper critical magnetic flux density than NbTi (Its B_{C2} at 4.2 K and –0.25% strain can reach 25 T), but, once formed, it becomes very brittle and, thereby, is more difficult to use. As a result, only a few Nb_3Sn dipole or quadrupole magnet models have been built and cold tested [65]. Nevertheless, in recent years, two dipole magnet models, relying on $\cos\theta$ coils wound from Nb_3Sn Rutherford-type cables, have exhibited quite spectacular quench performances.

2.4.2.2 Twente University Dipole Magnet Model MSUT

The first of the two aforementioned magnets is a short, 50-mm-single-aperture model, referred to as MSUT. MSUT was designed and built at Twente University, near Enschede in the Netherlands [85]. It was cold tested at CERN in the summer of 1995 and reached 11.03 T on its first quench at 4.4 K [86], [87]. The second quench was at 10.92 T, and the third (and last) quench of this test campaign, was at 10.86 T. The magnet was re-tested in July 1997, but the results of this second campaign, although equally good, have not been published.

2.4.2.3 LBNL Dipole Magnet Model D20

The second of the two aforementioned magnets, is also a short, 50-mm-single-aperture dipole magnet model that is referred to as D20. D20, shown in Figure 17(b), was built and cold tested at LBNL [88]–[90]. It was initially cooled down to 4.4 K, and exhibited its first quench at 10.2 T. After 16 quenches at 4.4 K, where it appeared to train more or less regularly up to 11.34 T, the magnet was cooled down further to 1.8 K, and reached 12.3 T on its first 1.8K-quench. After more training quenches, both at 4.4 K and 1.8 K, the magnet achieved a maximum magnetic flux density of 12.8 T at 4.4 K on its 34^{th} quench, and a record magnetic flux density of 13.5 T at 1.8 K on its 40^{th} quench (which took place on March 13, 1997). The 13.5 T mark was only reached once, and the subsequent quenches were at lower levels. The magnet was then thermal cycled to room temperature and re-tested at 4.4 K, where it reached a maximum magnetic flux density of 12.14 T.

As of today, D20 is the record holder in terms of highest magnetic flux density achieved on a dipole magnet.

2.4.3 ONGOING R&D PROGRAMS

A number of laboratories are presently involved in various types of R&D programs aimed at high field or high field gradient accelerator magnets.

CEA/Saclay is developing a Nb_3Sn cable with optimized interstrand resistances [91] and is investigating various types of insulation systems [92] to build a short, single-aperture quadrupole magnet model relying on the same coil geometry as the LHC arc quadrupole magnets. Such quadrupole magnet could be used for the final focus system of TESLA, the electron/positron linear collider now under development at DESY [93].

FNAL has launched an aggressive program to build several single-aperture Nb_3Sn dipole magnet models with a coil inner bore diameter of 44.5 mm and a maximum magnetic flux density of 12.3 T at 4.2 K [94], [95]. This program is part of an emerging effort in the USA to promote the development of a post-LHC machine, referred to as the Very Large Hadron Collider (VLHC) [96]. The VLHC parameters are far from being settled, but beam energies as high as 100 TeV are being considered.

INFN/Milan has studied various designs of large aperture, high gradient quadrupole magnets for a possible upgrade of the LHC inner triplets [97] and is working on a high performance Nb_3Sn cable [98].

KEK is developing a high critical current density Nb_3Al wire for accelerator magnet applications. The wire is made up Nb_3Al filaments embedded in a Nb matrix and, for now, does not include copper stabilization. The main specifications are: 0.8-mm diameter, Nb to Nb_3Al ratio of 0.6, and overall critical current density of 2000 A/mm^2 at 4.2 K and 10 T [99]. KEK is also working on Nb_3Sn, saddle-shaped, insert coils to be tested at LBNL, in the aperture of dipole magnet model D20 [100].

LBNL is investigating an innovative, twin-aperture dipole magnet design relying on pairs of parallel racetrack-type coils (see section 5.1.7 and Figure 35) [101]. A "proof of principle" dipole magnet model, made up of one pair of coils, spaced by 40 mm and wound from Nb_3Sn cables, has already been built and cold tested. The model reached 5.9 T on its first quench at 4.2 K [102]. Work is now under way on a 14 to 16 T dipole magnet model [103]. In parallel, LBNL is also launching a program to improve the performances and reduce the production costs of copper-stabilized Nb_3Sn wires, with a critical current density goal of 3000 A/mm^2 at 4.2 K and 12 T in the non-copper [104].

Texas A&M University (TAMU), located in College Station, Texas, has been working for some time on a ambitious 16 T block-coil dual dipole magnet design, incorporating a sophisticated management scheme to limit stresses on the conductors to less than 100 MPa [105], [106]. A single-bore, dipole magnet model, with a 25-mm coil aperture, and relying on NbTi cables is presently being built to evaluate fabrication techniques [107].

Finally, Twente University is collaborating with CERN on the design and fabrication of a high field, large bore Nb_3Sn dipole magnet [108]. Such a magnet could be used as a second generation, beam-separation D1 magnet to replace the present low-field magnets and free up some space near the crowded LHC interaction points. The coil aperture is 88 mm and the nominal magnetic flux density is 10.0 T at 4.4 K.

3 CONDUCTOR AND CONDUCTOR INSULATION FOR PARTICLE ACCELERATOR MAGNETS

3.1 REVIEW OF SUPERCONDUCTING MATERIALS

3.1.1 NIOBIUM-TITANIUM ALLOY

The most widely used superconductor is a ductile alloy of niobium and titanium (NbTi) [109]–[111]. Niobium and titanium, which have very similar atomic sizes, are mutually soluble over a wide composition range [112], [113]. At high temperatures, they combine into a body-centered cubic phase, referred to as *β–phase*. When cooled down to temperatures below about 9 K, the β–phase becomes a type-II superconductor. Furthermore, when the alloy is severely cold-worked and presents a large number of lattice dislocations, heat treatments at moderate temperatures lead to precipitations of other phases at grain boundaries. Among them is an hexagonal close packed phase, rich in titanium (of the order of 95% in weight), referred to as *α–phase*. The α–phase remains normal resistive at low temperatures and has been shown to be a significant source of fluxon pinning sites [114], [115]. The α–Ti precipitates can be engineered to achieve high critical current densities in the desired ranges of operating field and temperature.

The critical temperature, T_C, and the upper critical magnetic flux density, B_{C2}, of niobium-titanium are mainly determined by the alloy composition and are little affected by subsequent processing. The Ti content of practical conductors is in the range 45 to 50% in weight and corresponds to an optimum in B_{C2}. For such alloy compositions, the critical temperature at zero magnetic flux density, T_{C0}, is between 9 and 9.2 K and the upper critical magnetic flux density at zero temperature, B_{C20}, is about 14.5 T. The upper critical magnetic flux density can be raised slightly by addition of a high-atomic-number ternary component such as tantalum [116]. The increase in B_{C2} is small at 4.2 K (0.1 to 0.2 T) but can reach 1 T at 1.8 K.

The critical current density, J_C, is mainly determined by the microstructure of the alloy. It can be optimized by submitting the alloy to a succession of cold-work cycles and heat treatments. The heat treatments are carried out as to favor the development of α–Ti precipitates, while preventing the formation of other phases, which may be deleterious [117], [118]. The optimization parameters have been well studied for binary NbTi, but much less work has been carried out on ternary alloys [119]. At present, only binary niobium-titanium is used for large-scale applications.

As already mentioned in section 2.4.1, the best performing dipole magnet relying on binary NbTi conductor is a short LHC dipole magnet model, referred to as MFISC, which was built and cold tested at CERN, and which reached 10.53 T at 1.77 K [73], [74]. Magnet designers consider that this is about the limit for NbTi and that, to produce higher fields, it is necessary to change material.

3.1.2 Nb_3Sn Compound

The only other superconducting material that is readily available at (small) industrial scale is an intermetallic compound of niobium and tin (Nb_3Sn) belonging to the A15 crystallographic family [109]–[111]. Nb_3Sn is also a type-II superconductor, with a critical temperature at zero magnetic flux density and zero strain, T_{C0m}, of the order of 16 K and an upper critical magnetic flux density at zero temperature and zero strain, B_{C20m}, of the order of 24 T. The superconducting properties can be significantly enhanced by a small addition of titanium or tantalum, bringing T_{C0m} to about 18 K and B_{C20m} to about 28 T. However, the formation of binary or ternary compounds requires a heat treatment at temperatures up to 700 °C for times up to 300 hours in a vacuum or in inert atmosphere such as argon or nitrogen. Furthermore, once reacted, the compounds become brittle and their superconducting properties are strain sensitive [120], [121]. The processing difficulties and the higher cost of Nb_3Sn have so far limited its use. As indicated in section 2.4.2, the highest magnetic flux density reached on a Nb_3Sn dipole magnet model is 13.5 T at 1.8 K [89], [90].

3.1.3 High Temperature Superconductors

Although great progresses have been made in the development of so-called *High Temperature Superconductors* (HTS), such as bismuth copper oxides, $Bi_2Sr_2CaCu_2O_x$ and $(Bi,Pb)_2Sr_2Ca_2Cu_3O_x$, and yttrium copper oxides, $YBa_2Cu_3O_7$, these materials are not ready yet for applications requiring low costs, mass-production and high critical current densities [122].

3.2 SUPERCONDUCTING MULTIFILAMENTARY COMPOSITES

For practical applications, the superconductor is subdivided into fine filaments, which are twisted together and embedded in a low resistivity matrix of normal metal. The subdivision into fine filaments is required to eliminate instabilities in the superconductor known as *flux jumping* (chapter 7 of Reference [123]). The filament twisting is introduced to reduce inter-filament coupling under time-varying fields (chapter 8 of Reference [123]). The low resistivity matrix is used as current shunt in the case of transition of the filaments to the normal resistive state, thereby limiting power dissipation and conductor heating (the

resistivity of superconductors in the normal state is usually much larger than the low-temperature resistivity of normal metals such as high purity copper or aluminum).

Accelerator magnets rely on cables made from round wires of superconducting multifilamentary composites. Except for a few R&D magnet models, the filaments are made of binary niobium-titanium alloy and the matrix is high purity copper. Wire diameter ranges from 0.5 to 1.3 mm. For accelerator magnets, there is an additional requirement on filament diameter to limit field distortions resulting from superconductor magnetization (see section on field quality). The superconductor magnetization per unit volume can be shown to be directly proportional to filament diameter (p. 166 of Reference [123]), and to minimize its effects it is desirable to use fine filaments. The filament diameter of HERA wires is of the order of 15 μm while that of SSC, RHIC and LHC wires is of the order of 5 μm. The copper-to-superconductor ratio, λ_{wire} (defined as the ratio of the area of copper to the area of niobium-titanium in the wire cross-section), varies from 1.3 to 1.8, except for RHIC wire where it is 2.25. There are several thousand filaments per wire.

3.3 TRANSITION OF MULTIFILAMENTARY WIRES

3.3.1 VOLTAGE-CURRENT CURVE

The maximum current-carrying capacity of a superconducting multifilamentary wire at a given temperature and field can be determined by measuring the voltage-current curve of a wire short sample. As illustrated in Figure 18(a), the transition from the superconducting state to the normal resistive state is not abrupt but takes place over a certain current range. At low transport currents, the voltage, V_{wire}, across the wire short sample is nil. Then, as the current, I_{wire}, is increased, there appears a domain where V_{wire} starts to rise. At the beginning, the voltage rise is reversible, *i.e.*, if the current is lowered, the voltage decreases following the same curve as during the up-ramp. However, above a certain current, the phenomenon becomes irreversible, and the voltage takes off rapidly and uncontrollably. Such irreversible voltage run-away is the signature of a quench. The current at which the run-away occurs is referred to as *quench current*, I_q. For the data of Figure 18(a), I_q = 385 A.

3.3.2 CRITICAL CURRENT

For the particular environment of the wire short sample in its test set-up, a quench only occurs when the current reaches I_q. However, for a different environment with different cooling conditions (*e.g.*, when the wire is part of a cable that is insulated and wound in a coil), the quench current may be different. The question then arises of what engineering value to use to characterize the maximum current capability of a wire in a magnet environment.

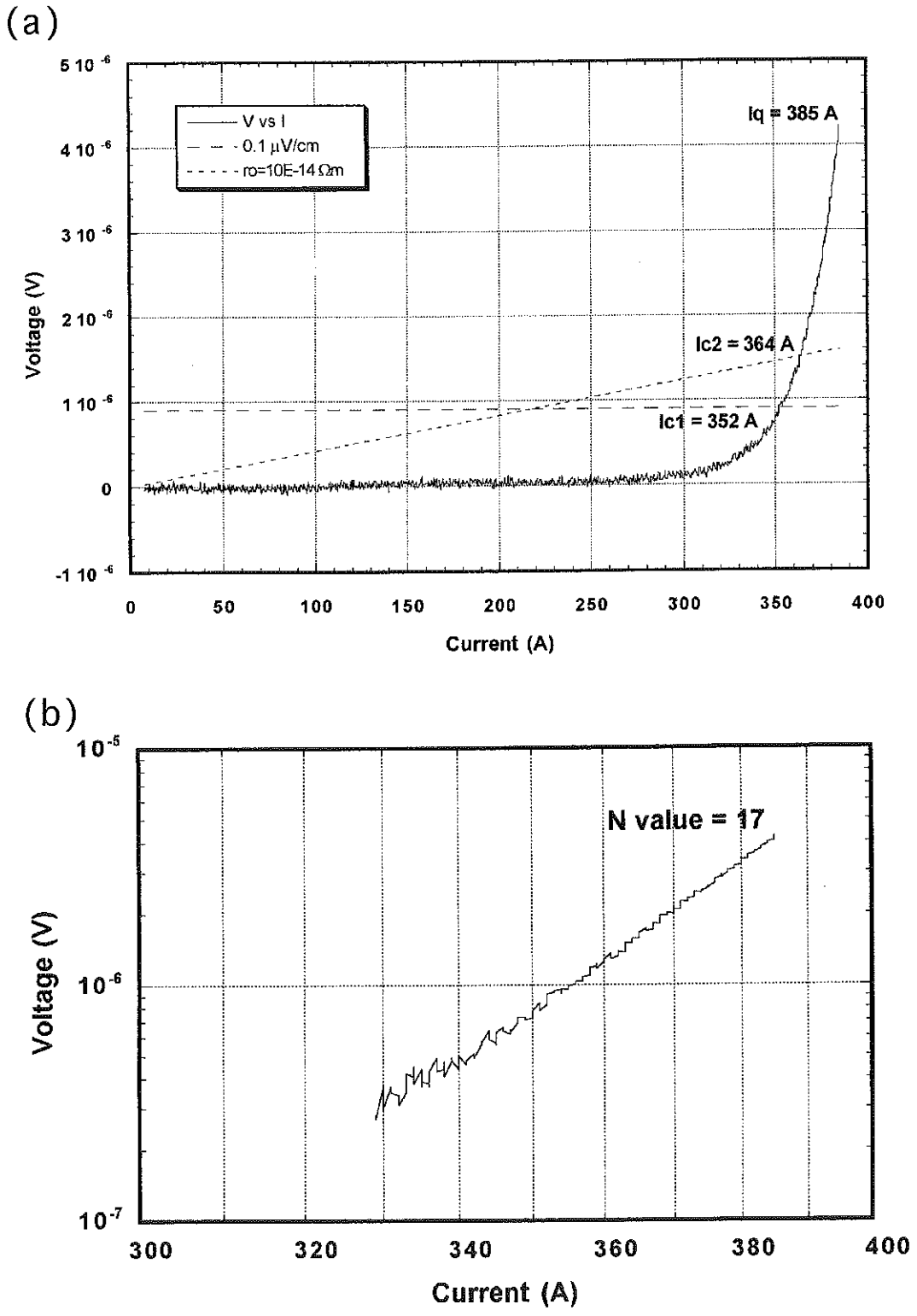

Figure 18. Transition from the superconducting to the normal resistive state of a multifilamentary composite wire: (a) voltage-current curve, and (b) voltage-current curve re-plotted in logarithmic scales. Data correspond to a 9-mm long sample of Nb_3Sn wire measured at 4.2 K and 7.5 T.

The engineering value used by magnet designers is referred to as *critical current*, I_C, and is defined by relying on empirical criterions.

To explain these criterions, let us consider a sample of multifilamentary composite wire of length, L_{wire}, cross-sectional area, S_{wire}, and overall copper-to-superconductor ratio, λ_{wire}, and let V_{wire} designate the voltage across the wire sample. An apparent electrical field, E_{super}, and an apparent resistivity of the superconductor, ρ_{super}, can be defined as

$$E_{super} = \frac{V_{wire}}{L_{wire}} \qquad \text{and} \qquad \rho_{super} = \frac{1}{1+\lambda_{wire}} \frac{V_{wire}}{L_{wire}} \frac{S_{wire}}{I_{wire}} \tag{10}$$

In the case of NbTi and Nb_3Sn wires, the two criterions the most commonly used to define the critical current are: (1) the current value corresponding to an apparent electrical field, E_C, of 0.1 μV/cm or (2) the current value corresponding to an apparent resistivity of the superconductor, ρ_C, of 10^{-14} Ωm. (Note that the latter definition is preferred in the accelerator magnet community.) For the data of Figure 18(a), the critical current based on the electric field criterion, I_{C1}, is 352 A, while that based on the resistivity criterion, I_{C2}, is 364 A. Hence, I_{C1} is 3.4% smaller than I_{C2}, which is itself 5.5% smaller than I_q.

The critical current determined by either of the aforementioned criterions is usually lower than the quench current. It can be translated into an average critical current density in the superconductor, J_C, by writing

$$I_C = J_C \frac{S_{wire}}{1+\lambda_{wire}} \tag{11}$$

It is verified in the section on quench performance that the critical current values can be used to make accurate estimations of the maximum quench currents of accelerator magnets.

3.3.3 N-VALUE

To fully characterize the wire, it is also interesting to quantify the sharpness of the transition from the superconducting to the normal resistive state. This can be done by plotting $\ln(V_{wire})$ [or $\ln(\rho_{super})$], as a function of $\ln(I_{wire})$.

As illustrated in Figure 18(b) for the data of Figure 18(a), it appears that $\ln(V_{wire})$ [and similarly, $\ln(\rho_{super})$] increases quasi-linearly as a function $\ln(I_{wire})$ over a broad range (typically, from E_C to $10E_C$ or ρ_C to $10\rho_C$).

Hence, simple power laws can fit the onset of the resistive transition

$$\frac{V_{\text{wire}}}{V_C} = \left(\frac{I_{\text{wire}}}{I_C}\right)^N \qquad \text{or} \qquad \frac{\rho_{\text{super}}}{\rho_C} = \left(\frac{I_{\text{wire}}}{I_C}\right)^{N-1} \tag{12}$$

where $V_C = E_C L_{\text{wire}}$ is the voltage across the wire sample corresponding to E_C. The index N is referred to as *resistivity transition index*, or more simply, *N-value*. It is representative of the curvature of the voltage-current curve: the larger N, the sharper the transition. For the data of Figure 18(b), $N \approx 17$.

The N-value, like I_C, depends on temperature and field [124]. Its field dependence can be used as a criterion to determine if the critical current is limited by intrinsic factors, related to fluxon-microstructure interactions within the superconducting material, or by extrinsic parameters, related to macroscopic irregularities, such as local reductions in filament cross-sectional areas [125]. In the case of NbTi wires, there is a clear correlation between filament distortions, often referred to as *sausaging*, and N-value: the wider the distribution of filament diameters in the wire cross-section, the lower the N-value [126]. A typical N-value for SSC wire is 30 at 4.2 K and 5 T.

3.4 NBTI WIRES

3.4.1 PROCESSING

NbTi alloys are very ductile and have very low work-hardening coefficients making them easy to co-process with copper. A multifilamentary wire is fabricated by extrusion and drawing of a *multi-filament billet*. The multi-filament billet is made up of hexagonal, mono-filament rods stacked into a thick-walled copper can. There are as many rods in the multi-filament billet as filaments in the final wire. The rods themselves are produced by extrusion and drawing of a *mono-filament billet*. The mono-filament billet is made up of a cylindrical ingot of high homogeneity niobium-titanium alloy inserted into a copper can.

The drawing-down of the billets is realized in multiple passes and heat treatments are applied at well-defined strain intervals (corresponding to integer numbers of standard die passes). The cold-work and heat treatment schedule is established so as to produce the desired amount of α–Ti precipitates and to reduce the dimensions and spacing of these precipitates to optimum sizes for fluxon pinning. As the characteristics of the fluxon lattice depend on temperature and field, the schedule may be different for different applications with different operating conditions. The wire twist is applied prior to the final drawing pass, with a typical twist pitch of 25 mm. Figure 19 shows an example of high performance wire for accelerator magnet applications at final size [127].

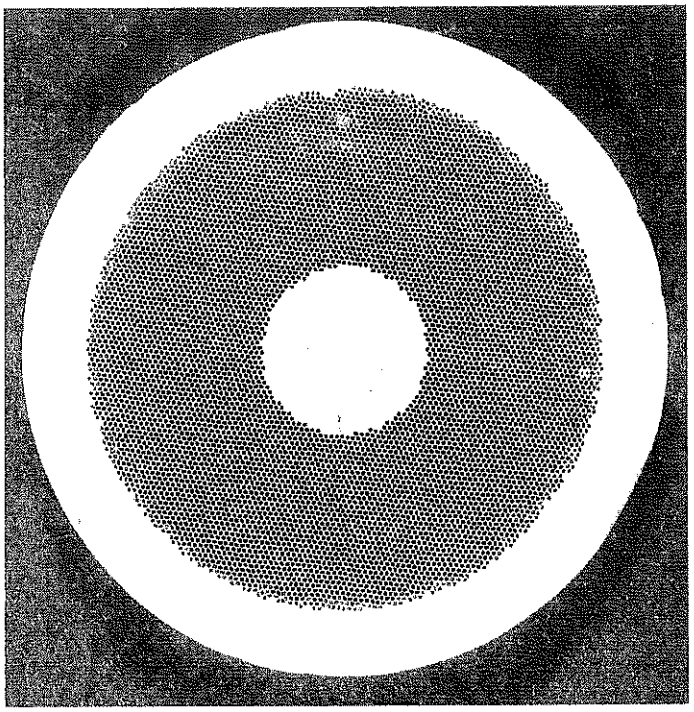

Figure 19. Cross-sectional view of a single-stacking, NbTi multifilamentary composite wire [127].

For the production of fine filament wires, such as those used for SSC, RHIC and LHC, the niobium-titanium ingot of the mono-filament billet is wrapped with a niobium foil. The niobium barrier prevents the formation, during the multiple heat treatments, of hard and brittle intermetallic compounds such as $TiCu_4$. The $TiCu_4$ compounds do not deform well, resulting in filament sausaging and, ultimately, wire breakages upon subsequent drawing operations [128].

When the number of filaments is very large, rods made from a drawn-down multi-filament billet can be re-stacked into a new multi-filament billet, which, in turn is extruded and drawn. Such process is referred-to as *double stacking* as opposed to *single stacking*.

3.4.2 Design and Manufacturing Issues

The main issues for NbTi wire design are: (1) copper-to-superconductor ratio, which should not be too small to limit conductor heating in case of a quench and should not be too large to achieve a high overall critical current, (2) filament size, which should be optimized to limit field distortions resulting from superconductor magnetization while keeping wire processing cost down and (3) inter-filament spacing, which should not be too large to allow mutual support of the filaments during wire processing (see the discussion that follows) and should not be too small to avoid proximity effect coupling [129].

The inter-filament spacing is determined by the local copper-to-superconductor ratio of the mono-filament rod assembly in the stacking of the multi-filament billet. For sub-micrometer inter-filament spacing, the proximity effect coupling can be limited by doping the copper of the mono-filament billet with manganese [130]. In addition, it is desirable to leave a copper core at the wire center and a copper sheath at the wire periphery to protect the multifilamentary area from cabling degradation. For SSC and LHC wires, the interfilament spacing is of the order of 1 μm (which does not require Mn doping), the cross-sectional area of the copper core is less than 10% of the total wire cross-sectional area and the thickness of the copper outer sheath is in the range 50 to 100 μm.

The main issues regarding wire manufacturing are: (1) piece length and (2) critical current optimization. Breakages during wire drawing are unavoidable, resulting in multiple piece lengths. As most magnet builders prefer to wind coils with weld-free cables made from single-piece wires, the average wire piece length must be at least equal to the cable length needed to wind a coil. Also, a low breakage rate in wire production is an assurance of quality and uniformity. For LHC, wires are accepted on a billet basis, and it is required that, for each billet, at least 90% of the final-size pieces be longer than 1 km. The factors influencing piece length are: (1) cleanliness of billet assembly, to avoid inclusions of foreign particles, (2) precipitation of unwanted, hard-to-draw phases in NbTi alloy, which must be prevented and (3) formation of $TiCu_4$ compounds at the matrix/filament interface, which must be limited. As already mentioned, the formation of $TiCu_4$ compounds can be restricted by surrounding the filaments with niobium barriers, but it has been shown that the barriers were not totally impermeable to Cu and Ti diffusion when subjected to multiple heat treatments [131].

The factors influencing critical current density can be classified into two categories: (1) intrinsic factors, related to NbTi alloy microstructure and affecting fluxon pinning, and (2) extrinsic factors, related to macroscopic irregularities and causing local reductions in filament cross-sectional areas. Among the intrinsic factors are: (1) homogeneity of the NbTi ingots used for the mono-filament billets, which must be tightly controlled (typically +/- 1% in weight of Ti) and (2) parameters and schedule of cold-work and heat treatment cycles during wire production. The extrinsic factors are basically the same as the factors influencing piece length. In addition, it is preferable to maintain a small inter-filament spacing, so that the NbTi filaments, which are much harder than the high purity copper matrix, can support each other during the multiple drawing operations. As we have seen, a way of determining if the critical current of a wire is limited by intrinsic or extrinsic parameters, is to study the evolution of its *N*-value as a function of magnetic flux density.

3.4.3 CRITICAL SURFACE PARAMETRIZATION

The upper critical magnetic flux density, B_{C2}, of binary NbTi can be estimated as a function of temperature, T, using [132]

$$B_{C2}(T) = B_{C20}\left[1-\left(\frac{T}{T_{C0}}\right)^{1.7}\right] \tag{13}$$

where B_{C20} is the upper critical magnetic flux density at zero temperature (about 14.5 T) and T_{C0} is the critical temperature at zero magnetic flux density (about 9.2 K).

The critical current density, J_C, can be parametrized as a function of temperature, magnetic flux density, B, and critical current density at 4.2 K and 5 T, J_{Cref}, using [133]

$$\frac{J_C(B,T)}{J_{Cref}} = \frac{D_{NbTi}}{B}\left[\frac{B}{B_{C2}(T)}\right]^{\beta_1}\left[1-\frac{B}{B_{C2}(T)}\right]^{\beta_2}\left[1-\left(\frac{T}{T_{C0}}\right)^{1.7}\right]^{\beta_3} \tag{14}$$

where D_{NbTi}, β_1, β_2 and β_3 are fitting parameters.

Since the time of Tevatron, a factor of about 2 has been gained on the critical current density at 4.2 K and 5 T, thanks to the understanding of the role played by α–Ti precipitates in pinning mechanisms. Values of J_{Cref} in excess of 3000 A/mm^2 are now obtained in industrial production [134]. Typical fitting parameters values for LHC strands are: D_{NbTi} = 31.4 T, β_1 = 0.63, β_2 = 1.0 and β_3 = 2.3. Note that the "J_C versus B" curve shifts by about (+3 T) when lowering the temperature from 4.2 K to 1.9 K.

3.5 NB_3SN WIRES

3.5.1 PROCESSING

There are at least four ways of industrially processing Nb_3Sn multifilamentary wires, which are well described in the literature [109]–[111]: (1) bronze process, (2) internal-tin process, (3) Modified Jelly Roll (MJR) process and (4) Powder-In-Tube (PIT) process. Each process has its advantages and its disadvantages and none of them is fully satisfactory. Figure 20 presents a cross-sectional view of an un-reacted, internal-tin wire at final size [127].

Given that reacted Nb_3Sn conductors are very fragile and cannot be bent on small radii, the manufacturing of Nb_3Sn coils calls for special fabrication processes, which are risky and onerous. In the case of accelerator magnet coils, the cable is manufactured and wound un-reacted, and the whole coil is subjected to heat-treatment, according to the so-called *wind-and-react* technique.

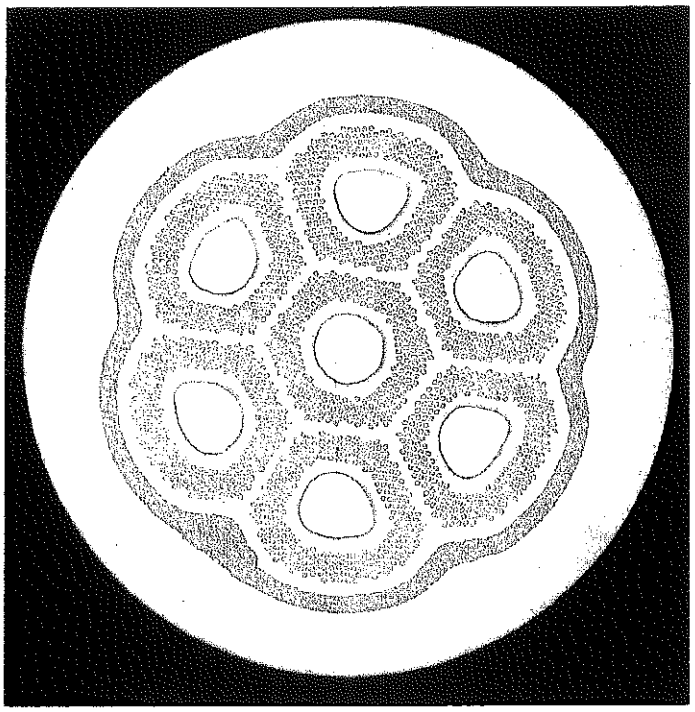

Figure 20. Cross-sectional view of an un-reacted, Nb_3Sn multifilamentary composite wire prepared by the internal-tin process [127].

3.5.2 CRITICAL SURFACE PARAMETRIZATION

The upper critical magnetic flux density, B_{C2}, of binary or ternary Nb_3Sn, can be estimated as a function of temperature, T, and strain, ε, using [135]

$$\frac{B_{C2}(T,\varepsilon)}{B_{C20}(\varepsilon)} = \left[1-\left(\frac{T}{T_{C0}(\varepsilon)}\right)^2\right]\left\{1-0.31\left(\frac{T}{T_{C0}(\varepsilon)}\right)^2\left[1-1.77\ln\left(\frac{T}{T_{C0}(\varepsilon)}\right)\right]\right\} \tag{15}$$

where B_{C20} is the upper critical magnetic flux density at zero temperature

$$B_{C20}(\varepsilon) = B_{C20m}\left(1-\beta|\varepsilon|^{1.7}\right) \tag{16}$$

and T_{C0} is the critical temperature at zero magnetic flux density

$$T_{C0}(\varepsilon) = T_{C0m}\left(1-\beta|\varepsilon|^{1.7}\right)^{1/3} \tag{17}$$

Here, β is a parameter equal to 900 for compressive strain ($\varepsilon \leq 0$) and to 1250 for tensile strain ($0 \leq \varepsilon$), B_{C20m} is the upper critical magnetic flux density at zero temperature and zero strain and T_{C0m} is the critical temperature at zero magnetic flux density and zero strain. For binary compounds, T_{C0m} and B_{C20m} can be taken equal to 16 K and 24 T, while for ternary compounds, they can be taken equal to 18 K and 28 T.

The critical current density can be parametrized as a function of temperature, magnetic flux density, B, and strain, using [135]

$$J_C(B,T,\varepsilon) = \frac{D(\varepsilon)}{\sqrt{B}}\left[1-\frac{B}{B_{C2}(T,\varepsilon)}\right]^2\left[1-\left(\frac{T}{T_{C0}(\varepsilon)}\right)^2\right]^2 \tag{18}$$

where

$$D(\varepsilon) = D_{Nb_3Sn}\,(1-\beta|\varepsilon|^{1.7})^{1/2} \tag{19}$$

Here D_{Nb_3Sn} is a fitting parameter.

In recent years, a significant R&D work has been carried out to improve the performance of Nb_3Sn multifilamentary wires, thanks to the International Thermonuclear Experimental Reactor (ITER) program [136]. Critical current density values of 750 A/mm^2 at 4.2 K and 12 T with effective filament diameters of 15 to 20 μm are now reached in industrial production [137]. Such values correspond to a D_{Nb_3Sn} of the order 12000 AT$^{1/2}$mm^{-2}. Note that the strain in the Nb_3Sn filaments of a reacted, freestanding composite wire is estimated at about –0.25%.

3.6 RUTHERFORD-TYPE CABLE

Superconducting particle accelerator magnet coils are wound from so-called *Rutherford-type* cables. As illustrated in Figure 21, a Rutherford-type cable consists of a few tens of strands, twisted together, and shaped into a flat, two-layer, slightly keystoned cable [111], [138]. As explained in the section on magnetic design, the slight keystone is introduced to allow stacking of the conductors into an arch and forming coils of the desired shape.

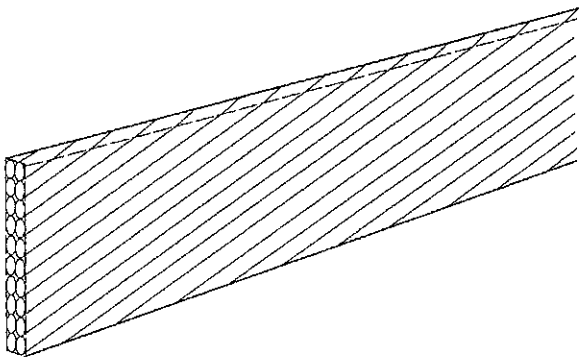

Figure 21. Sketch of a Rutherford-type cable for particle accelerator magnets.

The small radii of curvature of the coil ends preclude the use of a monolithic conductor because it would be too hard to bend. A multi-strand cable is preferred to a single wire for at least four reasons: (1) it limits the piece length requirement for wire manufacturing (a coil wound with a N-strand cable requires piece lengths which are $1/N$ shorter than for a similar coil wound with a single wire), (2) it allows strand-to-strand current redistribution in the case of a localized defect or when a quench originates in one strand [139], [140], (3) it limits the number of turns and facilitates coil winding, and (4) it limits coil inductance (the inductance of a coil wound with a N-strand cable is $1/N^2$ smaller than that of a similar coil wound with a single wire). A smaller inductance reduces the voltage requirement on the power supply to ramp-up the magnets to their operating current in a given time and limits the maximum voltage to ground in the case of a quench (see section on quench protection). The main disadvantage of using a cable is the high operating current (over a few thousand amperes) which requires large current supplies and large current leads.

The main issues for cable design and fabrication are: (1) compaction, which should be large enough to ensure good mechanical stability and high overall current density while leaving enough void (typically of the order of 10% in volume) for liquid helium cooling, (2) control of outer dimensions to achieve suitable coil geometry and mechanical properties, (3) limitation of critical current degradation due to strand and filament degradations at the cable edges [141], [142], and (4) control of interstrand resistance, which should not be too small to limit field distortions induced by interstrand coupling currents while ramping (see section on field quality) and should not be too large to allow current redistribution among cable strands.

The compaction of a keystoned cable is not uniform. It is customary to define an *overall compaction*, K_{cable}, as the ratio of the sum of the areas of undeformed strand cross sections to the area of the enclosing trapezoid [143]. As the strands are twisted together, their cross-sectional area is computed in a plane perpendicular to the cable axis. Then, we have

$$K_{\text{cable}} = \frac{N_{\text{cable}}\, \pi\, d_{\text{wire}}^2}{4\, w_{\text{cable}}\, t_{\text{cable,m}}\, \cos\psi_{\text{cable}}} \tag{20}$$

where N_{cable} is the number of cable strands, d_{wire} is the strand diameter, w_{cable} is the cable width, $t_{\text{cable,m}}$ is the cable mid-thickness, and ψ_{cable} is the cable pitch angle, defined as

$$\tan\psi_{\text{cable}} = \frac{2\, w_{\text{cable}}}{p_{\text{cable}}} \tag{21}$$

Here, p_{cable} is the cable pitch length.

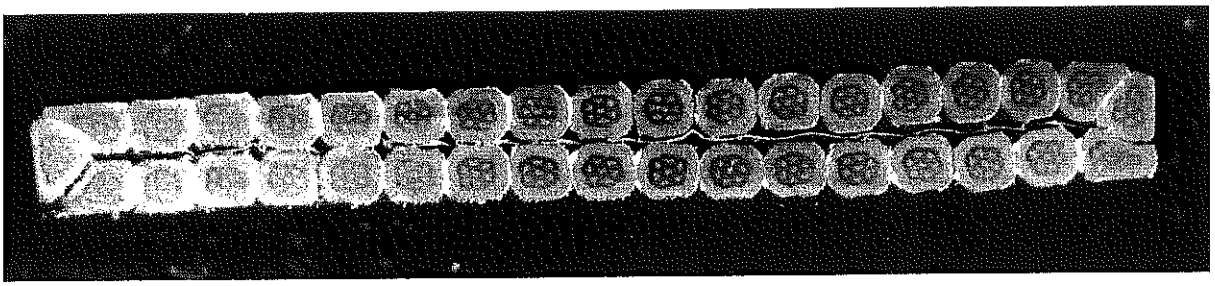

Figure 22. Cross-sectional view of an un-reacted, Nb_3Sn Rutherford-type cable with a 25-μm-thick stainless steel (annealed 316L) foil between the strand layers.

As an illustration, for the cable used in the outer layer of the LHC arc dipole magnet coils, we have: w_{cable} = 15.1 mm and p_{cable} = 100 mm, which yields: ψ_{cable} = 16.8°. Furthermore, we also have: N_{cable} = 36, d_{wire} = 0.825 mm and $t_{cable,m}$ = 1.48 mm, and we get: $K_{cable} \approx 90\%$. The manufacturing of about 5000, 14-m-long dipole outer coils and of over 3500, 3-m-long, two-layer quadrupole coils will require of the order 4600 km (736 metric tons) of this cable. The specification on the minimum overall current capacity is 12960 A at 9 T and 1.9 K, and the minimum unit length is 750 m.

The interstrand resistance can be modified by oxidizing or by coating strand surface [144], [145]. Also, and as shown in Figure 22, a thin, insulating foil (such as stainless steel) can be inserted between the two layers of cable strands in order to increase the resistances at the strand crossovers [146]. Half of the strands of the Tevatron cable is coated with a silver-tin solder, called *stabrite*, while the other half is coated with *ebanol*, a chemical that favors the development of black copper oxide. The stabrite- and ebanol-coated strands are alternated, yielding a pattern of black and silver stripes. Such cable is referred to as *zebra* cable. The strands of the UNK, SSC and RHIC cables are bare, while the strands of the HERA and LHC cables are stabrite-coated. In addition, the LHC cables are subjected, at the end of cabling, to a heat treatment at 200 °C for 8 to 12 hours on special reels allowing air circulation. This heat treatment is optimized to prevent alterations of the niobium-titanium alloy microstructure, while favoring oxidation of the stabrite coating so as to achieve a suitable level of crossover resistance (20±10 μΩ). Also, it contributes to an annealing of the high purity copper of the strand matrix that is cold-worked by the cabling operation. Up to now, no foiled cable has been used in a magnet.

Similarly to wires, the maximum current-carrying capacity of cables can be determined from measurements on short samples. The voltage-current curves of cable short samples are similar to that of wire short samples and the cable performances can be characterized using the same definitions of critical current and *N*-value. BNL has developed a cable short sample test facility that is widely used as a bench mark for NbTi Rutherford-type

cables [147]. The critical current of Nb_3Sn Rutherford-type cables has been shown to be sensitive to transverse pressure and requires elaborate test setups to be measured in conditions relevant to accelerator magnet operations [148], [149].

3.7 CABLE INSULATION

3.7.1 INSULATION REQUIREMENTS

The main requirements for cable insulation are: (1) good dielectric strength in helium environment and under high transverse pressure (up to 100 MPa), (2) small thickness (to maximize overall current density in the magnet coil) and good physical uniformity (to ensure proper conductor positioning for field quality), (3) retention of mechanical properties over a wide temperature range, and (4) ability to withstand radiations in an accelerator environment. In addition, the insulation system is required to provide a mean of bonding the coil turns together to give the coil a semi-rigid shape and facilitate its manipulation during the subsequent steps of magnet assembly. It is also desirable that the insulation be somewhat porous to helium for conductor cooling.

Note that the dielectric strength of helium gas at 4.2 K is far worse than that of liquid helium and that it degrades significantly with increasing temperature [150].

3.7.2 INSULATION OF NBTI CABLES

The insulation of Tevatron, HERA and UNK magnets, of most SSC magnets and of the early LHC magnet models is made up of one or two inner layers of polyimide film, wrapped helically with a 50-to-60% overlap, completed by an outer layer of resin-impregnated glass fiber tape, wrapped helically with a small gap. The inner layer is wrapped with an overlap for at least two reasons: (1) the polyimide film may contain pin holes which have to be covered (the probability of having two superimposed pin holes in the overlapping layer is very low) and (2) the Tevatron experience has shown that it was preferable to prevent the resin impregnating the glass wrap from entering in contact with the NbTi cable (the energy released by cracks in the resin is believed to be sufficient to initiate a quench; p. 784 of Ref. [23]). The outer layer is wrapped with a gap to set up helium cooling channels between coil turns. The resin is of thermosetting-type and requires heat to increase cross link density and cure into a rigid bonding agent. The curing is realized after winding completion in a mold of very accurate dimensions to control coil geometry and Young's modulus [151].

RHIC magnets and the most recent LHC magnet models use a so-called *all-polyimide* insulation where the outer glass fiber wrap is replaced by another layer of polyimide film with a polyimide adhesive on its surface [152]. The all-polyimide insulation

has a better resistance to puncture, but the softening temperature of the adhesive can be higher than the temperature needed to cure a conventional resin (225 °C for RHIC-type all-polyimide insulation compared to 135 °C for SSC-type polyimide/glass insulation).

In addition, and for NbTi cables cooled by superfluid helium, it has been shown that the static heat transfer to the coolant strongly depended on the conductor insulation scheme (see section 9.4). Hence, in this case, the conductor insulation scheme can also be optimized to improve heat transfer and limit the effects of energy depositions by beam losses on magnet coils.

3.7.3 INSULATION OF Nb_3Sn CABLES

The insulation of Nb_3Sn cables is usually based on a glass fiber tape or a glass fiber sleeve put on the un-reacted conductor prior to winding. Upon winding completion, the coil is heat-treated to form Nb_3Sn. It is then transferred to a precision molding fixture to be vacuum-impregnated with resin. The glass fibers used for the tape or the sleeve must be able to sustain the required heat treatment without degradation. Also, all organic materials, such as sizing or finish, must be removed from the fibers to prevent the formation of carbon compounds that lower the dielectric strength. The sizing removal is performed by carbonization in air prior to conductor insulation. The implementation of such an insulation system adds to the difficulty of manufacturing Nb_3Sn coils for at least two reasons: (1) de-sized glass fiber tapes or sleeves are fragile and easy to tear off by friction [153] and (2) vacuum impregnation is a delicate operation. Furthermore, a full impregnation prevents any helium penetration in the coil, thereby reducing greatly cooling capabilities.

4 COMPLEX FORMALISM FOR TWO-DIMENSIONAL FIELDS

4.1 CONDUCTOR MODEL AND PROBLEM SYMMETRY

Let $(O,\vec{x},\vec{y},\vec{z})$ designate a rectangular coordinate system, and let us consider an ensemble of conductors parallel to the z-axis and uniform in z. Let Σ_{cond} designate the conductors' surface and let $V(\Sigma_{cond})$ designate the volume inside the conductors [note that Σ_{cond} and $V(\Sigma_{cond})$ may be multiply connected]. Furthermore, let us assume that the conductors carry a constant current density, parallel to the z-axis and uniform in z. Let G designate a given point of space, and let $\overrightarrow{J_G}$ designate the current density at G. We have

$$\overrightarrow{J_G} = J_{G,z}(x,y)\ \vec{z} \qquad \text{for G, G} \in V(\Sigma_{cond}) \tag{22a}$$

and

$$\overrightarrow{J_G} = \vec{0} \qquad \text{for G, G} \notin V(\Sigma_{cond}) \tag{22b}$$

where $J_{G,z}$ is the z-component of $\overrightarrow{J_G}$.

Given the problem symmetry, the magnetic flux density, $\overrightarrow{B_M}$, produced at a given point, M, of space by the currents carried by the conductors is expected to be uniform in z. Hence, we can write

$$\overrightarrow{B_M} = B_{M,x}(x,y)\ \vec{x} + B_{M,y}(x,y)\ \vec{y} + B_{M,z}(x,y)\ \vec{z} \tag{23}$$

where $B_{M,x}$, $B_{M,y}$ and $B_{M,z}$ are the x-, y- and z-components of $\overrightarrow{B_M}$.

4.2 PROPERTIES DERIVED FROM BIOT AND SAVART'S LAW

According to Biot and Savart's law, $\overrightarrow{B_M}$ can be computed as

$$\overrightarrow{B_M} = \iiint_{V(\Sigma_{cond})} dV_G\ \overrightarrow{J_G}\ x\ \frac{\overrightarrow{GM}}{GM^3} \tag{24}$$

where G is a given point of $V(\Sigma_{cond})$, dV_G is an elementary volume in the vicinity of G, and GM is the modulus of $\overrightarrow{GM}$.

By combining Eqs. (22a) and (24) it follows that

$$\overrightarrow{B_M} = \vec{z}\ x \iiint_{V(\Sigma_{cond})} dV_G\ J_{G,z}\ \frac{\overrightarrow{GM}}{GM^3} \tag{25}$$

which shows that the magnetic flux density is perpendicular to the z-axis and that

$$B_{M,z}(x,y) = 0 \qquad \text{for all } x \text{ and all } y \tag{26}$$

In the following, we drop the indices M and G and we simply refer to the current density and the magnetic flux density at a given point of space by $\vec{J}$ and $\vec{B}$. Also, we designate by Γ_{cond} the intersection of Σ_{cond} with the $(O,\vec{x},\vec{y})$ plane, and we designate by $I(\Gamma_{cond})$ [respectively, $E(\Gamma_{cond})$] the interior (respectively, exterior) of Γ_{cond}.

4.3 PROPERTIES DERIVED FROM MAXWELL-GAUSS' EQUATION

According to Maxwell-Gauss' equation, the magnetic flux density, $\vec{B}$, everywhere satisfies

$$\vec{\nabla}.\vec{B} = 0 \tag{27}$$

By combining Eqs. (23), (26) and (27), we get

$$\frac{\partial B_x(x,y)}{\partial x} + \frac{\partial B_y(x,y)}{\partial y} = 0 \qquad \text{for all } x \text{ and all } y \tag{28}$$

4.4 PROPERTIES DERIVED FROM MAXWELL-AMPERE'S EQUATION

According to Maxwell-Ampere's equation, the magnetic field, $\vec{H}$, is everywhere related to the current density, $\vec{J}$, by

$$\vec{\nabla} \times \vec{H} = \vec{J} \tag{29}$$

Furthermore, let us assume that, everywhere in space [including in $V(\Sigma_{cond})$], $\vec{B}$ is related to $\vec{H}$ by

$$\vec{B} = \mu_0 \vec{H} \tag{30}$$

where $\mu_0 = 4\pi\ 10^{-7}$ H/m is the magnetic permeability of vacuum.

Then, by combining Eqs. (29) and (30), we get

$$\vec{\nabla} \times \vec{B} = \mu_0 \vec{J} \tag{31}$$

and by combining Eqs. (22a), (22b), (23), (26) and (31), we get

$$\frac{\partial B_y(x,y)}{\partial x} - \frac{\partial B_x(x,y)}{\partial y} = \mu_0 J_z(x,y) \qquad \text{for } (x,y), (x,y) \in I(\Gamma_{cond}) \tag{32a}$$

and

$$\frac{\partial B_y(x,y)}{\partial x} - \frac{\partial B_x(x,y)}{\partial y} = 0 \qquad \text{for } (x,y), (x,y) \in E(\Gamma_{cond}) \tag{32b}$$

4.5 COMPLEX MAGNETIC FLUX DENSITY OUTSIDE THE CONDUCTORS

Let us start by considering the exterior of the conductors, $E(\Gamma_{cond})$, and let $\mathbf{s}$ designate the complex variable defined as

$$\mathbf{s} = x + \mathrm{i}\, y \tag{33}$$

Furthermore, and as suggested by Ref. [154], let us introduce the complex magnetic flux density, $\mathbf{B_E}$, defined as

$$\mathbf{B_E(s)} = B_y(x,y) + \mathrm{i}\, B_x(x,y) \qquad \text{for } \mathbf{s},\ \mathbf{s} \in E(\Gamma_{cond}) \tag{34}$$

The real and imaginary parts, $\mathrm{Re}(\mathbf{B_E})$ and $\mathrm{Im}(\mathbf{B_E})$, of $\mathbf{B_E}$ are simply

$$\mathrm{Re}(\mathbf{B_E}) = B_y(x,y) \qquad \text{and} \qquad \mathrm{Im}(\mathbf{B_E}) = B_x(x,y) \tag{35}$$

The complex function, $\mathbf{B_E}$, is continuous and single-valued. Let us show that it is differentiable on $E(\Gamma_{cond})$. This can be done by demonstrating that $\mathrm{Re}(\mathbf{B_E})$ and $\mathrm{Im}(\mathbf{B_E})$ satisfy Cauchy-Riemann's conditions for the functions of complex variable (p. 110 of Ref. [155])

$$\frac{\partial \mathrm{Re}(\mathbf{B_E})}{\partial x} - \frac{\partial\, \mathrm{Im}(\mathbf{B_E})}{\partial y} = 0 \tag{36a}$$

and

$$\frac{\partial \mathrm{Re}(\mathbf{B_E})}{\partial y} + \frac{\partial\, \mathrm{Im}(\mathbf{B_E})}{\partial x} = 0 \tag{36b}$$

On one hand, we have

$$\frac{\partial \mathrm{Re}(\mathbf{B_E})}{\partial x} - \frac{\partial\, \mathrm{Im}(\mathbf{B_E})}{\partial y} = \frac{\partial B_y(x,y)}{\partial x} - \frac{\partial B_x(x,y)}{\partial y} \tag{37}$$

which, by combination with Eq. (32b), yields Eq. (36a).

On the other hand, we have

$$\frac{\partial \mathrm{Re}(\mathbf{B_E})}{\partial y} + \frac{\partial \mathrm{Im}(\mathbf{B_E})}{\partial x} = \frac{\partial B_y(x,y)}{\partial y} + \frac{\partial B_x(x,y)}{\partial x} \tag{38}$$

which, by combination with Eq. (28), yields Eq. (36b).

It follows that $\mathbf{B_E}$ is single-valued and analytic on $\mathrm{E}(\Gamma_{\mathrm{cond}})$.

Note that to derive Cauchy-Riemann's conditions from Maxwell's equations, the complex magnetic flux density must be defined as $(B_y + \mathrm{i}\, B_x)$ [or $(B_x - \mathrm{i}\, B_y)$], and that the function defined as $(B_x + \mathrm{i}\, B_y)$ is not analytic.

4.6 COMPLEX MAGNETIC FLUX DENSITY INSIDE THE CONDUCTORS

Let us now consider the conductors' interior, $\mathrm{I}(\Gamma_{\mathrm{cond}})$, and let us assume that the z-component of the current density is uniform over $\mathrm{I}(\Gamma_{\mathrm{cond}})$

$$J_z(x,y) = J_0 \qquad \text{for } (x,y),\ (x,y) \in \mathrm{I}(\Gamma_{\mathrm{cond}}) \tag{39}$$

where J_0 is a constant.

As, again, suggested by Ref. [154], let us introduce the complex magnetic flux density, $\mathbf{B_I}$, defined as

$$\mathbf{B_I(s)} = B_y(x,y) + \mathrm{i}\, B_x(x,y) - \frac{\mu_0 J_0}{2}\, \mathbf{s}^* \qquad \text{for } \mathbf{s},\ \mathbf{s} \in \mathrm{I}(\Gamma_{\mathrm{cond}}) \tag{40}$$

where $\mathbf{s}^*$ is the complex conjugate of $\mathbf{s}$. This time, the real and imaginary parts, $\mathrm{Re}(\mathbf{B_I})$ and $\mathrm{Im}(\mathbf{B_I})$], of $\mathbf{B_I}$ are given by

$$\mathrm{Re}(\mathbf{B_I}) = B_y(x,y) - \frac{\mu_0 J_0}{2}\, x \qquad \text{and} \qquad \mathrm{Im}(\mathbf{B_I}) = B_x(x,y) + \frac{\mu_0 J_0}{2}\, y \tag{41}$$

The complex function, $\mathbf{B_I}$, is continuous and single-valued. Similarly to what we did for $\mathbf{B_E}$, let us show that $\mathbf{B_I}$ is differentiable on $\mathrm{I}(\Gamma_{\mathrm{cond}})$ by demonstrating that $\mathrm{Re}(\mathbf{B_I})$ and $\mathrm{Im}(\mathbf{B_I})$ satisfy Cauchy-Riemann's conditions.

One hand, we have

$$\frac{\partial \mathrm{Re}(\mathbf{B_I})}{\partial x} - \frac{\partial \mathrm{Im}(\mathbf{B_I})}{\partial y} = \frac{\partial B_y(x,y)}{\partial x} - \frac{\partial B_x(x,y)}{\partial y} - \mu_0 J_0 \tag{42}$$

which, by combination with Eq. (32a) and (39), yields

$$\frac{\partial \mathrm{Re}(\mathbf{B_I})}{\partial x} - \frac{\partial \mathrm{Im}(\mathbf{B_I})}{\partial y} = 0 \qquad \text{for } (x,y),\,(x,y) \in \mathrm{I}(\Gamma_{\mathrm{cond}}) \tag{43}$$

On the other hand, we still have

$$\frac{\partial \mathrm{Re}(\mathbf{B_I})}{\partial y} + \frac{\partial \mathrm{Im}(\mathbf{B_I})}{\partial x} = \frac{\partial B_{\mathrm{y}}(x,y)}{\partial y} + \frac{\partial B_{\mathrm{x}}(x,y)}{\partial x} \tag{44}$$

which, by combination with Eq. (28), again yields

$$\frac{\partial \mathrm{Re}(\mathbf{B_I})}{\partial y} + \frac{\partial \mathrm{Im}(\mathbf{B_I})}{\partial x} = 0 \tag{45}$$

It follows that $\mathbf{B_I}$ is single-valued and analytic on $\mathrm{I}(\Gamma_{\mathrm{cond}})$.

4.7 INTEGRAL FORMULAE FOR COMPUTING TWO-DIMENSIONAL MAGNETIC FLUX DENSITIES

4.7.1 CONDUCTOR MODEL AND NOTATIONS

Let again $(\mathrm{O},\vec{\mathrm{x}},\vec{\mathrm{y}},\vec{\mathrm{z}})$ designate a rectangular coordinate system, and let us consider a single conductor parallel to the z-axis and uniform in z. Let Σ_{cond} designate the conductor surface, let Γ_{cond} designate the intersection of Σ_{cond} with the $(\mathrm{O},\vec{\mathrm{x}},\vec{\mathrm{y}})$ plane, and let $\mathrm{I}(\Gamma_{\mathrm{cond}})$ [respectively, $\mathrm{E}(\Gamma_{\mathrm{cond}})$] designate the interior [respectively, exterior] of Γ_{cond}. Furthermore, let us assume that the conductor carries an uniform and constant current density, of modulus, J_0, parallel to the z-axis. We have shown that, for this type of current distribution, the complex function, $\mathbf{B_I}$, defined by Eq. (40) is single-valued and analytic over $\mathrm{I}(\Gamma_{\mathrm{cond}})$, and that the complex function, $\mathbf{B_E}$, defined by Eq. (34) is single-valued and analytic over $\mathrm{E}(\Gamma_{\mathrm{cond}})$.

4.7.2 PROPERTIES DERIVED FROM CAUCHY'S INTEGRAL FORMULAE

Since $\mathbf{B_I}$ is a single-valued function, which is analytic on $\mathrm{I}(\Gamma_{\mathrm{cond}})$ and continuous on $\overline{\mathrm{I}(\Gamma_{\mathrm{cond}})} = \mathrm{I}(\Gamma_{\mathrm{cond}}) \cup \Gamma_{\mathrm{cond}}$, it can be shown, using a generalization of Cauchy's integral formula, that (p. 293 of Ref. [155], [156])

$$\frac{1}{2i\pi} \oint_{\Gamma_{\mathrm{cond}}} \mathbf{da}\, \frac{\mathbf{B_I(a)}}{\mathbf{a}-\mathbf{s}} = \mathbf{B_I(s)} \qquad \text{for } \mathbf{s},\ \mathbf{s} \in \mathrm{I}(\Gamma_{\mathrm{cond}}) \tag{46a}$$

and

$$\frac{1}{2i\pi}\oint_{\Gamma_{cond}} \mathbf{da}\,\frac{\mathbf{B_I(a)}}{\mathbf{a}-\mathbf{s}} = \mathbf{0} \qquad \text{for } \mathbf{s},\ \mathbf{s} \in E(\Gamma_{cond}) \tag{46b}$$

where the closed curve Γ_{cond} is traversed in the counter-clockwise direction.

Let us now consider $\mathbf{B_E}$. Infinitely far from the conductor in the complex plane, we can assume that

$$\lim_{|\mathbf{s}|\to+\infty}[\mathbf{B_E(s)}] = \mathbf{0} \tag{47}$$

Then, since $\mathbf{B_E}$ is a single-valued function, which is analytic on $E(\Gamma)$ and continuous on $\overline{E(\Gamma_{cond})} = E(\Gamma_{cond}) \cup \Gamma_{cond}$, it can be shown, using a generalization of Cauchy's integral formula for an unbounded domain, that (p. 318 of Ref. [155], [156])

$$\frac{1}{2i\pi}\oint_{\Gamma_{cond}} \mathbf{da}\,\frac{\mathbf{B_E(a)}}{\mathbf{a}-\mathbf{s}} = \lim_{|\mathbf{s}|\to+\infty}[\mathbf{B_E(s)}] = \mathbf{0} \qquad \text{for } \mathbf{s},\ \mathbf{s} \in I(\Gamma_{cond}) \tag{48a}$$

and

$$\frac{1}{2i\pi}\oint_{\Gamma_{cond}} \mathbf{da}\,\frac{\mathbf{B_E(a)}}{\mathbf{a}-\mathbf{s}} = -\mathbf{B_E(s)} + \lim_{|\mathbf{s}|\to+\infty}[\mathbf{B_E(s)}] = -\mathbf{B_E(s)}$$

$$\text{for } \mathbf{s},\ \mathbf{s} \in E(\Gamma_{cond}) \tag{48b}$$

4.7.3 Practical Formulae For Magnetic Flux Density Computation

By subtracting Eq. (48a) from Eq. (46a), we get

$$\frac{1}{2i\pi}\oint_{\Gamma_{cond}} \mathbf{da}\,\frac{\mathbf{B_I(a)} - \mathbf{B_E(a)}}{\mathbf{a}-\mathbf{s}} = \mathbf{B_I(s)} \qquad \text{for } \mathbf{s},\ \mathbf{s} \in I(\Gamma_{cond}) \tag{49a}$$

and by subtracting Eq. (48b) from Eq. (46b), we get

$$\frac{1}{2i\pi}\oint_{\Gamma_{cond}} \mathbf{da}\,\frac{\mathbf{B_I(a)} - \mathbf{B_E(a)}}{\mathbf{a}-\mathbf{s}} = \mathbf{B_E(s)} \qquad \text{for } \mathbf{s},\ \mathbf{s} \in E(\Gamma_{cond}) \tag{49b}$$

Let us now replace $\mathbf{B_I}$ and $\mathbf{B_E}$ by their definitions, we get

$$B_y(x,y) + i\,B_x(x,y) = \frac{\mu_0 J_0}{2}\,\mathbf{s}^* - \frac{\mu_0 J_0}{4i\pi}\oint_{\Gamma_{cond}} \mathbf{da}\,\frac{\mathbf{a}^*}{\mathbf{a}-\mathbf{s}} \qquad \text{for } \mathbf{s},\ \mathbf{s} \in I(\Gamma_{cond}) \tag{50a}$$

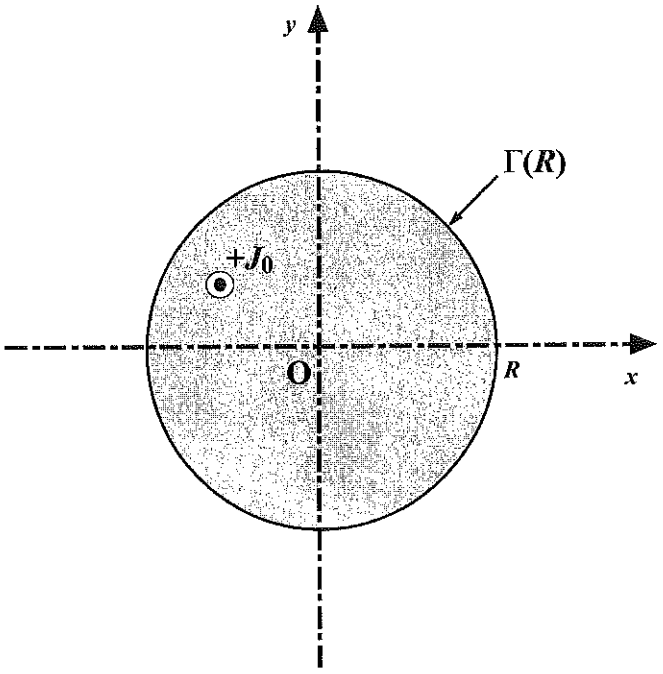

Figure 23. Straight cylindrical conductor with a circular cross-section.

and

$$B_y(x,y) + i\,B_x(x,y) = -\frac{\mu_0 J_0}{4i\pi}\oint_{\Gamma_{cond}} \mathbf{da}\,\frac{\mathbf{a}^*}{\mathbf{a}-\mathbf{s}} \qquad \text{for } \mathbf{s},\ \mathbf{s} \in E(\Gamma_{cond}) \tag{50b}$$

The above equations can be used to determine B_x and B_y anywhere in space by computation of simple integrals in the complex plane.

4.7.4 Example: Cylindrical Conductor With Circular Cross-Section

As an illustration on how to use Eqs. (50a) and (50b), let us consider the case of an infinite and straight cylindrical conductor, whose generator is parallel to the z-axis, and whose director is a circle, Γ_R, of center, O, and radius, R, located in the $(O,\vec{x},\vec{y})$ plane, as represented in Figure 23. Furthermore, let us assume that the conductor carries an uniform and constant current density, of modulus, J_0, parallel to the z-axis.

In this simple case, we can write

$$\mathbf{a}^* = \frac{R^2}{\mathbf{a}} \qquad \text{for } \mathbf{a},\ \mathbf{a} \in \Gamma_R \tag{51}$$

This yields

$$\frac{\mathbf{a}^*}{\mathbf{a}-\mathbf{s}} = \frac{R^2}{\mathbf{a}(\mathbf{a}-\mathbf{s})} = \frac{R^2}{\mathbf{s}}\left(\frac{-1}{\mathbf{a}} + \frac{1}{\mathbf{a}-\mathbf{s}}\right) \qquad \text{for } \mathbf{a},\ \mathbf{a} \in \Gamma_R \tag{52}$$

and we get

$$\oint_{\Gamma_R} \mathbf{da}\,\frac{\mathbf{a}^*}{\mathbf{a}-\mathbf{s}} = \frac{-R^2}{\mathbf{s}} \oint_{\Gamma_R} \frac{\mathbf{da}}{\mathbf{a}} + \frac{R^2}{\mathbf{s}} \oint_{\Gamma_R} \frac{\mathbf{da}}{\mathbf{a}-\mathbf{s}} \tag{53}$$

For the first integral, we simply have

$$\oint_{\Gamma_R} \frac{\mathbf{da}}{\mathbf{a}} = 2i\pi \tag{54}$$

while for the second integral, it comes

$$\oint_{\Gamma_R} \frac{\mathbf{da}}{\mathbf{a}-\mathbf{s}} = 2i\pi \qquad \text{for } \mathbf{s},\ \mathbf{s} \in \mathrm{I}(\Gamma_R) \tag{55a}$$

and

$$\oint_{\Gamma_R} \frac{\mathbf{da}}{\mathbf{a}-\mathbf{s}} = 0 \qquad \text{for } \mathbf{s},\ \mathbf{s} \in \mathrm{E}(\Gamma_R) \tag{55b}$$

where $\mathrm{I}(\Gamma_R)$ [respectively, $\mathrm{E}(\Gamma_R)$] designates the interior (respectively, the exterior) of Γ_R.

By combining Eqs. (50a), (53), (54) and (55a), we get for the inside of the conductor

$$B_y(x,y) + i\,B_x(x,y) = \frac{\mu_0 J_0}{2}\,\mathbf{s}^* \qquad \text{for } \mathbf{s},\ \mathbf{s} \in \mathrm{I}(\Gamma_R) \tag{56a}$$

while by combining Eqs. (50b), (53), (54) and (55b), we get for the outside of the conductor

$$B_y(x,y) + i\,B_x(x,y) = \frac{\mu_0 I_0}{2\pi}\,\frac{1}{\mathbf{s}} \qquad \text{for } \mathbf{s},\ \mathbf{s} \in \mathrm{E}(\Gamma_R) \tag{56b}$$

In Eq. (56b), I_0 designates the total intensity of the current carried by the conductor

$$I_0 = \pi R^2 J_0 \tag{57}$$

It can easily be verified that, for $\mathbf{s} \in \Gamma_R$, Eqs. (56a) and (56b) yield the same result.

4.8 MULTIPOLE EXPANSION FOR TWO-DIMENSIONAL FIELDS

4.8.1 POWER SERIES EXPANSION

Let us again consider an ensemble of conductors parallel to the z-axis and uniform in z, but let us assume that these conductors are located outside a cylinder whose generator is parallel to the z-axis and whose director is a circle, Γ_i, of center, O, and radius, R_i, located in the $(O,\vec{x},\vec{y})$ plane. This case is representative of a coil assembly around the aperture of an accelerator magnet. Within the cylinder, the current distribution produces a two-dimensional magnetic flux density, which can be represented by the single-valued and analytic function $\mathbf{B_E}$ defined by Eq. (34). From now on, we only concern ourselves with the magnetic flux density produced outside the conductors, and we drop the index E.

Furthermore, let $S(\Gamma_i)$ designate the disk of center, O, and of radius, R_i, based on Γ_i. Since $\mathbf{B}$ is analytic on $S(\Gamma_i)$, it can be expanded into a Taylor's series around the disk origin, and we have (p. 348 of Ref. [155])

$$\mathbf{B(s)} = \sum_{n=0}^{+\infty} \mathbf{B^{(n)}}(0)\,\frac{\mathbf{s}^n}{n!} \qquad \text{for } \mathbf{s},\ |\mathbf{s}| < R_i \tag{58}$$

where $\mathbf{B^{(n)}}$ is the n-th derivative of $\mathbf{B}$ with respect to $\mathbf{s}$.

In the United States (US), it is customary to re-write Eq. (58) under the form

$$\mathbf{B(s)} = \sum_{n=0}^{+\infty} (B_n + \mathrm{i}\,A_n)\left(\frac{\mathbf{s}}{R_{ref}}\right)^n \qquad \text{for } \mathbf{s},\ |\mathbf{s}| < R_i \qquad \text{(US)} \tag{59}$$

where R_{ref} is a reference radius (see section 4.8.3) and A_n and B_n are constant coefficients related to $\mathbf{B^{(n)}(0)}$ by

$$B_n + \mathrm{i}\,A_n = \frac{\mathbf{B^{(n)}}(0)}{n!}\,R_{ref}^n \qquad \text{for } n,\ n \geq 0 \qquad \text{(US)} \tag{60}$$

Note that A_n and B_n have the dimensions of magnetic flux densities (in teslas).

In the European Community (EC), most authors prefer to re-write Eq. (58) under the form

$$\mathbf{B(s)} = \sum_{n=1}^{+\infty} (B_n + \mathrm{i}\,A_n)\left(\frac{\mathbf{s}}{R_{ref}}\right)^{n-1} \qquad \text{for } \mathbf{s},\ |\mathbf{s}| < R_i \qquad \text{(EC)} \tag{61}$$

Here, A_n and B_n are related to $\mathbf{B^{(n-1)}(0)}$ by

$$B_n + i\,A_n = \frac{\mathbf{B^{(n-1)}(0)}}{(n-1)!} R_{ref}^{n-1} \qquad \text{for } n,\ n \geq 1 \qquad \text{(EC)} \tag{62}$$

The representation of the magnetic flux density by a power series expansion is that used in the accelerator physics community to compute beam orbits through magnet strings and to carry out particle tracking simulations. As a consequence, the field quality requirements for accelerator magnets are usually formulated as tolerances on the various terms of the power series expansion of the magnetic flux density. When computing or measuring the magnetic flux density of an accelerator magnet, it is therefore required to determine the coefficients of the power series expansion around the magnet center, and most of the discussions and/or interpretations are based on these coefficients.

In the following, we rely on the EC customary notation.

4.8.2 Interpretation of Power Series Expansion Coefficients

4.8.2.1 Coefficients of Order n = 1

Let us first consider a magnet such that, in the power series expansion of **B**, all the coefficients are nil, except B_1. Then we have

$$\mathbf{B} = B_y + i\,B_x = B_1 \tag{63}$$

The magnetic flux density is thus uniform and vertical. This corresponds to a pure normal dipole magnetic flux density with a pole axis parallel to the y-axis, as defined by Eq. (4) and as represented in Figure 10.

Let us now consider a magnet such that, in the power series expansion of **B**, the only non-zero coefficient is A_1. Then we have

$$\mathbf{B} = B_y + i\,B_x = i\,A_1 \tag{64}$$

The magnetic flux density is thus uniform and horizontal. This corresponds to a so-called pure *skew* dipole magnetic flux density, with a pole axis rotated by an angle $(-\pi/2)$ with respect to the y-axis.

Although A_1 and B_1 have the dimensions of magnetic flux densities, it is customary to refer to them as *skew* and *normal dipole field coefficients*.

4.8.2.2 Coefficients of Order n = 2

Let us now consider a magnet such that, in the power series expansion of **B**, all the coefficients are nil, except B_2. Then we have

$$\mathbf{B} = B_y + i B_x = \frac{B_2}{R_{ref}} (x + i y) \tag{65}$$

The y-component of the magnetic flux density is thus proportional to x, while the x-component is proportional to y, and the coefficients of proportionality are equal. This corresponds to a pure normal quadrupole magnetic flux density, with pole axes parallel to the first and second bisectors of the $(O, \vec{x}, \vec{y})$ plane, as defined by Eq. (6) and as represented in Figure 11. The quadrupole field gradient, g, is simply

$$g = \frac{B_2}{R_{ref}} \tag{66}$$

The units of g are teslas per meter.

Let us now consider a magnet such that, in the series expansion of **B**, the only non-zero coefficient is A_2. Then we have

$$\mathbf{B} = B_y + i B_x = \frac{A_2}{R_{ref}} (-y + i x) \tag{67}$$

This corresponds to a so-called pure *skew* quadrupole magnetic flux density, with pole axes rotated by an angle $(-\pi/4)$ with respect to the first and second bisectors. Here, the gradient, g, is given by

$$g = \frac{A_2}{R_{ref}} \tag{68}$$

The coefficients A_2 and B_2 are called *skew* and *normal quadrupole field coefficients.*

4.8.2.3 Coefficients of Order n

Similarly to the cases $n = 1$ and $n = 2$, it can be shown that the coefficients A_n and B_n correspond to pure $2n$-pole magnetic flux densities, and that the pole axes of the magnetic flux density associated with A_n are rotated by an angle $[-\pi/(2n)]$ with respect to the pole axes of the magnetic flux density associated with B_n. The coefficients A_n and B_n are called *skew* and *normal 2n-pole field coefficients.*

4.8.3 REFERENCE RADIUS

Equation (62) shows, that, except for $n = 1$, the multipole field coefficients depend on the reference radius, and that their values change when the reference radius is changed. Let A_n and B_n designate the multipole field coefficients defined for a reference radius, R_{ref}, and let A_n' and B_n' designate the multipole field coefficients defined for a different reference radius, R_{ref}'. From Eq. (62), it is easy to derive that

$$B_n' + i\,A_n' = \left(\frac{R_{ref}'}{R_{ref}}\right)^{n-1} (B_n + i\,A_n) \tag{69}$$

The choice of reference radius has evolved in time. It was 1 inch (25.4 mm) for the magnets developed for the Tevatron, which had a 3-inch (76.2-mm) aperture, and it was 25 mm for the magnets developed for HERA, which had a 75-mm aperture. In those days, the rule of thumb was to take for R_{ref}, one third of the magnet aperture. For the magnets developed for SSC and for early LHC model and prototype magnets, the value of R_{ref} was taken to be 10 mm, while the magnet apertures ranged from 40 to 56 mm. There are no compelling reasons to prefer one definition over the other, except the fact that, for a given magnetic design, and as can be seen in Eq. (69), the smaller the reference radius, the smaller the multipole field coefficients, and, therefore, the more politically correct they may appear... The LHC reference radius was recently (1998) increased to 17 mm.

4.8.4 COORDINATE SYSTEM TRANSFORMATIONS

We have shown how the complex magnetic flux density, **B**, could be expanded into a power series. Let us now study how the multipole field coefficients are affected by simple coordinate system transformations.

4.8.4.1 Translation

Let us first consider a rectangular coordinate system, $(O', \vec{x}', \vec{y}')$, such that the x'- and y'-axes are parallel and of same direction as the x- and y-axes, and

$$\overrightarrow{OO'} = \Delta x\,\vec{x} + \Delta y\,\vec{y} \tag{70}$$

as represented in Figure 24.

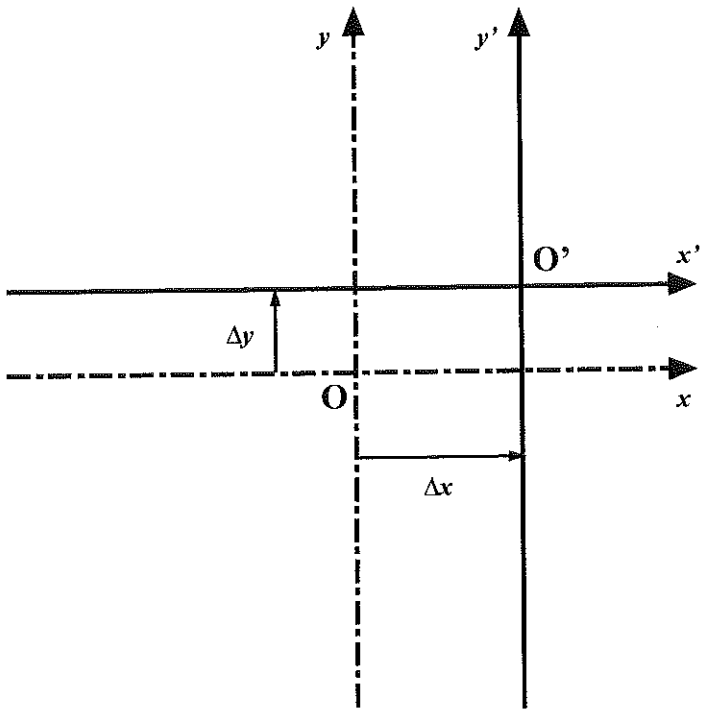

Figure 24. Coordinate system translation.

Let **s'** and **B'** designate the complex variable and the complex magnetic flux density associated with the new coordinate system. We have

$$\mathbf{B} = \mathbf{B'} \tag{71}$$

and

$$\mathbf{s} = \mathbf{s'} + \Delta x + \mathrm{i}\,\Delta y \tag{72}$$

By combining Eqs. (61), (71) and (72), we get

$$\begin{aligned}
\mathbf{B'(s')} = \mathbf{B(s)} &= \sum_{n=1}^{+\infty} (B_\mathrm{n} + \mathrm{i}\,A_\mathrm{n}) \left(\frac{\mathbf{s'} + \Delta x + \mathrm{i}\,\Delta y}{R_\mathrm{ref}} \right)^{n-1} \\
&= \sum_{n=1}^{+\infty} (B_\mathrm{n} + \mathrm{i}\,A_\mathrm{n}) \left[\sum_{k=0}^{n-1} \frac{(n-1)!}{k!(n-1-k)!} \left(\frac{\mathbf{s'}}{R_\mathrm{ref}} \right)^{k} \left(\frac{\Delta x + \mathrm{i}\,\Delta y}{R_\mathrm{ref}} \right)^{n-1-k} \right] \\
&= \sum_{n=1}^{+\infty} \left[\sum_{k=n}^{+\infty} (B_\mathrm{k} + \mathrm{i}\,A_\mathrm{k}) \frac{(k-1)!}{(n-1)!(k-n)!} \left(\frac{\Delta x + \mathrm{i}\,\Delta y}{R_\mathrm{ref}} \right)^{k-n} \right] \left(\frac{\mathbf{s'}}{R_\mathrm{ref}} \right)^{n-1}
\end{aligned} \tag{73}$$

where we recognize the multipole field expansion of **B'** around the new origin.

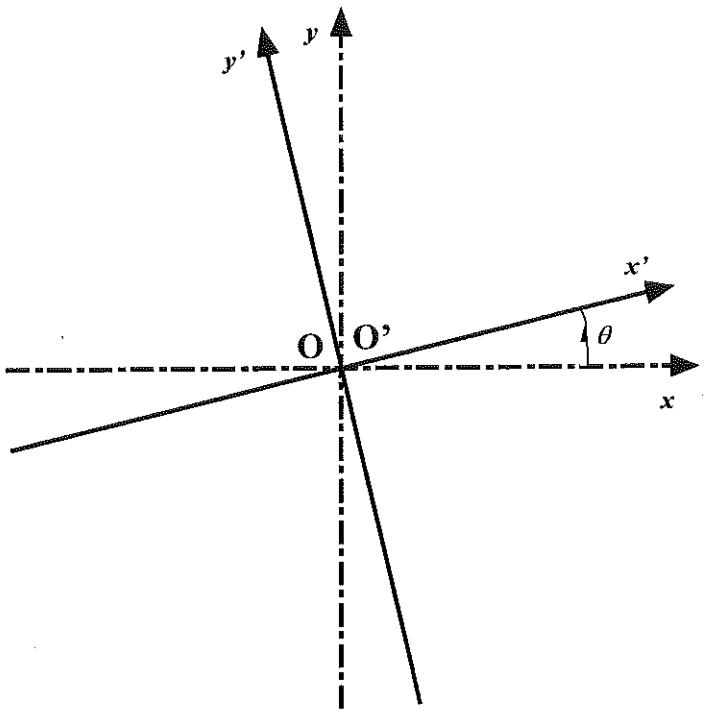

Figure 25. Coordinate system rotation.

Hence, the multipole field coefficients, A_n' and B_n', in the new coordinate system are related to the multipole field coefficients, A_n and B_n, in the old coordinate system by

$$B_n' + \mathrm{i}\,A_n' = \sum_{k=n}^{+\infty} (B_k + \mathrm{i}\,A_k) \frac{(k-1)!}{(n-1)!(k-n)!} \left(\frac{\Delta x + \mathrm{i}\,\Delta y}{R_{\mathrm{ref}}} \right)^{k-n}$$
$$= (B_n + \mathrm{i}\,A_n) + n(B_{n+1} + \mathrm{i}\,A_{n+1}) \left(\frac{\Delta x + \mathrm{i}\,\Delta y}{R_{\mathrm{ref}}} \right) + \ldots \qquad (74)$$

Equation (74) shows that the $2n$-pole field coefficients in the translated coordinate system are equal to the $2n$-pole field coefficients in the original coordinate system plus so-called *feed-down* terms from higher order multipole field coefficients.

4.8.4.2 Rotation

Let us now consider a rectangular coordinate system, $(O', \vec{x}', \vec{y}')$, such that O' and O are one and the same and the x'- and y'-axes are rotated by an angle, θ, with respect to the x- and y-axes, as represented in Figure 25.

Let again **s'** and **B'** designate the complex variable and the complex magnetic flux density associated with the new coordinate system.

We have

$$\mathbf{B} = \mathbf{B}' \, e^{-i\theta} \tag{75}$$

and

$$\mathbf{s} = \mathbf{s}' \, e^{i\theta} \tag{76}$$

By combining Eqs. (61), (75) and (76), we get

$$\mathbf{B}'(\mathbf{s}') = \mathbf{B}(\mathbf{s}) \, e^{i\theta} = \left[\sum_{n=1}^{+\infty} (B_n + i A_n) \left(\frac{\mathbf{s}' \, e^{i\theta}}{R_{ref}} \right)^{n-1} \right] e^{i\theta}$$

$$= \sum_{n=1}^{+\infty} \left[(B_n + i A_n) e^{in\theta} \right] \left(\frac{\mathbf{s}'}{R_{ref}} \right)^{n-1} \tag{77}$$

where we recognize the multipole field expansion of $\mathbf{B}'$ around O'. Hence, the multipole field coefficients, A_n' and B_n', in the new coordinate system are related to the multipole field coefficients, A_n and B_n, in the old coordinate system by

$$B_n' + i A_n' = (B_n + i A_n) \, e^{in\theta} \tag{78}$$

Equation (78) shows that the $2n$-pole field coefficients in the rotated coordinate system are equal to the $2n$-pole field coefficients in the original coordinate system rotated by an angle $(n\theta)$.

4.8.4.3 Change of x-axis Orientation

Let us now consider a rectangular coordinate system, $(O', \vec{x}', \vec{y}')$, such that O' and O are one and the same, the y'-axis is parallel and of same direction as the y-axis, and the x'-axis is parallel but of opposite direction to the x-axis, as represented in Figure 26. (This happens when facing a magnet from different ends.)

Let again $\mathbf{s}'$ and $\mathbf{B}'$ designate the complex variable and the complex magnetic flux density associated with the new coordinate system. We have

$$\mathbf{B} = (\mathbf{B}')^* \tag{79}$$

and

$$\mathbf{s} = -(\mathbf{s}')^* \tag{80}$$

where the asterisk designates the complex conjugate.

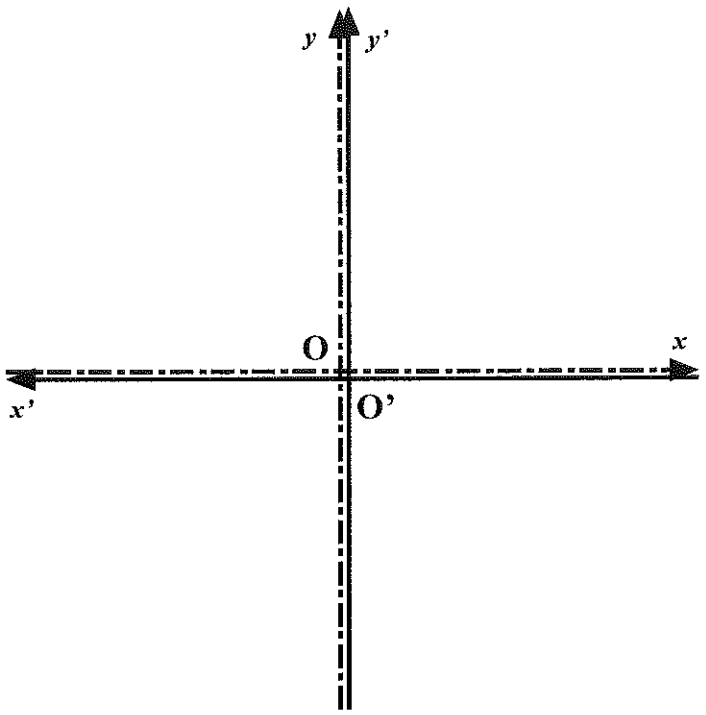

Figure 26. Coordinate system with change of x-axis orientation.

By combining Eqs. (61), (79) and (80), we get

$$\mathbf{B'(s')} = \mathbf{[B(s)]^*} = \left\{ \sum_{n=1}^{+\infty} \left(B_n + \mathrm{i}\, A_n\right) \left[\frac{-(\mathbf{s'})^*}{R_{\mathrm{ref}}} \right]^{n-1} \right\}^* \tag{81}$$

$$= \sum_{n=1}^{+\infty} \left[(-1)^{n-1} \left(B_n + \mathrm{i}\, A_n\right)^* \right] \left(\frac{\mathbf{s'}}{R_{\mathrm{ref}}} \right)^{n-1} \tag{82}$$

where we recognize the multipole field expansion of **B'** around O'. Hence, the multipole field coefficients, A_n' and B_n', in the new coordinate system are related to the multipole field coefficients, A_n and B_n, in the old coordinate system by

$$B_n' + \mathrm{i}\, A_n' = (-1)^{n-1} \left(B_n - \mathrm{i}\, A_n\right) \tag{83}$$

4.8.4.4 Change of y-axis Orientation

For completeness, let us now consider a rectangular coordinate system, $(O', \vec{x}', \vec{y}')$, such that O' and O are one and the same, the x'-axis is parallel and of same direction as the x-axis, and the y'-axis is parallel but of opposite direction to the y-axis, as represented in Figure 27. (This happens when performing magnetic measurements with a rotating coil array and when changing the direction of rotation of the array.)

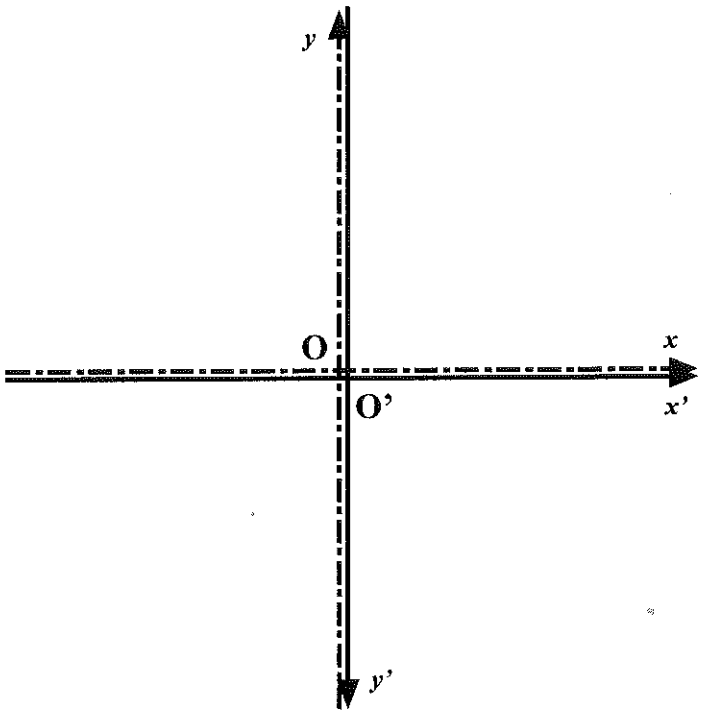

Figure 27. Coordinate system with change of y-axis orientation.

Let again **s'** and **B'** designate the complex variable and the complex magnetic flux density associated with the new coordinate system. We have

$$\mathbf{B} = -(\mathbf{B}')^* \tag{84}$$

and

$$\mathbf{s} = (\mathbf{s}')^* \tag{85}$$

where the asterisk designates the complex conjugate.

By combining Eqs. (61), (84) and (85), we get

$$\mathbf{B}'(\mathbf{s}') = -[\mathbf{B}(\mathbf{s})]^* = -\left\{\sum_{n=1}^{+\infty}\left(B_n + \mathrm{i}\,A_n\right)\left[\frac{(\mathbf{s}')^*}{R_{\mathrm{ref}}}\right]^{n-1}\right\}^*$$

$$= \sum_{n=1}^{+\infty} -\left(B_n + \mathrm{i}\,A_n\right)^*\left(\frac{\mathbf{s}'}{R_{\mathrm{ref}}}\right)^{n-1} \tag{86}$$

where we recognize the multipole field expansion of **B'** around O'. Hence, the multipole field coefficients, A_n' and B_n', in the new coordinate system are related to the multipole field coefficients, A_n and B_n, in the old coordinate system by

$$B_n' + \mathrm{i}\,A_n' = -B_n + \mathrm{i}\,A_n \tag{87}$$

4.9 MAGNETIC FLUX DENSITIES PRODUCED BY SIMPLE CURRENT DISTRIBUTIONS

4.9.1 SINGLE CURRENT LINE IN FREE SPACE

4.9.1.1 At the Origin of the Coordinate System

Let $(O,\vec{x},\vec{y},\vec{z})$ designate a rectangular coordinate system and let us consider a current line of intensity, $(-I)$, parallel to the z-axis, and crossing the $(O,\vec{x},\vec{y})$ plane at O, as represented in Figure 28(a). [The current line intensity is chosen to be negative to end up with a positive factor in the right member of Eq. (95).]

As shown in the previous sections, the magnetic flux density, $\vec{B}$, produced by this current line is independent of z and is parallel to the $(\vec{x},\vec{y})$ plane. It can be represented by the complex function, **B**, defined by Eq. (34). Furthermore, in the present case, **B** can be derived from Eq. (56b), and we simply have

$$\mathbf{B(s)} = -\frac{\mu_0 I}{2\pi}\frac{1}{\mathbf{s}} \qquad \text{for } \mathbf{s},\ \mathbf{s} \neq 0 \tag{88}$$

where **s** is the complex variable defined by Eq. (33).

4.9.1.2 Outside the Origin of the Coordinate System

Let us now consider a current line, $(-I,R,\alpha)$, of intensity, $(-I)$, parallel to the z-axis, and crossing the complex plane, $(O,\vec{x},\vec{y})$, at a point, **a**, different from O, and defined as [see Figure 28(b)]

$$\mathbf{a} = R\,e^{i\alpha} \tag{89}$$

It is straightforward to show that the magnetic flux density produced by this current line at a point, **s**, different from **a**, can be represented by the complex function, **B**, given by

$$\mathbf{B(s)} = -\frac{\mu_0 I}{2\pi}\frac{1}{\mathbf{s}-\mathbf{a}} \qquad \text{for } \mathbf{s},\ \mathbf{s} \neq \mathbf{a} \tag{90}$$

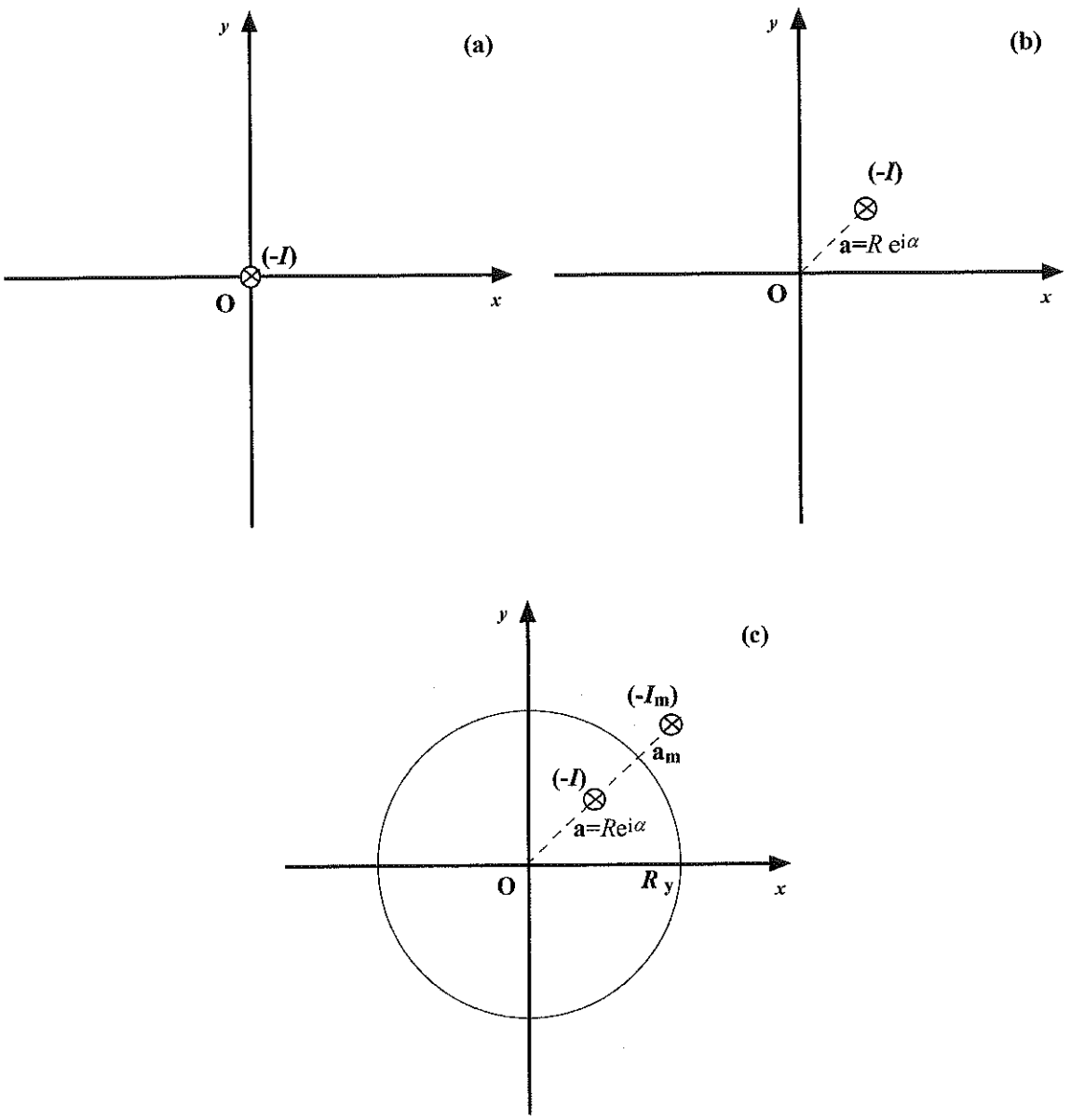

Figure 28. Representations of a single current-line: (a) in free space and at the coordinate system origin, (b) in free space and outside the coordinate system origin, and (c) in a cylindrical hollow space surrounded by a ferromagnetic medium.

4.9.1.3 Power Series Expansion

Equation (90) can be rewritten

$$\mathbf{B(s)} = \frac{\mu_0 I}{2\pi}\,\frac{1}{\mathbf{a}}\,\frac{1}{1-\left(\frac{\mathbf{s}}{\mathbf{a}}\right)} \tag{91}$$

Furthermore, we have

$$\frac{1}{1-\left(\frac{\mathbf{s}}{\mathbf{a}}\right)} = \sum_{n=0}^{+\infty} \left(\frac{\mathbf{s}}{\mathbf{a}}\right)^n \qquad \text{for } \mathbf{s},\ |\mathbf{s}| < |\mathbf{a}| \tag{92}$$

By combining Eqs. (91) and (92), we get

$$\mathbf{B}(\mathbf{s}) = \sum_{n=0}^{+\infty} \frac{\mu_0 I}{2\pi} \frac{\mathbf{s}^n}{\mathbf{a}^{n+1}} = \sum_{n=1}^{+\infty} \frac{\mu_0 I}{2\pi} \frac{\mathbf{s}^{n-1}}{\mathbf{a}^n} \qquad \text{for } \mathbf{s},\ |\mathbf{s}| < |\mathbf{a}| \tag{93}$$

The terms of Eq. (93) can be identified easily to the terms of the multipole expansion in Eq. (61) by introducing

$$B_n + \mathrm{i}\, A_n = \frac{\mu_0 I}{2\pi R_{\mathrm{ref}}} \left(\frac{R_{\mathrm{ref}}}{\mathbf{a}}\right)^n \tag{94}$$

Replacing **a** by its definition [see Eq. (89)] yields

$$B_n + \mathrm{i}\, A_n = \frac{\mu_0 I}{2\pi R_{\mathrm{ref}}} \left(\frac{R_{\mathrm{ref}}}{R}\right)^n \mathrm{e}^{-\mathrm{i}n\alpha} = \frac{\mu_0 I}{2\pi R_{\mathrm{ref}}} \left(\frac{R_{\mathrm{ref}}}{R}\right)^n [\cos(n\alpha) - \mathrm{i}\sin(n\alpha)] \tag{95}$$

Note again that A_n and B_n have the dimensions of magnetic flux densities (in teslas).

4.9.2 Single Current Line Within a Circular Iron Yoke

Let us now assume that the current line of Figure 28(b) is located within a cylindrical hollow space of z-axis and of radius, R_y, surrounded by a ferromagnetic medium, such as the iron yoke enclosing the coil assembly of an accelerator magnet [see Figure 28(c)].

The contribution of the ferromagnetic medium to the magnetic flux density produced within the hollow space can be shown to be the same as that of a mirror current line, of intensity, $(-I_m)$, and position, $\mathbf{a_m}$, in the complex plane, where [11], [157]

$$I_m = \frac{\mu - 1}{\mu + 1} I \qquad \text{and} \qquad \mathbf{a_m} = \frac{R_y^2}{\mathbf{a}^*} \tag{96}$$

Here μ designates the relative magnetic permeability of the ferromagnetic medium and $\mathbf{a}^*$ designates the complex conjugate of **a**. Note that the mirror image method is only applicable if the ferromagnetic medium is not saturated and as long as its permeability is uniform.

It follows that the contribution from the ferromagnetic medium can be represented by a complex function, $\mathbf{B}^{\mathbf{yoke}}$, which is expandable into a power series of the form given by Eq. (61), and where the multipole field coefficients, A_n^{yoke} and B_n^{yoke}, are given by

$$B_n^{\text{yoke}} + \mathrm{i}\, A_n^{\text{yoke}} = \frac{\mu-1}{\mu+1}\,\frac{\mu_0 I}{2\pi R_{\text{ref}}}\left(\frac{R_{\text{ref}}}{\mathbf{a_m}}\right)^n$$

$$= \frac{\mu-1}{\mu+1}\,\frac{\mu_0 I}{2\pi R_{\text{ref}}}\left(\frac{R_{\text{ref}} R}{R_y^2}\right)^n \left[\cos(n\alpha) - \mathrm{i}\sin(n\alpha)\right]$$

$$= \frac{\mu-1}{\mu+1}\left(\frac{R}{R_y}\right)^{2n}\left(B_n^{\text{line}} + \mathrm{i}\, A_n^{\text{line}}\right) \tag{97}$$

Here, A_n^{line} and B_n^{line} designate the multipole field coefficients produced by the current line alone in free space as given by Eq. (95).

Hence, the presence of the ferromagnetic material causes enhancements of the multipole field coefficients, which can be estimated as

$$\frac{B_n^{\text{tot}} + \mathrm{i}\, A_n^{\text{tot}}}{B_n^{\text{line}} + \mathrm{i}\, A_n^{\text{line}}} = 1 + \frac{\mu-1}{\mu+1}\left(\frac{R}{R_y}\right)^{2n} \tag{98}$$

where A_n^{tot} and B_n^{tot} are the multipole field coefficients of the resulting magnetic flux density in the hollow space.

4.9.3 Quadruplet of Current Lines with Dipole Symmetry

Let us now consider the quadruplet of current lines, $(-I,R,\alpha)$, $(+I,R,\pi-\alpha)$, $(+I,R,\pi+\alpha)$, and $(-I,R,-\alpha)$, shown in Figure 29(a). The magnetic flux density produced by this quadruplet can be estimated by summing the contributions from each current line. It follows that, within the circle of center, O, and radius, R, the magnetic flux density can be represented by the complex function, $\mathbf{B}$, given by Eq. (61), where

$$B_n + \mathrm{i}A_n = \frac{\mu_0 I}{2\pi R_{\text{ref}}}\left(\frac{R_{\text{ref}}}{R}\right)^n \left[\mathrm{e}^{-\mathrm{i}n\alpha} - \mathrm{e}^{-\mathrm{i}n(\pi-\alpha)} - \mathrm{e}^{-\mathrm{i}n(\pi+\alpha)} + \mathrm{e}^{+\mathrm{i}n\alpha}\right] \tag{99}$$

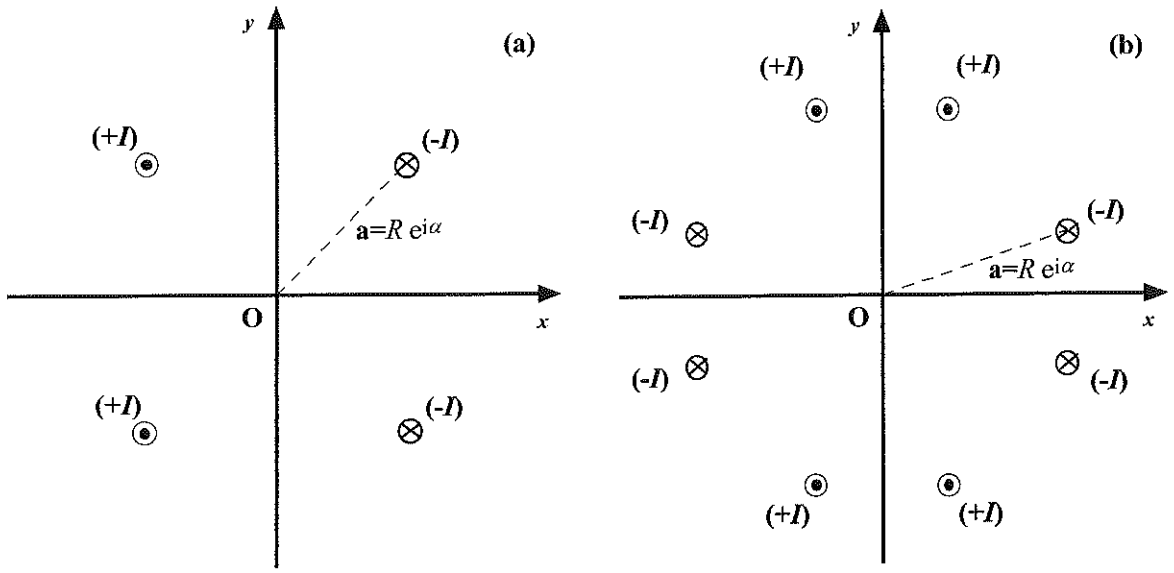

Figure 29. Examples of current-line distributions with selected symmetries: (a) quadruplet of current-lines with an even symmetry about the x-axis and an odd symmetry about the y-axis, and (b) octuplet of current-lines with even symmetries with respect to the x- and y-axes and odd symmetries with respect to the first and second bisectors.

Furthermore, it is easy to verify that

$$e^{-in\alpha} + e^{-in(\pi-\alpha)} + e^{-in(\pi+\alpha)} + e^{+in\alpha} = 2\left[1-(1)^n\right]\cos(n\alpha) \tag{100}$$

which is only non-zero when n is odd. Hence, the complex magnetic flux density can be written

$$\mathbf{B(s)} = \sum_{k=0}^{+\infty} B_{2k+1}\left(\frac{\mathbf{s}}{R_{\text{ref}}}\right)^{2k} \qquad \text{for } \mathbf{s},\ |\mathbf{s}| < R \tag{101}$$

where

$$B_{2k+1} = \frac{2\mu_0 I}{\pi R_{\text{ref}}}\left(\frac{R_{\text{ref}}}{R}\right)^{2k+1}\left[\cos(2k+1)\alpha\right] \tag{102}$$

The first term ($k = 0$) of the series corresponds to a pure normal dipole field parallel to the y-axis (see section 4.8.2.1). The B_{2k+1} coefficients are called the *allowed* multipole field coefficients of this current distribution.

4.9.4 OCTUPLET OF CURRENT LINES WITH QUADRUPOLE SYMMETRY

Similarly, the complex magnetic flux density produced by the octuplet of current lines represented in Figure 29(b) is given by

$$\mathbf{B(s)} = \sum_{k=0}^{+\infty} B_{4k+2} \left(\frac{\mathbf{s}}{R_{\text{ref}}} \right)^{4k+1} \qquad \text{for } \mathbf{s},\ |\mathbf{s}| < R \tag{103}$$

where

$$B_{4k+2} = \frac{4\mu_0 I}{\pi R_{\text{ref}}} \left(\frac{R_{\text{ref}}}{R} \right)^{4k+2} \left[\cos(4k+2)\alpha \right] \tag{104}$$

The first term ($k = 0$) of the series corresponds to a pure normal quadrupole field whose axes are parallel to the first and second bisectors (see section 4.8.2.2). For this current distribution, the allowed multipole field coefficients are the normal $2(4k+2)$-pole field coefficients.

4.9.5 COS$p\theta$ AND SIN$p\theta$ CURRENT SHEETS

Let us now consider a cylindrical current sheet of radius, R, carrying a linear current density of the form: $[-j_{\text{sheet}}\cos(p\theta)]$, where j_{sheet} is a constant (in A/m). The magnetic flux density produced within the cylinder can be computed by dividing the sheet into elementary current lines of intensity, $[-j_{\text{sheet}}R\cos(p\theta)\mathrm{d}\theta]$, and by integrating the current line contributions between 0 and (2π). It follows that, within the circle of center, O, and radius, R, **B** is given by Eq. (61) where

$$B_n + \mathrm{i}\, A_n = \frac{\mu_0 j_{\text{sheet}}}{2\pi} \left(\frac{R_{\text{ref}}}{R} \right)^{n-1} \left[\int_0^{2\pi} \mathrm{d}\theta \cos(p\theta)\cos(n\theta) - \mathrm{i} \int_0^{2\pi} \mathrm{d}\theta \cos(p\theta)\sin(n\theta) \right] \tag{105}$$

Furthermore, it is easy to verify that

$$\int_0^{2\pi} \mathrm{d}\theta \cos(p\theta)\cos(n\theta) = 0 \qquad \text{for } n,\ n \neq p \tag{106a}$$

$$\int_0^{2\pi} \mathrm{d}\theta \cos^2(n\theta) = \pi \tag{106b}$$

and

$$\int_0^{2\pi} d\theta \cos(p\theta)\sin(n\theta) = 0 \qquad \text{for all } n \tag{106c}$$

Hence, all multipole field coefficients are nil except B_p, and we have

$$\mathbf{B(s)} = B_p \left(\frac{\mathbf{s}}{R_{ref}}\right)^{p-1} = \frac{\mu_0 j_{sheet}}{2}\left(\frac{\mathbf{s}}{R}\right)^{p-1} \qquad \text{for } \mathbf{s},\ |\mathbf{s}| < R \tag{107}$$

Equation (107) shows that a $\cos(p\theta)$-type current sheet produces a pure, normal, $2p$-pole field.

Similarly, it can be shown that a cylindrical current sheet of radius, R, carrying a linear current density, $[+j_{sheet}\sin(p\theta)]$, produces a pure, skew, $2p$-pole field

$$\mathbf{B(s)} = \mathrm{i}\, A_p \left(\frac{\mathbf{s}}{R_{ref}}\right)^{p-1} = \mathrm{i}\,\frac{\mu_0 j_{sheet}}{2}\left(\frac{\mathbf{s}}{R}\right)^{p-1} \qquad \text{for } \mathbf{s},\ |\mathbf{s}| < R \tag{108}$$

4.9.6 CYLINDRICAL CURRENT SHELLS

Let us now consider a cylindrical current shell of inner radius, R_i, outer radius, R_o, extending between the angles, $(-\alpha_0)$ and $(+\alpha_0)$, in the half-space, x, $x \geq 0$, and between the angles, $(\pi-\alpha_0)$ and $(\pi+\alpha_0)$, in the half-space, x, $x \leq 0$. Let us further assume that the shell carries an uniform current density, $(-J)$, for x, $x > 0$ and, $(+J)$, for x, $x < 0$, as represented in Figure 30(a). The magnetic flux density produced within the cylinder of radius, R_i, can be computed by dividing the shell into quadruplets of current lines having the symmetry o(a) and carrying intensities $[\pm JR\mathrm{d}\alpha\mathrm{d}R]$, and by integrating the quadruplet contributions over a shell quadrant. It follows that the magnetic flux density can be represented by the complex function, **B**, given by Eq. (101) where

$$B_{2k+1} = \frac{2\mu_0 J}{\pi}\int_{R_i}^{R_o} dR\left(\frac{R_{ref}}{R}\right)^{2k}\int_0^{\alpha_0} d\alpha\left[\cos(2k+1)\alpha\right] \tag{109}$$

After integration we get

$$B_1 = \frac{2\mu_0 J}{\pi}(R_o - R_i)\sin\alpha_0 \tag{110a}$$

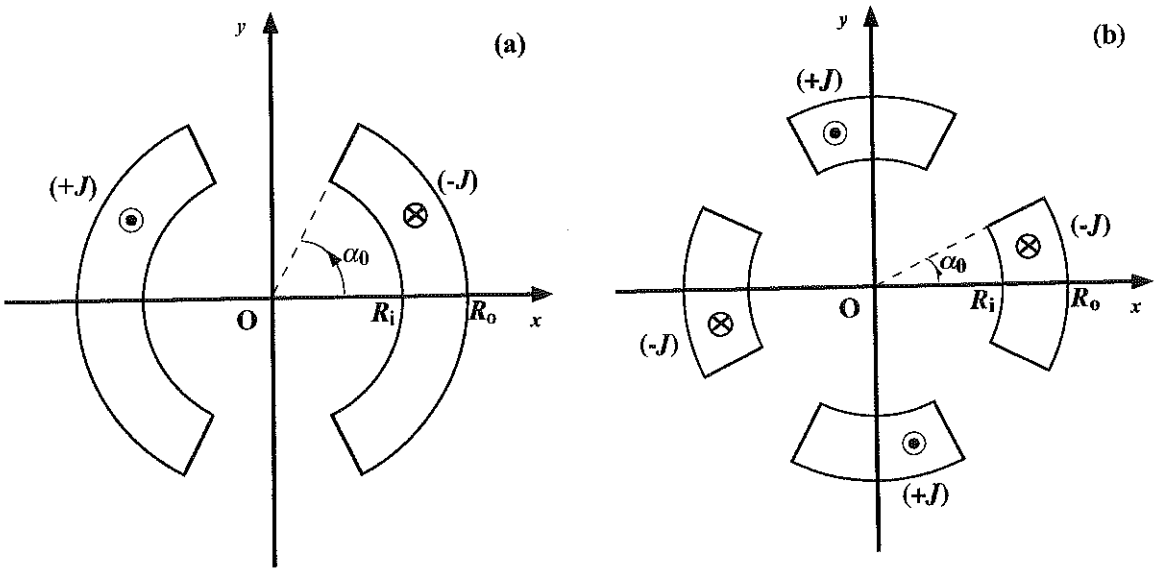

Figure 30. Examples of cylindrical current shells with selected symmetries: (a) shell with dipole symmetry and (b) shell with quadrupole symmetry.

and

$$B_{2k+1} = \frac{2\mu_0 J R_{ref}}{\pi(2k+1)(2k-1)}\left[\left(\frac{R_{ref}}{R_i}\right)^{2k-1} - \left(\frac{R_{ref}}{R_o}\right)^{2k-1}\right]\sin[(2k+1)\alpha_0]$$

$$\text{for } k,\ k \geq 1 \qquad (110b)$$

Note that B_3 (first allowed multipole field coefficient after B_1 in a current distribution with a dipole symmetry) is nil for $\alpha_0 = \pi/3$.

In this configuration, the regions around $\theta = \pi/2$ and $\theta = 3\pi/2$, which are free of current, are referred to as *pole areas*, and the y-axis is referred to as *pole axis*. By extension, α_0 is the *pole angle*.

Similarly, it can be shown that the magnetic flux density produced by the current shell of Figure 30(b) can be represented by the complex function, **B**, given by Eq. (103), where

$$B_2 = \frac{2\mu_0 J R_{ref}}{\pi}\ln\left(\frac{R_o}{R_i}\right)\sin(2\alpha_0) \qquad (111a)$$

and

$$B_{4k+2} = \frac{\mu_0 J R_{ref}}{\pi k(4k+2)}\left[\left(\frac{R_{ref}}{R_i}\right)^{4k} - \left(\frac{R_{ref}}{R_o}\right)^{4k}\right]\sin[(4k+2)\alpha_0]$$

$$\text{for } k,\ k \geq 1 \qquad (111b)$$

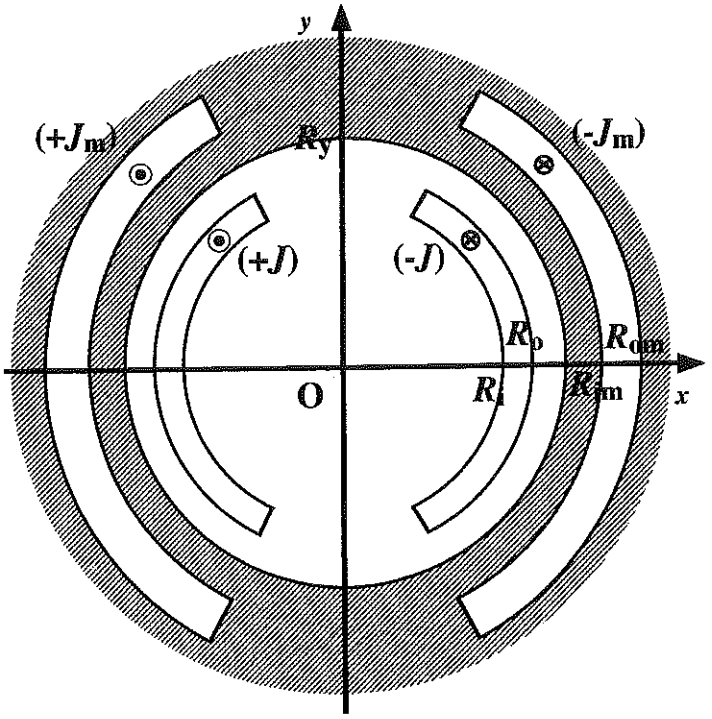

Figure 31. Mirror image of a cylindrical current shell within a circular iron yoke.

Note that B_6 (first allowed multipole field coefficient after B_2 in a current distribution with a quadrupole symmetry) is nil for $\alpha_0 = \pi/6$.

In this configuration, the pole areas are the regions around $\theta = \pi/4$, $3\pi/4$, $5\pi/4$ and $7\pi/4$ and the pole axes are the first and second bisectors.

4.9.7 Cylindrical Current Shells Within a Circular Iron Yoke

Let us now place the cylindrical current shell Figure 30(a) within a circular iron yoke of inner radius, R_y. As illustrated in Figure 31, the contribution of the iron yoke to the magnetic flux density can be shown to be the same as that of a mirror current shell, of inner radius, R_{im}, and outer radius, R_{om}, where [11]

$$R_{im} = \frac{R_y^2}{R_o} \qquad \text{and} \qquad R_{om} = \frac{R_y^2}{R_i} \tag{112}$$

and carrying an uniform current density, J_m, such that

$$J_m = \frac{\mu - 1}{\mu + 1} \frac{R_o^2 - R_i^2}{R_{om}^2 - R_{im}^2} J = \frac{\mu - 1}{\mu + 1} \frac{R_o^2 R_i^2}{R_y^4} J \tag{113}$$

Here μ designates the relative magnetic permeability of the iron yoke. Equation (113) expresses that the total intensity of the current circulating in the mirror shell is the same as that circulating in the original shell times the ratio $[(\mu-1)/(\mu+1)]$.

Introducing the expressions of the radii and of the current density of the mirror shell into Eqs. (110a) and (110b), it is easy to show that the contribution of the iron yoke to the allowed, $2n$-pole field coefficient, B_n^{yoke}, is

$$B_n^{\text{yoke}} = \frac{\mu-1}{\mu+1}\left(\frac{R_o R_i}{R_y^2}\right)^n B_n^{\text{shell}} \tag{114}$$

where B_n^{shell} is the $2n$ pole field coefficient produced by the current shell alone in free space.

Hence, the presence of the iron yoke results in enhancements of the allowed, $2n$-pole field coefficients, which can be estimated as

$$\frac{B_n^{\text{shell}} + B_n^{\text{yoke}}}{B_n^{\text{shell}}} = 1 + \frac{\mu-1}{\mu+1}\left(\frac{R_o R_i}{R_y^2}\right)^n \tag{115}$$

As an illustration, for the inner coils of the 50-mm-aperture SSC dipole magnet, we have [158]: $R_i \approx 25$ mm, $R_o \approx 37.5$ mm, while: $R_y \approx 68$ mm. For μ infinite, this yields an enhancement of the order of 1.2 for the dipole field coefficient, 1.008 for the sextupole field coefficient, and 1.0003 for the decapole field coefficient. This example shows that the enhancement can be substantial for the main field component, but is usually quite small on the higher order, allowed multipole field coefficients.

It is easy to verify that Eqs. (114) and (115) remain the same for a cylindrical current shell with a quadrupole symmetry placed within a circular iron yoke.

4.9.8 Cylindrical Current Shell Assemblies with Multiple Layers

Le us now consider an assembly made up of nested cylindrical current shells similar to the ones in Figure 30(a) and Figure 30(b). The magnetic flux density produced by this assembly within the aperture of the innermost layer can be derived by summing the contributions from the various shells. As an illustration, the magnetic flux density produced by the two-layer coil assembly with a dipole symmetry shown in Figure 32 can be represented by the complex function, **B**, given by Eq. (101) where

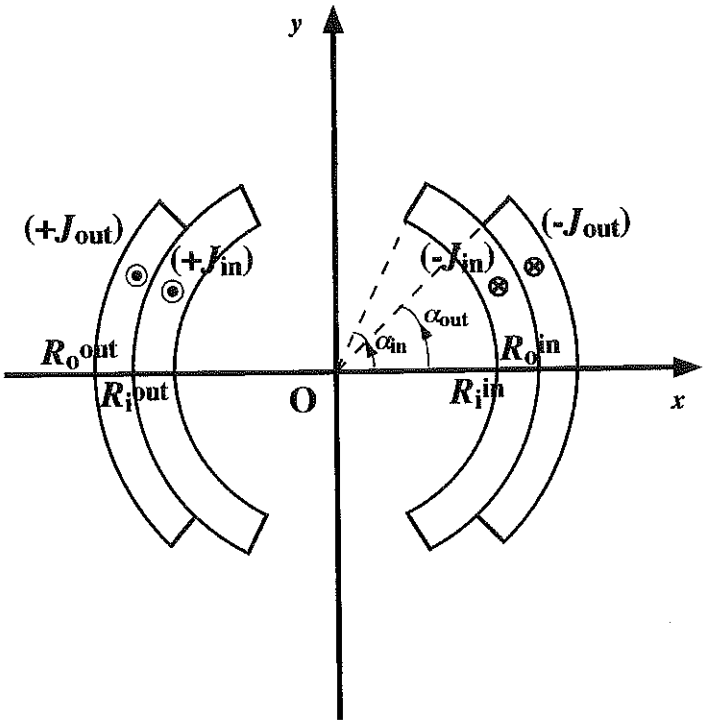

Figure 32. Two-layer cylindrical current shell assembly with a dipole symmetry.

$$B_1 = \frac{2\mu_0 J_{\text{in}}}{\pi}\,(R_{\text{o}}^{\text{in}} - R_{\text{i}}^{\text{in}})\sin\alpha_0^{\text{in}} + \frac{2\mu_0 J_{\text{out}}}{\pi}\,(R_{\text{o}}^{\text{out}} - R_{\text{i}}^{\text{out}})\sin\alpha_0^{\text{out}} \qquad (116a)$$

and

$$B_{2k+1} = \frac{2\mu_0 J_{\text{in}} R_{\text{ref}}}{\pi(2k+1)(2k-1)}\left[\left(\frac{R_{\text{ref}}}{R_{\text{i}}^{\text{in}}}\right)^{2k-1} - \left(\frac{R_{\text{ref}}}{R_{\text{o}}^{\text{in}}}\right)^{2k-1}\right]\sin[(2k+1)\alpha_0^{\text{in}}]$$

$$+ \frac{2\mu_0 J_{\text{out}} R_{\text{ref}}}{\pi(2k+1)(2k-1)}\left[\left(\frac{R_{\text{ref}}}{R_{\text{i}}^{\text{out}}}\right)^{2k-1} - \left(\frac{R_{\text{ref}}}{R_{\text{o}}^{\text{out}}}\right)^{2k-1}\right]\sin[(2k+1)\alpha_0^{\text{out}}]$$

$$\text{for } k,\ k \geq 1 \qquad (116b)$$

Here, the parameter definitions are the same as in section 4.9.6 and the indices in and out refer to the inner and the outer coil layers.

4.9.9 Cylindrical Current Shells with Angular Wedges

Let us finally consider a cylindrical current shell similar to that of Figure 30(a), but let us assume that it includes four angular wedges dividing each shell quadrant into two current blocks as represented in Figure 33. The four wedges are assumed to extend between the angles, α_2 and α_1, where $\alpha_2 \leq \alpha_1 \leq \alpha_0$, in the top right quadrant, between the angles, $(\pi - \alpha_1)$ and $(\pi - \alpha_2)$, in the top left quadrant, between the angles, $(\pi + \alpha_2)$ and $(\pi + \alpha_1)$, in the

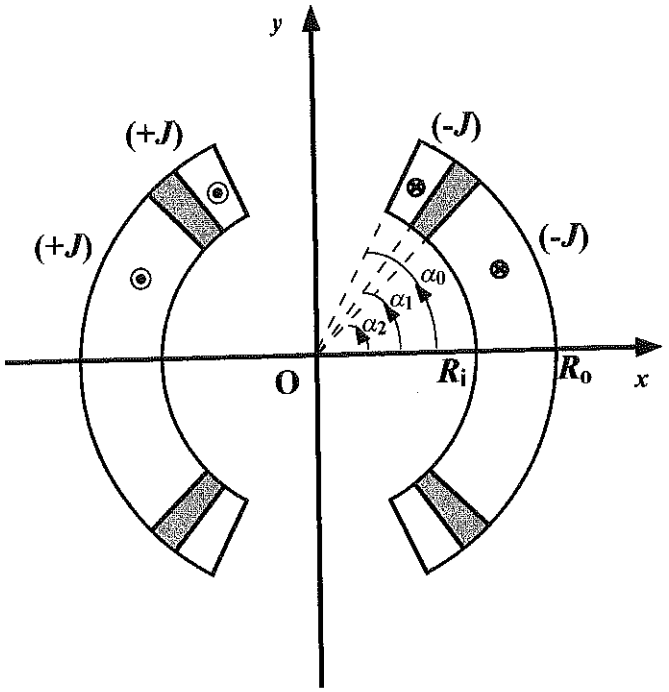

Figure 33. Cylindrical current shell with dipole symmetry and angular wedges.

bottom left quadrant, and between the angles, $(-\alpha_1)$ and $(-\alpha_2)$, in the bottom right quadrant. It is straightforward to show that the magnetic flux density produced by this current distribution can again be represented by the complex function, **B**, given by Eq. (101) with

$$B_1 = \frac{2\mu_0 J}{\pi}(R_o - R_i)\left[\sin\alpha_0 - \sin\alpha_1 + \sin\alpha_2\right] \tag{117a}$$

and

$$B_{2k+1} = \frac{2\mu_0 J R_{ref}}{\pi(2k+1)(2k-1)}\left[\left(\frac{R_{ref}}{R_i}\right)^{2k-1} - \left(\frac{R_{ref}}{R_o}\right)^{2k-1}\right] \times \left\{\sin[(2k+1)\alpha_0] - \sin[(2k+1)\alpha_1] + \sin[(2k+1)\alpha_2]\right\} \quad \text{for } k,\ k \geq 1 \tag{117b}$$

We have seen that in the case of a cylindrical shell with a dipole symmetry and no angular wedge, the sextupole field coefficient, B_3, could be set to zero by choosing a pole angle, α_0, such that: $\sin(3\alpha_0) = 0$. This gave: $\alpha_0 = 60°$.

The main interest of angular wedges is that they provide additional free parameters to set to zero other high-order, allowed multipole field coefficients. For instance, in the case of a cylindrical shell with a dipole symmetry and one angular wedge per quadrant, the angles α_0, α_1 and α_2 can be chosen to constrain simultaneously: $B_3 = B_5 = B_7 = 0$.

This yields the following system of three equations and three unknowns

$$\sin(3\alpha_0) - \sin(3\alpha_1) + \sin(3\alpha_2) = 0 \tag{118a}$$

$$\sin(5\alpha_0) - \sin(5\alpha_1) + \sin(5\alpha_2) = 0 \tag{118b}$$

and

$$\sin(7\alpha_0) - \sin(7\alpha_1) + \sin(7\alpha_2) = 0 \tag{118c}$$

The solutions of the above system are: $\alpha_0 \approx 67.2753°$, $\alpha_1 \approx 52.1526°$ and $\alpha_2 \approx 43.1791°$. Implementing a second wedge per quadrant (which divides each quadrant into three current blocks) provides two additional parameters which can be determined to obtain: $B_3 = B_5 = B_7 = B_9 = B_{11} = 0$. And so on. In theory, P wedges allow to set to zero up to $(2P+1)$ allowed multipole field coefficients. Note that the wedges introduce a geometric spacing in the current distribution which, on a circle of radius, R, where R, $R_i \leq R \leq R_o$, tends to imitate the ideal $\cos\theta$ current sheet distribution that was shown to produce a pure dipole magnetic flux density.

In a similar fashion, angular wedges can be implemented into cylindrical current shells having a quadrupole symmetry. In the case of one angular wedge per octant, dividing each octant into two current blocks, the angles α_0, α_1 and α_2 can be chosen to constrain simultaneously: $B_6 = B_{10} = B_{14} = 0$. This yields the following system of three equations and three unknowns

$$\sin(6\alpha_0) - \sin(6\alpha_1) + \sin(6\alpha_2) = 0 \tag{119a}$$

$$\sin(10\alpha_0) - \sin(10\alpha_1) + \sin(10\alpha_2) = 0 \tag{119b}$$

and

$$\sin(14\alpha_0) - \sin(14\alpha_1) + \sin(14\alpha_2) = 0 \tag{119c}$$

The solutions of the system of Eqs. (119) are equal to one half of the solutions of the system of Eqs. (118).

5 MAGNETIC DESIGN OF PARTICLE ACCELERATOR MAGNETS

5.1 TWO-DIMENSIONAL GEOMETRY

5.1.1 SYMMETRY CONSIDERATIONS

The field computations presented in section 4.9 have shown that current distributions with the symmetries of Figure 29(a) (*i.e.*, even with respect to the x-axis and odd with respect to the y-axis) were suitable for generating dipole fields, whereas current distributions with the symmetries of Figure 29(b) (*i.e.*, even with respect to the x- and y-axes and odd with respect to the first and second bisectors) were suitable for generating quadrupole fields. Starting from these premises, the coil geometry can be optimized to obtain the required dipole or quadrupole field strength within the desired aperture. In addition, in most accelerator magnet designs, it is required that the high order multipole fields be as small as possible. Hence, the coil geometry optimization is also carried out so as to minimize the contributions from non-dipole or non-quadrupole terms.

5.1.2 CURRENT SHELL APPROXIMATIONS

The coil geometries the most commonly used for dipole and quadrupole magnets are approximations of the cylindrical current shells shown in Figure 30(a) and Figure 30(b). The approximation is obtained by stacking into an arch the slightly keystoned cables described in section 3.6. The low-field dipole and low-field-gradient quadrupole magnets for RHIC rely on a single coil layer, while Tevatron, HERA, UNK, SSC and LHC magnets rely on two coil layers whose field contributions add up. The high-field LBNL dipole magnet model D20 counts four layers. All coil designs, but that for Tevatron magnets, include copper wedges which are introduced between some of the turns to separate the conductors into blocks. As explained in section 4.9.9, the blocks (or wedges) angles are tuned to eliminate high order multipole field coefficients and approach ideal $\cos\theta$ and $\cos 2\theta$ current distributions [159]. By analogy, such coil geometries are referred to as $cos\theta$ and $cos2\theta$ designs. They are very compact and make the most effective use of conductors by bringing them close to the useful aperture.

In the case of Tevatron, HERA and UNK magnets, the coil apertures are large enough to limit the requirements on cable keystone angles to values that are acceptable on the point of view of cabling degradation. As a result, the cables used in these magnets are stacked into arches of the desired shapes, and each coil turn lies along a radius vector pointing toward the aperture's center.

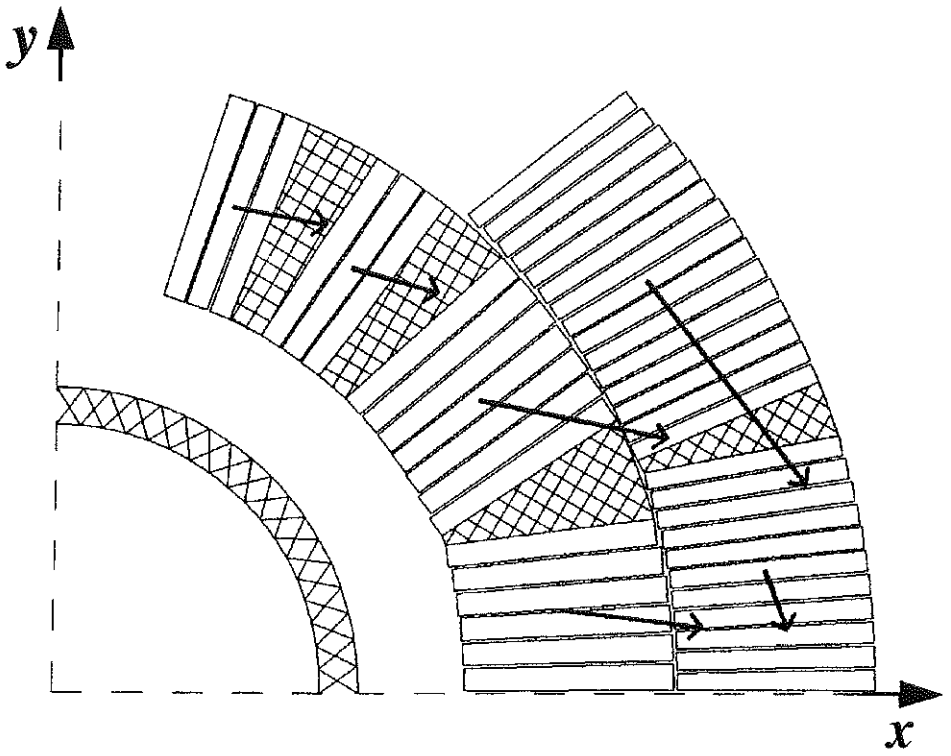

Figure 34. Conductor and Lorentz force distributions in a quadrant of a 50-mm-aperture SSC arc dipole magnet coil [158].

In the case of SSC and LHC magnets, the coil apertures are reduced to minimize the volume of superconductor. This requires larger values of keystone angles that are deemed to cause unacceptable cabling degradations. Hence, in these magnets, the cables are not sufficiently keystoned to assume the desired arch shapes, and the wedges between conductor blocks must be made asymmetrical to compensate for this lack [158]. Also, the coil turns end up being non-radial, as illustrated in Figure 34, which shows the conductor distribution in a quadrant of a 50-mm-aperture SSC dipole magnet coil (the vectors represent the components of the Lorentz force discussed in the oncoming section on mechanical design).

5.1.3 Iron Yoke Contribution

The coils of particle accelerator magnets are usually surrounded by a circular iron yoke, which provides a return path for the magnetic flux while enhancing the central field or field gradient. Eq. (115) shows that the smaller R_y, the larger the field enhancement. However, there are two limitations on how close the iron can be brought to the coils: (1) room must be left for the support structure, and (2) iron saturates for fields above 2 T, resulting in undesirable distortions (see section on field quality).

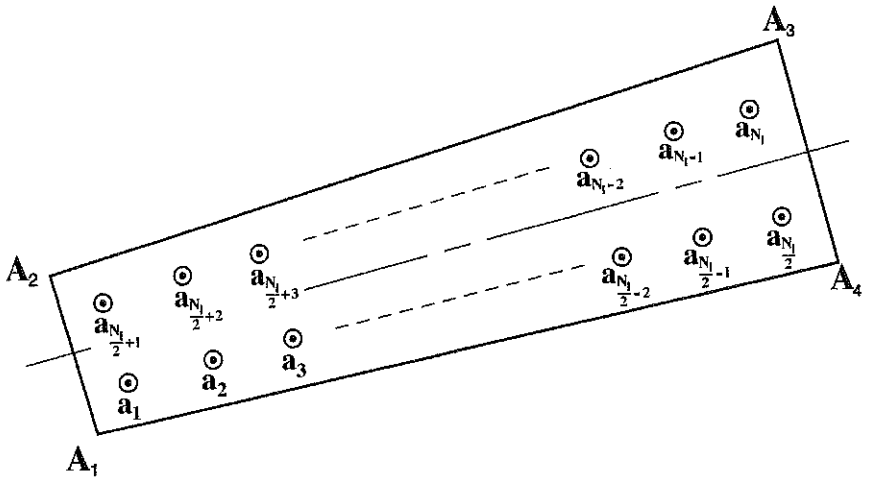

Figure 35. Current line model for the computation of the transport-current field produced by a given turn of a $\cos\theta$ or $\cos 2\theta$ coil assembly wound from a Rutherford-type cable.

As already mentioned, the Tevatron magnets use a warm iron yoke (*i.e.*, placed outside the helium containment and vacuum vessel), but starting with HERA, the iron yoke is included within the magnet cold mass. For SSC dipole magnets, we have seen that the field enhancement due to the yoke was of the order of 20%. In LHC magnets, two coil assemblies (powered with opposite polarity) are placed within a common iron yoke. This twin-aperture design results in left/right asymmetries in the yoke around each coil assembly taken individually, which must be taken into account.

5.1.4 COMPUTING TRANSPORT CURRENT FIELD

The magnetic flux density produced by the coil of Figure 34 can be computed by dividing each turn into elementary current lines parallel to the z-axis, as illustrated in Figure 35 (p. 226 of Ref. [160]).

Let N_l designate the number of current lines representing a given coil turn, and let $\mathbf{a_j}$, where j, $1 \leq j \leq N_l$, designate the coordinates in the complex plane of the current lines. The resulting magnetic flux density produced by the N_l current lines is the sum of the magnetic flux density produced by each current line. It follows from section 4.9.1 that it can be represented by the complex function, **B**, given by

$$\mathbf{B(s)} = \zeta \frac{\mu_0}{2\pi} \left(\frac{I}{N_l} \right) \sum_{j=1}^{N_l} \frac{1}{\mathbf{s} - \mathbf{a_j}} \tag{120}$$

where I is the total current intensity in the conductor, $\zeta = -1$ for a turn in quadrant 1 or 4 [$\mathrm{Re}(\mathbf{a_j}) \geq 0$] and $\zeta = +1$ for a turn in quadrant 2 or 3 [[$\mathrm{Re}(\mathbf{a_j}) \leq 0$].

If the coil is placed within a circular iron yoke of inner radius, R_y, and relative magnetic permeability, μ, we simply have

$$\mathbf{B(s)} = \zeta \frac{\mu_0}{2\pi} \left(\frac{I}{N_1} \right) \sum_{j=1}^{N_1} \left[\frac{1}{\mathbf{s} - \mathbf{a_j}} + \frac{\mu - 1}{\mu + 1} \frac{1}{\mathbf{s} - \frac{R_y^2}{\mathbf{a_j^*}}} \right] \tag{121}$$

The coil turn contribution to the multipole field coefficients, A_n and B_n, expressed at a reference radius, R_{ref}, can be computed directly using

$$B_n + i\, A_n = -\zeta \frac{\mu_0}{2\pi R_{ref}} \left(\frac{I}{N_1} \right) \sum_{j=1}^{N_1} \left[\left(\frac{R_{ref}}{\mathbf{a_j}} \right)^n + \frac{\mu - 1}{\mu + 1} \left(\frac{R_{ref}\, \mathbf{a_j^*}}{R_y^2} \right)^n \right] \tag{122}$$

In practice, a good computational accuracy can be achieved by taking for N_1 an even number of the order of N_{cable}, where N_{cable} is the number of cable strands, and by representing each coil turn by two layers of equally spaced current-lines (see Figure 35). For instance, one can use

$$N_1 = N_{cable} \qquad \text{for } N_{cable} \text{ even,} \tag{123a}$$

and

$$N_1 = N_{cable} - 1 \qquad \text{for } N_{cable} \text{ odd,} \tag{123b}$$

and one can take for $\mathbf{a_j}$

$$\mathbf{a_j} = \left(1 - \frac{2j-1}{N_1} \right) \left(\frac{3\mathbf{A_1} + \mathbf{A_2}}{4} \right) + \left(\frac{2j-1}{N_1} \right) \left(\frac{\mathbf{A_3} + 3\mathbf{A_4}}{4} \right) \qquad \text{for } j,\ 1 \le j \le \frac{N_1}{2} \tag{124a}$$

and

$$\mathbf{a_j} = \left(1 - \frac{2j - N_1 - 1}{N_1} \right) \left(\frac{\mathbf{A_1} + 3\mathbf{A_2}}{4} \right) + \left(\frac{2j - N_1 - 1}{N_1} \right) \left(\frac{3\mathbf{A_3} + \mathbf{A_4}}{4} \right) \qquad \text{for } j,\ \frac{N_1}{2} + 1 \le j \le N_1 \tag{124b}$$

Here, $\mathbf{A_1}$ through $\mathbf{A_4}$ designate the localizations in the complex plane of the four corners of the coil turn.

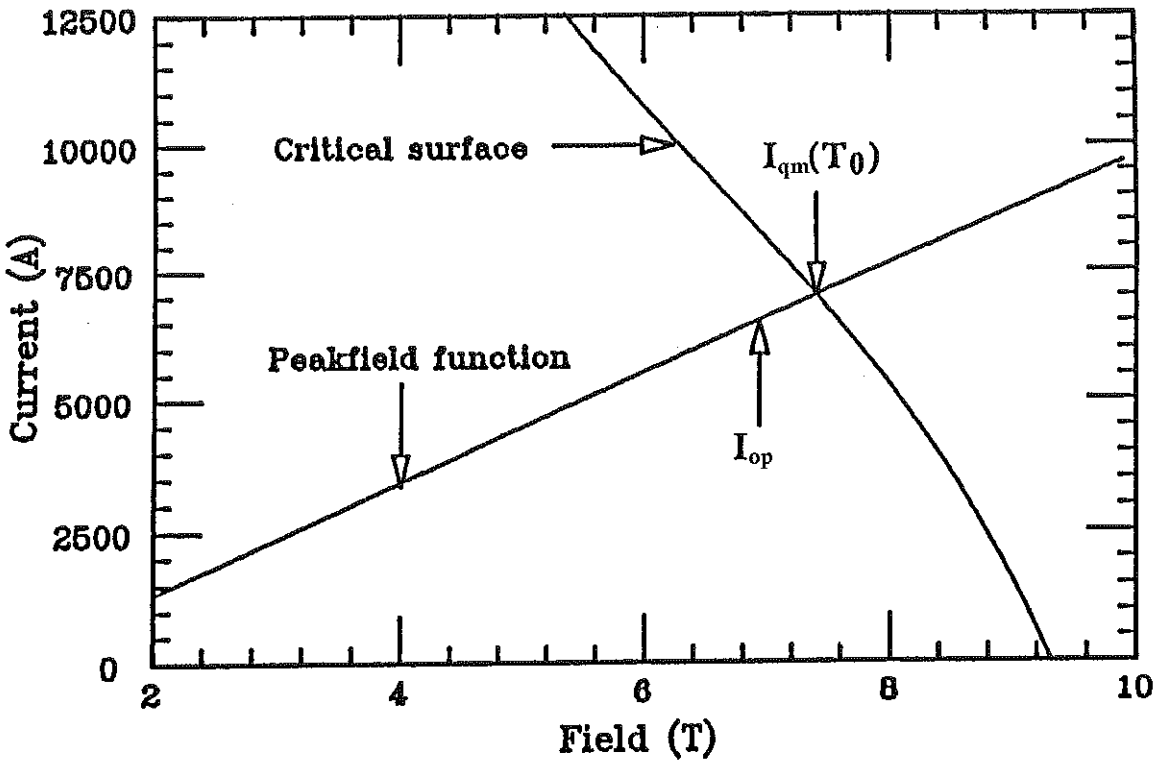

Figure 36. Defining the current margin of a superconducting magnet (at $T = T_0$).

5.1.5 OPERATING CURRENT MARGIN

Equations (110a) and (111a) show that to achieve high fields and high field gradients, it is desirable to maximize the overall current density in the magnet coil. This can be done by three means: (1) maximizing the superconductor performance, (2) minimizing the copper-to-superconductor ratio in the cable strands, and (3) minimizing the turn-to-turn insulation thickness.

As explained in other sections of this review paper, there are lower bounds on the values of copper-to-superconductor ratio and insulation thickness in order to limit conductor heating in the case of a quench and to ensure proper electrical insulation. As for the superconductor, the upper limit is the critical current density at the operating temperature and magnetic flux density.

The magnetic flux density to which the conductor is exposed is non-uniform over the magnet coil, but the maximum current-carrying capability of the conductor is determined by the area where the magnetic flux density is the highest. For $\cos\theta$ dipole magnet coils, this usually corresponds to the pole turn of the innermost coil layer. Let $B_{peak} = f(I)$ designate the peak magnetic flux density on the coil as a function of supplied current, I, and let $I_C = f(B,T_0)$

designate the supposedly known cable critical current as a function of applied magnetic flux density, B, at the operating temperature, T_0. As illustrated in Figure 36, the intersection between these two curves determines the maximum quench current of the magnet at T_0, $I_{qm}(T_0)$.

In practice, magnets must be operated below I_{qm} so as to ensure that the entire coil is in the superconducting state and as to limit the risks of quenching. Let I_{op} designate the operating current. Then, the operating current margin of the magnet, m_I, is defined as

$$m_i(T_0) = 1 - \frac{I_{op}}{I_{qm}(T_0)} \tag{125}$$

The excellent quench performance of the HERA magnets [31] suggests that the current margin can be set to as little as 10%, but it is safer to aim for 20%. In comparison to other superconducting magnets, such as solenoids for magnetic resonance imaging, a current margin of 10 to 20% is quite small. This implies that accelerator magnets are operated very close to the superconductor critical surface and are very sensitive to any kind of disturbances that may cause the magnet to cross the critical surface and lead to a quench.

5.1.6 Conductor Grading

A particularity of two-layer, $\cos\theta$ dipole magnet coil designs is that the peak magnetic flux density in the outermost layer is quite a bit lower than in the innermost layer. For instance, in the case of the 50-mm-aperture SSC dipole magnet design, the peak field on the outer layer is about 17% smaller than the peak field on the inner layer [158]. Hence, when using the same cable and current for both layers, the outer layer is operated with a much higher current margin than the inner layer, which can be considered as a waste of costly superconductor.

The conductors used for the outer layers of SSC and LHC dipole magnet coils have smaller cross-sectional areas than the conductors used for the inner layers. This results in a higher overall current density in the outer layer and reduces the difference in current margins. Such action is referred to as conductor *grading* [161]. The main disadvantage of grading is that it requires splices between the cables of the two layers (which, of course, are connected electrically in series and require only one power supply).

It should be noted that for two-layer, $\cos 2\theta$ quadrupole magnet coil designs, the peak magnetic flux density is almost the same for the two layers and that there is no point in conductor grading.

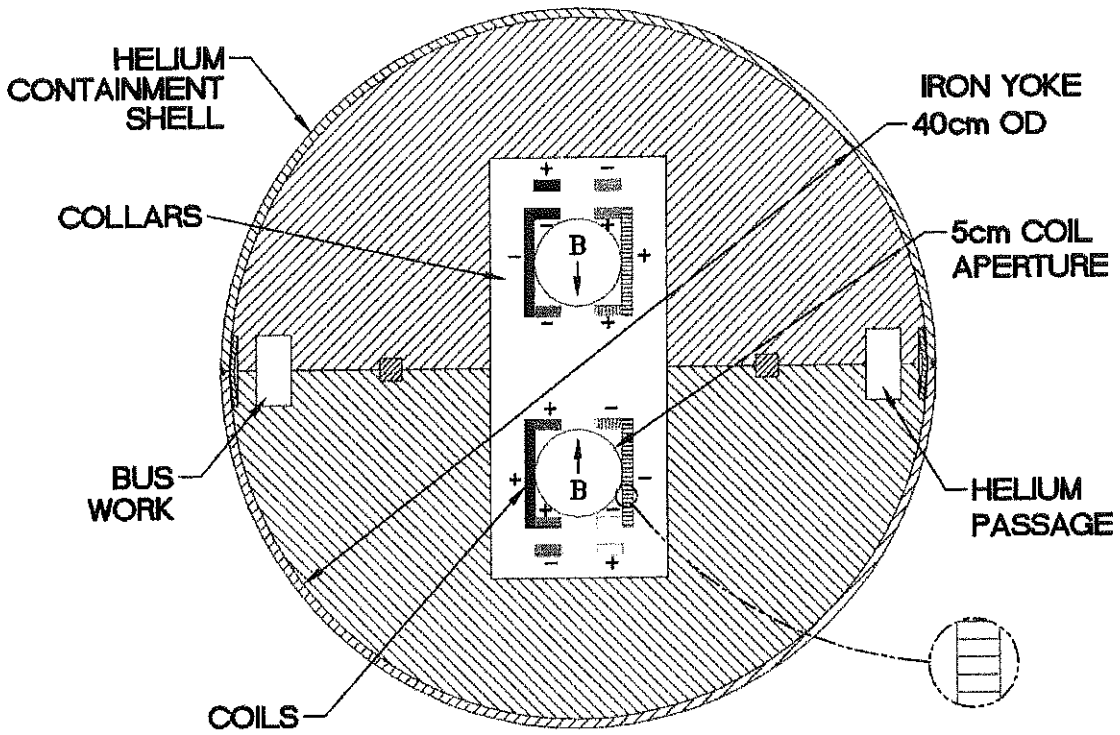

Figure 37. Conceptual block design developed at BNL for a high field, twin-aperture dipole magnet [101].

5.1.7 LIMITS OF COSθ COIL DESIGN

The cosθ coil design has been very successful until now, with a record dipole field of 13.5 T reached by LBNL short dipole magnet model D20 (using Nb_3Sn cables at 1.8 K; see section 2.4.2.3). However, it has two main drawbacks: (1) coil ends are difficult to make (see section on coil ends), and (2) due to the Lorentz force distribution, there is a stress accumulation in the azimuthal direction which results in high transverse pressures on the midplane conductors of coil assemblies (see Figure 34). For very high field magnets, requiring the use of A15 (or even possibly HTS) superconductors, which are strain sensitive, the high transverse pressures can result in significant critical current degradation [148], [149].

Alternative coil designs are being investigated, which may allow a better management of the Lorentz stress within the magnet coil. As an illustration, Figure 37 presents a conceptual *block* design for a twin-aperture dipole magnet, now under consideration at LBNL (see section 2.4.3), which relies on pairs of parallel racetrack-type coils [101]. Note, however, that such designs make a less effective use of superconductor.

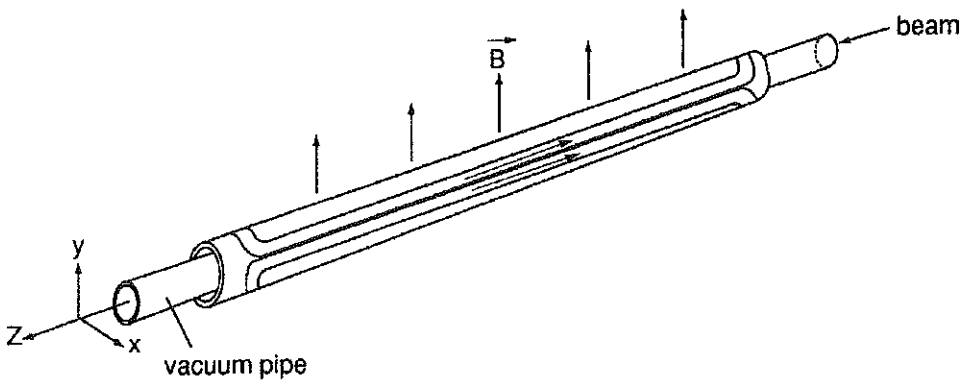

Figure 38. Perspective view of a saddle-shape coil assembly for a dipole magnet.

5.2 COIL END DESIGN

As mentioned above, one of the main difficulties of $\cos\theta$ and $\cos 2\theta$ designs is the realization of coil ends. In the coil straight section, the conductors run parallel to the magnet axis, but, in the ends, the conductors must be bent sharply to make U-turns over the beam pipe inserted within the magnet coil assembly. This confers to the coil a *saddle shape* as illustrated in Figure 38.

Over the years, sophisticated algorithms have been developed to determine the conductor trajectories that minimize strain energy [162]. These algorithms, which often require winding tests to determine correction factors, can be coupled with three-dimensional electromagnetic computations evaluating end field distortions. SSC and LHC magnets use precisely machined end spacers, designed by the optimization programs, which are positioned between conductor blocks [163]. In addition, the iron yoke does not extend over the coil ends to reduce the magnetic flux density on the conductors and ensure that the peak magnetic flux density is located in the coil straight section where the conductors are better supported.

5.3 SAGITTA

To limit the number of coil ends and of magnet interconnects around the accelerator ring, the arc dipole and quadrupole magnets are made as long as possible. As we have seen, the circulation of a beam of charged particles in a dipole magnet, of magnetic length, l_{dip}, results in an angular deflection, ϕ_{dip}, given by Eq. (5). Consequently, the long dipole magnets used in large accelerator rings are bent slightly to accompany the particle trajectories. This bending, which is implemented in the $(\vec{x},\vec{z})$ plane, is referred to as *sagitta*.

In practice, the bending radius of the dipole magnets is determined by the radius of curvature of the ring arcs, χ, given by Eq. (3). Furthermore, the horizontal sagitta, ξ_{dip}, is maximum at the magnet axial center, where it can be estimated as

$$\xi_{dip} = \left(1 - \cos\frac{\phi_{dip}}{2}\right)\chi \tag{126}$$

For small values of ϕ_{dip} we can write

$$\cos\frac{\phi_{dip}}{2} \approx 1 - \frac{\phi_{dip}^2}{8} \qquad \text{for } \phi_{dip},\ \phi_{dip} << 1 \tag{127}$$

and by combining Eqs. (5), (126) and (127), we get

$$\xi_{dip} \approx \chi\frac{\phi_{dip}^2}{8} \approx \frac{l_{dip}^2}{8\chi} \tag{128}$$

In the case of the dipole magnets for the LHC arcs at CERN, we have (see Table 1): l_{dip} = 14.2 m and χ = 2784.36 m. It follows from Eq. (128) that the required ξ_{dip} is of the order of 9.05 mm.

Of course, no sagitta is required for the arc quadrupole magnets, through which the ideal particle trajectories are straight lines.

6 MECHANICAL DESIGN OF PARTICLE ACCELERATOR MAGNETS

6.1 SUPPORT AGAINST THE LORENTZ FORCE

6.1.1 COMPONENTS OF THE LORENTZ FORCE

The high currents and fields in an accelerator magnet coil produce large Lorentz forces on the conductors. In a dipole coil, the resulting Lorentz force has three main components, which are represented in Figure 34 [158], [164]: (1) an azimuthal component, which tends to squeeze the coil towards the coil assembly midplane [in the coordinate system defined previously, the coil assembly midplane corresponds to the horizontal $(\vec{x},\vec{z})$ plane], (2) a radial component, which tends to bend the coil outwardly, with a maximum displacement at the coil assembly midplane (along the horizontal x-axis), and (3) an axial component, arising from the solenoidal field produced by the conductors' turnarounds at the coil ends, and which tends to stretch the coil outwardly (along the z-axis).

6.1.2 STABILITY AGAINST MECHANICAL DISTURBANCES

Because accelerator magnets are operated close to the critical current limit of their cables, their Minimum Quench Energy, referred to as MQE, and defined as the minimum energy deposition needed to trigger a quench, is very small. As a matter of fact, the MQE of accelerator magnets is of the same order of magnitude as the electromagnetic work produced by minute wire motions in the coil [165]. If the motions are purely elastic, no heat is dissipated and the coil remains superconducting, but if the motions are frictional, the associated heat dissipation may be sufficient to initiate a quench. This leaves two possibilities: either to prevent wire or coil motion by providing a rigid support against the various components of the Lorentz force, or to reduce to a minimum the friction coefficients between potentially moving parts of magnet assembly.

6.1.3 CONCEPTUAL DESIGN

The mechanical design concepts used in present accelerator magnets are more or less the same and were developed at the time of the Tevatron [23], [24]. In the radial direction: the coils are confined within a rigid cavity defined by laminated collars which are locked around the coils by means of keys or tie rods. In the azimuthal direction: the collars are assembled so as to pre-compress the coils. In the axial direction: the coils either are free to expand or are restrained by means of stiff end-plates.

The use of laminated collars, pioneered at the Tevatron, was a real breakthrough in achieving a rigid mechanical support while keeping tight tolerances over magnet assemblies which are a few meters in length and which must be mass-produced. The laminations are usually stamped by a fine blanking process allowing a dimensional accuracy of the order of one hundredth of a millimeter to be achieved.

6.2 AZIMUTHAL PRE-COMPRESSION

6.2.1 PREVENTING COLLAR POLE UNLOADING

As described above, the azimuthal component of the Lorentz force tends to squeeze the coil towards the midplane. At high fields, it may happen that the coil pole turns move away from the collar poles, resulting in variations of coil pole angle, which distort the central field, and creating a risk of mechanical disturbances. (The collar poles designate the collar extensions, which fill up the empty spaces, left by the conductor distribution in the pole areas, and the coil pole turns designate the coil turns directly in contact with these extensions.) To prevent conductor displacements, the collars are assembled and locked around the coils so as to apply an azimuthal pre-compression. The pre-compression is applied at room temperature and must be sufficient to ensure that, after cooldown and energization, there is still contact between coil pole turns and collar poles.

6.2.2 PRE-COMPRESSION REQUIREMENTS

To determine the proper level of room temperature azimuthal pre-compression, at least three effects must be taken into account: (1) stress relaxation and insulation creep following the collaring operation, (2) thermal shrinkage differentials between coil and collars during cooldown (if any), and (3) stress redistribution due to the azimuthal component of the Lorentz force. In addition, the collaring procedure must be optimized to ensure that the peak pressure seen by the coils during the operation (which may be significantly higher than the residual pre-compression) does not overstress the insulation (p. 1326 of Ref. [164]).

The pre-compression loss during cooldown, $\Delta\sigma_{cd}$, can be estimated from

$$\Delta\sigma_{cd} \approx E_{coil}\,(\alpha_{coil} - \alpha_{collar}) \tag{129}$$

where E_{coil} is the coil Young's modulus in the azimuthal direction, and α_{coil} and α_{collar} are the thermal expansion coefficients of the coil (in the azimuthal direction) and of the collars, integrated between room and operating temperatures. Note that Eq. (129) is derived with the assumptions that E_{coil} does not depend on temperature and that the collars are infinitely rigid.

Table 6. Integrated thermal expansion coefficients between 4.2 K and room temperature (10^{-3} m/m).

Low carbon steel	2.0
Stainless steel (304/316)	2.9
Copper (OFHC)	3.1
Aluminum	4.2
Insulated cable (polyimide/glass)	5.1[a)]
Insulated cable (all-polyimide)	5.6[a)]

[a)] transverse direction; SSC inner cable.

6.2.3 CHOICE OF COLLAR MATERIAL

To limit cooldown loss, it is preferable to use for the collars a material whose integrated thermal expansion coefficient matches more or less that of the coil. For NbTi coils with polyimide/glass or all-polyimide insulation, this suggests aluminum alloy (see Table 6). However, and as will be described in the next section, it is also desirable that the collars be as rigid as possible or have an integrated thermal expansion coefficient approaching that of the low carbon steel used for the yoke. This favors austenitic stainless steel, which has a lower integrated thermal expansion coefficient and a higher Young's modulus (the Young's modulus of austenitic steel is 195 GPa at room temperature and 203 GPa at 4.2 K, while that of aluminum alloy is 72 GPa at room temperature and 80 GPa at 4.2 K).

When assessing the respective merits of austenitic stainless steel and aluminum alloy, it should be noted that austenitic stainless steel presents a better resistance to stress cycling at low temperature [166], but that it has a higher density (7800 kg/m^3 compared to 2800 kg/m^3 for aluminum alloy) and is more expensive.

There is no ideal choice between stainless steel and aluminum alloy and magnets with both types of collar materials have been built: HERA dipole magnets and early LHC dipole magnet prototypes use aluminum alloy collars, whereas Tevatron dipole magnets, most SSC dipole magnet prototypes, and recent LHC dipole magnet prototypes rely on stainless steel collars. In any case, and whichever collar material is chosen, a thorough mechanical analysis of the structure under the various loading conditions is required.

6.3 RADIAL SUPPORT

6.3.1 LIMITING RADIAL DEFLECTIONS

As described above, the radial component of the Lorentz force tends to bend the coil outwardly, with a maximum displacement at the coil assembly midplane. At high fields, this bending results in shear stresses between coil turns and in an ovalization of the coil assembly (along the horizontal x-axis for a dipole magnet), which generates field distortions. To prevent displacements or deformations, the radial deflections of the coil assembly must be limited to, typically, less than 0.05 mm.

6.3.2 SEEKING YOKE SUPPORT

The main support against the radial component of the Lorentz force is provided by the collars, whose stiffness and radial width must be optimized to limit collared-coil assembly deflections. However, in the magnetic design of high field magnets, the field enhancement provided by the iron yoke is maximized by bringing it as close as possible to the coil. This reduces the space left for the collars, whose rigidity then becomes insufficient to hold the Lorentz force, and the yoke and helium containment shell must also be used as part of the coil support system.

The mechanical design of magnets where the yoke is needed to support the collared-coil assembly is complicated by the fact that the collar material (stainless steel or aluminum) shrinks more during cooldown than the low carbon steel used for the yoke (see Table 6). This thermal shrinkage differential must be compensated to ensure that, when the magnet is cold and energized, there is a proper contact between the collared-coil assembly and the yoke along the axis of maximum potential displacements. Such contact limits the deformations of the collared-coil assembly and allows a partial transfer (up to 50% in some LHC dipole magnet prototypes) of the radial component of the Lorentz force to the yoke and the shell.

The aforementioned thermal shrinkage differential during cooldown, Δr_{cd}, can be estimated as

$$\Delta r_{cd} = R_{collar} (\alpha_{collar} - \alpha_{yoke}) \tag{130}$$

where R_{collar} is the collar outer radius and α_{yoke} is the thermal expansion coefficient of the yoke, integrated between room and operating temperatures.

To limit contact loss due to thermal shrinkage differential it is preferable to use for the collars a material whose integrated thermal expansion coefficient approaches that of low carbon steel. This suggests the use of austenitic stainless steel (see Table 6). However, and as was described in section 6.2.3, it is also desirable to limit the cooldown loss of coil pre-compression, which favors the use of aluminum alloy.

6.3.3 Mechanical Design with Fully Mated Yoke Assembly

To facilitate assembly, the yoke of dipole magnets is usually split into two halves, which are mounted around the collared-coil assembly. The shell, which is also made up of two halves, is then placed around the yoke and welded. If the thermal shrinkage differential between collar and yoke is not too large (as in the case of stainless steel collars), it can be compensated for by designing and assembling the structure so that the two yoke halves apply a compressive load over selected areas of the collared-coil assembly. This compressive load is obtained by introducing a shrinkage allowance into the geometry of either the collars or the yoke and by welding the shell so as to press radially onto the two yoke halves and force them to mate at room temperature. During cooldown, the collared-coil assembly shrinks away from the two yoke halves, which remain fully mated. This results in a progressive decrease of the compressive load exerted by the yoke but a suitable contact can be maintained over the chosen areas of the collared-coil assembly.

In practice, the compressive load provided by the yoke is directed along a given axis. The choice of the axis drives the choice of yoke split orientation. The SSC dipole magnet prototypes built at BNL use a horizontally-split yoke with a yoke/collar compressive load directed along the vertical y-axis as shown in Figure 39(a), while the SSC dipole magnet prototypes built at FNAL use a vertically-split yoke with a yoke/collar compressive load directed along the horizontal x-axis as shown in Figure 39(b) [37]. Both types of magnets performed very well.

6.3.4 Mechanical Design with Yoke Midplane Gap at Room Temperature

For large thermal shrinkage differentials (as in the case of aluminum collars), the yoke/collar compressive load required at room temperature for a full compensation would overstress the collared-coil assembly and a more sophisticated mechanical design must be used. The twin-aperture LHC dipole magnet prototypes with aluminum collars rely on a two-piece, vertically-split yoke with an open gap at room temperature and a welded outer shell made of a material (stainless steel or aluminum) that shrinks more during cooldown than the low carbon steel yoke [167].

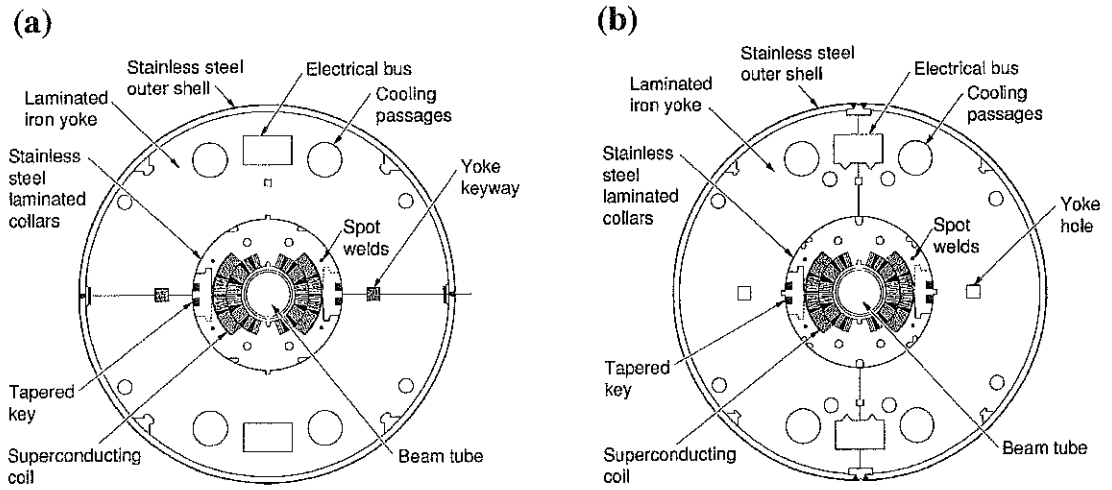

Figure 39. 50-mm-aperture SSC dipole magnet cross-sections [37]: (a) BNL-style with horizontally-split yoke and (b) FNAL-style with vertically-split yoke.

In these magnets, the yoke is designed so that, when placed around the collared-coil assembly at room temperature with no pressure applied to it, there remains an opening between the two yoke halves of the order of the expected thermal shrinkage differential. The yoke midplane gap is then closed in two stages: (1) during shell welding, as a result of the compressive load arising from weld shrinkage, and (2) during cooldown, as a result of the compressive load arising from thermal shrinkage differential between yoke and shell. The initial gap closure during shell welding is limited to avoid overstressing the collared-coil assembly. The closure is completed during cooldown, thanks to the radial pressure exerted by the shell, which forces the two yoke halves to follow the shrinkage of the collared-coil assembly while maintaining a contact along the horizontal x-axis. The yoke midplane gap must be fully closed at the end of cooldown to ensure that the structure is very rigid and to avoid any risk of oscillation during energization.

A crucial issue in such a design is the ability of performing the shell welding operation in a reproducible way during mass production while achieving the desired yoke midplane gap value at room temperature and keeping a tight tolerance on this value (of the order of 0.1 mm). As we have seen, a gap too close may result in coil overstressing at room temperature whereas a gap too open may result in contact loss during cooldown.

In some LHC prototypes, the yoke midplane gap is controlled by means of aluminum spacers located between the two yoke halves [168]. The spacers are dimensioned to have a spring rate similar to that of the collared-coil assembly and they prevent the gap from closing at room temperature. During cooldown, however, they shrink more than the yoke and cease to be effective.

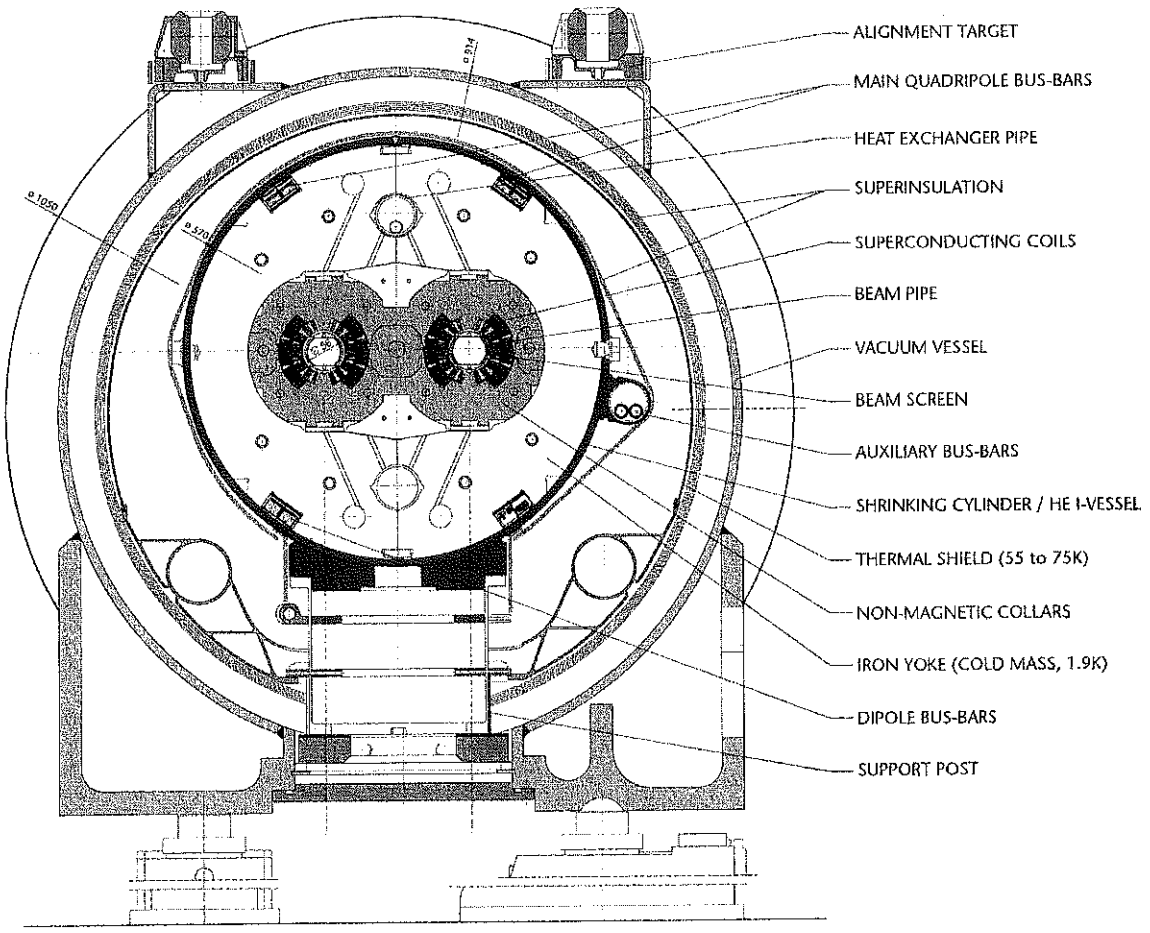

Figure 40. Present (1999) cross-section of the 56-mm-twin aperture LHC arc dipole magnet in its cryostat.

The concept of aluminum control gap spacer was first thought of at SSC [169] and was first tried on the short LBNL dipole magnet model D19 discussed in section 2.4.1.3.

At present (1999), CERN is developing a new dipole magnet design, relying on common, stainless steel collars and a two-piece, vertically split yoke, assembled with a closed midplane gap at room temperature [170], [171]. In this very robust design, shown in Figure 40, 80% of the radial component of the Lorentz force is taken by the collars and only 20% is transmitted to the yoke and shell.

6.3.5 RHIC Magnets

In RHIC magnets, collar and yoke designs are altogether simplified by replacing the collars by reinforced plastic spacers and by using directly the yoke to pre-compress the one-layer coils [46]. It remains to be seen if this structure could be scaled-up to higher field magnets.

6.4 END SUPPORT

As described above, the axial component of the Lorentz force tends to stretch the coil outwardly along the *z*-axis. In magnets where the yoke is not needed to support the collared-coil assembly, a clearance can be left between the two. Then, if the axial stresses resulting from the Lorentz force do not exceed the yield stress of the coil, it is possible to let the collared-coil expand freely within the iron yoke. This is the case of the quadrupole magnets designed at CEA/Saclay for HERA, SSC and LHC [57]. However, in magnets where there is contact between collar and yoke, it is essential to prevent stick/slip motions of the laminated collars against the laminated yoke and to provide a stiff support against the axial component of the Lorentz force [164], [172]. The ends of SSC and LHC dipole magnet coils are contained by thick stainless steel end plates welded to the shell.

7 COMPLEX FORMALISM FOR PICK-UP COILS ROTATING IN A TWO DIMENSIONAL FIELD

7.1 CONDUCTOR MODEL AND NOTATIONS

Similarly to what we did in section 4.8, let us consider an ensemble of conductors parallel to the z-axis and uniform in z, which are located outside a cylinder, whose generator is parallel to the z-axis and whose director is a circle, Γ_i, of center, O, and radius, R_i, located in the $(O,\vec{x},\vec{y})$ plane. As we have shown, such conductor distribution produces, within the cylinder, a two-dimensional magnetic flux density, $\vec{B}$, parallel to the $(\vec{x},\vec{y})$ plane and uniform in z, which can be represented by the complex function, **B**, defined by Eq. (34). **B** is a single-valued, analytic function of the complex variable, **s**, defined by Eq. (33), and, within the disk, $S(\Gamma_i)$, of center, O, and radius, R_i, can be expanded into the power series given by Eq. (61).

7.2 COMPLEX POTENTIAL

7.2.1 VECTOR POTENTIAL

Let us first go back to Biot and Savart's law. It is straightforward to derive from Eq. (24) that the magnetic flux density, $\overrightarrow{B_M}$, produced at a given point M of space can be rewritten under the form

$$\overrightarrow{B_M} = \vec{\nabla} \times \overrightarrow{A_M} \tag{131}$$

where $\overrightarrow{A_M}$ is the so-called *vector potential* at point M, defined as

$$\overrightarrow{A_M} = \iiint_{V(\Sigma_{cond})} dV_G \frac{\overrightarrow{J_G}}{GM} \tag{132}$$

Here, $V(\Sigma_{cond})$ designates the conductors' interior, G is a given point of $V(\Sigma_{cond})$, dV_G is an elementary volume in the vicinity of G, $\overrightarrow{J_G}$ is the current density at G, and GM is the modulus of $\overrightarrow{GM}$.

Given the problem symmetry, $\overrightarrow{B_M}$ and $\overrightarrow{A_M}$ are expected to be uniform in z. Furthermore, Eq. (132) shows that, when $\overrightarrow{J_G}$ is parallel to the z-axis, $\overrightarrow{A_M}$ is also parallel to the z-axis and reduces to

$$\overrightarrow{A_M} = A_{M,z}(x,y)\,\vec{z} \tag{133}$$

Combining Eqs. (131) and (133), it follows that, everywhere in space, we have

$$B_{M,x}(x,y) = \frac{\partial A_{M,z}(x,y)}{\partial y} \tag{134a}$$

and

$$B_{M,y}(x,y) = -\frac{\partial A_{M,z}(x,y)}{\partial x} \tag{134b}$$

7.2.2 SCALAR POTENTIAL

Let us now go back to Maxwell-Ampere's equation. In the conductors' exterior, Eq. (31) reduces to

$$\vec{\nabla} \times \overrightarrow{B_M} = \vec{0} \tag{135}$$

which shows that $\overrightarrow{B_M}$ can be derived as

$$\overrightarrow{B_M} = -\vec{\nabla}\,\psi_M \tag{136}$$

where ψ_M is the so-called *scalar potential*.

Since $\overrightarrow{B_M}$ is parallel to the $(O,\vec{x},\vec{y})$ plane, it follows that the z-derivative of ψ_M is nil and, therefore, that ψ_M is independent of z. Then, in the conductors' exterior, we have

$$B_{M,x}(x,y) = -\frac{\partial \psi_M(x,y)}{\partial x} \tag{137a}$$

and

$$B_{M,y}(x,y) = -\frac{\partial \psi_M(x,y)}{\partial y} \tag{137b}$$

7.2.3 COMPLEX POTENTIAL DEFINITION

Using the same definition as in Ref. [173], let us introduce the complex potential, **W**

$$\mathbf{W(s)} = A_{M,z}(x,y) + i\,\psi_M(x,y) \tag{138}$$

Let us first verify that, in the conductors' exterior, Re(**W**) and Im(**W**) satisfy Cauchy-Riemann's conditions for the function of complex variable. On one hand, we have

$$\frac{\partial \mathrm{Re}(\mathbf{W})}{\partial x} - \frac{\partial\, \mathrm{Im}(\mathbf{W})}{\partial y} = \frac{\partial A_{M,z}(x,y)}{\partial x} - \frac{\partial \psi_M(x,y)}{\partial y} \tag{139}$$

which, by combination with Eqs. (134b) and (137b), yields Eq. (36a).

On the other hand, we have

$$\frac{\partial \mathrm{Re}(\mathbf{W})}{\partial y} + \frac{\partial \mathrm{Im}(\mathbf{W})}{\partial x} = \frac{\partial A_{\mathrm{M,z}}(x,y)}{\partial y} + \frac{\partial \psi_{\mathrm{M}}(x,y)}{\partial x} \tag{140}$$

which, by combination with Eq. (134a) and (137a), yields Eq. (36b).

It follows that, **W** is a single-valued and analytic function on the conductors' exterior.

7.2.4 Relationship Between Complex Potential and Complex Magnetic Flux Density

Let us now differentiate **W**. For an analytic function, we have (see p. 110 of Ref. [155])

$$\frac{\mathbf{dW(s)}}{\mathbf{ds}} = \frac{\partial \mathrm{Re}[\mathbf{W}]}{\partial x} + \mathrm{i}\frac{\partial \mathrm{Im}[\mathbf{W}]}{\partial x} = -\mathrm{i}\frac{\partial \mathrm{Re}[\mathbf{W}]}{\partial y} + \frac{\partial \mathrm{Im}[\mathbf{W}]}{\partial y} \tag{141}$$

which yields

$$\frac{\mathbf{dW(s)}}{\mathbf{ds}} = \frac{\partial A_{\mathrm{M,z}}(x,y)}{\partial x} + \mathrm{i}\frac{\partial \psi_{\mathrm{M}}(x,y)}{\partial x} = -\mathrm{i}\frac{\partial A_{\mathrm{M,z}}(x,y)}{\partial y} + \frac{\partial \psi_{\mathrm{M}}(x,y)}{\partial y} \tag{142}$$

By combining Eq. (142) with Eqs. (134b) and (137a) [or with Eqs. (134a) and (137b)], it follows that, in the conductors' exterior

$$\frac{\mathbf{dW(s)}}{\mathbf{ds}} = -\left[B_{\mathrm{M,y}}(x,y) + \mathrm{i}\ B_{\mathrm{M,x}}(x,y)\right] \tag{143}$$

where, in the bracketed term of the right member, we recognize the complex magnetic flux density, **B**, defined by Eq. (34).

Hence, in the conductor' exterior, and, in particular, within the disk $S(\Gamma_i)$, the complex potential, **W(s)**, is the opposite of a primitive of the complex magnetic flux density, **B(s)**, and we simply have

$$\mathbf{B(s)} = -\frac{\mathbf{dW(s)}}{\mathbf{ds}} \tag{144}$$

7.2.5 Power Series Expansion of Complex Potential

Since **W** is single-valued and analytic on $S(\Gamma_i)$, it can be expanded into a power series around the disk origin.

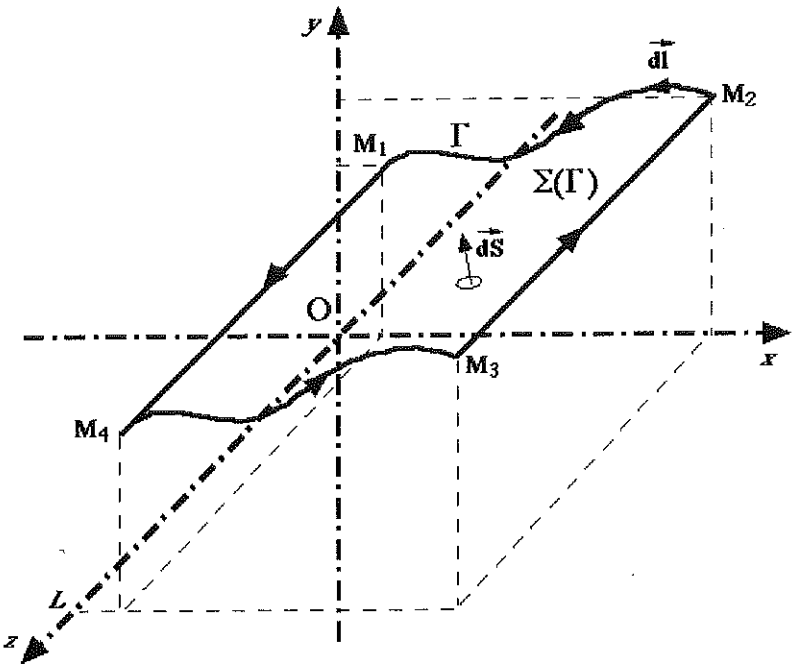

Figure 41. Surface parallel to the z-axis.

It is easy to derive from Eq. (61) that the power series expansion of **W** is given by

$$\mathbf{W(s)} = -\sum_{n=1}^{+\infty} \frac{1}{n} \left(B_n + \mathrm{i}\, A_n\right) \frac{\mathbf{s}^n}{R_{\mathrm{ref}}^{n-1}} + \mathbf{c} \qquad \text{for } \mathbf{s},\ |\mathbf{s}| < R_i \tag{145}$$

where A_n and B_n are the $2n$-pole field coefficients introduced in section 4.8 and **c** is a complex integration constant.

7.3 MAGNETIC FLUX TROUGH A SURFACE

Let Γ designate an arc located in the plane of equation ($z = 0$) and extending between the point, M_1, of coordinates (x_1, y_1,0), and the point, M_2, of coordinates (x_2, y_2,0), where $x_1 < x_2$. Furthermore, let us consider a surface, $\Sigma(\Gamma)$, generated by translation of the arc Γ along the z-direction, between the plane of equation ($z = 0$) and the plane of equation ($z = L$), as illustrated in Figure 41.

Such a surface is representative of the surface of a pick-up coil parallel to the z-axis. Let M_3 designate the point of coordinates (x_2, y_2, L), and let M_4 designate the point of coordinates (x_1, y_1, L). The orientation of the arc Γ is determined by traversing it from M_2 to M_1, while the orientation of the surface $\Sigma(\Gamma)$ is determined by traversing its contour from M_1 to M_4 to M_3 to M_2 and back to M_1.

The magnetic flux, $\phi_{\Sigma(\Gamma)}$, through the surface $\Sigma(\Gamma)$ is simply

$$\phi_{\Sigma(\Gamma)} = \iint_{\Sigma(\Gamma)} \vec{B}.\vec{dS} \tag{146}$$

where $\vec{dS}$ is a surface element vector, whose orientation is determined by the orientation of the surface $\Sigma(\Gamma)$.

Since the surface is parallel to the z-axis, and since $\vec{B}$ and $\Sigma(\Gamma)$ are uniform in z, we can write

$$\phi_{\Sigma(\Gamma)} = L \int_{\Gamma} \vec{B}.\left(\vec{dl} \times \vec{z}\right) \tag{147}$$

where $\vec{dl}$ is an arc element vector, whose orientation is determined by the orientation of Γ. [Note that to be consistent with the orientation of $\vec{dS}$ in Eq. (146), the surface element vector of Eq. (147) must be computed as $\left(\vec{dl} \times \vec{z}\right)$ and not as $\left(\vec{z} \times \vec{dl}\right)$.]

Let $(dx,dy,0)$ designate the coordinates of $\vec{dl}$. The coordinates of the vector $\left(\vec{dl} \times \vec{z}\right)$ are simply $(dy,-dx,0)$ and Eq. (147) can be rewritten

$$\phi_{\Sigma(\Gamma)} = -L \int_{\Gamma} \left(dx\, B_y - dy\, B_x\right) \tag{148}$$

where B_x and B_y designate the x- and y- components of $\vec{B}$.

It is easy to show that

$$\left(dx\, B_y - dy\, B_x\right) = \mathrm{Re}\left[(dx + i\, dy)\left(B_y + i\, B_x\right)\right] = \mathrm{Re}\left[\mathbf{ds\, B(s)}\right] \tag{149}$$

where $\mathbf{ds} = dx + i\, dy$.

By combining Eqs. (148) and (149), it follows that

$$\phi_{\Sigma(\Gamma)} = -L \int_{\Gamma} \mathrm{Re}\left[\mathbf{ds\, B(s)}\right] = -L\, \mathrm{Re}\left[\int_{s_2}^{s_1} \mathbf{ds\, B(s)}\right] \tag{150}$$

and by combining Eqs. (144) and (150), we get

$$\phi_{\Sigma(\Gamma)} = -L\ \mathrm{Re}\left\{\int_{\mathbf{s}_2}^{\mathbf{s}_1} [-\mathbf{dW(s)}]\right\} = -L\ \mathrm{Re}[\mathbf{W(s_2)} - \mathbf{W(s_1)}] \tag{151}$$

Here $\mathbf{s_1} = x_1 + \mathrm{i}\, y_1$ and $\mathbf{s_2} = x_2 + \mathrm{i}\, y_2$ designate the complex coordinates of points M_1 and M_2.

Equation (151) shows that the magnetic flux through the surface $\Sigma(\Gamma)$ is directly proportional to the real part of the difference between the complex potential values at both extremities of the arc Γ. Note that, as expected from Cauchy's theorem on the integral of analytical functions of complex variable, the result of the integral does not depend on the path chosen between $\mathbf{s_1}$ and $\mathbf{s_2}$ (p. 281 of Ref. [155]).

Replacing **W** by its power series expansion, we also have

$$\phi_{\Sigma(\Gamma)} = L\ \mathrm{Re}\left[\sum_{n=1}^{+\infty} \frac{1}{n} (B_n + \mathrm{i}\, A_n) \frac{\mathbf{s}_2^n - \mathbf{s}_1^n}{R_{\mathrm{ref}}^{n-1}}\right] \tag{152}$$

7.4 MAGNETIC FLUX PICKED-UP BY A ROTATING COIL

Let us assume that the surface $\Sigma(\Gamma)$ represents the average surface of a turn of a pick-up coil rotating around the z-axis. Let θ be an angle reckoning the coil rotation with respect to a zero mark and let $\mathbf{s_{1,0}}$ and $\mathbf{s_{2,0}}$ designate the positions of the two extremities of the arc Γ for $\theta = 0$. For any given angle we have

$$\mathbf{s_1} = \mathbf{s_{1,0}} \exp(\mathrm{i}\theta) \tag{153a}$$

and

$$\mathbf{s_2} = \mathbf{s_{2,0}} \exp(\mathrm{i}\theta) \tag{153b}$$

Combining Eqs. (152), (153a) and (153b), it follows that the flux, $\phi_{\text{pick-up}}$, picked-up by the rotating coil can be derived as

$$\phi_{\text{pick-up}}(\theta) = \mathrm{Re}\left[\sum_{n=1}^{+\infty} \mathbf{K_n} (B_n + \mathrm{i}\, A_n) \exp(in\theta)\right] \tag{154}$$

where

$$\mathbf{K_n} = \frac{N_{\text{pick-up}}\, L_{\text{pick-up}}\, R_{\mathrm{ref}}}{n} \left[\left(\frac{\mathbf{s_{2,0}}}{R_{\mathrm{ref}}}\right)^n - \left(\frac{\mathbf{s_{1,0}}}{R_{\mathrm{ref}}}\right)^n\right] \tag{155}$$

Here, $N_{\text{pick-up}}$ and $L_{\text{pick-up}}$ designate the number of turns and the length of the pick-up coil.

In the following, $\mathbf{K_n}$ is referred to as the *sensitivity factor of order n* of the rotating pick-up coil. Eq. (155) shows that $\mathbf{K_n}$ only depends on the coil geometry and can be real or complex depending on the values of $\mathbf{s_{1,0}}$ and $\mathbf{s_{2,0}}$. The units of $\mathbf{K_n}$ are square meters.

7.5 VOLTAGE INDUCED IN A ROTATING PICK-UP COIL

Let us assume that the pick-up coil considered in the previous section is rotating around the z-axis with an angular velocity, ω. Then, at any given time, t, we have

$$\theta(t) = \omega t + \theta_0 \tag{156}$$

where θ_0 is the coil angle at $t = 0$.

According to Faraday's law, the voltage, $V_{\text{pick-up}}$, induced during coil rotation is

$$V_{\text{pick-up}} = - \frac{\mathrm{d}\phi_{\text{pick-up}}}{\mathrm{d}t} \tag{157}$$

By combining Eqs. (154), (156) and (157), we get

$$V_{\text{pick-up}}(t) = - \omega \,\mathrm{Re}\left\{ \sum_{n=1}^{+\infty} \mathrm{i}\, n\, \mathbf{K_n} \left(B_n + \mathrm{i}\, A_n\right) \exp\left[in(\omega t + \theta_0)\right] \right\} \tag{158}$$

Some authors prefer to work with the integrated voltage. Let $U_{\text{pick-up}}$ designate the integral of $V_{\text{pick-up}}$ between t_0 and t. From Eq. (157), we get

$$U_{\text{pick-up}}(t) = \int_{t_0}^{t} \mathrm{d}t\, V_{\text{pick-up}}(t) = - \left\{ \phi_{\text{pick-up}}\left[\theta(t)\right] - \phi_{\text{pick-up}}\left[\theta(t_0)\right] \right\} \tag{159}$$

which shows that $U_{\text{pick-up}}$ is directly proportional to the magnetic flux picked-up by the rotating coil, thereby justifying its use.

By combining Eqs. (154), (156) and (159), we get

$$U_{\text{pick-up}}(t) = -\mathrm{Re}\left\langle \sum_{n=1}^{+\infty} \mathbf{K_n} \left(B_n + \mathrm{i}\, A_n\right) \left\{ \exp\left[in(\omega t + \theta_0)\right] - \exp\left[in(\omega t_0 + \theta_0)\right] \right\} \right\rangle \tag{160}$$

7.6 MAGNETIC FLUX PICKED-UP BY A ROTATING COIL ARRAY

Let us consider an array of P pick-up coils connected electrically, either in series or in opposition. Let us assume that this array is rotating around the z-axis, and let θ be an angle reckoning the array rotation with respect to a zero mark. The total magnetic flux, ϕ_{array}, picked-up by this array can be derived as

$$\phi_{\text{array}} = \sum_{p=1}^{P} \zeta_p \, \phi_p \tag{161}$$

where ϕ_p is the flux picked-up by the p-th coil, $\zeta_p = +1$ if the p-th coil is connected in series and $\zeta_p = -1$ if the p-th coil is connected in opposition.

Replacing ϕ_p by its expression, we can write

$$\phi_{\text{array}}(\theta) = \text{Re}\left[\sum_{n=1}^{+\infty} \mathbf{K_n^{array}} \left(B_n + \text{i}\, A_n\right) \exp(in\theta)\right] \tag{162}$$

where the sensitivity factor of order n of the pick-up coil array, $\mathbf{K_n^{array}}$, is given by

$$\mathbf{K_n^{array}} = \sum_{p=1}^{P} \zeta_p \, \mathbf{K_n^{C_p}} \tag{163}$$

Here, $\mathbf{K_n^{C_p}}$ designates the sensitivity factor of order n of the p-th coil.

Equation (163) shows that the sensitivity factor of order n of a pick-up coil array is equal to a linear combination of the sensitivity factors of order n of the various pick-up coils making up the array.

7.7 EFFECTIVE VOLTAGE READOUT FROM A ROTATING PICK-UP COIL ARRAY

Let us consider a rotating array of P pick-up coils connected to a multi-channel electronic card. Let us assume that the card includes a summator and that each channel is equipped with a polarity invertor and an amplifier. Let V_p designate the voltage induced in the p-th coil and let ζ_p and G_p designate the polarity and the gain of the channel to which the p-th coil is connected ($\zeta_p = +1$ if the polarity is positive and $\zeta_p = -1$ is the polarity is negative).

The voltage at the output of the summator, V_{out}, is

$$V_{out} = \sum_{p=1}^{P} \zeta_p G_p V_p \tag{164}$$

Replacing V_p by its expression, we can write

$$V_{out}(t) = -\omega \mathrm{Re}\left\{\sum_{n=1}^{+\infty} \mathrm{i}\, n\, \mathbf{K}_n^{out} (B_n + \mathrm{i}\, A_n) \exp[in(\omega t + \theta_0)]\right\} \tag{165}$$

where θ_0 is the array angle at $t = 0$, and $\mathbf{K}_n^{out}$ is the effective sensitivity factor of order n of the array given by

$$\mathbf{K}_n^{out} = \sum_{p=1}^{P} \zeta_p G_p \mathbf{K}_n^{C_p} \tag{166}$$

Furthermore, if the card is also equipped with an integrator, the voltage at the output of the integrator, U_{out}, is simply

$$U_{out}(t) = -\mathrm{Re}\left\langle \sum_{n=1}^{+\infty} \mathbf{K}_n^{out} (B_n + \mathrm{i}\, A_n) \{\exp[in(\omega t + \theta_0)] - \exp[in(\omega t_0 + \theta_0)]\} \right\rangle \tag{167}$$

where t_0 is the integration start time.

7.8 EXAMPLES OF ROTATING PICK-UP COILS AND PICK-UP COIL ARRAYS

7.8.1 NOTATIONS

Let us again consider a rectangular coordinate system $(O,\vec{x},\vec{y},\vec{z})$ and a magnet which, within a cylinder of z-axis and of radius, R_i, produces a two-dimensional magnetic flux density, $\vec{B}$, parallel to the $(\vec{x},\vec{y})$ plane and uniform in z. As in previous sections, let B_x and B_y designate the x- and y-components of $\vec{B}$ and let **B** designate the complex magnetic flux density defined by Eq. (34). Within the cylinder, **B** is a regular analytic function of the complex variable **s** defined by Eq. (33) and can be expanded into the power series given by Eq. (61).

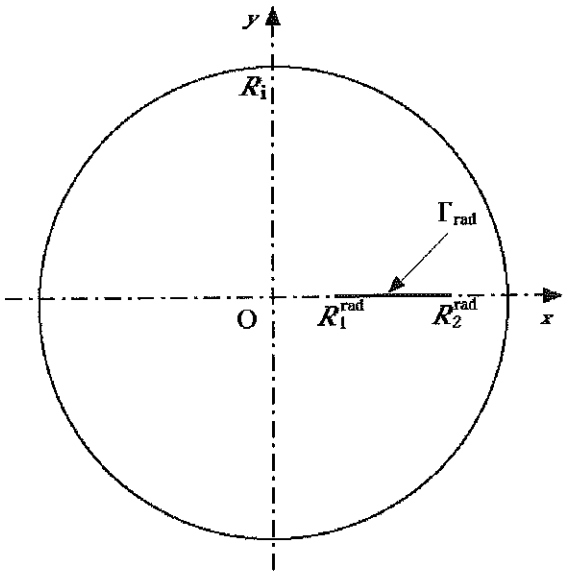

Figure 42. Cross-sectional view of a radial pick-up coil rotating around the z-axis.

In the following, we consider various geometries and arrays of pick-up coils. The coils are assumed to be parallel to the z-axis and uniform in z. They are inserted within the cylinder of radius, R_i, and rotate at a constant angular velocity, ω, around the z-axis.

Note that the formulae derived here are similar to those presented in Ref. [174].

7.8.2 RADIAL COILS

7.8.2.1 Definition

Let Γ_{rad} designate a straight line segment of the $(O,\vec{x},\vec{y})$ plane, extending between the point, M_1^{rad}, of coordinates $(R_1^{rad},0,0)$, and the point, M_2^{rad}, of coordinates $(R_2^{rad},0,0)$, where $0 \leq R_1^{rad} < R_2^{rad} < R_i$. Furthermore, let us consider a surface, $\Sigma(\Gamma_{rad})$, generated by translation of the segment Γ_{rad} along the z-direction, between the plane of equation $(z = 0)$ and the plane of equation $(z = L_{rad})$, and let us assume that $\Sigma(\Gamma_{rad})$ represents the average surface of a N_{rad}-turn pick-up coil rotating around the z-axis, as illustrated in Figure 42. Such a pick-up coil is referred to as a *radial coil.*

7.8.2.2 Sensitivity Factors

Let θ designate the radial pick-up coil angle with respect to the x-axis. Using the notations of section 7.4, we can write

$$s_{1,0} = R_1^{rad} \tag{168a}$$

and

$$\mathbf{s_{2,0}} = R_2^{\text{rad}} \tag{168b}$$

Hence, according to Eq. (155), the sensitivity factor of order n, $\mathbf{K_n^{rad}}$, is simply

$$\mathbf{K_n^{rad}} = J_n^{\text{rad}} = \frac{N_{\text{rad}}\, L_{\text{rad}}\, R_{\text{ref}}}{n}\left[\left(\frac{R_2^{\text{rad}}}{R_{\text{ref}}}\right)^n - \left(\frac{R_1^{\text{rad}}}{R_{\text{ref}}}\right)^n\right] \tag{169}$$

Equation (169) shows that the sensitivity factors of a radial coil are purely real.

7.8.2.3 Magnetic Flux and Induced Voltages

Combining Eqs. (154) and (169), it follows that the flux, ϕ_{rad}, picked-up by the rotating radial coil is

$$\phi_{\text{rad}}(\theta) = \sum_{n=1}^{+\infty} J_n^{\text{rad}}\left[B_n\cos(n\theta) - A_n\sin(n\theta)\right] \tag{170}$$

Similarly, by combining Eqs. (158) and (169), it follows that the induced voltage, V_{rad}, is

$$V_{\text{rad}}(t) = \omega \sum_{n=1}^{+\infty} n\, J_n^{\text{rad}}\left\{A_n\cos\left[n(\omega t+\theta_0)\right] + B_n\sin\left[n(\omega t+\theta_0)\right]\right\} \tag{171}$$

where θ_0 is the coil angle at $t = 0$. Furthermore, by combining Eqs. (160) and (169), it follows that the integrated voltage between t_0 and t, U_{rad}, is

$$U_{\text{rad}}(t) = \sum_{n=1}^{+\infty} J_n^{\text{rad}}\left\{A_n\sin\left[n(\omega t+\theta_0)\right] - B_n\cos\left[n(\omega t+\theta_0)\right]\right\} + \phi_{\text{rad}}(\omega t_0+\theta_0) \tag{172}$$

7.8.2.4 Case of a Radial Pick-Up Coil with a Thick Winding

The above equation for the sensitivity factor of order n, $\mathbf{K_n^{rad}}$, was derived assuming that the N_{rad}-turn winding was infinitely thin. In practice, a multi-turn winding does take some space, and its height and thickness must be taken into account.

As illustrated in Figure 43, let us assume that the radial pick-up coil is wound in a groove of rectangular cross-section machined around a support mandrel.

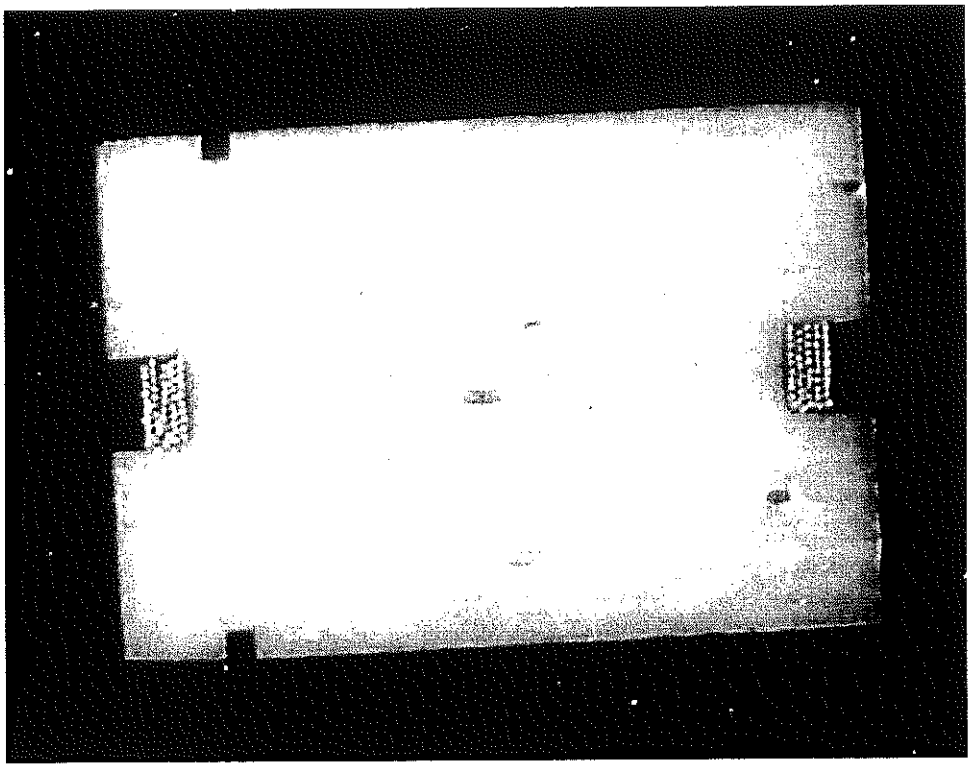

Figure 43. Example of radial pick-up coil winding realized at CERN for CEA/Saclay.

Furthermore, and as shown in Figure 44, let us assume that the pick-up coil is parallel to the z-axis, and let θ designate its angle with respect to the x-axis. Let us also assume that, at $\theta = 0$, the pick-up coil lies on the $(O,\vec{x},\vec{z})$ plane, and let R_c^{rad} designate the distance between the pick-up coil central axis and the z-axis. Finally, let R_i^{rad} (respectively, R_o^{rad}) designate the distance between the bottom (respectively, the top) of the winding groove and the pick-up coil central axis, and let h_{rad} designate the groove height.

The sensitivity factors of such a pick-up coil can be computed by dividing its winding into elementary turns and by summing the contributions from each turn. Let $\mathbf{s_{1,0}}$ designate the position in the complex plane of a given elementary turn on one side of the winding at $\theta = 0$. We have

$$\mathbf{s_{1,0}} = R_c^{rad} - x + \mathrm{i}\, y \tag{173a}$$

where (x,y), $R_i^{rad} \le x \le R_o^{rad}$, $-h_{rad}/2 \le y \le h_{rad}/2$.

If the winding is perfectly symmetrical, we can assume that the position of this elementary turn on the other side of the winding, $\mathbf{s_{2,0}}$, is simply

$$\mathbf{s_{2,0}} = R_c^{rad} + x + \mathrm{i}\, y \tag{173b}$$

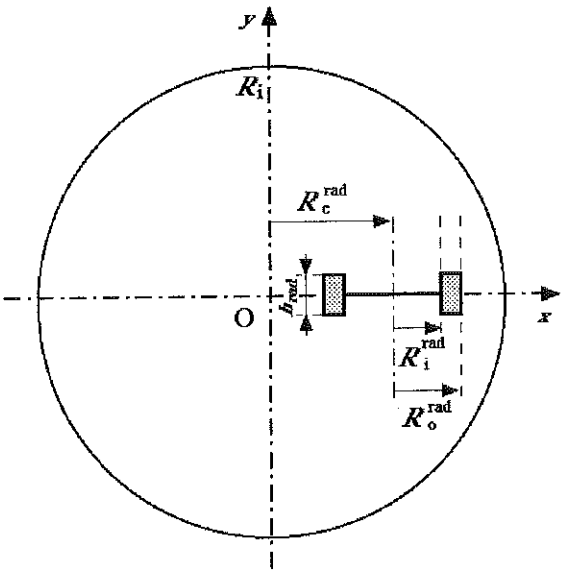

Figure 44. Cross-sectional view of a radial pick-up coil with a thick winding.

It follows that the sensitivity factor of order n, $\mathbf{K_n^{rad}}$, of a radial pick-up coil with a thick and symmetrical winding can be derived from

$$\mathbf{K_n^{rad}} = \frac{N_{rad}\, L_{rad}\, R_{ref}}{n\, h_{rad}\left(R_o^{rad} - R_i^{rad}\right)} \int_{R_i^{rad}}^{R_o^{rad}} dx \int_{-h_{rad}/2}^{+h_{rad}/2} dy \left[\left(\frac{R_c^{rad} + x + i\, y}{R_{ref}} \right)^n - \left(\frac{R_c^{rad} - x + i\, y}{R_{ref}} \right)^n \right] \tag{174}$$

The first integration yields

$$\begin{aligned} \int_{-h_{rad}/2}^{+h_{rad}/2} dy \left[\left(\frac{R_c^{rad} + x + i\, y}{R_{ref}} \right)^n - \left(\frac{R_c^{rad} - x + i\, y}{R_{ref}} \right)^n \right] = \\ \frac{R_{ref}}{i(n+1)} \left[\left(\frac{R_c^{rad} + x + i\, h_{rad}/2}{R_{ref}} \right)^{n+1} - \left(\frac{R_c^{rad} + x - i\, h_{rad}/2}{R_{ref}} \right)^{n+1} \right] \\ - \frac{R_{ref}}{i(n+1)} \left[\left(\frac{R_c^{rad} - x + i\, h_{rad}/2}{R_{ref}} \right)^{n+1} - \left(\frac{R_c^{rad} - x - i\, h_{rad}/2}{R_{ref}} \right)^{n+1} \right] \end{aligned} \tag{175}$$

where it appears that the two bracketed terms in the right member correspond to differences between a complex member and its conjugate.

Hence, we can write

$$\int_{-h_{\mathrm{rad}}/2}^{+h_{\mathrm{rad}}/2} \mathrm{d}y \left[\left(\frac{R_{\mathrm{c}}^{\mathrm{rad}} + x + \mathrm{i}\, y}{R_{\mathrm{ref}}} \right)^{n} - \left(\frac{R_{\mathrm{c}}^{\mathrm{rad}} - x + \mathrm{i}\, y}{R_{\mathrm{ref}}} \right)^{n} \right] =$$

$$\frac{2\, R_{\mathrm{ref}}}{(n+1)}\, \mathrm{Im}\left[\left(\frac{R_{\mathrm{c}}^{\mathrm{rad}} + x + \mathrm{i}\, h_{\mathrm{rad}}/2}{R_{\mathrm{ref}}} \right)^{n+1} - \left(\frac{R_{\mathrm{c}}^{\mathrm{rad}} - x + \mathrm{i}\, h_{\mathrm{rad}}/2}{R_{\mathrm{ref}}} \right)^{n+1} \right] \tag{176}$$

where Im designates the imaginary part function.

After the second integration, we get

$$\mathbf{K}_{\mathbf{n}}^{\mathbf{rad}} = \frac{2\, N_{\mathrm{rad}}\, L_{\mathrm{rad}}\, R_{\mathrm{ref}}^{3}}{n(n+1)(n+2)\, h_{\mathrm{rad}} \left(R_{\mathrm{o}}^{\mathrm{rad}} - R_{\mathrm{i}}^{\mathrm{rad}} \right)}$$

$$\mathrm{Im}\left[\left(\frac{R_{\mathrm{c}}^{\mathrm{rad}} + R_{\mathrm{o}}^{\mathrm{rad}} + \mathrm{i}\, h_{\mathrm{rad}}/2}{R_{\mathrm{ref}}} \right)^{n+2} - \left(\frac{R_{\mathrm{c}}^{\mathrm{rad}} + R_{\mathrm{i}}^{\mathrm{rad}} + \mathrm{i}\, h_{\mathrm{rad}}/2}{R_{\mathrm{ref}}} \right)^{n+2} \right.$$

$$\left. + \left(\frac{R_{\mathrm{c}}^{\mathrm{rad}} - R_{\mathrm{o}}^{\mathrm{rad}} + \mathrm{i}\, h_{\mathrm{rad}}/2}{R_{\mathrm{ref}}} \right)^{n+2} - \left(\frac{R_{\mathrm{c}}^{\mathrm{rad}} - R_{\mathrm{i}}^{\mathrm{rad}} + \mathrm{i}\, h_{\mathrm{rad}}/2}{R_{\mathrm{ref}}} \right)^{n+2} \right] \tag{177}$$

Equation (177) shows that, similarly to the case of an infinitely thin winding, the sensitivity factors of a radial pick-up coil with a thick and symmetrical winding are purely real.

Let us now verify that when the winding height and thickness tend towards zero, Eq. (177) tends towards Eq. (169). To do so, let us define $R_{\mathrm{a}}^{\mathrm{rad}}$ and r_{rad} as

$$R_{\mathrm{a}}^{\mathrm{rad}} = \frac{R_{\mathrm{i}}^{\mathrm{rad}} + R_{\mathrm{o}}^{\mathrm{rad}}}{2} \tag{178a}$$

and

$$r_{\mathrm{rad}} = \frac{R_{\mathrm{o}}^{\mathrm{rad}} - R_{\mathrm{i}}^{\mathrm{rad}}}{2} \tag{178b}$$

Furthermore, let us introduce the distances with respect to O of the centers of each winding side, R_{1}^{rad} and R_{2}^{rad}, which, using the above notations, can be written

$$R_{1}^{\mathrm{rad}} = R_{\mathrm{c}}^{\mathrm{rad}} - R_{\mathrm{a}}^{\mathrm{rad}} \tag{179a}$$

and

$$R_2^{\mathrm{rad}} = R_{\mathrm{c}}^{\mathrm{rad}} + R_{\mathrm{a}}^{\mathrm{rad}} \tag{179b}$$

Then, we have

$$\mathbf{K}_{\mathbf{n}}^{\mathbf{rad}} = \frac{N_{\mathrm{rad}}\, L_{\mathrm{rad}}\, R_{\mathrm{ref}}^3}{n(n+1)(n+2)\, h_{\mathrm{rad}}\, r_{\mathrm{rad}}} \mathrm{Im}\left[\left(\frac{R_2^{\mathrm{rad}} + r_{\mathrm{rad}} + \mathrm{i}\, h_{\mathrm{rad}}/2}{R_{\mathrm{ref}}} \right)^{n+2} - \left(\frac{R_2^{\mathrm{rad}} - r_{\mathrm{rad}} + \mathrm{i}\, h_{\mathrm{rad}}/2}{R_{\mathrm{ref}}} \right)^{n+2} + \left(\frac{R_1^{\mathrm{rad}} - r_{\mathrm{rad}} + \mathrm{i}\, h_{\mathrm{rad}}/2}{R_{\mathrm{ref}}} \right)^{n+2} - \left(\frac{R_1^{\mathrm{rad}} + r_{\mathrm{rad}} + \mathrm{i}\, h_{\mathrm{rad}}/2}{R_{\mathrm{ref}}} \right)^{n+2} \right] \tag{180}$$

Considering that, for values of x small with respect to 1, we have

$$(1+x)^{n+2} \approx 1 + (n+1)x + (n+1)(n+2)\frac{x^2}{2} \tag{181}$$

it is easy to show that, for values of r_{rad} and h_{rad} small with respect to R_1^{rad} and R_2^{rad}, we have

$$\mathrm{Im}\left[\left(\frac{R_2^{\mathrm{rad}} + r_{\mathrm{rad}} + \mathrm{i}\, h_{\mathrm{rad}}/2}{R_{\mathrm{ref}}} \right)^{n+2} - \left(\frac{R_2^{\mathrm{rad}} - r_{\mathrm{rad}} + \mathrm{i}\, h_{\mathrm{rad}}/2}{R_{\mathrm{ref}}} \right)^{n+2} \right] \approx (n+1)(n+2)\, r_{\mathrm{rad}}\, h_{\mathrm{rad}} \frac{\left(R_2^{\mathrm{rad}}\right)^n}{R_{\mathrm{ref}}^{n+2}} \tag{182a}$$

and

$$\mathrm{Im}\left[\left(\frac{R_1^{\mathrm{rad}} - r_{\mathrm{rad}} + \mathrm{i}\, h_{\mathrm{rad}}/2}{R_{\mathrm{ref}}} \right)^{n+2} - \left(\frac{R_1^{\mathrm{rad}} + r_{\mathrm{rad}} + \mathrm{i}\, h_{\mathrm{rad}}/2}{R_{\mathrm{ref}}} \right)^{n+2} \right] \approx -(n+1)(n+2)\, r_{\mathrm{rad}}\, h_{\mathrm{rad}} \frac{\left(R_1^{\mathrm{rad}}\right)^n}{R_{\mathrm{ref}}^{n+2}} \tag{182b}$$

Combining Eqs. (180), (182a) and (182b) yields Eq. (169).

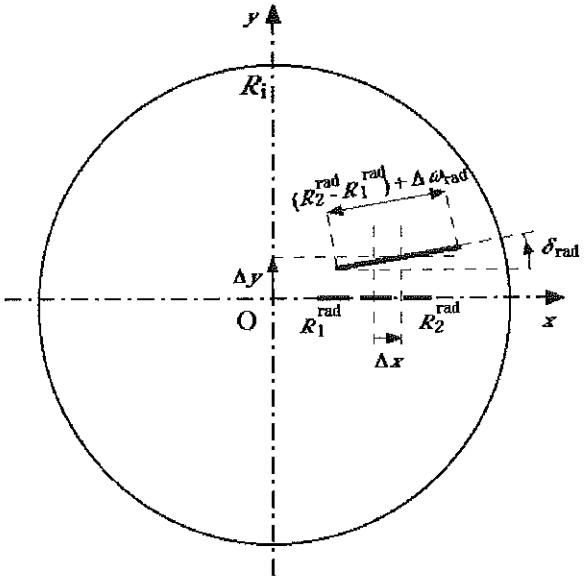

Figure 45. Cross-sectional view of an imperfect radial pick-up coil rotating around the z-axis.

7.8.2.5 Case of an Imperfect Radial Pick-Up Coil

Let us again consider a radial pick-up with an infinitely thin winding, but, as illustrated in Figure 45, let us now assume that the coil wires running parallel to the z-axis are displaced in the complex plane with respect to their design positions at $\theta = 0$, defined by Eqs. (168a) and (168b).

Let Δx and Δy designate the transverse displacements of the pick-up coil central axis with respect to z-axis (at $\theta = 0$), let δ_{rad} designate the coil angle with respect to the x-axis (at $\theta = 0$), and let Δw_{rad} designate the deformation in coil width (at $\theta = 0$). Then, we can write

$$\mathbf{s_{1,0}} = \frac{R_1^{rad} + R_2^{rad}}{2} + \Delta x + i\,\Delta y - \frac{1}{2}\left[\left(R_2^{rad} - R_1^{rad}\right) + \Delta w_{rad}\right] e^{i\delta_{rad}} \tag{183a}$$

and

$$\mathbf{s_{2,0}} = \frac{R_1^{rad} + R_2^{rad}}{2} + \Delta x + i\,\Delta y + \frac{1}{2}\left[\left(R_2^{rad} - R_1^{rad}\right) + \Delta w_{rad}\right] e^{i\delta_{rad}} \tag{183b}$$

Combining Eqs. (155), (183a) and (183b), we get

$$\mathbf{K_n^{rad}} = \frac{N_{rad}\, L_{rad}}{n\, R_{ref}^{n-1}} \left\langle \left\{ \frac{R_1^{rad} + R_2^{rad}}{2} + \Delta x + i\,\Delta y + \frac{1}{2}\left[\left(R_2^{rad} - R_1^{rad}\right) + \Delta w_{rad}\right] e^{i\delta_{rad}} \right\}^n \right.$$

$$-\left\{\frac{R_1^{\text{rad}}+R_2^{\text{rad}}}{2}+\Delta x+\mathrm{i}\,\Delta y-\frac{1}{2}\left[\left(R_2^{\text{rad}}-R_1^{\text{rad}}\right)+\Delta w_{\text{rad}}\right]\mathrm{e}^{\mathrm{i}\delta_{\text{rad}}}\right\}^n\Bigg\rangle \tag{184}$$

Considering that, for values of δ_{rad} small with respect to 1, we have

$$\mathrm{e}^{\mathrm{i}\delta_{\text{rad}}}\approx 1+\mathrm{i}\,\delta_{\text{rad}} \tag{185}$$

the above equation can be approximated by

$$\mathbf{K}_{\mathbf{n}}^{\mathbf{rad}}\approx\frac{N_{\text{rad}}\,L_{\text{rad}}}{n\,R_{\text{ref}}^{n-1}}\Bigg\langle\left\{R_2^{\text{rad}}+\Delta x+\frac{\Delta w_{\text{rad}}}{2}+\mathrm{i}\left[\Delta y+\frac{\left(R_2^{\text{rad}}-R_1^{\text{rad}}\right)+\Delta w_{\text{rad}}}{2}\delta_{\text{rad}}\right]\right\}^n$$
$$-\left\{R_1^{\text{rad}}+\Delta x-\frac{\Delta w_{\text{rad}}}{2}+\mathrm{i}\left[\Delta y-\frac{\left(R_2^{\text{rad}}-R_1^{\text{rad}}\right)+\Delta w_{\text{rad}}}{2}\delta_{\text{rad}}\right]\right\}^n\Bigg\rangle \tag{186}$$

Furthermore, considering that, for values of x small with respect to 1, we also have

$$(1+x)^n\approx 1+n\,x \tag{187}$$

it can be shown that, for small imperfections, and neglecting the second order term in $(\Delta w_{\text{rad}}\delta_{\text{rad}})$, we have

$$\left\{R_1^{\text{rad}}+\Delta x-\frac{\Delta w_{\text{rad}}}{2}+\mathrm{i}\left[\Delta y-\frac{\left(R_2^{\text{rad}}-R_1^{\text{rad}}\right)+\Delta w_{\text{rad}}}{2}\delta_{\text{rad}}\right]\right\}^n\approx$$
$$\left(R_1^{\text{rad}}\right)^n+n\left(R_1^{\text{rad}}\right)^{n-1}\left\{\Delta x-\frac{\Delta w_{\text{rad}}}{2}+\mathrm{i}\left[\Delta y-\frac{1}{2}\left(R_2^{\text{rad}}-R_1^{\text{rad}}\right)\delta_{\text{rad}}\right]\right\} \tag{188a}$$

and

$$\left\{R_2^{\text{rad}}+\Delta x+\frac{\Delta w_{\text{rad}}}{2}+\mathrm{i}\left[\Delta y+\frac{\left(R_2^{\text{rad}}-R_1^{\text{rad}}\right)+\Delta w_{\text{rad}}}{2}\delta_{\text{rad}}\right]\right\}^n\approx$$
$$\left(R_2^{\text{rad}}\right)^n+n\left(R_2^{\text{rad}}\right)^{n-1}\left\{\Delta x+\frac{\Delta w_{\text{rad}}}{2}+\mathrm{i}\left[\Delta y+\frac{1}{2}\left(R_2^{\text{rad}}-R_1^{\text{rad}}\right)\delta_{\text{rad}}\right]\right\} \tag{188b}$$

Combining Eqs. (186), (188a) and (188b), we get

$$\mathbf{K}_{\mathbf{n}}^{\mathbf{rad}}\approx\frac{N_{\text{rad}}\,L_{\text{rad}}\,R_{\text{ref}}}{n}\left[\left(\frac{R_2^{\text{rad}}}{R_{\text{ref}}}\right)^n-\left(\frac{R_2^{\text{rad}}}{R_{\text{ref}}}\right)^n\right]$$

$$+ N_{\text{rad}}\, L_{\text{rad}}\, R_{\text{ref}} \left[\left(\frac{R_2^{\text{rad}}}{R_{\text{ref}}} \right)^{n-1} - \left(\frac{R_2^{\text{rad}}}{R_{\text{ref}}} \right)^{n-1} \right] \frac{\Delta x + \mathrm{i}\,\Delta y}{R_{\text{ref}}}$$

$$+ \frac{N_{\text{rad}}\, L_{\text{rad}}\, R_{\text{ref}}}{2} \left[\left(\frac{R_2^{\text{rad}}}{R_{\text{ref}}} \right)^{n-1} + \left(\frac{R_2^{\text{rad}}}{R_{\text{ref}}} \right)^{n-1} \right] \frac{\Delta w_{\text{rad}} + \mathrm{i} \left(R_2^{\text{rad}} - R_1^{\text{rad}} \right) \delta_{\text{rad}}}{R_{\text{ref}}} \tag{189}$$

Let us define $Y_{\text{n}}^{\text{rad}}$ as

$$Y_{\text{n}}^{\text{rad}} = \frac{N_{\text{rad}}\, L_{\text{rad}}\, R_{\text{ref}}}{2\, n} \left[\left(\frac{R_2^{\text{rad}}}{R_{\text{ref}}} \right)^{n} + \left(\frac{R_1^{\text{rad}}}{R_{\text{ref}}} \right)^{n} \right] \tag{190}$$

Combining Eqs. (189) and (190) and using the expression of the real part of the sensitivity factor of order n of an ideal radial pick-up coil, $J_{\text{n}}^{\text{rad}}$, given by Eq. (169), we get

$$\mathbf{K_1^{rad}} \approx J_1^{\text{rad}} + N_{\text{rad}}\, L_{\text{rad}}\, R_{\text{ref}} \frac{\Delta w_{\text{rad}} + \mathrm{i} \left(R_2^{\text{rad}} - R_1^{\text{rad}} \right) \delta_{\text{rad}}}{R_{\text{ref}}} \tag{191a}$$

and

$$\mathbf{K_n^{rad}} \approx J_{\text{n}}^{\text{rad}} + (n-1)\, J_{\text{n-1}}^{\text{rad}} \frac{\Delta x + \mathrm{i}\,\Delta y}{R_{\text{ref}}} + (n-1)\, Y_{\text{n-1}}^{\text{rad}} \frac{\Delta w_{\text{rad}} + \mathrm{i} \left(R_2^{\text{rad}} - R_1^{\text{rad}} \right) \delta_{\text{rad}}}{R_{\text{ref}}} \tag{191b}$$

Equations (191a) and (191b) show that, compared to the case of an ideal radial pick-up coil, a displacement along the x-axis or a deformation in coil width modifies the real parts of the sensitivity factors, while a displacement along the y-axis or an error in coil alignment result in non-zero imaginary parts.

7.8.3 TANGENTIAL COILS

7.8.3.1 Definition

Let Γ_{tan} designate a straight line segment of the $(\text{O}, \vec{\text{x}}, \vec{\text{y}})$ plane, extending between the point, M_1^{tan}, of coordinates $[R_{\text{tan}}\cos(\delta_{\text{tan}}/2), -R_{\text{tan}}\sin(\delta_{\text{tan}}/2), 0]$, and the point, M_2^{tan}, of coordinates $[R_{\text{tan}}\cos(\delta_{\text{tan}}/2),\ R_{\text{tan}}\sin(\delta_{\text{tan}}/2), 0]$, where $0 < R_{\text{tan}} < R_{\text{i}}$ and δ_{tan} is a small, positive angle.

Furthermore, let us consider a surface, $\Sigma(\Gamma_{\text{tan}})$, generated by translation of Γ_{tan} along the z-direction, between the plane of equation $(z = 0)$ and the plane of equation $(z = L_{\text{tan}})$, and let us assume that $\Sigma(\Gamma_{\text{tan}})$ represents the average surface of a N_{tan}-turn pick-up coil rotating around the z-axis, as illustrated in Figure 46.

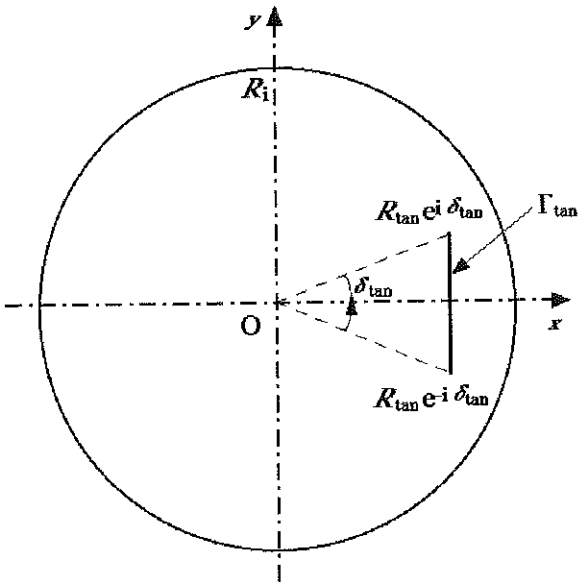

Figure 46. Cross-sectional view of a tangential pick-up coil rotating around the z-axis.

Such a pick-up coil is referred to as a *tangential coil* and δ_{tan} is referred to as its *opening angle.*

7.8.3.2 Sensitivity Factors

Let θ designate the angle of the bisector of a tangential pick-up coil with respect to the x-axis. Using the notations of section 7.4, we can write

$$\mathbf{s_{1,0}} = R_{tan}\, e^{i\delta_{tan}/2} \tag{192a}$$

and

$$\mathbf{s_{2,0}} = R_{tan}\, e^{-i\delta_{tan}/2} \tag{192b}$$

Hence, according to Eq. (155), the sensitivity factor of order n, $\mathbf{K_n^{tan}}$, is simply

$$\mathbf{K_n^{tan}} = -i\, I_n^{tan} = -i\,\frac{2\,N_{tan}\,L_{tan}\,R_{ref}}{n}\left(\frac{R_{tan}}{R_{ref}}\right)^n \sin\left(\frac{n\delta_{tan}}{2}\right) \tag{193}$$

Equation (193) shows that the sensitivity factors of a tangential coil are purely imaginary.

7.8.3.3 Magnetic Flux and Induced Voltages

Combining Eqs. (154) and (193), it follows that the flux, ϕ_{tan}, picked-up by a rotating tangential coil is

$$\phi_{\tan}(\theta) = \sum_{n=1}^{+\infty} I_n^{\tan}\left[A_n \cos(n\theta) + B_n \sin(n\theta)\right] \tag{194}$$

Similarly, by combining Eqs. (158) and (193), it follows that the induced voltage, $V_{\tan}$, is

$$V_{\tan}(t) = -\omega \sum_{n=1}^{+\infty} n\, I_n^{\tan}\left\{ B_n \cos\left[n(\omega t + \theta_0)\right] - A_n \sin\left[n(\omega t + \theta_0)\right]\right\} \tag{195}$$

where θ_0 is the coil angle at $t = 0$.

Finally, by combining Eqs. (160) and (193), it follows that the integrated voltage between t_0 and t, $U_{\tan}$, is

$$U_{\tan}(t) = -\sum_{n=1}^{+\infty} I_n^{\tan}\left\{ B_n \sin\left[n(\omega t + \theta_0)\right] + A_n \cos\left[n(\omega t + \theta_0)\right]\right\} + \phi_{\tan}(\omega t_0 + \theta_0) \tag{196}$$

7.8.3.4 Case of a Tangential Pick-Up Coil With a Thick Winding

Similarly to what we did in section 7.8.2.4 for the case of a radial pick-up coil, and as illustrated in Figure 47, let us consider a tangential pick-up coil with a thick winding housed in a groove machined around a support mandrel. Let $R_c^{\tan}$ designate the distance between the pick-up coil central axis and the z-axis, let $R_i^{\tan}$ (respectively, $R_o^{\tan}$) designate the distance between the bottom (respectively, the top) of the winding groove and the pick-up coil central axis, and let $h_{\tan}$ designate the groove height.

Once again, the sensitivity factors of such a pick-up coil can be computed by dividing its winding into elementary turns and by summing the contributions from each turn. Let $\mathbf{s}_{1,0}$ and $\mathbf{s}_{2,0}$ designate the positions in the complex plane of a given elementary turn on both sides of the winding at $\theta = 0$. If the winding is perfectly symmetrical, we can assume

$$\mathbf{s}_{1,0} = R_c^{\tan} + x + \mathrm{i}\, y \tag{197a}$$

and

$$\mathbf{s}_{2,0} = R_c^{\tan} + x - \mathrm{i}\, y \tag{197b}$$

where (x,y), $-h_{\tan}/2 \le x \le h_{\tan}/2$, $R_i^{\tan} \le y \le R_o^{\tan}$.

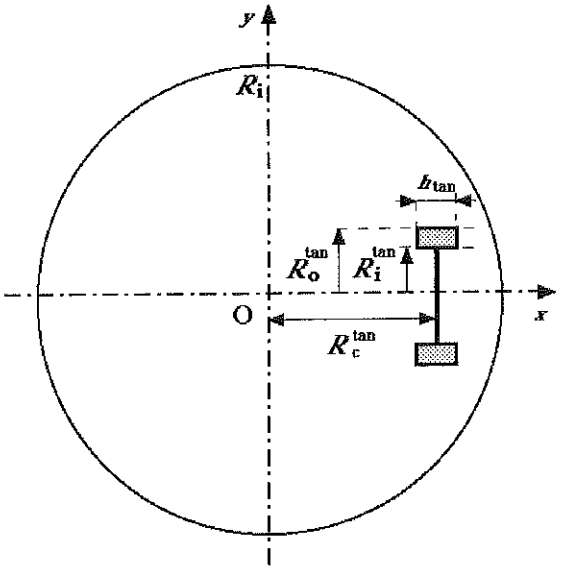

Figure 47. Cross-sectional view of a tangential pick-up coil with a thick winding.

It follows that the sensitivity factor of order n, $\mathbf{K}_n^{tan}$, of a tangential pick-up coil with a thick and symmetrical winding can be derived from

$$\mathbf{K}_n^{tan} = \frac{N_{tan}\, L_{tan}\, R_{ref}}{n\, h_{tan}\left(R_o^{tan} - R_i^{tan}\right)} \int_{-h_{tan}/2}^{+h_{tan}/2} dx \int_{R_i^{tan}}^{R_o^{tan}} dy \left[\left(\frac{R_c^{tan} + x - i\, y}{R_{ref}} \right)^n - \left(\frac{R_c^{tan} + x + i\, y}{R_{ref}} \right)^n \right] \tag{198}$$

The first integration yields (after some re-ordering)

$$\begin{aligned} \int_{R_i^{tan}}^{R_o^{tan}} dy \left[\left(\frac{R_c^{tan} + x - i\, y}{R_{ref}} \right)^n - \left(\frac{R_c^{tan} + x + i\, y}{R_{ref}} \right)^n \right] = \\ - \frac{R_{ref}}{i\,(n+1)} \left[\left(\frac{R_c^{tan} + x - i\, R_o^{tan}}{R_{ref}} \right)^{n+1} + \left(\frac{R_c^{tan} + x + i\, R_o^{tan}}{R_{ref}} \right)^{n+1} \right] \\ + \frac{R_{ref}}{i\,(n+1)} \left[\left(\frac{R_c^{tan} + x - i\, R_i^{tan}}{R_{ref}} \right)^{n+1} + \left(\frac{R_c^{tan} + x + i\, R_i^{tan}}{R_{ref}} \right)^{n+1} \right] \end{aligned} \tag{199}$$

where it appears that the two bracketed terms in the right member correspond to sums of a complex member and its conjugate.

Hence, we can write

$$\int_{R_i^{\tan}}^{R_o^{\tan}} \mathrm{d}y \left[\left(\frac{R_c^{\tan} + x - \mathrm{i}\, y}{R_{\mathrm{ref}}} \right)^n - \left(\frac{R_c^{\tan} + x + \mathrm{i}\, y}{R_{\mathrm{ref}}} \right)^n \right] =$$

$$\mathrm{i} \frac{2\, R_{\mathrm{ref}}}{(n+1)} \, \mathrm{Re} \left[\left(\frac{R_c^{\tan} + x + \mathrm{i}\, R_o^{\tan}}{R_{\mathrm{ref}}} \right)^{n+1} - \left(\frac{R_c^{\tan} + x + \mathrm{i}\, R_i^{\tan}}{R_{\mathrm{ref}}} \right)^{n+1} \right] \tag{200}$$

where Re designates the real part function.

After the second integration, we get

$$\mathbf{K}_{\mathbf{n}}^{\tan} = \mathrm{i} \frac{2\, N_{\tan}\, L_{\tan}\, R_{\mathrm{ref}}^3}{n(n+1)(n+2)\, h_{\tan} \left(R_o^{\tan} - R_i^{\tan} \right)}$$

$$\mathrm{Re} \left[\left(\frac{R_c^{\tan} + h_{\tan}/2 + \mathrm{i}\, R_o^{\tan}}{R_{\mathrm{ref}}} \right)^{n+2} - \left(\frac{R_c^{\tan} - h_{\tan}/2 + \mathrm{i}\, R_o^{\tan}}{R_{\mathrm{ref}}} \right)^{n+2} \right.$$

$$\left. - \left(\frac{R_c^{\tan} + h_{\tan}/2 + \mathrm{i}\, R_i^{\tan}}{R_{\mathrm{ref}}} \right)^{n+2} + \left(\frac{R_c^{\tan} - h_{\tan}/2 + \mathrm{i}\, R_i^{\tan}}{R_{\mathrm{ref}}} \right)^{n+2} \right] \tag{201}$$

Equation (201) shows that, similarly to the case of an infinitely thin winding, the sensitivity factors of a tangential pick-up coil with a thick and symmetrical winding are purely imaginary.

Let us now verify that when the winding height and thickness tends towards zero, Eq. (201) tends towards Eq. (193). To do so, let us define $R_a^{\tan}$ and $r_{\tan}$ as

$$R_a^{\tan} = \frac{R_i^{\tan} + R_o^{\tan}}{2} \tag{202a}$$

and

$$r_{\tan} = \frac{R_o^{\tan} - R_i^{\tan}}{2} \tag{202b}$$

Then, we have

$$\mathbf{K}_{\mathbf{n}}^{\tan} = \mathrm{i} \frac{N_{\tan}\, L_{\tan}\, R_{\mathrm{ref}}^3}{n(n+1)(n+2)\, h_{\tan}\, r_{\tan}}$$

$$\mathrm{Re}\left[\left(\frac{R_c^{\tan}+\mathrm{i}\,R_a^{\tan}+h_{\tan}/2+\mathrm{i}\,r_{\tan}}{R_{\mathrm{ref}}}\right)^{n+2}-\left(\frac{R_c^{\tan}+\mathrm{i}\,R_a^{\tan}-h_{\tan}/2+\mathrm{i}\,r_{\tan}}{R_{\mathrm{ref}}}\right)^{n+2}\right.$$
$$\left.-\left(\frac{R_c^{\tan}+\mathrm{i}\,R_a^{\tan}+h_{\tan}/2-\mathrm{i}\,r_{\tan}}{R_{\mathrm{ref}}}\right)^{n+2}+\left(\frac{R_c^{\tan}+\mathrm{i}\,R_a^{\tan}-h_{\tan}/2-\mathrm{i}\,r_{\tan}}{R_{\mathrm{ref}}}\right)^{n+2}\right] \quad (203)$$

Using Eq. (181), it can be shown that, for values of $r_{\tan}$ and $h_{\tan}$ small with respect to $R_c^{\tan}$ and $R_a^{\tan}$, we have

$$\left(\frac{R_c^{\tan}+\mathrm{i}\,R_a^{\tan}+h_{\tan}/2+\mathrm{i}\,r_{\tan}}{R_{\mathrm{ref}}}\right)^{n+2}-\left(\frac{R_c^{\tan}+\mathrm{i}\,R_a^{\tan}-h_{\tan}/2+\mathrm{i}\,r_{\tan}}{R_{\mathrm{ref}}}\right)^{n+2}$$
$$-\left(\frac{R_c^{\tan}+\mathrm{i}\,R_a^{\tan}+h_{\tan}/2-\mathrm{i}\,r_{\tan}}{R_{\mathrm{ref}}}\right)^{n+2}+\left(\frac{R_c^{\tan}+\mathrm{i}\,R_a^{\tan}-h_{\tan}/2-\mathrm{i}\,r_{\tan}}{R_{\mathrm{ref}}}\right)^{n+2}$$
$$\approx \mathrm{i}\,2(n+1)(n+2)\,h_{\tan}\,r_{\tan}\,\frac{\left(R_c^{\tan}+\mathrm{i}\,R_a^{\tan}\right)^n}{R_{\mathrm{ref}}^{n+2}} \quad (204)$$

Combining Eqs. (203) and (204), we get

$$\mathbf{K_n^{tan}} \approx \mathrm{i}\,\frac{2\,N_{\tan}\,L_{\tan}\,R_{\mathrm{ref}}}{n}\,\mathrm{Re}\left[\mathrm{i}\,\frac{\left(R_c^{\tan}+\mathrm{i}\,R_a^{\tan}\right)^n}{R_{\mathrm{ref}}^n}\right] \quad (205)$$

Furthermore, let $R_{\tan}$ and $(\delta_{\tan}/2)$ designate the modulus and the argument of $\left(R_c^{\tan}+\mathrm{i}\,R_a^{\tan}\right)$. Then, we have

$$\mathbf{K_n^{tan}} \approx \mathrm{i}\,\frac{2\,N_{\tan}\,L_{\tan}\,R_{\mathrm{ref}}}{n}\left(\frac{R_{\tan}}{R_{\mathrm{ref}}}\right)^n \mathrm{Re}\left(\mathrm{i}\,\mathrm{e}^{\mathrm{i}n\delta_{\tan}/2}\right) \quad (206)$$

where we recognize Eq. (193).

7.8.3.5 Case of an Imperfect Tangential Pick-Up Coil

Similarly to the case of an imperfect radial pick-up coil, it can be shown that a displacement along the x-axis or a deformation in the width of a tangential pick-up coil modifies the imaginary parts of the sensitivity factors, while a displacement along the y-axis or an error in coil alignment result in non-zero real parts.

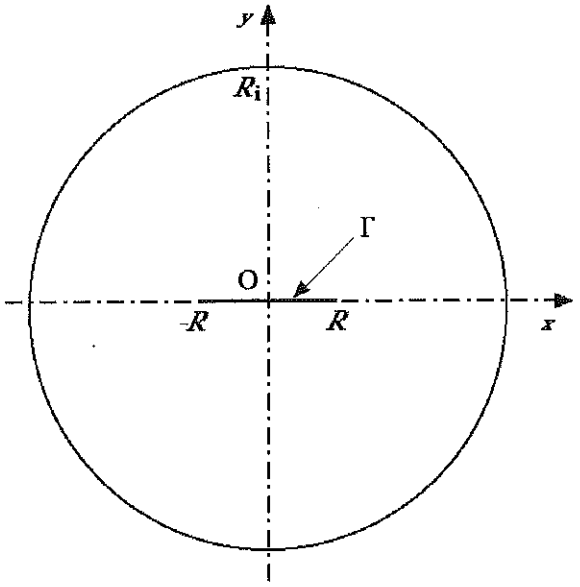

Figure 48. Cross-sectional view of a dipole pick-up coil rotating around the z-axis.

7.8.4 MORGAN COIL ARRAYS

7.8.4.1 Dipole Coils

Let Γ_{dip} designate a straight line segment of the $(O,\vec{x},\vec{y})$ plane, extending between the point, M_1^{dip}, of coordinates $(-R,0,0)$, and the point, M_2^{dip}, of coordinates $(R,0,0)$, where $0 < R < R_i$, and let us consider the surface, $\Sigma(\Gamma_{dip})$, generated by translation of Γ_{dip} along the z-direction, between the plane of equation $(z = 0)$ and the plane of equation $(z = L)$, as illustrated in Figure 48.

Let us further assume that $\Sigma(\Gamma_{dip})$ represents the average surface of an N-turn pick-up coil rotating around the z-axis, and let θ designate the coil angle with respect to the x-axis. Such a pick-up coil is referred to as a *dipole coil*.

Using the notations of section 7.4, we can write

$$\mathbf{s_{1,0}} = R\,e^{i\pi} \tag{207a}$$

and

$$\mathbf{s_{2,0}} = R \tag{207b}$$

Hence, the sensitivity factor of order n, $\mathbf{K_n^{dip}}$, is simply

$$\mathbf{K_n^{dip}} = J_n^{dip} = \frac{N\,L\,R_{ref}}{n}\left(\frac{R}{R_{ref}}\right)^n\left(1 - e^{in\pi}\right)$$

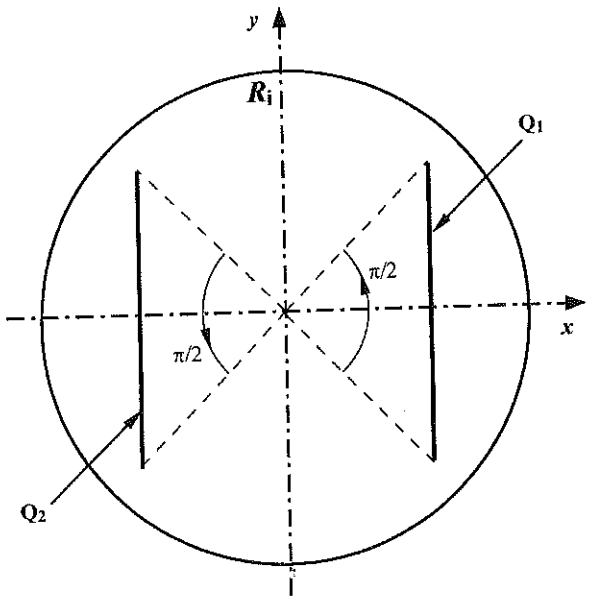

Figure 49. Cross-sectional view of a (Morgan) quadrupole, pick-up coil array rotating around the z-axis.

$$= \frac{N\,L\,R_{\text{ref}}}{n}\left(\frac{R}{R_{\text{ref}}}\right)^{n}\left[1-(-1)^{n}\right] \tag{208}$$

Equation (208) shows that the sensitivity factors of a dipole coil are purely real for n odd and are nil for n even. Hence, a dipole coil is only sensitive to $[2(2k+1)]$-pole fields where k is an integer. In particular, a dipole pick-up coil is sensitive to dipole and sextupole fields, but is not sensitive to quadrupole fields.

7.8.4.2 Quadrupole Coil Array

A *quadrupole coil array* is an array made up of two identical tangential coils, (Q_1) and (Q_2), with an opening angle of ($\pi/2$), and rotated by π with respect to each other, as represented in Figure 49. The two coils are connected electrically in series.

Let us consider a quadrupole coil array rotating around the z-axis and let θ designate the azimuth of the center of coil (Q_1) with respect to the x-axis. Let N designate the common number of turns of the two pick-up coils, and let R and L designate the average radius and length of the coils' wires running parallel to the z-axis. According to Eq. (193), the sensitivity factor of order n of coil (Q_1), $\mathbf{K}_{\mathbf{n}}^{\mathbf{Q}_1}$, is simply

$$\mathbf{K}_{\mathbf{n}}^{\mathbf{Q}_1} = -\,\mathrm{i}\,\frac{2\,N\,L\,R_{\text{ref}}}{n}\left(\frac{R}{R_{\text{ref}}}\right)^{n}\sin\left(\frac{n\pi}{4}\right) \tag{209}$$

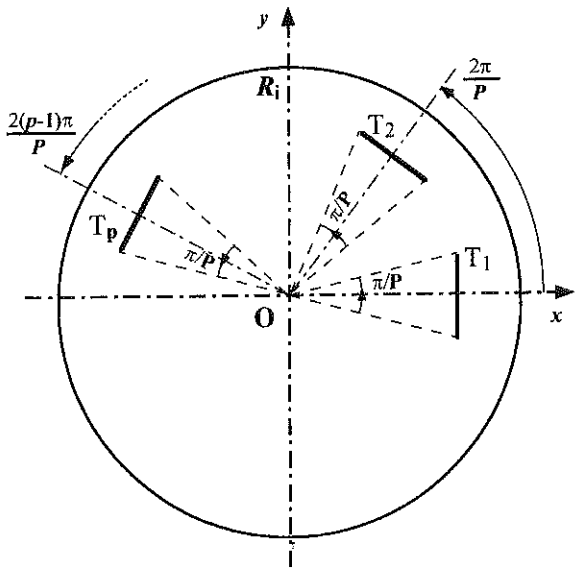

Figure 50. Cross-sectional view of a (Morgan) $2P$-pole, pick-up coil array rotating around the z-axis.

It can be verified that the sensitivity factor of order n of coil (Q_2), $\mathbf{K}_n^{Q_2}$, is given by

$$\mathbf{K}_n^{Q_2} = e^{in\pi}\,\mathbf{K}_n^{Q_1} = (-1)^n\,\mathbf{K}_n^{Q_1} \tag{210}$$

Combining Eqs. (163), (209) and (210), it follows that the sensitivity factor of order n of the quadrupole coil array, $\mathbf{K}_n^{quad}$, is

$$\mathbf{K}_n^{quad} = \mathbf{K}_n^{Q_1} + \mathbf{K}_n^{Q_2} = \left[1+(-1)^n\right]\mathbf{K}_n^{Q_1}$$

$$= -\,i\,\frac{2\,N\,L\,R_{ref}}{n}\left(\frac{R}{R_{ref}}\right)^n\left[1+(-1)^n\right]\sin\left(\frac{n\pi}{4}\right) \tag{211}$$

Equation (211) shows that the sensitivity factors of a quadrupole coil array are only non-zero if n is an even number that is not a multiple of 4, *i.e.*, if n is an odd multiple of 2. Hence, a quadrupole coil array is only sensitive to $[4(2k+1)]$-pole fields where k is an integer. In particular, a quadrupole coil array is sensitive to quadrupole and dodecapole fields, but is not sensitive to dipole, sextupole, octupole, and decapole fields.

7.8.4.3 2P-Pole Coil Array

A *2P-pole coil array* is an array made up of P identical tangential coils, (T_1), (T_2), ..., (T_P), with an opening angle of (π/P), and such that coil (T_{p+1}) is rotated by $(2\pi/P)$ with respect to coil (T_p), as represented in Figure 50. The P coils are connected in series.

Let us consider a $2P$-pole coil array rotating around the z-axis and let θ designate the azimuth of the center of coil (T_1) with respect to the x-axis. Let N designate the common number of turns of the P pick-up coils, and let R and L designate the average radius and length of the coil wires running parallel to the z-axis.

According to Eq. (193), the sensitivity factor of order n of coil (T_1), $\mathbf{K_n^{T_1}}$, is simply

$$\mathbf{K_n^{T_1}} = -\mathrm{i}\frac{2NLR_{\mathrm{ref}}}{n}\left(\frac{R}{R_{\mathrm{ref}}}\right)^n \sin\left(\frac{n\pi}{2P}\right) \tag{212}$$

It is easy to verify that the sensitivity factor of order n of coil (T_p), $\mathbf{K_n^{T_p}}$, is given by

$$\mathbf{K_n^{T_p}} = \exp\left[\mathrm{i}\frac{2n(p-1)\pi}{P}\right]\mathbf{K_n^{T_1}} \tag{213}$$

Combining Eqs. (163), (212) and (213), it follows that the sensitivity factor of order n of the $2P$-pole coil array, $\mathbf{K_n^{2P\text{-pole}}}$, is

$$\mathbf{K_n^{2P\text{-pole}}} = \sum_{p=1}^{P}\mathbf{K_n^{T_p}} = \left\{\sum_{p=1}^{P}\exp\left[\mathrm{i}\frac{2n(p-1)\pi}{P}\right]\right\}\mathbf{K_n^{T_1}}$$

$$= -\mathrm{i}\frac{2NLR_{\mathrm{ref}}}{n}\left(\frac{R}{R_{\mathrm{ref}}}\right)^n\left\{\sum_{p=1}^{P}\exp\left[\mathrm{i}\frac{2n(p-1)\pi}{P}\right]\right\}\sin\left(\frac{n\pi}{2P}\right) \tag{214}$$

Furthermore, we have

$$\sum_{p=1}^{P}\exp\left[\mathrm{i}\frac{2n(p-1)\pi}{P}\right] = \sum_{p=0}^{P-1}\left[\exp\left(\mathrm{i}\frac{2n\pi}{P}\right)\right]^p \tag{215}$$

where we recognize a geometric progression.

The summation yields

$$\sum_{p=0}^{P-1}\left[\exp\left(\mathrm{i}\frac{2n\pi}{P}\right)\right]^p = P \qquad \text{if } n \text{ is a multiple of } P \tag{216a}$$

and

$$\sum_{p=0}^{P-1}\left[\exp\left(\mathrm{i}\frac{2n\pi}{P}\right)\right]^{p} = \frac{\exp\left(\mathrm{i}\frac{2nP\pi}{P}\right)-1}{\exp\left(\mathrm{i}\frac{2n\pi}{P}\right)-1} = 0 \qquad \text{otherwise} \qquad (216b)$$

It follows from Eqs. (214), (216a) and (216b) that the sensitivity factors of a $2P$-pole coil array are only non-zero if n is an odd multiple of P. Hence, a $2P$-pole coil array is only sensitive to $[2(2k+1)P]$-pole fields where k is an integer. In particular, the first multipole fields to which a $2P$-pole coil array is sensitive are the $2P$-pole fields. This type of multipole pick-up coil array was first introduced by G. Morgan [175].

7.9 EFFECTS OF IMPERFECTIONS IN PICK-UP COIL ROTATION

7.9.1 NOTATIONS

Let us again consider a rectangular coordinate system $(O,\vec{x},\vec{y},\vec{z})$ and a magnet which, within a cylinder of z-axis and of radius, R_i, produces a two-dimensional magnetic flux density, $\vec{B}$, parallel to the $(\vec{x},\vec{y})$ plane and uniform in z. As in previous sections, let B_x and B_y designate the x- and y-components of $\vec{B}$ and let **B** designate the complex magnetic flux density defined by Eq. (34). Within the cylinder, **B** is a regular analytic function of the complex variable **s** defined by Eq. (33) and can be expanded into the power series given by Eq. (61).

In addition, let us consider a pick-up coil, made up of $N_{\text{pick-up}}$ turns, parallel to the z-axis and uniform in z, and inserted within the cylinder of radius, R_i. Let $\mathbf{s_1}$ and $\mathbf{s_2}$ designate the average positions in the complex plane of the coil wires running parallel to the z-axis and let $L_{\text{pick-up}}$ designate the average lengths of these wires. The coil is designed to rotate with a constant angular velocity, ω, around the z-axis and is equipped with an angle encoder reckoning its angle, θ, with respect to a zero mark. In section 7.4, we have derived the basic equations describing an ideal coil rotation. Let us now study the effects of imperfections in coil rotation.

7.9.2 EFFECTS OF TRANSVERSE DISPLACEMENTS OF ROTATION AXIS

7.9.2.1 Basic Equations

Let us first consider the case where the coil rotation is accompanied by a displacement of the rotation axis, which is parallel to the $(\vec{x},\vec{y})$ plane, and which varies as a function of θ.

Let $\mathbf{D}(\theta)$ designate the position of the rotation axis in the complex plane when the coil is at angle θ. Starting from Eqs. (153a) and (153b), we can write

$$\mathbf{s_1} = \mathbf{s_{1,0}} \exp(\mathrm{i}\theta) + \mathbf{D}(\theta) \tag{217a}$$

and

$$\mathbf{s_2} = \mathbf{s_{2,0}} \exp(\mathrm{i}\theta) + \mathbf{D}(\theta) \tag{217b}$$

where $\mathbf{s_{1,0}}$ and $\mathbf{s_{2,0}}$ designate the nominal values of $\mathbf{s_1}$ and $\mathbf{s_2}$ at $\theta = 0$.

Combining Eqs. (154), (155), (217a) and (217b), the flux, $\phi_{\text{pick-up}}$, picked-up by the coil is

$$\phi_{\text{pick-up}}(\theta) = \mathrm{Re}\left\langle \sum_{n=1}^{+\infty} \frac{N_{\text{pick-up}}\, L_{\text{pick-up}}}{n\, R_{\text{ref}}^{n-1}} \left\{ \left[\mathbf{s_{2,0}} \exp(\mathrm{i}\theta) + \mathbf{D}(\theta)\right]^n - \left[\mathbf{s_{1,0}} \exp(\mathrm{i}\theta) + \mathbf{D}(\theta)\right]^n \right\} (B_n + \mathrm{i}\, A_n) \right\rangle \tag{218}$$

7.9.2.2 Case of a Transverse Displacement in a Pure Dipole Field

Let us assume that the pick-up coil is rotating in a pure dipole field. Then, in the multipole expansion of **B**, only the terms of order 1 are non zero, and Eq. (218) becomes

$$\phi_{\text{pick-up}}(\theta) = \mathrm{Re}\left[N_{\text{pick-up}}\, L_{\text{pick-up}} \left(\mathbf{s_{2,0}} - \mathbf{s_{1,0}}\right)(B_1 + \mathrm{i}\, A_1) \exp(\mathrm{i}\theta)\right] \tag{219}$$

Introducing the definition of the sensitivity factor of order 1, $\mathbf{K_1}$, given by Eq. (155), we get

$$\phi_{\text{pick-up}}(\theta) = \mathrm{Re}\left[\mathbf{K_1} (B_1 + \mathrm{i}\, A_1) \exp(\mathrm{i}\theta)\right] \tag{220}$$

Equation (220) shows that, in a pure dipole field, the flux picked-up by a rotating coil is not distorted by transverse displacements of the rotation axis.

7.9.2.3 Case of a Transverse Displacement in a Pure Quadrupole Field

Let us now assume that the pick-up coil is rotating in a pure quadrupole field. Then, in the multipole expansion of **B**, only the terms of order 2 are non zero, and Eq. (218) becomes

$$\phi_{\text{pick-up}}(\theta) = \mathrm{Re}\left[\frac{N_{\text{pick-up}}\, L_{\text{pick-up}}}{2R_{\text{ref}}} \left(\mathbf{s_{2,0}^2} - \mathbf{s_{1,0}^2}\right)(B_2 + \mathrm{i}\, A_2) \exp(\mathrm{i}2\theta)\right]$$

$$+ \mathrm{Re}\left[N_{\text{pick-up}}\, L_{\text{pick-up}} \left(\mathbf{s}_{2,0} - \mathbf{s}_{1,0}\right) \frac{\mathbf{D}(\theta)}{R_{\text{ref}}} \left(B_2 + \mathrm{i}\, A_2\right) \exp\left(\mathrm{i}\theta\right) \right] \tag{221}$$

Introducing the definitions of the sensitivity factors of order 1 and 2, $\mathbf{K_1}$ and $\mathbf{K_2}$, given by Eq. (155), we get

$$\phi_{\text{pick-up}}(\theta) = \mathrm{Re}\left[\mathbf{K_2} \left(B_2 + \mathrm{i}\, A_2\right) \exp\left(\mathrm{i}2\theta\right)\right] + \mathrm{Re}\left[\mathbf{K_1} \frac{\mathbf{D}(\theta)}{R_{\text{ref}}} \left(B_2 + \mathrm{i}\, A_2\right) \exp\left(\mathrm{i}\theta\right) \right] \tag{222}$$

Equation (222) shows that, in a pure quadrupole field, the flux picked-up by a rotating coil is distorted by transverse displacements of the rotation axis, and the distortions are proportional to the sensitivity factor of order 1, $\mathbf{K_1}$.

7.9.2.4 Case of a Periodic Transverse Displacement in a Pure Quadrupole Field

Let us further assume that $\mathbf{D}$ is an entire and periodic function, with a period equal to (2π). Then, it can be expanded into a Fourier series of the form (p. 141 of Ref. [176])

$$\mathbf{D}(\theta) = \sum_{p=-\infty}^{+\infty} \mathbf{D_p} \exp\left(\mathrm{i}p\theta\right) \tag{223}$$

where $\mathbf{D_p}$ is the constant and complex Fourier coefficient of order p.

Then, we have

$$\mathbf{D}(\theta)\exp\left(\mathrm{i}\theta\right) = \sum_{p=2}^{+\infty} \mathbf{D_{-p}} \exp\left[-\mathrm{i}(p-1)\theta\right] + \mathbf{D_{-1}} + \sum_{p=0}^{+\infty} \mathbf{D_p} \exp\left[\mathrm{i}(p+1)\theta\right] \tag{224}$$

By combining Eqs. (222) and (224), we get

$$\phi_{\text{pick-up}}(\theta) = \mathrm{Re}\left[\mathbf{K_2} \left(B_2 + \mathrm{i}\, A_2\right) \exp\left(\mathrm{i}2\theta\right)\right] + \mathrm{Re}\left\{ \sum_{p=2}^{+\infty} \mathbf{K_1} \frac{\mathbf{D_{-p}}}{R_{\text{ref}}} \left(B_2 + \mathrm{i}\, A_2\right) \exp\left[-\mathrm{i}(p-1)\theta\right] \right\}$$
$$+ \mathrm{Re}\left[\mathbf{K_1} \frac{\mathbf{D_{-1}}}{R_{\text{ref}}} \left(B_2 + \mathrm{i}\, A_2\right) \right] + \mathrm{Re}\left\{ \sum_{p=0}^{+\infty} \mathbf{K_1} \frac{\mathbf{D_p}}{R_{\text{ref}}} \left(B_2 + \mathrm{i}\, A_2\right) \exp\left[\mathrm{i}(p+1)\theta\right] \right\} \tag{225}$$

Let us define the real constant, c_{D}, as

$$c_{\mathrm{D}} = \mathrm{Re}\left[\mathbf{K_1} \frac{\mathbf{D_{-1}}}{R_{\text{ref}}} \left(B_2 + \mathrm{i}\, A_2\right) \right] \tag{226}$$

and let us use the fact that the real part of a complex number is equal to the real part of its conjugate. Then, we can write

$$\mathrm{Re}\left\{\sum_{p=2}^{+\infty} \mathbf{K_1} \frac{\mathbf{D_{-p}}}{R_{\mathrm{ref}}} (B_2 + \mathrm{i}\, A_2) \exp[-\mathrm{i}(p-1)\theta]\right\} = \mathrm{Re}\left\{\sum_{p=2}^{+\infty} \mathbf{K_1^*} \frac{\mathbf{D^*_{-p}}}{R_{\mathrm{ref}}} (B_2 - \mathrm{i}\, A_2) \exp[\mathrm{i}(p-1)\theta]\right\} \tag{227}$$

Furthermore, let us note that

$$\sum_{p=2}^{+\infty} \mathbf{K_1^*} \frac{\mathbf{D^*_{-p}}}{R_{\mathrm{ref}}} (B_2 - \mathrm{i}\, A_2) \exp[\mathrm{i}(p-1)\theta] = \sum_{p=1}^{+\infty} \mathbf{K_1^*} \frac{\mathbf{D^*_{-p-1}}}{R_{\mathrm{ref}}} (B_2 - \mathrm{i}\, A_2) \exp(\mathrm{i}p\theta) \tag{228a}$$

and that

$$\sum_{p=0}^{+\infty} \mathbf{K_1} \frac{\mathbf{D_p}}{R_{\mathrm{ref}}} (B_2 + \mathrm{i}\, A_2) \exp[\mathrm{i}(p+1)\theta] = \sum_{p=1}^{+\infty} \mathbf{K_1} \frac{\mathbf{D_{p-1}}}{R_{\mathrm{ref}}} (B_2 + \mathrm{i}\, A_2) \exp(\mathrm{i}p\theta) \tag{228b}$$

By combining Eqs. (225), (226), (227), (228a) and (228b), we get

$$\phi_{\text{pick-up}}(\theta_{\mathrm{m}}) \approx \mathrm{Re}[\mathbf{K_2} (B_2 + \mathrm{i}\, A_2) \exp(\mathrm{i}2\theta)] + \mathrm{Re}\left[\sum_{p=1}^{+\infty} \mathbf{K_p} \left(B_{\mathrm{p}}^{\mathrm{s}} + \mathrm{i}\, A_{\mathrm{p}}^{\mathrm{s}}\right) \exp(\mathrm{i}p\theta)\right] + c_{\mathrm{D}} \tag{229}$$

where

$$B_{\mathrm{p}}^{\mathrm{s}} + \mathrm{i}\, A_{\mathrm{p}}^{\mathrm{s}} = \frac{\mathbf{K_1}}{\mathbf{K_p}} \frac{\mathbf{D_{p-1}}}{R_{\mathrm{ref}}} (B_2 + \mathrm{i}\, A_2) + \frac{\mathbf{K_1^*}}{\mathbf{K_p}} \frac{\mathbf{D^*_{-p-1}}}{R_{\mathrm{ref}}} (B_2 - \mathrm{i}\, A_2) \quad \text{for } p,\ 1 \le p \tag{230}$$

Equation (230) resembles Eq. (154), and $A_{\mathrm{p}}^{\mathrm{s}}$ and $B_{\mathrm{p}}^{\mathrm{s}}$ can be interpreted as *spurious multipole field coefficients*, which are superimposed to the genuine multipole field coefficients and which result from transverse displacements of the rotation axis. Note that $A_{\mathrm{p}}^{\mathrm{s}}$ and $B_{\mathrm{p}}^{\mathrm{s}}$ are directly proportional to the sensitivity factor of order 1.

7.9.2.5 Case of a Translation in a Pure Quadrupole Field

Let us now assume that the transverse displacement of the rotation axis is a simple translation, independent of θ.

Then the Fourier expansion of $\mathbf{D}(\theta)$ reduces to

$$\mathbf{D}(\theta) = \mathbf{D_0} \tag{231}$$

where $\mathbf{D_0}$ is the complex Fourier coefficient of order 0.

It follows from Eqs. (229) and (230) that, when measuring a pure quadrupole field, a translation of the rotation axis generates spurious dipole field coefficients, where

$$B_1^s + \mathrm{i}\, A_1^s = \frac{\mathbf{D_0}}{R_{\mathrm{ref}}}\left(B_2 + \mathrm{i}\, A_2\right) \tag{232}$$

The above equation is consistent with Eq. (74).

7.9.2.6 Case of a Cos(pθ) Displacement in a Pure Quadrupole Field

Let us now assume that the transverse displacement of the rotation axis is of the form

$$\mathbf{D}(\theta) = \mathbf{D_{max}} \cos(p\theta) \tag{233}$$

where $\mathbf{D_{max}}$ is a complex constant.

Then, the Fourier expansion of $\mathbf{D}(\theta)$ reduces to

$$\mathbf{D}(\theta) = \mathbf{D_{-p}} \exp(-\mathrm{i}p\theta) + \mathbf{D_p} \exp(\mathrm{i}p\theta) \tag{234}$$

where

$$\mathbf{D_{-p}} = \mathbf{D_p} = \frac{\mathbf{D_{max}}}{2} \tag{235}$$

It follows from Eqs. (229) and (230) that, when measuring a pure quadrupole field, transverse displacements of the rotation axis in $\cos(p\theta)$ generate spurious multipole fields of order $(p+1)$ and $(p-1)$, where

$$B_{p+1}^s + \mathrm{i}\, A_{p+1}^s = \frac{\mathbf{K_1}}{\mathbf{K_{p+1}}} \frac{\mathbf{D_{max}}}{2R_{\mathrm{ref}}}\left(B_2 + \mathrm{i}\, A_2\right) \qquad \text{for } p,\ 1 \le p \tag{236a}$$

and

$$B_{p-1}^s + \mathrm{i}\, A_{p-1}^s = \frac{\mathbf{K_1^*}}{\mathbf{K_{p-1}}} \frac{\mathbf{D_{max}^*}}{2R_{\mathrm{ref}}}\left(B_2 - \mathrm{i}\, A_2\right) \qquad \text{for } p,\ 2 \le p \tag{236b}$$

The above equations are consistent with the results given in Appendix A of Ref. [11].

7.9.2.7 Case of a Sin(pθ) Displacement in a Pure Quadrupole Field

Let us now assume that the transverse displacement of the rotation axis is of the form

$$\mathbf{D}(\theta) = \mathbf{D_{max}} \sin(p\theta) \tag{237}$$

where $\mathbf{D_{max}}$ is again a complex constant.

Then, the Fourier expansion of $\mathbf{D}(\theta)$ also reduces to Eq. (234) with

$$\mathbf{D_p} = -\mathbf{D_{-p}} = \frac{\mathbf{D_{max}}}{2\mathrm{i}} \tag{238}$$

Similarly to the $\cos(p\theta)$ case, it follows from Eqs. (229) and (230) that when measuring a pure quadrupole field, transverse displacements of the rotation axis in $\sin(p\theta)$ generate spurious multipole fields of order $(p+1)$ and $(p-1)$, where

$$B^s_{p+1} + \mathrm{i}\, A^s_{p+1} = \frac{\mathbf{K_1}}{\mathbf{K_{p+1}}} \frac{\mathbf{D_{max}}}{2R_{ref}} (A_2 - \mathrm{i}\, B_2) \qquad \text{for } p,\ 1 \le p \tag{239a}$$

and

$$B^s_{p-1} + \mathrm{i}\, A^s_{p-1} = -\frac{\mathbf{K_1^*}}{\mathbf{K_{p-1}}} \frac{\mathbf{D^*_{max}}}{2R_{ref}} (A_2 + \mathrm{i}\, B_2) \qquad \text{for } p,\ 2 \le p \tag{239b}$$

7.9.2.8 Case of a Transverse Displacement in a Pure 2n-Pole Field

Let us finally assume that the pick-up coil is rotating in a pure $2n$-pole field, where n, $n \ge 2$. Then, in the multipole expansion of $\mathbf{B}$, only the terms of order n are non zero, and Eq. (218) yields

$$\phi_{\text{pick-up}}(\theta) = \mathrm{Re}\left\{ \sum_{p=0}^{n} \mathrm{C}_n^p \frac{N_{\text{pick-up}}\, L_{\text{pick-up}}}{n R_{ref}^{n-1}} \left[(\mathbf{s_{2,0}})^{n-p} - (\mathbf{s_{1,0}})^{n-p} \right] [\mathbf{D}(\theta)]^p \, (B_n + \mathrm{i}\, A_n) \exp[\mathrm{i}(n-p)\theta] \right\} \tag{240}$$

Introducing the definition of the sensitivity factor of order $(n\text{-}p)$, $\mathbf{K_{n-p}}$, we get

$$\phi_{\text{pick-up}}(\theta) = \mathrm{Re}[\mathbf{K_n} (B_n + \mathrm{i}\, A_n) \exp(\mathrm{i}n\theta)] + \mathrm{Re}\left\{ \sum_{p=1}^{n} \mathrm{C}_{n-1}^p \mathbf{K_{n-p}} \left[\frac{\mathbf{D}(\theta)}{R_{ref}} \right]^p (B_n + \mathrm{i}\, A_n) \exp[\mathrm{i}(n-p)\theta] \right\} \quad \text{for } n,\ 2 \le n \tag{241}$$

Equation (241) shows that, in a pure $2n$-pole field, the flux picked-up by a rotating coil is distorted by transverse displacements of the rotation axis, and the distortions are proportional to the sensitivity factors of order lower than $(n\text{-}1)$.

7.9.3 Effects of Angular Shifts Between Angle Encoder and Coil

7.9.3.1 Basic Equations

Let us now consider the case where there is a shift between the angle measured by the angle encoder, θ_m, and the coil angle, θ, which varies as a function of θ_m.

Let $\vartheta(\theta_m)$ designate the angular shift, defined as

$$\vartheta(\theta_m) = \theta - \theta_m \tag{242}$$

Starting again from Eqs. (153a) and (153b), we can write

$$\mathbf{s_1} = \mathbf{s_{1,0}} \exp[i\vartheta(\theta_m)] \exp(i\theta_m) \tag{243a}$$

and

$$\mathbf{s_2} = \mathbf{s_{2,0}} \exp[i\vartheta(\theta_m)] \exp(i\theta_m) \tag{243b}$$

Combining Eqs. (154), (155), (243a) and (243b), the flux, $\phi_{\text{pick-up}}$, picked-up by the coil is

$$\phi_{\text{pick-up}}(\theta_m) = \text{Re}\left\{\sum_{n=1}^{+\infty} \frac{N_{\text{pick-up}}\, L_{\text{pick-up}}}{n\, R_{\text{ref}}^{n-1}} \left(\mathbf{s}_{\mathbf{2,0}}^{n} - \mathbf{s}_{\mathbf{1,0}}^{n}\right) \exp[in\vartheta(\theta_m)](B_n + i\, A_n) \exp(in\theta_m)\right\} \tag{244}$$

Introducing the definitions of the sensitivity factors given by Eq. (155), we get

$$\phi_{\text{pick-up}}(\theta_m) = \text{Re}\left\{\sum_{n=1}^{+\infty} \mathbf{K_n} \exp[in\vartheta(\theta_m)](B_n + i\, A_n) \exp(in\theta_m)\right\} \tag{245}$$

Note that if the angular shift is constant

$$\vartheta(\theta_m) = \Delta\theta \tag{246}$$

Eq. (245) then shows that, compared to Eq. (154), the multipole field coefficients are rotated by an angle $(n\Delta\theta)$. This result is consistent with Eq. (78).

7.9.3.2 Case of a Pure 2n-Pole Field

To simplify the formalism, let us assume that the pick-up coil is rotating in a pure $2n$-pole field.

Then, in the multipole expansion of **B**, only the terms of order n are non zero, and Eq. (245) becomes

$$\phi_{\text{pick-up}}(\theta_{\text{m}}) = \text{Re}\left\{\mathbf{K_n} \exp\left[in\,\vartheta(\theta_{\text{m}})\right](B_{\text{n}} + \text{i}\,A_{\text{n}})\exp(in\theta_{\text{m}})\right\} \tag{247}$$

Furthermore, we have

$$\exp\left[in\,\vartheta(\theta_{\text{m}})\right] = 1 + \sum_{p=1}^{+\infty} \frac{\left[in\,\vartheta(\theta_{\text{m}})\right]^p}{p} \tag{248}$$

By combining Eqs. (247) and (248), we get

$$\phi_{\text{pick-up}}(\theta_{\text{m}}) = \text{Re}\left[\mathbf{K_n}(B_{\text{n}} + \text{i}\,A_{\text{n}})\exp(in\theta_{\text{m}})\right]$$

$$+ \text{Re}\left\langle n\,\mathbf{K_n}\vartheta(\theta_{\text{m}})\left\{\sum_{p=1}^{+\infty}\frac{\left[in\,\vartheta(\theta_{\text{m}})\right]^{p-1}}{p}\right\}(-A_{\text{n}} + \text{i}\,B_{\text{n}})\exp(in\theta_{\text{m}})\right\rangle \tag{249}$$

Equation (249) shows that, in a pure $2n$-pole field, the flux picked-up by a rotating coil is distorted by shifts between the angle measured by the angle encoder and the coil angle, and the distortions are proportional to the sensitivity factor of order n, $\mathbf{K_n}$.

7.9.3.3 Approximation for Small Angular Shifts

Let us now assume that the amplitude of $\vartheta(\theta_{\text{m}})$ is small. Then, we can write

$$\exp\left[in\,\vartheta(\theta_{\text{m}})\right] \approx 1 + \text{i}\,n\,\vartheta(\theta_{\text{m}}) \tag{250}$$

and Eq. (249) reduces to

$$\phi_{\text{pick-up}}(\theta_{\text{m}}) \approx \text{Re}\left[\mathbf{K_n}(B_{\text{n}} + \text{i}\,A_{\text{n}})\exp(in\theta_{\text{m}})\right] + \text{Re}\left[n\,\mathbf{K_n}\vartheta(\theta_{\text{m}})(-A_{\text{n}} + \text{i}\,B_{\text{n}})\exp(in\theta_{\text{m}})\right] \tag{251}$$

7.9.3.4 Approximation for Small, Periodic Angular Shifts

Let us further assume that the angular shift is small and periodic, with a period equal to (2π).

Then, the function $\mathcal{G}(\theta_m)$ can be expanded into a Fourier series of the form

$$\mathcal{G}(\theta_m) = \sum_{p=-\infty}^{+\infty} \mathcal{G}_{\mathbf{p}} \exp(ip\theta_m) \tag{252}$$

where $\mathcal{G}_{\mathbf{p}}$ is the constant and complex Fourier coefficient of order p.

Then, we have

$$\mathcal{G}(\theta_m)\exp(in\theta_m) = \sum_{p=n+1}^{+\infty} \mathcal{G}_{-\mathbf{p}} \exp[-i(p-n)\theta_m] + \mathcal{G}_{-\mathbf{n}} + \sum_{p=-(n-1)}^{+\infty} \mathcal{G}_{\mathbf{p}} \exp[i(p+n)\theta_m] \tag{253}$$

By combining Eqs. (251) and (253), we get

$$\begin{aligned} \phi_{\text{pick-up}}(\theta_m) \approx\ & \mathrm{Re}\left[\mathbf{K_n}(B_n + i\,A_n)\exp(in\theta_m)\right] \\ & + \mathrm{Re}\left\{\sum_{p=n+1}^{+\infty} n\mathbf{K_n}\mathcal{G}_{-\mathbf{p}}(-A_n + i\,B_n)\exp[-i(p-n)\theta_m]\right\} + \mathrm{Re}\left[n\mathbf{K_n}\mathcal{G}_{-\mathbf{n}}(-A_n + i\,B_n)\right] \\ & + \mathrm{Re}\left\{\sum_{p=-(n-1)}^{+\infty} n\mathbf{K_n}\mathcal{G}_{\mathbf{p}}(-A_n + i\,B_n)\exp[i(p+n)\theta_m]\right\} \end{aligned} \tag{254}$$

Let us define the real constant, $c_{\mathcal{G}}$, as

$$c_{\mathcal{G}} = \mathrm{Re}\left[n\mathbf{K_n}\mathcal{G}_{-\mathbf{n}}(-A_n + i\,B_n)\right] \tag{255}$$

and let us again use the fact that the real part of a complex number is equal to the real part of its conjugate. Then, we can write

$$\begin{aligned} \mathrm{Re}\left\{\sum_{p=n+1}^{+\infty} n\mathbf{K_n}\mathcal{G}_{-\mathbf{p}}(-A_n + i\,B_n)\exp[-i(p-n)\theta_m]\right\} = \\ - \mathrm{Re}\left\{\sum_{p=n+1}^{+\infty} n\mathbf{K_n^*}\mathcal{G}_{-\mathbf{p}}^*(A_n + i\,B_n)\exp[i(p-n)\theta_m]\right\} \end{aligned} \tag{256}$$

Furthermore, let us note that

$$\sum_{p=n+1}^{+\infty} n\mathbf{K_n^*}\mathcal{G}_{-\mathbf{p}}^*(A_n + i\,B_n)\exp[i(p-n)\theta_m] = \sum_{p=1}^{+\infty} n\mathbf{K_n^*}\mathcal{G}_{-\mathbf{n}-\mathbf{p}}^*(A_n + i\,B_n)\exp[ip\theta_m] \tag{257a}$$

and that

$$\sum_{p=-(n-1)}^{+\infty} n\mathbf{K_n}\vartheta_{\mathbf{p}}(-A_n + \mathrm{i}\,B_n)\exp[\mathrm{i}(p+n)\theta_m] = \sum_{p=1}^{+\infty} n\mathbf{K_n}\vartheta_{\mathbf{p-n}}(-A_n + \mathrm{i}\,B_n)\exp(\mathrm{i}p\theta_m) \tag{257b}$$

By combining Eqs. (254), (255), (256), (257a) and (257b), we get

$$\phi_{\text{pick-up}}(\theta_m) \approx \mathrm{Re}[\mathbf{K_n}(B_n + \mathrm{i}\,A_n)\exp(\mathrm{i}n\theta_m)] + \mathrm{Re}\left[\sum_{p=1}^{+\infty} \mathbf{K_p}\left(B_p^s + \mathrm{i}\,A_p^s\right)\exp(\mathrm{i}p\theta_m)\right] + c_\vartheta \tag{258}$$

where

$$B_p^s + \mathrm{i}\,A_p^s = \frac{n\mathbf{K_n}}{\mathbf{K_p}}\vartheta_{\mathbf{p-n}}(-A_n + \mathrm{i}\,B_n) - \frac{n\mathbf{K_n^*}}{\mathbf{K_p}}\vartheta^*_{\mathbf{-n-p}}(A_n + \mathrm{i}\,B_n) \qquad \text{for } p,\ 1 \le p \tag{259}$$

Similarly to Eq. (229), Eq. (258), which is consistent with the results given in Ref. [174], resembles Eq. (154), and A_p^s and B_p^s can be interpreted as *spurious multipole field coefficients*, which are superimposed to the genuine multipole field coefficients, and which result from the angular shifts. Note that, in the present case, A_p^s and B_p^s are directly proportional to the sensitivity factor of order n.

7.9.3.5 Case of Small Angular Shifts in Cos($p\theta_m$)

Let us now assume that the angular shifts are small and of the form

$$\vartheta(\theta_m) = \vartheta_{max}\cos(p\theta_m) \tag{260}$$

where ϑ_{max} is a constant.

Then, the Fourier expansion of $\vartheta(\theta_m)$ reduces to

$$\vartheta(\theta_m) = \vartheta_{\mathbf{-p}}\exp(-\mathrm{i}p\theta_m) + \vartheta_{\mathbf{p}}\exp(\mathrm{i}p\theta_m) \tag{261}$$

where

$$\vartheta_{\mathbf{-p}} = \vartheta_{\mathbf{p}} = \frac{\vartheta_{max}}{2} \tag{262}$$

It follows from Eqs. (258) and (259) that, when measuring a pure $2n$-pole field, angular shifts in $\cos(p\theta_m)$ generate spurious multipole fields of order $(p+n)$ and $(p-n)$, where

$$B^s_{p+n} + i\,A^s_{p+n} = \frac{n\mathbf{K_n}}{\mathbf{K_{p+n}}}\frac{\vartheta_{max}}{2}\left(-A_n + i\,B_n\right) \qquad \text{for } p,\ 1 \le p \qquad (263a)$$

and

$$B^s_{p-n} + i\,A^s_{p-n} = -\frac{n\mathbf{K}^*_{\mathbf{n}}}{\mathbf{K_{p-n}}}\frac{\vartheta_{max}}{2}\left(A_n + i\,B_n\right) \qquad \text{for } p,\ n+1 \le p \qquad (263b)$$

Equations (263a) and (263b) are consistent with the results given in Refs. [177] and [178].

7.9.3.6 Case of Small Angular Shifts in Sin($p\theta_m$)

Let us finally assume that the angular shifts are small and of the form

$$\vartheta(\theta_m) = \vartheta_{max}\sin(p\theta_m) \qquad (264)$$

where ϑ_{max} is a constant.

Then, the Fourier expansion of $\vartheta(\theta_m)$ also reduces to Eq. (261), with

$$\vartheta_{\mathbf{p}} = -\vartheta_{\mathbf{-p}} = \frac{\vartheta_{max}}{2i} \qquad (265)$$

Similarly to the $\cos(p\theta_m)$ case, it follows from Eqs. (258) and (259) that, when measuring a pure $2n$-pole field, angular shifts in $\sin(p\theta_m)$ generate spurious multipole fields of order $(p+n)$ and $(p-n)$, where

$$B^s_{p+n} + i\,A^s_{p+n} = \frac{n\mathbf{K_n}}{\mathbf{K_{p+n}}}\frac{\vartheta_{max}}{2}\left(B_n + i\,A_n\right) \qquad \text{for } p,\ 1 \le p \qquad (266a)$$

and

$$B^s_{p-n} + i\,A^s_{p-n} = \frac{n\mathbf{K}^*_{\mathbf{n}}}{\mathbf{K_{p-n}}}\frac{\vartheta_{max}}{2}\left(-B_n + i\,A_n\right) \qquad \text{for } p,\ n+1 \le p \qquad (266b)$$

Equations (266a) and (266b) are also consistent with the results given in Refs. [177] and [178].

7.9.4 Origins of Spurious Quadrupole Fields in a Pure Dipole Field Measured with a Rotating Pick-Up Coil

Let us consider a pick-up coil rotating in a pure dipole field and let us review the possible causes of spurious quadrupole fields.

Taking $n = 1$ and $p = 2$ in Eq. (259), we get

$$B_2^s + \mathrm{i}\, A_2^s = \frac{\mathbf{K_1}}{\mathbf{K_2}} \vartheta_1 (-A_1 + \mathrm{i}\, B_1) - \frac{\mathbf{K_1^*}}{\mathbf{K_2}} \vartheta_{-3}^* (A_1 + \mathrm{i}\, B_1) \tag{267}$$

Equation (267) shows that, when measuring a pure dipole field, spurious quadrupole fields can arise from small, periodic shifts between the angle measured by the angle encoder and the actual pick-up coil angle, which, in their Fourier expansions, have a non-zero coefficient of order 1, ϑ_1, such as in $\cos(\theta)$, or a non-zero coefficient of order (–3), ϑ_{-3}, such as in $\cos(3\theta)$.

7.9.5 Origins of Spurious Sextupole Fields in a Pure Quadrupole Field Measured with a Rotating Pick-Up Coil

Let us now consider a pick-up coil rotating in a pure quadrupole field and let us review the possible causes of spurious sextupole fields.

Taking $n = 2$ and $p = 3$ in Eq. (230), we get

$$B_3^s + \mathrm{i}\, A_3^s = \frac{\mathbf{K_1}}{\mathbf{K_3}} \frac{\mathbf{D_2}}{R_{\mathrm{ref}}} (B_2 + \mathrm{i}\, A_2) + \frac{\mathbf{K_1^*}}{\mathbf{K_3}} \frac{\mathbf{D_{-4}^*}}{R_{\mathrm{ref}}} (B_2 - \mathrm{i}\, A_2) \tag{268}$$

Equation (268) shows that, when measuring a pure quadrupole field, spurious sextupole fields can arise from transverse, periodic displacements of the pick-up coil rotation axis, which, in their Fourier expansions, have a non-zero coefficient of order 2, $\mathbf{D_2}$, such as in $\cos(2\theta)$, or a non-zero coefficient of order (–4), $\mathbf{D_{-4}}$, such as in $\cos(4\theta)$.

Similarly, taking $n = 2$ and $p = 3$ in Eq. (259), we get

$$B_3^s + \mathrm{i}\, A_3^s = \frac{2\,\mathbf{K_2}}{\mathbf{K_3}} \vartheta_1 (-A_2 + \mathrm{i}\, B_2) - \frac{2\,\mathbf{K_2^*}}{\mathbf{K_3}} \vartheta_{-5}^* (A_2 + \mathrm{i}\, B_2) \tag{269}$$

Equation (269) shows that, when measuring a pure quadrupole field, spurious sextupole fields can arise also from small, periodic shifts between the angle measured by the angle encoder and the actual pick-up coil angle, which, in their Fourier expansions, have a non-zero coefficient of order 1, ϑ_1, such as in $\cos(\theta)$, or a non-zero coefficient of order (–5), ϑ_{-5}, such as in $\cos(5\theta)$.

8 FIELD QUALITY OF PARTICLE ACCELERATOR MAGNETS

8.1 MULTIPOLE EXPANSION

Except near the short coil ends, the magnetic flux density produced in the bore of a particle accelerator magnet can be considered as two-dimensional. In practice, the power series expansion of Eq. (61) is usually rewritten under the more convenient form

$$B_y + iB_x = B_{ref}\, 10^{-4} \sum_{n=1}^{+\infty} (b_n + i\, a_n) \left(\frac{\mathbf{s}}{R_{ref}} \right)^{n-1} \qquad \text{for } \mathbf{s} = x + iy,\ |\mathbf{s}| < R_i \qquad (270)$$

where B_{ref} is the absolute value of the dipole or quadrupole component at R_{ref}, a_n and b_n are the dimensionless skew and normal $2n$-pole coefficients expressed in so-called *units*, and R_i is the coil inner radius. Note the presence of the 10^{-4} scale factor.

Given the symmetries of current distributions in magnet coil assemblies, and as explained in sections 4.9 and 5.1, only selected normal multipole coefficients are expected to be non-zero. These allowed multipole coefficients can be tuned up by iterating on the electromagnetic design. In practice, however, non-uniformities in material properties and manufacturing errors result in symmetry violations, which produce *un-allowed* multipole coefficients. For instance, a top/bottom asymmetry in a dipole magnet produces a non-zero skew quadrupole coefficient (a_2), while a left/right asymmetry produces a non-zero normal quadrupole coefficient (b_2). These unwanted coefficients can only be eliminated by improving material selection, tooling and assembly procedures.

8.2 FIELD QUALITY REQUIREMENTS

From the accelerator point of view, the beam optics is primarily governed by integrated field effects over the magnet ring. The main field quality requirements are: (1) suitable dipole field integral and small dipole field angle variations [the former to ensure that the integrated bending angle over the magnet ring is (2π) and the latter to ensure that the particle trajectory is planar], (2) accurate quadrupole alignment and suitable quadrupole field integral (the former to avoid coupling of particle motions along the x- and y-axes and the latter to ensure proper focusing), and (3) small high order multipole coefficients (to ensure large beam dynamic aperture).

In the case of high order multipole coefficients, it is customary to specify tables of mean values and standard deviations over the entire magnet population [179]. The tables of mean values are referred to as *systematic* multipole specifications whereas those of standard

deviations are referred to as *random* multipole specifications. The specified values are all expressed at the reference radius, R_{ref}.

In large machines such as SSC or LHC, the dipole and quadrupole field integrals must be controlled with a relative precision of the order of 10^{-3}. The variations in dipole field angles must be kept within a few milli-radians and the tolerance on quadrupole alignment is of the order of 0.1 mm. Systematic and random multipole specifications are given up to the 18th or 20th pole and get tighter with increasing pole order. For SSC magnets at 10 mm, the specifications went from a few tenths of a unit for low order coefficients to a few thousandths of a unit for higher order coefficients.

8.3 FIELD QUALITY MEASUREMENTS

8.3.1 MAGNETIC MEASUREMENT SYSTEMS

In order to verify that the magnets satisfy field quality requirements, various types of magnetic measurements must be performed, either warm, on-line with magnet production, or cold, before installation in the tunnel. Among them are: (1) field integral measurements, (2) field angle measurements, and (3) high order multipole coefficients measurements.

The magnetic measurement systems the most commonly used are rotating arrays of radial and/or tangential pick-up coils, such as the ones described in section 7.8 (Appendix A of Reference [11], [177], [178]). Such systems are well suited to the determination of high order multipole coefficients, but can also be carefully calibrated to measure the main field component with a sufficient accuracy. In addition, they can be equipped with a system reckoning their position with respect to a known reference for field angle measurements.

Other magnetic measurement equipments include NMR-Hall probe arrays for the measurements of dipole field strength and dipole field integrals [180] and stretched wire systems for the measurements of field integrals and average field angles (Appendix B of Reference [11]).

8.3.2 FIELD ERRORS CLASSIFICATION

The field errors can be classified into five main categories: (1) errors related to *cold mass geometry*, (2) errors related to *saturation effects*, (3) errors related to *superconductor magnetization*, (5) errors related to *time drifts of superconductor* magnetization during the injection phase, and (5) errors related to *interstrand coupling currents* during magnet ramping.

The geometric errors are studied by performing measurements as a function of axial position at a constant transport current (low enough to avoid saturation effects, but high enough to avoid significant time drifts). The effects of saturation and of superconductor magnetization are studied by performing measurements as a function of current at a slow ramp rate (to avoid interstrand coupling current effects). The time drift of the multipole coefficients are studied by performing measurements as a function of time at the injection current, while the effects of interstrand coupling currents are studied by performing measurements as a function of current at varying ramp rates.

8.4 GEOMETRIC ERRORS

8.4.1 TYPES OF GEOMETRIC ERRORS

The specifications on multipole coefficients require that the individual conductors and the yoke surrounding the coil assembly be positioned with a very good accuracy (typically: a few hundredths of a millimeter in the two-dimensional cross-section). Improper positioning results in geometric errors that distort the central field and produce unwanted coefficients.

The geometric errors can be classified in at least five categories: (1) errors in coil inner and outer radii and in yoke inner radius, (2) errors in coil pole angle, wedge angle and conductor angular distribution, (3) symmetry violations in coil assembly, (4) centering errors with respect to the iron yoke, and (5) residual twist of magnet assembly.

8.4.2 EFFECTS OF AZIMUTHAL COIL SIZE MISMATCH

A common cause of geometric error is a mismatch between the azimuthal sizes of the various coils making up a coil assembly. Such mismatch results in displacements of the coil assembly symmetry planes, which produce non-zero, low order un-allowed multipole coefficients [181]. For instance, a mismatch between the azimuthal sizes of the top and bottom coils used in a dipole magnet coil assembly causes an upward or downward displacement of the coil parting planes which produces a non-zero skew quadrupole coefficient (a_2). Similarly, a systematic mismatch between the left and right sides of the coils used in a dipole magnet coil assembly causes a rotation of the coil parting planes which produces a non-zero skew sextupole coefficient (a_3). A systematic a_2 can be limited by randomly mixing coil production, whereas the occurrence of a systematic a_3 can only be avoided by correcting tooling.

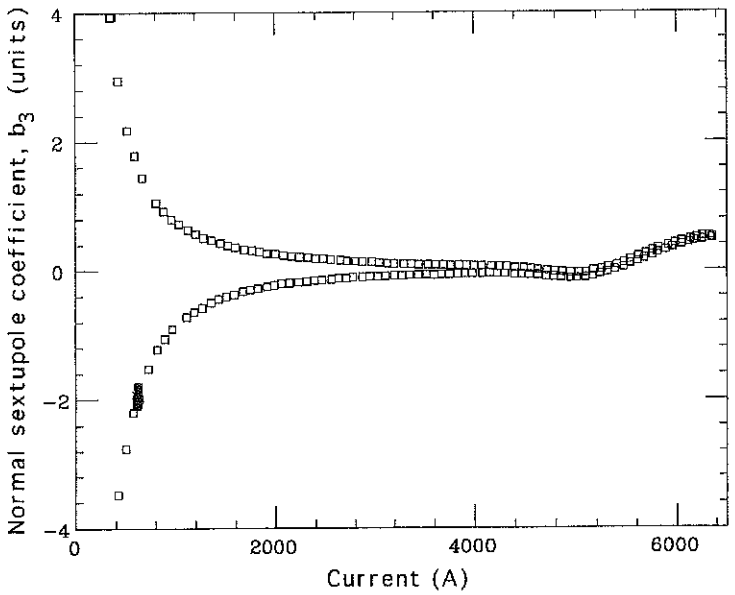

Figure 51. Measurements of normal sextupole coefficient (b_3) as a function of current in the central part of a SSC dipole magnet showing the hysteresis resulting from superconductor magnetization and the distortions at high currents resulting from iron saturation.

8.5 IRON SATURATION

When the magnetic flux density in the iron yoke is less than 2 T, the relative magnetic permeability of the yoke can be considered as very large and uniform, and the iron contribution to the central field increases linearly as a function of transport current in the magnet coil. For magnetic flux densities above 2 T, parts of the iron start to saturate and their relative magnetic permeability drops. As a result, the iron contribution becomes a less-than-linear function of transport current. This relative decrease in iron contribution appears as a sag in the magnet transfer function [158]. (The transfer function is defined as the ratio of B_{ref} to the transport current). The transfer function sag can exceed a few percents in dipole magnets but is usually negligible in quadrupole magnets.

In the case of a single aperture magnet with a symmetrical iron yoke, the saturation first occurs in the pole areas producing a positive shift in normal sextupole coefficient (b_3). At higher currents, the saturation reaches the midplane areas, producing a negative shift in b_3, which partially compensates for the effects of pole saturation. The midplane saturation can be forced to occur sooner by punching notches (*i.e.*, removing matter) at appropriate locations in the yoke, or by giving an elliptical shape to the yoke inner boundary. As an illustration, Figure 51 presents measurements of b_3 as a function of current in the central part of a SSC dipole magnet prototype. The measurements above 3 kA clearly show the effect of pole saturation at high currents (the origin of the hysteresis is explained in the next section).

In the case of a twin-aperture dipole, the central part of the yoke saturates before the outer parts, resulting in left/right asymmetries in the yoke contributions to each aperture which affect the normal quadrupole coefficient (b_2). The saturation effects in b_2 are of opposite sign in the two apertures.

In any case, the iron contribution depends on the packing factor of the yoke laminations, which must be tightly controlled over the magnet length. Also, the iron yoke must be carefully aligned to limit magnet assembly twist.

8.6 SUPERCONDUCTOR MAGNETIZATION

8.6.1 CRITICAL STATE MODEL

According to the so-called *critical state model*, bipolar magnetization currents are induced at the periphery of the superconducting filaments in the cable strands each time the field to which the filaments are exposed is varied [182]. The magnetization currents distribute themselves with a density equal to the superconductor critical current density at the given temperature and field, J_C, in order to screen the filament cores from the applied field change. Unlike regular eddy currents, the magnetization currents do not depend on the rate of field variations. Also, because they can flow with zero resistance, they do not decay as soon as the field ramp is stopped. They are called *persistent magnetization currents*.

8.6.2 EFFECTS OF SUPERCONDUCTOR MAGNETIZATION

When an accelerator magnet is cycled in current, the bipolar shells of magnetization currents induced in the filaments behave as small magnetic moments, which contribute to – and distort– the central field. The magnetic moments depend on J_C and are proportional to filament diameter. Their distribution follows the symmetries of the transport-current field (*i.e.*, the field produced by the transport current in the magnet coil) and, if the superconductor properties are uniform, only the allowed multipole coefficients are affected. Computer models have been developed which can accurately predict the field distortions resulting from superconductor magnetization [183].

The field distortions are the most significant at low transport current, where the transport-current field is low and J_C is large. They are progressively overcome as the transport-current field increases and J_C diminishes, and they become negligible at high transport current. They change sign and regain influence as the transport current is ramped down. As a result, the allowed multipole coefficients exhibit sizable hystereses as a function of transport current, which depend on magnet excitation history.

This is illustrated in Figure 51, which shows measurements of b_3 as a function of current in the central part of a SSC dipole magnet. In Figure 51, the magnetization effects can clearly be seen at currents below 3 kA (as explained in the previous section, the distortions at high field result from iron yoke saturation).

The field distortions resulting from superconductor magnetization are one of the major drawbacks of using superconducting magnets in a particle accelerator. They can be reduced by reducing filament size (typically, to 5 μm for SSC and LHC strands), but they cannot be eliminated. The powering cycle of the magnets must be adapted to avoid brutal jumps between the two branches of the multipole coefficient hystereses while the beam circulates. Also, elaborate beam optics correction schemes must be developed, which can include superconducting, high-order multipole corrector magnets (chapter 9 of Ref. [11]).

8.6.3 TIME DECAY

In addition, the effects of superconductor magnetization are not indefinitely persistent, but exhibit a slow time decay, which, at low transport current, can result in significant drifts of the allowed multipole coefficients [184], [185]. These drifts are particularly disturbing during the injection phase of machine operation, where the magnet current is maintained at a constant and low level for some period of time [186], [187]. Also, they complicate the early stages of acceleration, for, as the current is increased at the end of injection, the drifting multipoles *snap-back* rapidly to values on the hysteresis curves [188]. Part of the observed time decay can be attributed to flux creep in the superconductor [189], but flux creep cannot account for the large drifts observed after a high current cycle [185]. The nature of the other mechanisms that may be involved is not well understood.

8.7 COUPLING CURRENTS

As described in section 3.6, accelerator magnet coils are wound from Rutherford-type cables, which consist of a few tens of strands twisted together and shaped into a flat, two-layer, slightly keystoned cable. The cable mid-thickness is smaller than twice the strand diameter, which results in strand deformation and large contact surfaces at the crossovers between the strands of the two layers. Furthermore, and as explained in section 6.2, the coils are pre-compressed azimuthally during magnet assembly. Large pressures that keep the strands firmly in contact are thus applied perpendicularly to the cables. The large contact surfaces and the high pressures can result in low contact resistances at the strand crossovers.

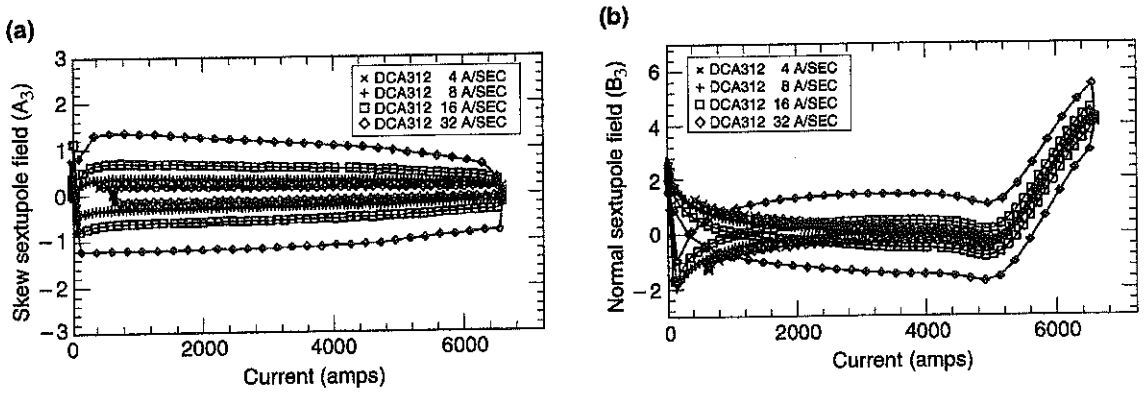

Figure 52. Effects of interstrand coupling currents on multipole field coefficients measured as a function of ramp rate in the central part of a SSC dipole magnet [160]: (a) skew sextupole field coefficient (A_3) and (b) normal sextupole field coefficient (B_3). The transport-current contribution has been subtracted from the data.

In the steady state, the transport current flows in the superconducting filaments, which offer no resistance. When the cable is subjected to a transverse varying field, the network of low interstrand resistances allows the formation of current loops, which are superimposed on the transport current. The loop currents, referred to as *interstrand coupling currents*, circulate along the superconducting filaments and cross over from strand to strand through the interstrand resistances. Unlike persistent magnetization currents, the interstrand coupling currents are directly proportional to the rate of field variations and they start to decay as soon as the field ramp is stopped.

Interstrand coupling currents have three main effects on magnet performance [160]: (1) heat dissipation (when crossing the interstrand resistances), (2) field distortions, and (3) quench current degradation (for they are superimposed on the transport current). The field distortions issue is the most critical for accelerator magnet applications [190].

The coupling current contribution to the central field does not depend on transport current and increases linearly as a function of current ramp rate. If the interstrand resistance is uniform throughout the coil assembly, the coupling current distribution follows the symmetries of the transport-current field and only the allowed multipole field coefficients are affected. In practice, however, there can be large coil-to-coil differences as well as large non-uniformities within the coils themselves, which result in sizable effects in the un-allowed multipole coefficients. This is illustrated in Figure 52(a) and Figure 52(b), which present plots of skew and normal sextupole field coefficients (A_3 and B_3) as functions of current, measured at various ramp rates in the central part of SSC dipole magnet prototype DCA312. (Note that the transport-current contribution has been subtracted from the data.) No particular treatment (such as stabrite) was applied to the strands of the cable used in this prototype.

The effects of interstrand coupling currents can be limited by ensuring that the interstrand resistances are not too low. However, and as mentioned in section 3.6, the interstrand resistances should not be too large either to allow some possibility of current redistribution among cable strands.

8.8 LONGITUDINAL PERIODICITY

When measuring the field with a fine spatial resolution along the axis of an accelerator magnet, all multipole coefficients appear to exhibit periodic oscillations [191], [192]. The amplitude of the oscillations varies as a function of space, transport current, excitation history and time, but the wavelength is always approximately equal to the twist pitch length of the cable used in the innermost coil layer.

The longitudinal periodic oscillations are believed to result from imbalances in the current distribution among cable strands. The current imbalances may have at least three origins: (1) non-uniformities in the properties of cable strands, (2) non-uniformities in the solder joints connecting the coils in series to the current leads and (3) large and long-lasting interstrand coupling current loops superimposed on the transport current [193]. Such current loops can be induced by spatial variations in the time-derivative of the field to which the cable is exposed as it turns around the coil ends or exits towards the current leads [194]–[196].

The oscillation wavelength is too short to affect beam optics but may be an issue for magnetic measurements. It is recommended that the measurements be averaged over an integer number of cable pitch lengths. Also, the slow decay of the large interstrand coupling current loops associated with these periodic oscillations may contribute to the drifts of the allowed multipole coefficients observed at low and constant transport current (see section 8.6.3) [197].

9 PARTICLE ACCELERATOR MAGNET COOLING

9.1 SUPERCONDUCTOR CRITICAL TEMPERATURE

The superconducting state only exists at temperatures below the so-called *critical temperature*, T_C. For NbTi, T_C can be estimated as a function of applied magnetic flux density, B, using [132]

$$T_C(B) = T_{C0}\left(1 - \frac{B}{B_{C20}}\right)^{1/1.7} \tag{271}$$

where T_{C0} is the critical temperature at zero magnetic flux density and B_{C20} is the upper critical magnetic flux density at zero temperature. As explained in section 3.1.1, T_{C0} and B_{C20} depend on alloy composition. For commercial alloys, T_{C0} is between 9 and 9.2 K and B_{C20} is of the order of 14.5 T. Note that for B = 10 T, T_C is about one half of T_{C0}, which shows the limitation of NbTi at high magnetic flux densities.

9.2 MAGNET CRITICAL TEMPERATURE AT A GIVEN CURRENT

Let us consider a magnet coil initially in the superconducting state at an uniform temperature, T_0, and carrying a constant transport current, I, such that

$$I < I_{qm}(T_0) \tag{272}$$

where I_{qm} is the maximum quench current at T_0 defined in section 5.1.4.

Let us further assume that the magnet temperature is raised uniformly from T_0 to (T_0 + ΔT). The temperature increase results in a decrease of the superconductor critical current density and in a reduction of I_{qm}. The magnet coil remains in the superconducting state as long as

$$I \leq I_{qm}(T_0 + \Delta T) \tag{273}$$

It follows that, for a given value of I, the minimum temperature increase, ΔT_{qm}, that is likely to initiate a quench is determined by

$$I = I_{qm}(T_0 + \Delta T_{qm}) \tag{274}$$

The magnet critical temperature at current I, T_{CI}, is defined as

$$T_{CI}(I) = T_0 + \Delta T_{qm}(I) \tag{275}$$

Replacing I_{qm} by its definition shows that T_{CI} is the solution of the implicit equation

$$I = I_C[T_{CI}, B_{peak}(I)] \tag{276}$$

where $I_C(T,B)$ is the supposedly known parametrization of the cable critical current as a function of temperature, T, and of magnetic flux density, and $B_{peak}(I)$ is the computed peak magnetic flux density on the magnet coil. Note that, unlike T_C, which is an intrinsic characteristic of the superconducting material, T_{CI} depends on cable and magnet designs.

9.3 TEMPERATURE AND ENTHALPY MARGINS

Let us now consider a magnet that is designed to be operated at a current, I_{op}. To reach the superconducting state, the magnet coil must of course be cooled down to a temperature, T_0, that is lower than the critical temperature at I_{op}, $T_{CI}(I_{op})$.

The operating temperature margin, ΔT_{op}, is defined as

$$\Delta T_{op} = T_{CI}(I_{op}) - T_0 = \Delta T_{qm}(I_{op}) \tag{277}$$

and the operating enthalpy margin, ΔH_{op}, is defined as

$$\Delta H_{op} = \int_{T_0}^{T_{CI}(I_{op})} dT\, C_{cond}(T) \tag{278}$$

Here C_{cond} is the specific heat per unit volume of conductor (in J/m^3).

In the section on magnetic design, we have seen that to ensure suitable quench performance, the operating current margin should be set to at least 10%. In practice, however, most unwanted quenches occur because of energy depositions which result in local temperature increases (see section on quench performance). Hence, it is more suitable to set a specification on temperature margin. Of course, the larger the temperature margin, the larger the enthalpy margin, and the more stable the magnet operation against thermal disturbances.

The SSC dipole magnets were designed to operate at 4.35 K with a temperature margin of about 0.6 K while the LHC dipole magnets are designed to operate at 1.9 K with a temperature margin of about 1.4 K. Assuming that the cables have similar copper-to-

superconductor ratios, it can be verified that, due to the fact that the specific heat per unit volume of conductor is a strongly decreasing function of temperature, these two temperature margins correspond to enthalpy margins of the same magnitude.

9.4 EFFECTS OF BEAM LOSSES

At high energy, the particle beam circulated in the magnet ring generates losses of various kinds, which result in, more or less, static heat deposition over the magnet coils. The power is mainly deposited on the conductors located about the horizontal x-axis of the magnet cross-sections and can raise their temperature significantly. This temperature increase results in a decrease of the enthalpy margins of the heated conductors that may degrade quench performance.

It turns out, however, that the conductors close to the x-axis are also the conductors subjected to the lowest magnetic flux densities, and which have the largest temperature and enthalpy margins to begin with. All effects combined, the conductors with the smallest temperature and enthalpy margins usually remain the conductors close to the magnet poles, which are subjected to the largest magnetic flux densities. Hence, the beam losses, which are mainly deposited over the low field region of the coils, are not expected to strongly affect the maximum quench currents of the magnets.

The effects of beam losses can be cut down by implementing a so-called *beam screen* inside the magnet beam pipe [198]. This is illustrated in Figure 53, which shows a view of the beam screen under development for the twin-aperture magnets of the LHC arcs [199]. The design of this beam screen is quite sophisticated. It is made up of a low permeability, stainless steel tube, approximately 1-mm thick, with a carefully optimized cross section along both horizontal and vertical axes to preserve the largest possible dynamic aperture for the beam. It incorporates *pumping holes* on about 4% of its surface to be partially transparent to H_2 molecules, and its inner wall is coated with a 50-μm-thick layer of high conductivity copper to keep a low electric impedance. It is cooled by two longitudinal helium pipes positioned on top and bottom and will be operated at temperatures between 5 and 20 K.

The effects of beam losses on magnet coils can be reduced also by improving heat removal capabilities. In the case of NbTi cables cooled by superfluid helium (see section 9.8), it has been shown that the steady state heat transfer to the coolant strongly depended on the number and nature of insulation layers, and on the type of wrapping around the conductors [200], [201]. The conductor insulation scheme can therefore be optimized to obtain a more favorable heat transfer and limit temperature rises due to beam losses.

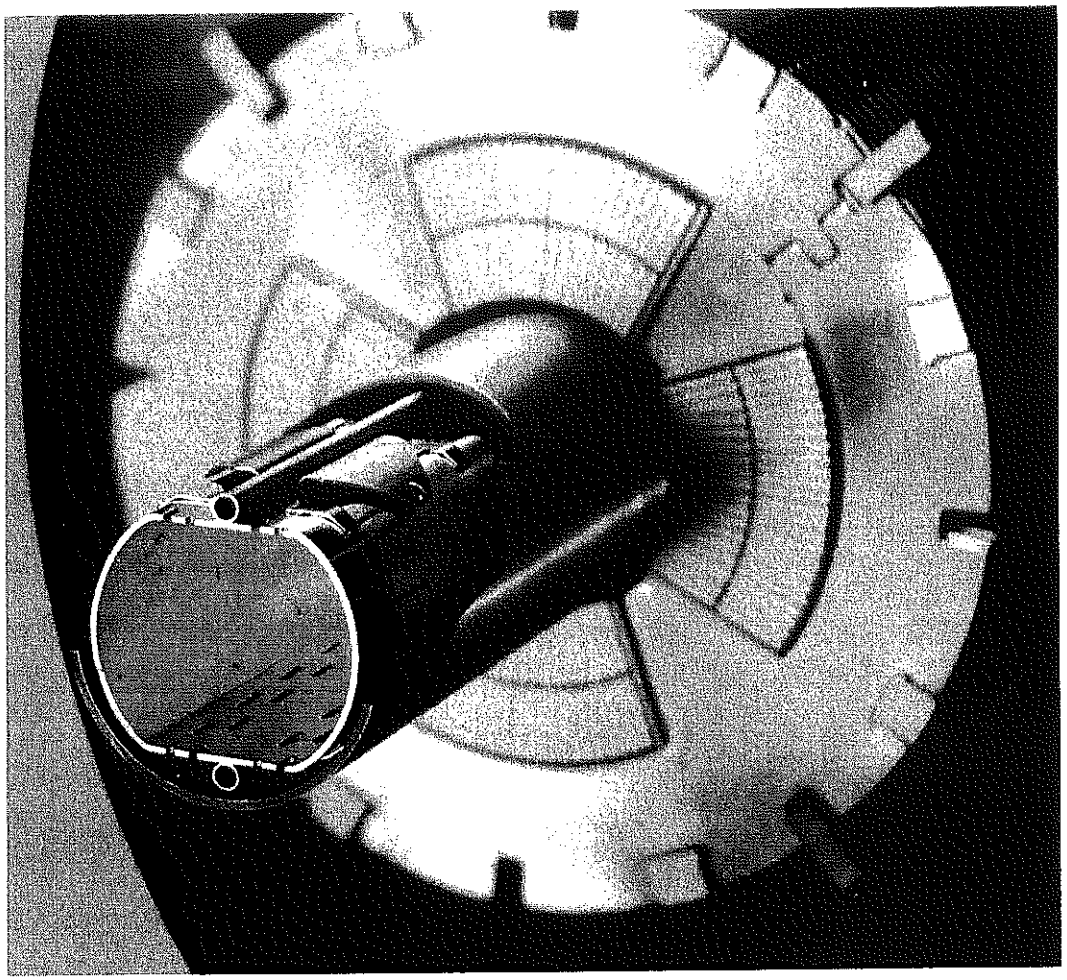

Figure 53. View of the beam screen under development for the twin-aperture magnets of the LHC arcs.

9.5 HELIUM COOLING

Among the cryogenic fluids, liquid helium, which has a boiling temperature of 4.2 K at 1 atmosphere (1 atmosphere $\approx$ 0.1 MPa), is the most appropriate for cooling down superconducting magnets wound from NbTi or Nb_3Sn conductors [202]. In the case of accelerator magnets, the coils are fully immersed into liquid helium and the superconducting cable is directly in contact with the coolant, which, thereby, participates to the stability against thermal disturbances.

The pressure-temperature phase diagram of helium is presented in Figure 54 [203]. It presents two main features: (1) the existence of a critical point at a temperature of 5.2 K and a pressure of 0.226 MPa, and (2) the occurrence of *superfluidity*, for temperatures below the so called *lambda-temperature*, T_λ. Liquid helium at a temperature above T_λ is usually referred to as *helium I*, while superfluid helium at a temperature below T_λ is referred to as *helium II*.

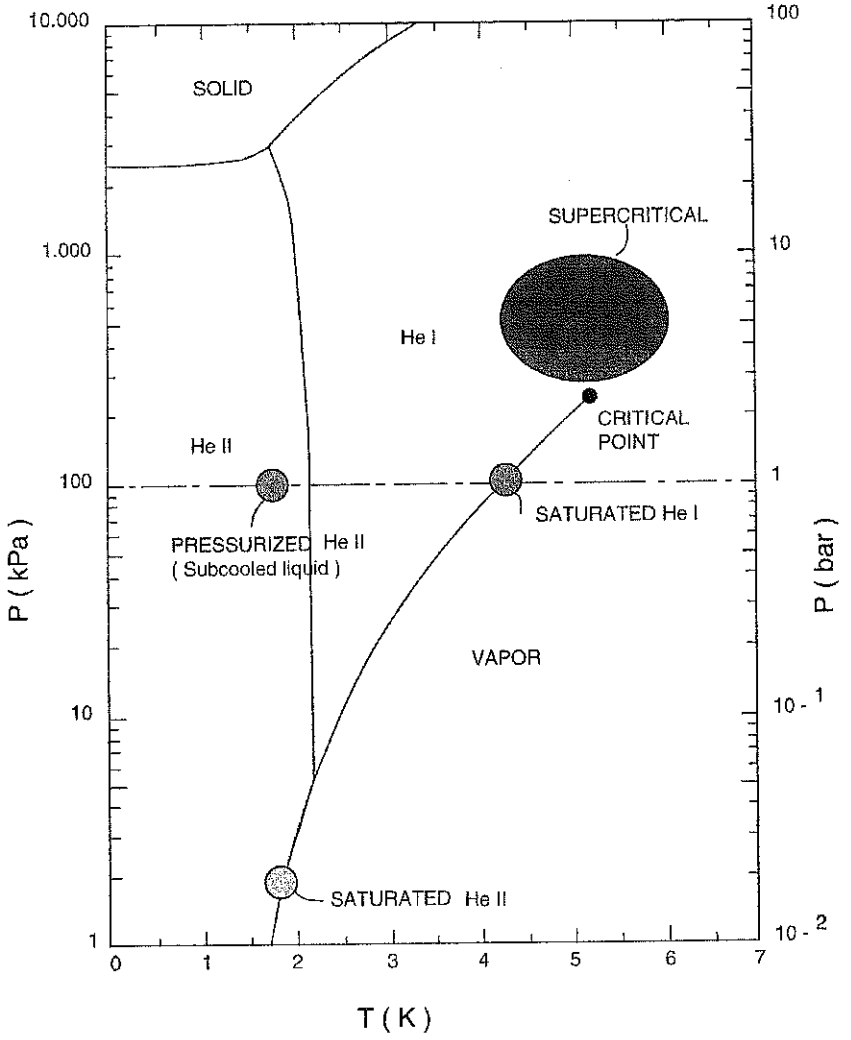

Figure 54. Pressure-Temperature phase diagram of helium [203].

For reference, the present (1999) market price of liquid helium is US$ 2.50 per liter (when bought in large quantities). As a comparison, the market price of liquid nitrogen is US$ 0.057 [204].

9.6 SATURATED HELIUM I VERSUS SUPERCRITICAL HELIUM

Small superconducting magnet systems usually rely on boiling helium at 1 atmosphere, also referred to as *saturated helium I* [203]. Boiling helium offers the advantage that, as long as the two phases are present, the temperature is well determined. However, in large-scale applications, such as superconducting particle accelerators, the fluid is forced to flow through numerous magnet cryostats and long cryogenic lines, where heat leaks are unavoidable. The heat leaks result in increases in vapor contents and create a risk of gas pocket formation that may block circulation. The aforementioned difficulty can be circumvented by taking advantage of the existence of the critical point at 5.2 K and

0.226 MPa. For temperatures and pressures beyond the critical point, the liquid and vapor phases become indistinguishable. The single-phase fluid, which is called *supercritical*, can be handled in a large system without risk of forming gas pockets. However, its temperature, unlike that of boiling helium, is not constant and may fluctuate as the fluid circulates and is subjected to heat losses.

9.7 HELIUM-I CRYOGENIC SYSTEMS

The cryogenic systems of Tevatron, HERA, and RHIC, and that designed for UNK and SSC, combine single-phase and two-phase helium I [203]. In the case of Tevatron, HERA and UNK, the inside of the magnet cold masses are cooled by a forced flow of supercritical helium whereas two-phase helium I is circulated in a pipe running at the cold mass periphery (around the collared-coil assembly for Tevatron magnets [205], [206], in a bypass hole in the iron yoke for HERA magnets [207], and in two bypass holes in the iron yoke for UNK magnets [35], [208]). In the case of SSC, it was planned also to circulate supercritical helium through the magnet cold masses, while so-called *re-coolers*, consisting of heat exchangers using two-phase helium I as primary fluid, would have been implemented at regular intervals along the cryogenic lines [209], [210]. The RHIC cryogenic system is inspired from that of SSC [211]. In all these schemes, the boiling liquid is used to limit temperature rises in the single-phase fluid.

9.8 SUPERFLUID HELIUM

A particularity of helium is the occurrence of *superfluidity* [202], [212]. When cooling down boiling helium I at 1 atmosphere, it stays liquid until a temperature of the order of 2.17 K, where appears a phase transition. For temperatures below 2.17 K (at 1 atmosphere) helium loses its viscosity and becomes a superconductor of heat. This property, unique to helium, is called superfluidity. Superfluidity is very similar to superconductivity, except that, instead of electrical conductibility, it is the thermal conductibility that becomes infinite. Note that the transition temperature between liquid helium I and superfluid helium II, T_λ, depends on pressure [213].

Superfluid helium was first used in a large scale application for Tore Supra, a superconducting tokamak built at CEA/Cadarache (Commissariat à l'Energie Atomique de Cadarache, near Aix en Provence in the South of France) and operating reliably since 1988 [214].

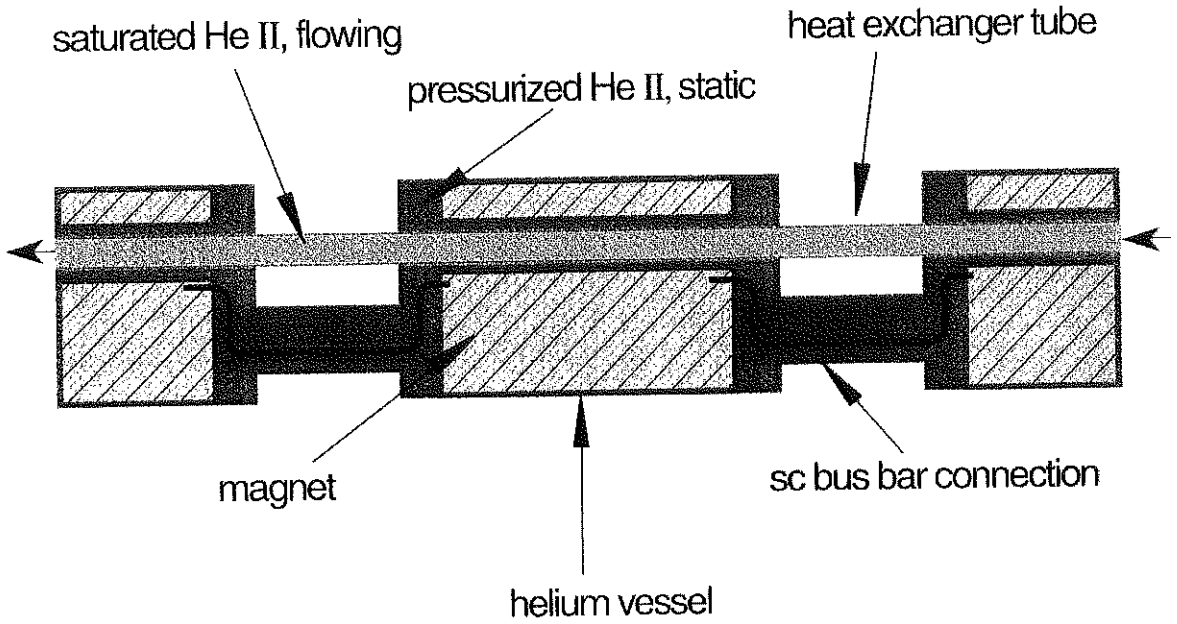

Figure 55. LHC magnet string cooling scheme.

9.9 HELIUM-II CRYOGENIC SYSTEMS

Similarly to what is done in helium I, one can operate either in *saturated helium II* or in *pressurized helium II* (see Figure 54). Saturated helium II exists only at pressure below 5 kPa and offers the advantage of a constant temperature, but its vapor content can vary. Pressurized helium II is obtained by subcooling liquid helium I below T_λ (at a pressure above 5 kPa) and offers the advantage of a single-phase fluid, but its temperature can vary.

The LHC magnets are cooled by superfluid helium and combine the advantages of both: the magnet cold masses are immersed in stagnant pressurized helium II, while a flow of saturated helium II is circulated in a pipe running at the periphery of the magnet yokes, as illustrated in Figure 55 [215]. The LHC cryogenic system will require of the order of 93500 kg of helium, mostly in the magnet cold masses (54.5% of the inventory) and in the pipes (41% of the inventory) [4].

The operating temperature of the LHC magnets is set to 1.9 K. As noted in section 3.4.3, the curve "critical current density as a function of magnetic flux density" of NbTi is shifted by about (+3 T) when lowering the temperature from 4.2 K to 1.9 K. Hence, lowering the operating temperature to 1.9 K improves the current carrying capability of NbTi dramatically and allows higher magnetic flux densities to be reached.

9.10 MAGNET CRYOSTAT

To maintain magnet cold masses at low temperature it is necessary to limit heat losses. There are three main mechanisms of heat transfer [216]: (1) convection, (2) radiation and (3) conduction. The convection losses are eliminated by mounting the cold masses into cryostats which are evacuated [203], [217]. The radiation losses, which scale in proportion with the effective emissivities of the surfaces facing each other and with the fourth power of their temperatures, are reduced by surrounding the cold masses with blankets of multilayer insulation and thermal shields at intermediate temperatures. The main sources of conduction losses are the support posts, the power leads and the cryogenic feedthroughs, which are designed to offer large thermal resistances.

10 QUENCH PERFORMANCE OF PARTICLE ACCELERATOR MAGNETS

10.1 WHAT IS A QUENCH?

As we have seen, for a given material, the boundary between the superconducting state and the normal resistive state can be represented by a three-dimensional surface which depends on operating temperature, applied magnetic flux density and transport current density. A magnet is normally operated at conditions corresponding to a volume located beneath the critical surface, where the entire coil is superconducting.

Starting from the operating conditions, let us ramp up the current supplied to a superconducting magnet, or let us assume that, somewhere in the magnet coil, there is an energy deposition which results in a local temperature rise. In ramping up the current (and thus, the magnetic field) or in raising the temperature, we get closer and closer to the critical surface, and soon, we cross it. Crossing the critical surface means that, somewhere in the coil, a small volume of conductor switches to the normal resistive state. When switching to the normal resistive state, the small volume of conductor starts dissipating power by the Joule effect. The dissipated power overheats the small volume, and, by thermal diffusion along the conductor (or by any other mechanism of heat transfer), the region surrounding the small volume. If the Joule heating is large enough (and if the cooling is not too strong), the surrounding region can, in turn, reach the transition temperature, switch to the normal resistive state, and start dissipating power. And so on. Under certain conditions, a self-maintained process can be established — from transition, to power dissipation, to thermal diffusion and then again to transition — in which the *normal zone*, *i.e.*, the zone where the conductors have switched to the normal resistive state, grows irreversibly and *propagates* through the entire coil. This process is called a *quench*.

10.2 MAGNET TRAINING AND QUENCH PLATEAU

As explained in the section on operating current margin (section 5.1.5), the current limit of a superconducting magnet at a given operating temperature is determined by the critical current of its cable and the peak magnetic flux density on the magnet coil. We referred to this limit as the maximum quench current, I_{qm}. However, as it is usually estimated from critical current values directly measured on a short sample of cable cut from the cable batch used in winding the magnet coil, it is also referred to as *short sample current limit*, I_{ss}. For a given magnet, the values of I_{qm} or I_{ss} can only be raised by decreasing the operating temperature.

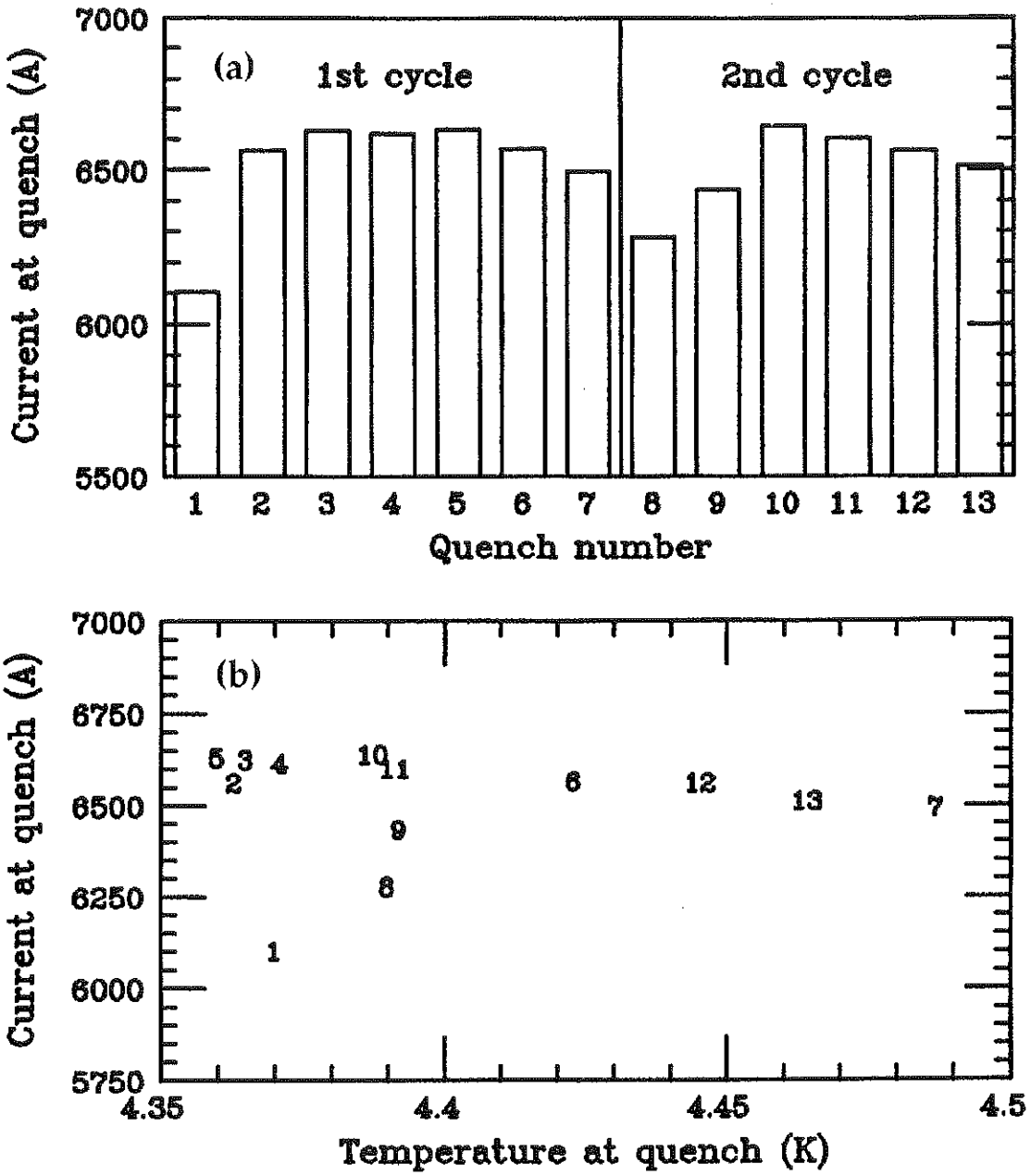

Figure 56. Selected testing results from 4-cm-aperture, 17-m-long SSC dipole magnet prototype DD0017: (a) current at quench versus quench number and (b) current at quench versus temperature at quench.

When cooling down and energizing a superconducting magnet for the first time, the first quenches usually occur at currents below I_{qm} or I_{ss} (chapter 5 of Ref. [123]). In most cases, however, it appears that, upon successive energizations, the quench currents gradually increase. This gradual improvement is called the magnet's *training*. The training often leads to a stable *plateau* corresponding more or less to the expected maximum quench current at the given temperature.

As an illustration, Figure 56(a) presents a plot of current at quench versus quench number for an early 4-cm aperture, 17-m long SSC dipole prototype (magnet DD0017) [218]. The magnet was first cooled down to a nominal temperature of 4.35 K and ramped up several times to quench. A *ramp to quench* consists in ramping up the magnet current until a quench occurs; the power supply is then switched off and the magnet is discharged. Following the quench, the magnet is cooled down again to 4.35 K, and the test is repeated. In the case of magnet DD0017, the magnet was ramped to quench seven times and then warmed up to room temperature for several days. After this *thermal cycle* to room temperature, it was cooled down again to 4.35 K, and ramped to quench six more times.

The data of Figure 56(a) shows that, after the first cooldown to 4.4 K, magnet DD0017 exhibited two training quenches and reached a plateau on the third quench (as explained in a later section, the lower currents observed for quenches 6 and 7 are due to slight increases in magnet temperature). It appears also in Figure 56(a), that, after the second cooldown to 4.4 K, it took again two training quenches to reach the level of plateau quench current previously achieved. This means that, during the thermal cycle to room temperature, magnet DD0017 lost the memory of its initial training and required *re-training*.

10.3 ACCURACY OF SHORT SAMPLE CURRENT LIMIT ESTIMATIONS

One question that arises is how reliable are the short sample current limit estimations. As we have seen, these estimations are usually based on critical current measurements on a well cooled short sample which may or may not be representative of the full length of cable in the magnet coil environment. Furthermore, and as explained in the section on transition of multifilamentary wires (section 3.3), the critical current is defined by relying on empirical criterions which may be suited for some applications but may turn out to be inadequate for some other. One way of answering this question is to compare short sample current limit estimations with actual plateau quench currents achieved in real magnets.

Figure 57 presents a summary plot of the highest plateau quench currents reached on selected 5-cm-aperture, 15-m-long SSC dipole magnet prototypes as a function of the estimated short sample current limits at the given temperatures. (The magnets were usually tested at three nominal temperatures: 4.35 K, 3.8 K and 3.5 K, at which they all reached a quench plateau with very little training [37].) Although most of the data points lie slightly below the first diagonal, the agreement is relatively good. This indicates that the short sample estimations are quite reliable.

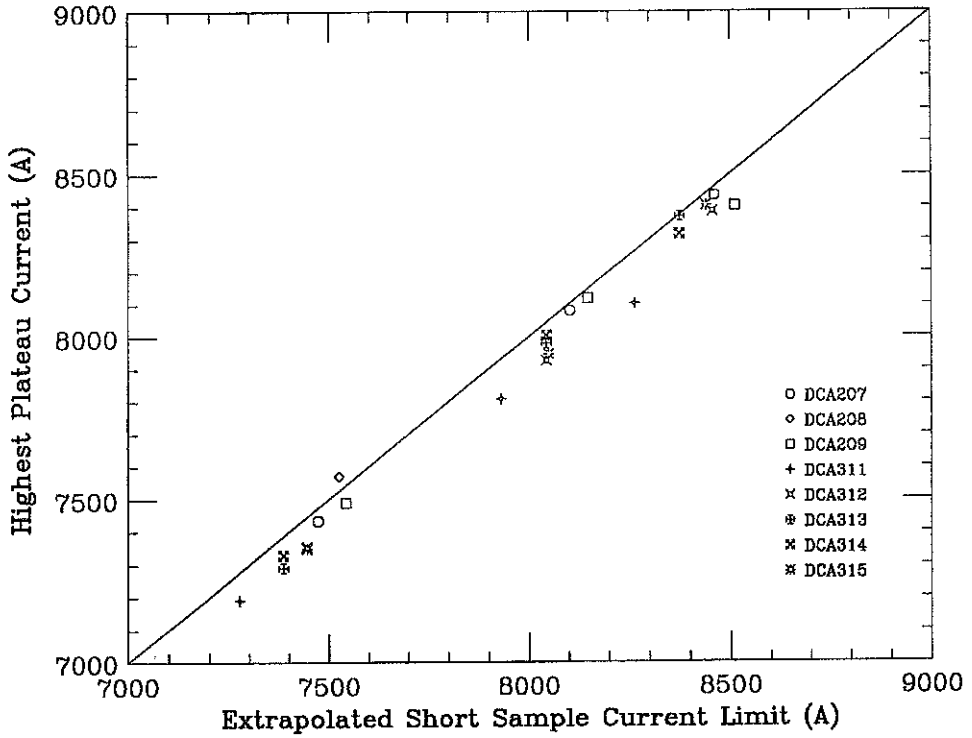

Figure 57. Comparison between quench plateau currents and estimated short sample current limits on selected 5-cm-aperture, 15-m-long SSC dipole magnet prototypes.

10.4 QUENCH ORIGINS

Quenches originate because of a crossing of the superconductor critical surface somewhere in the magnet coil. This crossing occurs either along the "peak magnetic flux density versus transport current density" line or along the temperature axis.

The maximum quench current at a given temperature is estimated using a parametrization of the superconductor critical surface such as the one given by Eq. (14) and assuming a uniform value of J_{Cref} over the magnet coil. The J_{Cref} value is usually determined from measurements on a cable short sample. Nevertheless, it can happen that the crossing of the critical surface along the peak field line occurs at an overall cable current that is below the expected I_{qm} or I_{ss}. Such quenches have at least two origins: (1) a local cable degradation, which results in a local decrease of the critical current and of the critical current density, and (2) a large imbalance in the current distribution among the cable strands, which results in a strand carrying much more current than average and hitting the critical surface ahead of the others. Quenches of the first kind are of the same nature as quenches occurring at the short-sample limit and they can all be identified as *conductor-limited* quenches. Quenches of the second kind are more likely to occur at high ramp rates and are discussed in the oncoming section on quench performance versus ramp rate.

The temperature rises which initiate quenches result from energy depositions on the magnet coil. These energy depositions have at least three origins: (1) mechanical disturbances such as stress relief or frictional motion under the Lorentz force, (2) synchrotron radiation or beam losses, and (3) power dissipation from interstrand coupling currents. Quenches of the first origin are referred to as *mechanically-induced* quenches and reveal flaws in the mechanical design or in the assembly procedures which must be analyzed and corrected. The effects of synchrotron radiation can be reduced by implementing an intercepting screen within the beam pipe and/or by optimizing the conductor insulation scheme (see section 9.4). Coupling losses are only of concern for fast current cycles.

10.5 DISCRIMINATING BETWEEN CONDUCTOR-LIMITED AND MECHANICALLY-INDUCED QUENCHES

Conductor-limited quenches correspond to a crossing of the critical surface along the peak magnetic flux density line. When changing the operating temperature from T_0 to (T_0 + ΔT_0), the quench current should follow the superconductor critical surface and vary from $I_q(T_0)$ to $I_q(T_0+\Delta T_0)$. Hence, the currents of conductor-limited quenches are expected to exhibit a strong correlation with temperature. Conversely, the energy depositions resulting from mechanical disturbances should mainly depend on the Lorentz force level and should be relatively insensitive to small temperature variations. Hence the currents of mechanically-induced quenches are not expected to be strongly related to magnet temperature. Thus a practical method for discriminating between conductor-limited quenches and mechanically-induced quenches is to vary the operating temperature of the magnet slightly — for example, to increase it and then decrease it by 50 mK — and to see if the quench current follows the change or not.

Figure 56(b) shows a plot of current at quench versus temperature at quench for the quench data of SSC dipole magnet prototype DD0017 presented in Figure 56(a). (The temperature is measured by carbon resistors located in the helium interconnect region at both extremities of the horizontal magnet test stand). Quenches 3 to 7 and 10 to 13 exhibit a clear correlation between quench current and temperature, while quenches 1 and 2, and 8 and 9 (the first two training quenches of each test cycle) are scattered. Hence, quenches 1, 2, 8, and 9 are likely to be mechanically-induced quenches, while all the others are conductor-limited quenches. Note that for quenches 6 and 7, on one hand, and quenches 12 and 13, on the other hand, the temperature was deliberately raised from its nominal 4.35 K value to check if the quench current decreased accordingly.

10.6 MECHANICAL TRAINING

Among the various quench origins considered above, only the mechanical disturbances are likely to be affected by successive ramps to quench and lead to the kind of improvement in magnet performance referred to as training. A phenomenological explanation of magnet training is as follows.

When energizing a magnet, strong Lorentz forces are applied to the conductor strands, which are transmitted to the coil support system through the insulation. In a geometry as complex as that of a dipole or a quadrupole coil assembly, there are many interfaces where the Lorentz forces have tangential components which are counteracted by friction. As the current is ramped up and the Lorentz forces increase, it can happen that, somewhere in the coil, a static-friction coefficient is exceeded. Sliding then occurs, which results in heat dissipation and a local temperature rise. If the local temperature rise is large enough, a quench is initiated.

In the case of a quench caused by a so-called *stick-slip motion* in the magnet assembly, the motion responsible for the quench and/or the thermal stresses developed in the magnet coil during the quench can improve the mechanical stability at the troubled interface. As a result, upon subsequent energizations, the Lorentz forces are better supported and the same current level can be achieved without exceeding the local static-friction coefficient. Then, the current can be further ramped up until, somewhere else in the coil, another static-friction coefficient is exceeded, which, in turn, provokes a frictional motion large enough to initiate a quench — and so on. Quench after quench, the current can be ramped up to higher levels until it is reaches the maximum quench current.

It goes without saying that if the mechanical flaws at the origins of the disturbances are too large, the magnet cannot be trained and keeps quenching erratically.

10.7 QUENCH PERFORMANCE AS A FUNCTION OF RAMP RATE

Let us consider an accelerator magnet, which has been trained to a stable plateau. When subsequently performing ramps to quench at increasing ramp rates, at least two mechanisms are in competition to degrade quench performance: (1) the generation of interstrand coupling currents, which are superimposed to the transport current and dissipate power when crossing the interstrand resistances, and (2) the possible modification of the transport-current distribution among the cable strands which can result in the apparition of large current imbalances.

The interstrand coupling currents, which have been described in section 8.7, are expected to increase as a function of ramp rate, leading to a monotonic decrease of the quench current. Determining how the distribution of transport current among the cable strands (briefly evoked section 8.8) is influenced by ramp rate requires additional background informations.

As we have seen, the Rutherford-type conductor used in superconducting particle accelerator magnets consists of a few tens of strands, twisted together, and shaped into a flat, two-layer, slightly keystoned cable. Each cable strand is characterized by a voltage-current curve and a self-inductance. Each strand pair is characterized by a mutual inductance. Also, all the strands are coupled through the interstrand resistances and the splice resistances at the coil ends. During energization, the current distributes itself among the cable strands according to this intricate network of resistances and inductances. At low ramp rate, the current distribution is mainly determined by the resistive elements of the circuit, but as the ramp rate is increased, the inductive elements start to play a role, and end up being the dominant elements at large ramp rate. If the strands are identical and interchangeable, they all carry the same current, and changing the ramp rate is not expected to have any influence. However, if for one reason or another, the strands are not identical or are not interchangeable, the static and dynamic current distributions can be different. Then, as the ramp rate is increased, the current distribution changes from one to the other, resulting in a quench current evolving between two asymptotic values: (1) one for ramp rates tending towards zero and (2) one for large ramp rates. This implies in particular that, unlike in the case of interstrand coupling currents, the quench current degradation arising from transport current imbalances is expected to flatten out at large ramp rates.

Illustrations of the different ramp rate behaviors that can be encountered are given in Figure 58(a) and Figure 58(b) which display summary plots of quench current versus ramp rate for selected 5-cm-aperture, 15-m-long SSC dipole magnet prototypes [37], [44], [160]. (The magnets are grouped according to the manufacturer and the production batch of their inner cable strands.) It appears that, for the magnets of Figure 58(a), the quench current remains roughly constant for ramp rates up to 25 A/s, above which it starts to decrease quasi-linearly as a function of ramp rate. The worst case is magnet DCA312, which, at 200 A/s, quenches at 2180 A, corresponding to about 30% of its low ramp rate quench current. In comparison, for the magnets of Figure 58(b), the quench current starts by dropping significantly at low ramp rates, while the degradation is much milder at large ramp rates. The worst case is magnet DCA319, for which the quench current decreases from 7334 A at 1 A/s to 6156 A/s at 25 A/s, but is still of the order of 5000 A at 250 A/s.

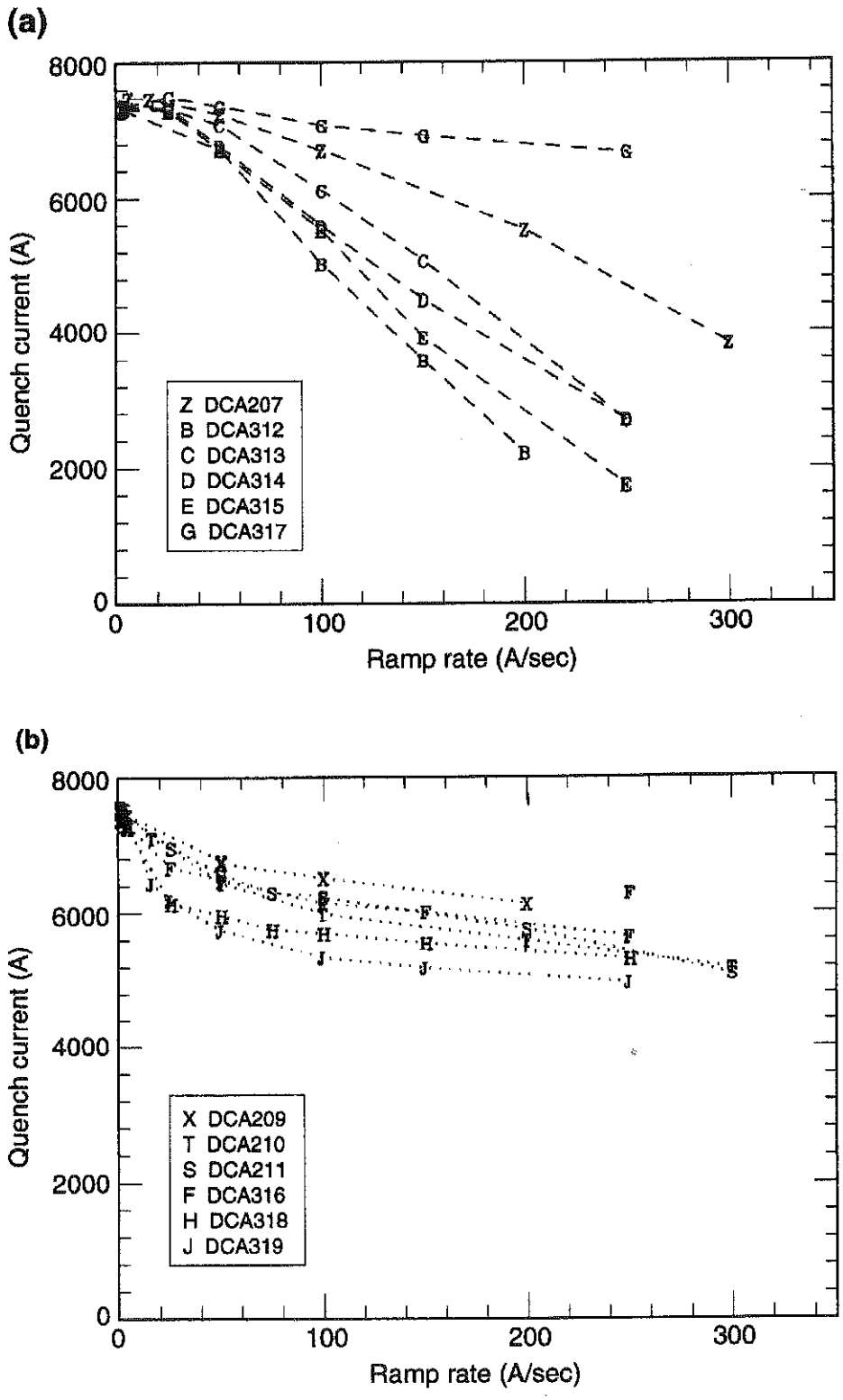

Figure 58. Ramp rate sensitivity of selected 5-cm-aperture, 15-m-long SSC dipole magnet prototypes: (a) Type A and (b) Type (b). (The magnets are grouped according to the manufacturer and the production batch of their inner cable strands.)

The behavior of the magnets in Figure 58(a) is referred to as *type-A* and is believed to be dominated by interstrand coupling currents arising from low and non-uniform interstrand resistances in the Rutherford-type cables [160]. The behavior of the magnets of Figure 58(b) is referred to as *type-B* and is believed to be dominated by imbalances in transport-current distribution. The exact origin of these imbalances has not been clearly identified.

It is worth mentioning that the quench performance of type-B magnets has been shown to depend on excitation history [160]. For instance, in the case of SSC dipole magnet prototype DCA318, which, according to the data of Figure 58(b), is the second worst type-B magnet after DCA319, the estimated plateau quench current at 4.35 K was 7450 A, while the quench current for a straight ramp to quench at 100 A/s was 5656 A. Subsequently, magnet DCA318 was subjected to a series of so-called *pre-cycled* ramps to quench [160]. In these tests (performed at 4.35 K nominal), the magnet was first ramped to a current, I_f, below 7450 A, at a succession of rates that did not cause the magnet to quench (typically: 16 A/s up to 6000 A and 1 A/s above). The current was then held constant at I_f for 600 s before being ramped down to 25 A at 100 A/s. After another pause of 600 s at 25 A, the magnet was ramped up to quench at 100 A/s. The measured quench currents were 5858 A for $I_f = 4000$ A, 6166 A for $I_f = 6000$ A, and 7061 A for $I_f = 7300$ A. Hence, the introduction of a pre-cycle to 7300 A, and of a ramp down from this high current to a near 0 value prior to the ramp up to quench, led to an improvement of about 1400 A in the 100-A/s quench current.

10.8 SPECIFICATION ON QUENCH PERFORMANCE

The possibility of training superconducting magnets is rather encouraging for it leaves the hope that, even if the first quenches are below the expected maximum quench current, the performance may improve and the magnet may finally reach the design current. Nevertheless, it is not reasonable to build an accelerator with several hundred or several thousand magnets that need to be trained each time they are put into operation (or at least, each time they are warmed up to room temperature). If the magnet prototypes exhibit some training, the origin of this training has to be understood, and the design of the magnet has to be modified so as to eliminate, or at least to limit, the training quenches to levels, which are well above the operating current of the accelerator.

In any case, it is indispensable to carry out systematic tests before installing the magnets into the tunnel to ensure that their quench performance is adequate and does not degrade upon extended current and thermal cycling [219].

11 QUENCH PROTECTION OF PARTICLE ACCELERATOR MAGNETS

11.1 THE EFFECTS OF A QUENCH

11.1.1 CONDUCTOR HEATING

Although most R&D programs have been successful in developing magnet designs that can be mass-produced and meet accelerator requirements, quenches do occur in accelerator operations. These quenches must be handled in order to avoid any damage of the quenching magnet, to ensure the safety of the installation and to minimize down time.

As we have seen in section 10.1, once a small volume of conductor has switched to the normal resistive state, it dissipates power by the Joule effect. A fraction of this dissipated power is transferred to the surroundings of the initial volume of transition (either along the conductor, or, transversely, to the conductor insulation or the helium), but the main part is consumed locally in overheating the conductor. In a very short time (a few tenths of a second in the case of a dipole or quadrupole magnet) the conductor temperature, initially that of the helium, reaches room temperature, and, if the magnet is not discharged, keeps on increasing.

11.1.2 MAXIMUM TEMPERATURE REQUIREMENT

The temperature rise consecutive to a quench must be limited for at least three reasons: (1) to restrict the thermal stresses induced in the quenching coil, (2) to prevent degradation of superconductor properties, and (3) to avoid insulation damage.

For most materials, thermal expansion starts to be significant for temperatures above 100 K. The critical current density of NbTi is affected by exposure to temperatures above 250 °C. The degradation amplitude depends on the temperature level and on the duration of the exposure: at 250 °C, it takes of the order of 1 hour to get a significant degradation, while it may take less than a minute at 400–450 °C [220]. This degradation results from a growth of the β-phase grains in the NbTi alloy microstructure, which affects the distribution of α-Ti precipitates and alters pinning. (The α-Ti precipitates get dissolved for temperatures above 600 °C). Finally, the polyimide materials used to insulate NbTi cables loose most of their mechanical properties for temperatures above 500 °C.

It follows that an upper limit for conductor heating consecutively to a quench is 400 °C. Most magnets are designed not to exceed 300 to 400 K, and whenever possible, the limit should be set to 100 K.

11.1.3 PROTECTING A QUENCHING MAGNET

The source of conductor heating in a quenching magnet is power dissipation by the Joule effect. Power keeps being dissipated as long as there is current in the magnet coil. To eliminate the heat source and limit the temperature rise, it is thus necessary to ramp the current down.

To discharge a quenching magnet, all its stored magnetic energy must be converted into resistive power. If the quench propagates very slowly, and the zone where the conductor has switched to the normal state remains confined to a small volume, there is a risk that a large fraction of the stored energy be dissipated in this volume. In the case of a string of magnets connected electrically in series, it may even happen that the energy of the whole string be dissipated in the quenching magnet. Hence, to prevent burnout, it is desirable to maximize the volume in which the energy is dissipated by ensuring that the normal resistive zone spreads rapidly throughout the quenching coil. This can be done by means of heaters, implemented near the magnet coils and fired as soon as a quench is detected. These heaters are referred to as *quench protection heaters*.

In comparison to other superconducting magnets, most accelerator magnets do require an active quench protection system because of the rapidity of the temperature rise resulting from the high current density and the low fraction of stabilizing copper in the cable strands. One notable exception are the RHIC dipole magnets, whose one-layer coil assemblies are wound from a cable with a high copper-to-superconductor ratio (2.25 to 1), and which do not rely on quench protection heaters.

11.2 HOT SPOT TEMPERATURE

11.2.1 ESTIMATING HOT SPOT TEMPERATURE

The volume of conductor that heats up the most significantly during a quench is the spot where the quench first originated. It is called the *hot spot*. An upper limit of the hot spot temperature, T_{max}, can be determined by assuming that, near the hot spot, all the power dissipated by the Joule effect is used to heat up the conductor. Then, near the hot sport, the heat balance equation reduces to

$$C_{cond}(T)\frac{dT}{dt} = \rho_{cond}(T)\left[\frac{I_{mag}(t)}{S_{cond}}\right]^2 \tag{279}$$

where C_{cond} is the overall specific heat per unit volume of conductor, ρ_{cond} is the overall conductor resistivity in the normal state, S_{cond} is the conductor cross-sectional area and $I_{mag}(t)$ is the magnet current at time t.

Equation (279) can be integrated under the form

$$S_{cond}^2 \int_{T_{quench}}^{T_{max}} dT \frac{C_{cond}(T)}{\rho_{cond}(T)} = \int_{t_{quench}}^{+\infty} dt\, I_{mag}^2(t) \tag{280}$$

where t_{quench} is the time of quench start and T_{quench} is the coil temperature at t_{quench}.

The left member of Eq. (280) depends only on conductor properties whereas the right member depends only on the characteristics of current decay. The right-hand side integral, divided by 10^6, is called the *MIIT integral* (Mega I times I versus Time integral) and its value is referred to as *number of MIITs*. The maximum temperatures computed from the numbers of MIITs have been shown to be in fairly good agreement with actual measurements of hot spot temperatures in quenching magnets [221].

11.2.2 Limiting Hot Spot Temperature

The hot spot temperature can be limited by acting on either member of Eq. (280). Regarding the left member, the only conceivable action is to reduce the overall conductor resistivity by increasing the copper-to-superconductor ratio. However, and as explained in section 3.4.2, the copper-to-superconductor ratio must also be optimized to ensure a high overall critical current. Regarding the right member, the MIIT integral can be minimized by: (1) detecting the quench as soon as possible, (2) turning off the power supply (case of a single magnet) or forcing the current to bypass the quenching magnet (case of a magnet string), (3) firing the quench protection heaters, and (4) discharging the quenching magnet or the magnet string.

11.3 QUENCH DETECTION

The magnets are connected to quench detection systems, which monitor the occurrence of a resistive voltage in the coil windings or the coils leads. The resistive voltage has to be discriminated from inductive voltages arising from magnet ramping. The inductive components are cancelled out by considering voltage differences across two identical coil assemblies or two identical parts of a given coil assembly (*e.g.*, the upper and lower half coils in a dipole magnet). When the resistive voltage exceeds a preset threshold over a time

exceeding a preset duration, the detection system generates a trigger which signals the occurrence of a quench.

11.4 PROTECTION OF A SINGLE MAGNET

11.4.1 CURRENT DISCHARGE

Let us first consider the case of a single magnet and let us assume that, once a quench is detected, the power supply is turned off and the magnet is switched to an external dump resistor, R_{ext}. The current decay is determined by

$$L_{mag} \frac{dI_{mag}}{dt} + [R_q(t)+R_{ext}]\ I_{mag} = 0 \tag{281}$$

where L_{mag} is the magnet inductance and $R_q(t)$ is the developing resistance in the quenching coils. Furthermore, the total voltage across the magnet, V_{mag}, is given by

$$V_{mag}(t) = R_{ext}\ I_{mag}(t) \tag{282}$$

To limit the number of MIITs, it is desirable to have a fast current decay. Equation (281) shows that fast decay rates are obtained either by means of a large R_{ext} or by ensuring that $R_q(t)$ grows rapidly. For some magnets, an external resistor can be used to extract a significant fraction of the stored magnetic energy. However, it is also required to keep V_{mag} to a reasonable level (typically: less than 1 kV) to avoid insulation breakdown. Given the order of magnitude of I_{mag} (up to 15 kA), this imposes a small R_{ext} (typically: a few hundredth of ohms) which, during a quench, is soon overcome by $R_q(t)$. Hence, for accelerator magnets, the current decay is largely dominated by the resistance development in the quenching coils and the decay rate can be increased only by speeding up $R_q(t)$.

11.4.2 MAXIMUM VOLTAGE TO GROUND

The developing resistance in the quenching coil separates the coil impedance into several parts (p. 137 of Reference [11]): un-quenched parts across which the voltage is mainly inductive and quenched parts across which the voltage is mainly resistive. The resistive and inductive voltages compensate each other partially so that their sum equals V_{mag}. The voltage distribution with respect to ground depends on the respective sizes and locations of these various parts. The more uniform the quench development, the lower the maximum voltage to ground. As an illustration, Figure 59 shows the voltage distribution in a quenching magnet. Here, V_{mag} is assumed to be nil and R_q is assumed to be concentrated near two thirds of the magnet length.

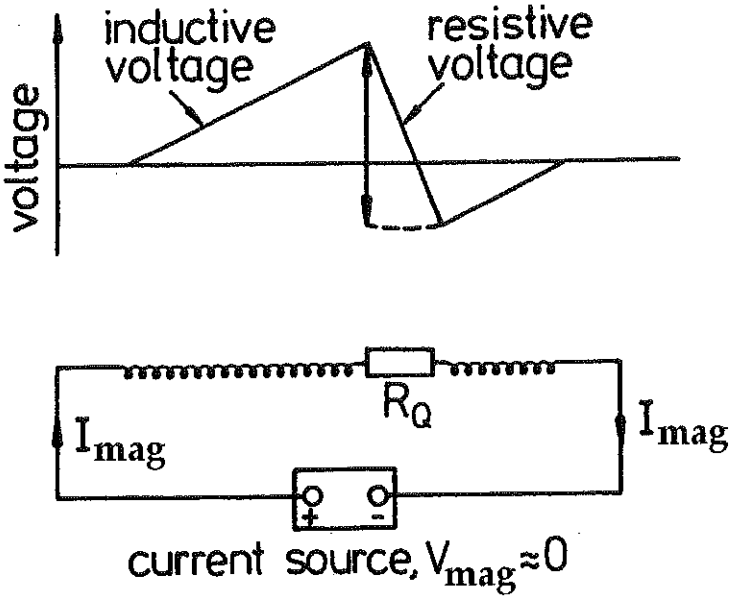

Figure 59. Voltage distribution in a quenching magnet. The total voltage across the magnet is assumed to be nil and the developing resistance is assumed to be concentrated near two third of the magnet length [11].

11.4.3 QUENCH PROTECTION HEATERS

As described earlier, to speed up and uniformize quench development, most accelerator magnets rely on quench protection heaters which are fired as soon as a quench is detected. The heaters are usually made of stainless steel strips, which are copper clad at regular intervals along their lengths and which are placed on the outer surface of the coil assemblies. Note, however, that the heater firing unit relies on a capacitor bank and that it takes some time for the energy to be released. Note also that the heaters have to be electrically insulated from the coil and that this electrical insulation introduces a thermal barrier. As a result, there is a non negligible delay between the firing of the heaters and their effect on the coils, during which, we must rely on natural quench propagation [222]. The heaters and their implementations in the magnet assembly are optimized to reduce this delay.

11.5 PROTECTION OF A MAGNET STRING

In an accelerator, the magnet ring is divided into several sectors made up of series-connected magnets. The sectors are powered independently and are electrically independent. Once a quench is detected in a magnet, the power supply of the sector to which the magnet belongs is turned off and the sector is discharged over a dump resistor.

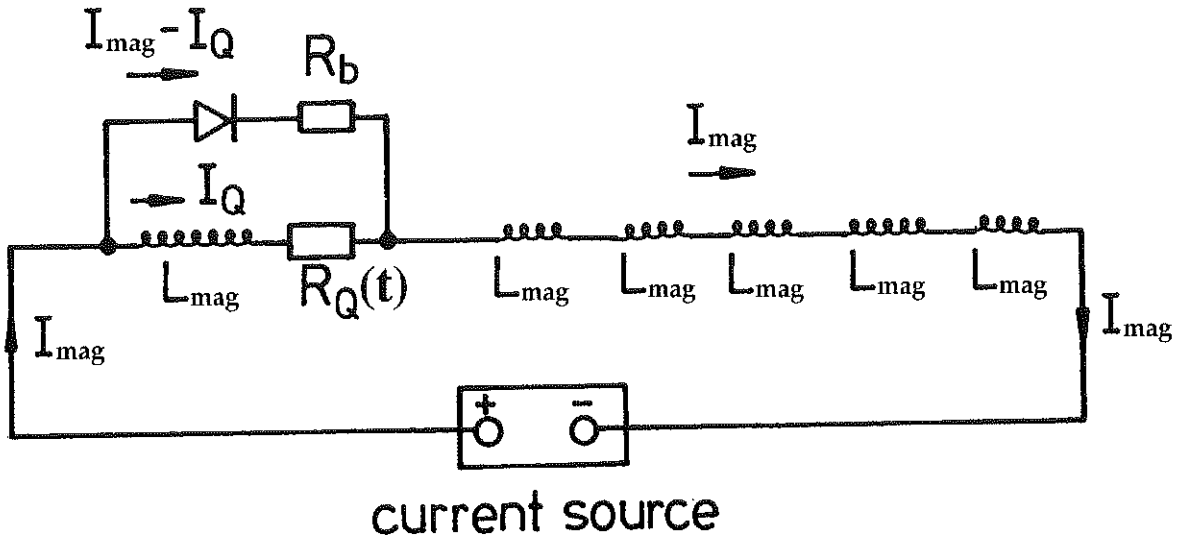

Figure 60. Electrical circuit of a quenching magnet in a magnet string [11].

Unlike in the case of a single magnet, the current decay rate in the sector must be limited for at least two reasons: (1) to prevent the induction of large coupling currents in the magnet coils (which may quench the remaining magnets in the sector, resulting in general warming and significant helium venting), and (2) to avoid the occurrence of unacceptable voltages to ground (because of the large overall inductance of the sector). A too slow decay rate, however, creates the risk that a significant fraction of the total energy stored in the sector be dissipated in the quenching magnet, resulting in destructive overheating.

These contradictory considerations can be reconciled by forcing the current to bypass the quenching magnet and by ramping the current down at the desired rate in the remaining un-quenched magnets. The bypass elements consist of diodes (or thyristors) connected in parallel to individual or small groups of magnets, as shown in Figure 60. As long as the magnets are superconducting, the current flows through the magnets. Once a magnet has quenched and starts to develop a resistive voltage, the main current is bypassed through the diode connected in parallel and the quenching magnet is discharged over the diode circuit. The current decay is determined by an equation similar to Eq. (281), except that R_{ext} has to be replaced by the resistance associated with the bypass element, R_b.

HERA, RHIC and LHC rely on silicon diodes, which are mounted inside the helium cryostats and operate at cryogenic temperatures. The main requirements for these cold diodes are [223]: (1) small forward voltage and low dynamic resistance (to limit power dissipation in the diodes), (2) good radiation hardness, and (3) large backward voltage.

In the case of the Tevatron, which has a short current ramp time resulting in large inductive voltages across the bypass elements, the diodes are replaced by thyristors operating as fast switches [224]. The thyristors are located outside the magnet cryostats and require additional power leads and cryogenic feedthroughs.

The protection system of the magnet ring must be carefully designed and thoroughly tested before starting up the machine. The system tests are usually carried out on a cell or a half-cell representative of the magnet lattice and all failure modes are investigated [225]–[227].

12 CONCLUSION AND PERSPECTIVES

High energy physics has been the main driving force for the development of high performance superconducting cables and magnets.

As of today, two large superconducting particle accelerator rings, Tevatron and HERA, have been built and are reliably operated for several years. The construction of RHIC at BNL has been completed and machine commissioning is underway. In addition, CERN is pursuing the development of LHC and significant programs are carried out at associated laboratories, such as CEA/Saclay, Fermilab and KEK. LHC is by far the most ambitious and most challenging project in applied superconductivity. Contracts for the production of 1210 metric tons of NbTi cables have already been signed, while contracts for the production of about 1250 arc dipole magnets and 400 arc quadrupole magnets, to be operated at 1.9 K in superfluid helium, are expected to be awarded in the next two years.

Since the time of the Tevatron (late 1970's), a factor of about two has been gained on the critical current density of NbTi at 4.2 K and 5 T and a dipole field of 10.5 T has been reached on a short magnet model relying on NbTi cables at 1.8 K. In recent years, encouraging results have been obtained on a couple of short dipole magnet models relying on Nb_3Sn cables, which may open the range 10 to 15 T. However, given the present (1999) cost of Nb_3Sn technology, its main application to particle accelerators in the oncoming decade is likely to be special dipole and quadrupole magnets for the insertion regions (especially, near the interaction points). In these crowded regions, the production of higher field and higher field gradient can be used to shorten magnet length and free up much needed space.

Regarding a possible post-LHC machine, it is widely thought that, after the collapse of SSC, the USA will not fund such a project until LHC is turned on and shows evidences that it is worthwhile to go to higher energies. It remains, however, that a number of accelerator physicists, especially in the USA, still believe that the 20-TeV-per-beam SSC was the right machine to built and fear that the 7-TeV-per-beam LHC could be too short sighted.

In any case, it is obvious that any big machine beyond LHC will require at least two things: (1) a significant improvement in magnet technology to achieve higher performances and (2) a significant value-engineering effort to reduce magnet costs. Given that, from the time of its inception to the time of its commissioning, LHC will have taken nearly 25 years to build, it seems imperative that reasonable R&D efforts, supported by adequate resources, be pursued in several laboratories around the world to develop the materials and work out the assembly processes that will be needed for the magnets of tomorrow's machines.

ACKNOWLEDGMENTS

The author wishes to thank C. Wyss for his continuous support and interest, and F. Simon for his comments on the sections on complex formalism for magnetic field and magnetic flux computations.

REFERENCES

[1] C. Quigg, *The Third Bernard Gregory Lectures*, CERN/89–11, Geneva: CERN, December 1989.

[2] *LEP Design Report, Vol. 2: The LEP Main Ring*, CERN–LEP/84–01, Geneva: CERN, June 1984.

[3] J.M. Baze, H. Desportes, R. Duthil, J.M. Garin, Y. Pabot, J. Heitzmann, M. Jacquemet, J.P. Jacquemin, F. Kircher, J.C. Languillat, J. Le Bars, A. Le Coroller, C. Lesmond, J.C. Lottin, J.P. Lottin, C. Mathis, C. Meuris, J.C. Sellier and C. Walter, "Design, construction and test of the large superconducting solenoid ALEPH," *IEEE Trans. Magn.*, Vol. 24 No. 2, pp. 1260–1263, 1988.

[4] P. Lefèvre and T. Petterson (eds.), *The Large Hadron Collider: Conceptual Design*, CERN/AC/95–05(LHC), Geneva: CERN, 20 October 1995.

[5] S. Humphries, Jr., *Principles of Charged Particle Acceleration*, New York: John Wiley & Sons, 1986.

[6] D.A. Edwards and M.J. Syphers, *An Introduction to the Physics of High Energy Particle Accelerators*, New York: John Wiley & Sons, 1993.

[7] H. Padamsee, J. Knobloch and T. Hays, *RF Superconductivity for Accelerators*, New York: John Wiley & Sons, 1998.

[8] C. Wyss (ed.), *LEP Design Report, Vol. 3: LEP2*, CERN–AC/96–01, Geneva: CERN, June 1996.

[9] M. Peckeler, "Experience with superconducting cavity operation in the TESLA Test Facility," *Proc. of the 1999 Particle Accelerator Conference*, IEEE Catalogue 99CH36366, pp. 245–249, 1999.

[10] R. Brinkmann, "Status of the design for the TESLA linear collider," *Proc. of the 1995 Particle Accelerator Conference*, IEEE Catalogue 95CH35843, pp. 674–676, 1996.

[11] K.-H. Mess, P. Schmüser and S. Wolf, *Superconducting Accelerator Magnets*, Singapore: World Scientific, 1996.

[12] K. Tsuchiya, T. Ogitsu, N. Ohuchi, T. Ozaki, N. Toge and H. Sakurabata, "Superconducting magnets for the interaction region of KEKB," *IEEE Trans. Appl. Supercond.*, Vol. 9 No. 2, pp. 1045–1048, 1999.

[13] H. Desportes, "Advanced features of very large superconducting magnets for SSC and LHC detectors," *IEEE Trans. Mag.*, Vol. 30 No. 4, pp. 1525–1532, 1994.

[14] R. Ostojic, T.M. Taylor and S. Weisz, "Systems layout of the low-β insertions for the LHC experiments," *Proc. of the 1997 Particle Accelerator Conference*, IEEE Catalogue 97CH36167, pp. 3696–3698, 1998.

[15] H.H.J. ten Kate, "The superconducting magnet system for the ATLAS detector," *IEEE Trans. Appl. Supercond.*, Vol. 9 No. 2, pp. 841–846, 1999.

[16] A. Yamamoto, T. Kondo, Y. Doi, Y. Makida, K. Tanaka, T. Haruyama, H. Yamaoka, H. ten Kate, L. Bjorset, K. Wada, S. Meguro, J.S.H. Ross, and K.D. Smith, "Design and development of the ATLAS Central Solenoid," *IEEE Trans. Appl. Supercond.*, Vol. 9 No. 2, pp. 852–855, 1999.

[17] J.M. Baze, C. Berriaud, C. Curé, A. Daël, H. Desportes, R. Duthil, B. Gallet, F.P. Juster, C. Lesmond, C. Mayri, and Y. Pabot, "Progress in the design of a superconducting toroidal magnet for the ATLAS detector on LHC," *IEEE Trans. Mag.*, Vol. 32 No. 4, pp. 2047–2050, 1996.

[18] A. Daël, J. Belorgey, C. Berriaud, R. Berthier, D. Cacaut, H. Desportes, B. Gallet, B. Gastineau, M. Jacquemet, F.P. Juster, C. Lesmond, C. Mayri, Y. Pabot, J.M. Rey, H. van Hille, Z. Sun, E. Acerbi, F. Alessandria, G. Ambrosio, F. Broggi, L. Rossi, M. Sorbi, G. Volpini, "Progress in the design of the barrel toroid magnet for the ATLAS experiment and associated R&D at CEA-Saclay and INFN-Milano," *Proc. of Fifteenth International Conference on Magnet Technology (MT15)*, Beijing: Science Press, pp. 92–95, 1998.

[19] D.E. Baynham, J. Butterworth, F.S. Carr, M.J.D. Couthold, D.A. Cragg, C.J. Densham, D. Evans, E. Holtom, S.J. Robertson, D. Sole, and E.F. Towndrow, "Engineering design and optimization of the superconducting End Cap Toroid magnets for the ATLAS experiment at LHC," *IEEE Trans. Appl. Supercond.*, Vol. 9 No. 2, pp. 856–859, 1999.

[20] J.C. Lottin, H. Desportes, C. Lesmond, C. Lyraud, C. Pes, and A. Hervé, "Conceptual design of the CMS 4 Tesla solenoid," *Adv. Cryo. Eng.*, Vol. 41A, pp. 819–825, 1996.

[21] F. Kircher, B. Levesy, Y. Pabot, D. Campi, B. Curé, A. Hervé, I.L. Horvath, P. Fabbricatore, and R. Musenich, "Status report on the CMS superconducting solenoid for LHC," *IEEE Trans. Appl. Supercond.*, Vol. 9 No. 2, pp. 837–840, 1999.

[22] H.T. Edwards, "The Tevatron energy doubler: a superconducting accelerator," *Ann. Rev. Nucl. Part. Sci.*, Vol. 35, pp. 605–660, 1985.

[23] A.V. Tollestrup, "Superconducting magnets." In R.A. Carrigan, F.R. Huson and M. Month (eds.), *Physics of High Energy Accelerators*, AIP Conference Proceedings, Vol. 87, pp. 699–804, 1982.

[24] K. Koepke, G. Kalbfleisch, W. Hanson, A. Tollestrup, J. O'Meara and J. Saarivirta, "Fermilab doubler magnet design and fabrication techniques," *IEEE Trans. Magn.*, Vol. MAG-15 No. 1, pp. 658–661, 1979.

[25] F. Turkot, W.E. Cooper, R. Hanft and A. McInturff, "Maximum field capabilities of energy saver superconducting magnets," *IEEE Trans. Nucl. Sci.*, Vol. NS–30 No. 4, pp. 3387–3389, 1983.

[26] R. Hanft, B.C. Brown, W.E. Cooper, D.A. Gross, L. Michelotti, E.E. Schmidt and F. Turkot, "Magnetic field properties of Fermilab energy saver dipoles," *IEEE Trans. Nucl. Sci.*, Vol. NS–30 No. 4, pp. 3381–3383, 1983.

[27] E.E. Schmidt, B.C. Brown, W.E. Cooper, H.E. Fisk, D.A. Gross, R. Hanft, S. Ohnuma and F.T. Turkot, "Magnetic field data on Fermilab energy saver quadrupoles," *IEEE Trans. Nucl. Sci.*, Vol. NS–30 No. 4, pp. 3384–3386, 1983.

[28] B.H. Wiik, "The status of HERA," *Conference Record of the 1991 IEEE Particle Accelerator Conference*, IEEE catalogue 91CH3038–7, pp. 2905–2909, 1991.

[29] S. Wolff, "Superconducting HERA magnets," *IEEE Trans. Magn.*, Vol. 24 No. 2, pp. 719–722, 1988.

[30] P. Schmüser, "Field quality issues in superconducting magnets," *Conference Record of the 1991 IEEE Particle Accelerator Conference*, IEEE catalogue 91CH3038–7, pp. 37–41, 1991.

[31] R. Meinke, "Superconducting magnet system for HERA," *IEEE Trans. Magn.*, Vol. 27 No. 2, pp. 1728–1734, 1991.

[32] R. Auzolle, A. Patoux, J. Pérot and J.M. Rifflet, "Construction and test of superconducting quadrupole prototypes for HERA," *Journal de Physique*, Vol. 45(Colloque C1, supplément au No. 1), pp. 263–270, 1984.

[33] R. Auzolle, J. Pérot, J.M. Rifflet, A. Fokken, O. Peters, and S. Wolff, "First industry made superconducting quadrupoles for HERA," *IEEE Trans. Magn.*, Vol. 25 No. 2, pp. 1660–1662, 1989.

[34] V.I. Balbekov and G.G. Gurov, "IHEP accelerating and storage complex: status and possibility of B–factory," *Nuclear Instruments and Methods in Physics Research*, Vol. A 333, pp. 189–195, 1993.

[35] A.V. Zlobin, "UNK superconducting magnets development," *Nuclear Instruments and Methods in Physics Research*, Vol. A 333, pp. 196–203, 1993.

[36] R.F. Schwitters, "Future hadron collider: the SSC." In J.R. Sanford (ed.), *Proc. of the 26th International Conference on High Energy Physics*, AIP Conference Proceedings, Vol. 272, pp. 306–320, 1993.

[37] A. Devred, T. Bush, R. Coombes, J. DiMarco, C. Goodzeit, J. Kuzminski, W. Nah, T. Ogitsu, M. Puglisi, P. Radusewicz, P. Sanger, R. Schermer, R. Stiening, G. Spigo, J. Tompkins, J. Turner, Y. Yu, Y. Zhao, H. Zheng, M. Anerella, J. Cottingham, G. Ganetis, M. Garber, A. Ghosh, A. Greene, R. Gupta, A. Jain, S. Kahn, E. Kelly, G. Morgan, J. Muratore, A. Prodell, M. Rehak, E.P. Rohrer, W. Sampson, R. Shutt, R. Thomas, P. Thompson, P. Wanderer, E. Willen, M. Bleadon, R. Bossert, J. Carson, S. Delchamps, S. Gourlay, R. Hanft, W. Koska, M. Kuchnir, M. Lamm, P. Mantsch, P.O. Mazur, D. Orris, J. Ozelis, T. Peterson, J. Strait, M. Wake, J. Royet, R. Scanlan and C. Taylor, "Review of SSC dipole magnet mechanics and quench performance." In J. Nonte (ed.), *Supercollider 4*, New York: Plenum Press, pp. 113–136, 1992.

[38] P. Wanderer, M. Anerella, J. Cottingham, G. Ganetis, M. Garber, A. Ghosh, A. Greene, R Gupta, A. Jain, S. Kahn, E. Kelly, G. Morgan, J. Muratore, A. Prodell, M. Rehak, E.P. Rohrer, W. Sampson, R. Shutt, R. Thomas, P. Thompson, E. Willen, A. Devred, T. Bush, R. Coombes, J. DiMarco,

C. Goodzeit, J. Kuzminski, W. Nah, T. Ogitsu, M. Puglisi, P. Radusewicz, P. Sanger, R. Schermer, J. Tompkins, J. Turner, Y. Yu, Y. Zhao, H. Zheng, M. Bleadon, R. Bossert, J. Carson, S. Delchamps, S. Gourlay, R. Hanft, W. Koska, M. Kuchnir, M. Lamm, P. Mantsch, P.O. Mazur, D. Orris, J. Ozelis, T. Peterson, J. Strait, M. Wake, J. Royet, R. Scanlan and C. Taylor, "A summary of SSC dipole magnet field quality measurements." In J. Nonte (ed.), *Supercollider 4*, New York: Plenum Press, pp. 137–149, 1992.

[39] W. Nah, A. Akhmetov, M. Anerella, R. Bossert, T. Bush, D.W. Capone II, J. Carson, R. Coombes, J. Cottingham, S.W. Delchamps, A. Devred, J. DiMarco, G. Ganetis, M. Garber, C. Goodzeit, A. Ghosh, S. Gourlay, A. Greene, R. Gupta, R. Hanft, A. Jain, S. Kahn, E. Kelly, W. Koska, M. Kuchnir, J. Kuzminski, M.J. Lamm, P. Mantsch, P.O. Mazur, G. Morgan, J. Muratore, T. Ogitsu, D. Orris, J. Ozelis, T. Peterson, E.G. Pewitt, A. Prodell, M. Puglisi, P. Radusewicz, M. Rehak, E.P. Rohrer, J. Royet, W. Sampson, P. Sanger, R. Scanlan, R. Schermer, R. Shutt, R. Stiening, J. Strait, C. Taylor, R. Thomas, P. Thompson, J.C. Tompkins, J. Turner, M. Wake, P. Wanderer, E. Willen, Y. Yu, J. Zbasnik, Y. Zhao and H. Zheng, "Quench characteristics of 5-cm aperture, 15-m Long SSC dipole magnet prototypes," *IEEE Trans. Appl. Supercond.*, Vol. 3 No. 1, pp. 658–661, 1993.

[40] Y. Zhao, A. Akhmetov, M. Anerella, R. Bossert, T. Bush, D.W. Capone II, J. Carson, R. Coombes, J. Cottingham, S.W. Delchamps, A. Devred, J. DiMarco, G. Ganetis, M. Garber, C. Goodzeit, A. Ghosh, S. Gourlay, A. Greene, R. Gupta, R. Hanft, A. Jain, S. Kahn, E. Kelly, W. Koska, M. Kuchnir, J. Kuzminski, M.J. Lamm, P. Mantsch, P.O. Mazur, G. Morgan, J. Muratore, W. Nah, T. Ogitsu, D. Orris, J. Ozelis, T. Peterson, E.G. Pewitt, A. Prodell, M. Puglisi, P. Radusewicz, M. Rehak, E.P. Rohrer, J. Royet, W. Sampson, P. Sanger, R. Scanlan, R. Schermer, R. Shutt, R. Stiening, J. Strait, C. Taylor, R. Thomas, P. Thompson, J.C. Tompkins, J. Turner, M. Wake, P. Wanderer, E. Willen, Y. Yu, J. Zbasnik and H. Zheng, "Current dependence of harmonic field coefficients of 5-cm aperture, 15-m Long SSC dipole magnet prototypes," *IEEE Trans. Appl. Supercond.*, Vol. 3 No. 1, pp. 674–677, 1993.

[41] T. Ogitsu, A. Akhmetov, M. Anerella, R. Bossert, T. Bush, D.W. Capone II, J. Carson, R. Coombes, J. Cottingham, S.W. Delchamps, A. Devred, J. DiMarco, G. Ganetis, M. Garber, C. Goodzeit, A. Ghosh, S. Gourlay, A. Greene, R. Gupta, R. Hanft, A. Jain, S. Kahn, E. Kelly, W. Koska, M. Kuchnir, J. Kuzminski, M.J. Lamm, P. Mantsch, P.O. Mazur, G. Morgan, J. Muratore, W. Nah, D. Orris, J. Ozelis, T. Peterson, E.G. Pewitt, A. Prodell, M. Puglisi, P. Radusewicz, M. Rehak, E.P. Rohrer, J. Royet, W. Sampson, P. Sanger, R. Scanlan, R. Schermer, R. Shutt, R. Stiening, J. Strait, C. Taylor, R. Thomas, P. Thompson, J.C. Tompkins, J. Turner, M. Wake, P. Wanderer, E. Willen, Y. Yu, J. Zbasnik, Y. Zhao and H. Zheng, "Mechanical performance of 5-cm aperture, 15-m long SSC dipole magnet prototypes," *IEEE Trans. Appl. Supercond.*, Vol. 3 No. 1, pp. 686–691, 1993.

[42] P. Wanderer, M. Anerella, J. Cottingham, G. Ganetis, M. Garber, A. Ghosh, A. Greene, R Gupta, A. Jain, S. Kahn, E. Kelly, G. Morgan, J. Muratore, A. Prodell, M. Rehak, E.P. Rohrer, W. Sampson, R. Shutt, R. Thomas, P. Thompson, E. Willen, C. Goodzeit and P. Radusewicz, "Magnetic design and field quality measurements of full length 50-mm aperture SSC model dipoles built at BNL," *Int. J. Mod. Phys. A*, Proc. Suppl. Vol. 2B, pp. 641–643, 1993.

[43] J. Strait, R. Bossert, J. Carson, S.W. Delchamps, S. Gourlay, R. Hanft, W. Koska, M. Kuchnir, M.J. Lamm, P.O. Mazur, A. Mokhtarani, D. Orris, J. Ozelis, M. Wake, A. Devred, J. DiMarco, J. Kuzminski, M. Puglisi, J.C. Tompkins, Y. Yu, Y. Zhao, H. Zheng and T. Ogitsu, "Magnetic field measurements of full length 50-mm aperture SSC dipole magnets at Fermilab," *Int. J. Mod. Phys. A*, Proc. Suppl. Vol. 2B, pp. 656–658, 1993.

[44] R.I. Schermer, "Status of superconducting magnets for the superconducting super collider," *IEEE Trans. Magn.*, Vol. 30 No. 2, pp. 1587–1594, 1994.

[45] H. Foelsche, H. Hahn, M. Harrison, S. Ozaki and M.J. Rhoades-Brown, "The relativistic heavy ion collider, RHIC." In H. Schopper (ed.), *Advances of Accelerator Physics and Technologies*, Advanced Series on Directions in High Energy Physics, Vol. 12, Singapore: World Scientific, pp. 104–131, 1993.

[46] P. Wanderer, J. Muratore, M. Anerella, G. Ganetis, A. Ghosh, A. Greene, R. Gupta, A. Jain, S. Kahn, E. Kelly, G. Morgan, A. Prodell, M. Rehak, W. Sampson, R. Thomas, P. Thompson and E. Willen, "Construction and testing of arc dipoles and quadrupoles for the relativistic heavy ion collider (RHIC) at BNL," *Proc. of the 1995 Particle Accelerator Conference*, IEEE catalogue 95CH35843, pp. 1293–1297, 1995.

[47] A. Greene, M. Anerella, J. Cozzolino, J. Escallier, D. Fisher, G. Ganetis, A. Ghosh, R. Gupta, A. Jain, S. Kahn, E. Kelly, R. Lebel, G. Morgan, A. Morgillo, S. Mulhall, J. Muratore, S. Plate, A. Prodell, M. Rehak, W. Sampson, R. Thomas, P. Thompson, P. Wanderer and E. Willen, "The magnet system of the relativistic heavy ion collider (RHIC)," *IEEE Trans. Mag.*, Vol. 32 No. 4, pp. 2041–2046, 1996.

[48] M. Anerella, D.H. Fisher, E. Sheedy and T. McGuire, "Industrial production of RHIC magnets," *IEEE Trans. Mag.*, Vol. 32 No. 4, pp. 2059–2064, 1996.

[49] R. Gupta, M. Anerella, G. Ganetis, M. Garber, A. Ghosh, A. Greene, A. Jain, S. Kahn, E. Kelly, E. Killian, G. Morgan, A. Morgillo, J. Muratore, A. Prodell, M. Rehak, W. Sampson, R. Shutt, P. Thompson, P. Wanderer and E. Willen, "Large aperture quadrupoles for RHIC interaction regions," *Proc. of the 1993 Particle Accelerator Conference*, IEEE Catalogue 93CH3279-7, pp. 2745–2747, 1993.

[50] J. Schmalze, M. Anerella, G. Ganetis, A. Ghosh, R. Gupta, A. Jain, S. Kahn, G. Morgan, A. Morgillo, J. Muratore, W. Sampson, P. Wanderer and E. Willen, "RHIC D0 insertion dipole design iteration during production," *Proc. of the 1997 Particle Accelerator Conference*, IEEE Catalogue 97CH36167, pp. 3356–3358, 1998.

[51] A.F. Greene, M.G. Garber, A.K. Ghosh, D. McChesney, A. Morgillo, R. Sah, S. DelRe, G. Epstein, S. Hong, J. Lichtenwalner, P. O'Larey, D. Smathers, M. Boivin and R. Meserve, "Manufacture and testing of the superconducting wire and cable for the RHIC dipoles and quadrupoles," *IEEE Trans. Appl. Supercond.*, Vol. 5 No. 2, pp. 397–399, 1995.

[52] L.R. Evans, "The large hadron collider project." In T. Haruyama, T. Mitsui and K. Yamafuji (eds.), *Proc. of the 16th International Cryogenic Engineering Conference/International Cryogenic Materials Conference*, London: Elsevier, pp. 45–52, 1997.

[53] The LHC Magnet Team, reported by R. Perin, "Status of the Large Hadron Collider magnet development," *IEEE Trans. Mag.*, Vol. 30 No. 4, pp. 1579–1586, 1994.

[54] R. Perin, "Status of LHC programme and magnet development," *IEEE Trans. Appl. Supercond.*, Vol. 5 No. 2, pp. 189–195, 1995.

[55] N. Siegel, "Status of the Large Hadron Collider and magnet program," *IEEE Trans. Appl. Supercond.*, Vol. 7 No. 2, pp. 252–257, 1997.

[56] J. Billan, M. Bona, L. Bottura, D. Leroy, O. Pagano, R. Perin, D. Perini, F. Savary, A. Siemko, P. Sievers, G. Spigo, J. Vlogaert, L. Walckiers, C. Wyss, and L. Rossi, "Test results on the long models and full scale prototypes of the second generation LHC arc dipoles," *IEEE Trans. Appl. Supercond.*, Vol. 9 No. 2, pp. 1039–1044, 1999.

[57] J.M. Baze, D. Cacaut, M. Chapman, J.P. Jacquemin, C. Lyraud, C. Michez, Y. Pabot, J. Perot, J.M. Rifflet, J.C. Toussaint, P. Védrine, R. Perin, N. Siegel and T. Tortschanoff, "Design and fabrication of the prototype superconducting quadrupole for the CERN LHC project," *IEEE Trans. Magn.*, Vol. 28 No. 1, pp. 335–337, 1992.

[58] J.M. Rifflet, J. Cortella, J. Deregel, P. Genevey, J. Pérot, P. Vedrine, K.H. Henrichsen, F. Rodriguez–Mateos, N. Siegel and T. Tortschanoff, "Cryogenic and mechanical measurements of the first two LHC lattice quadrupole prototypes." In V. Suller and Ch. Petit-Jean-Genaz (eds.), *Proc. of the Fourth European Particle Accelerator Conference.*, Singapore: World Scientific, pp. 2265–2267, 1994.

[59] A. Devred, J. Belorgey, J. Deregel, B. Gallet, P. Genevey, J.M. Rifflet, J.Cl. Sellier, P. Védrine and J. Billan, "Field quality of LHC/Saclay arc quadrupole magnet prototype." In S. Myers, A. Pacheco, R. Pascual, Ch. Petit-Jean-Genaz and J. Poole (eds.), *Proc. of the Fifth European Particle Accelerator Conference*, Bristol: Institute of Physics Publishing, pp. 2225–2227, 1996.

[60] J. Kerby, A.V. Zlobin, R. Bossert, J. Brandt, J. Carson, D. Chichili, J. Dimarco, S. Feher, M.J. Lamm, P.J. Limon, A. Makarov, F. Nobrega, I. Novitski, D. Orris, J. P. Ozelis, B. Robotham, G. Sabbi, P. Schlabach, J.B. Strait, M. Tartaglia, J.C. Tompkins, S. Caspi, A.D. McInturff, and R. Scanlan, "Design development and test of 2m quadrupole model magnets for the LHC inner triplet," *IEEE Trans. Appl. Supercond.*, Vol. 9 No. 2, pp. 689–692, 1999.

[61] T. Nakamoto, K. Tanaka, A. Yamamoto, K. Tsuchiya, E. Burkhardt, N. Higashi, N. Kimura, T. Ogitsu, N. Ohuchi, K. Sasaki, T. Shintomi, A. Terashima, G.A. Kirby, R. Ostojic, and T.M. Taylor, "Quench and mechanical behavior of an LHC low-β quadrupole model," *IEEE Trans. Appl. Supercond.*, Vol. 9 No. 2, pp. 697–700, 1999.

[62] R. Ostojic and T.M. Taylor, "Conceptual design of a 70 mm aperture quadrupole for LHC insertions," *IEEE Trans. Appl. Supercond.*, Vol. 3 No. 1, pp. 761–764, 1993.

[63] A. Jain, R. Gupta, P. Wanderer and E. Willen, "Magnetic design of dipoles for LHC Interaction Regions." In S. Myers, L. Liljeby, Ch. Petit-Jean-Genaz, J. Poole and K.-G. Rensfelt (eds.), *Proc. of the Sixth European Particle Accelerator Conference*, Bristol: Institute of Physics Publishing, pp. 1993–1995, 1998.

[64] M.N. Wilson, "Superconducting magnets for accelerators: a review," *IEEE Trans. Appl. Supercond.*, Vol. 7 No. 2, pp. 727–732, 1997.

[65] J. Pérot, "Special magnets." In S. Turner (ed.), *Proc. of the CERN Accelerator School on Superconductivity in Particle Accelerators*, CERN/89–04, Geneva: CERN, pp. 271–291, 1989.

[66] T. Shintomi, M. Wake, K. Tsuchiya, M. Kobayashi, H. Hirabayashi, K. Asano, F. Suzuki, T. Yamagiwa, R. Saito, K. Aihara, Y. Hakuraku and H. Moriai, "Development and test results of a 10 Tesla magnet for future accelerators." In C. Marinucci and P. Weymuth (eds.), *Proc. of 9th International Conference on Magnet Technology (MT9)*, Villigen, Switzerland: Swiss Institute for Nuclear Research (SIN), pp. 72–75, 1985.

[67] A. Siemko, private communication, December 1999.

[68] J.L. Borne, D. Bouichou, D. Leroy and W. Thomi, "Manufacturing of high (10 Tesla) twin aperture superconducting dipole magnet for LHC," *IEEE Trans. Magn.*, Vol. 28 No. 1, pp. 323–326, 1992.

[69] D. Leroy, J. Krzywinski, L. Oberli, R. Perin, F. Rodriguez-Mateos, A. Verweij and L. Walckiers, "Test results on 10 T LHC superconducting one metre long dipole models," *IEEE Trans. Appl. Supercond.*, Vol. 3 No. 1, pp. 614–621, 1993.

[70] J. Buckley, J.J. Hirsbrunner, T. Kurtyka, D. Leroy, D. Perini, A. Poncet, M. Karppinen, F. Robatto, F. Savary, G. Spigo and I. Vanenkov, "Mechanical behavior during excitation of the first CERN 10 T dipole magnet model for LHC." In V. Suller and Ch. Petit-Jean-Genaz (eds.), *Proc. of the Fourth European Particle Accelerator Conference*, Singapore: World Scientific, pp. 2286–2288, 1994.

[71] The LHC Machine Group reported by G. Brianti, "LHC progress and status," *Proc. of the 1993 Particle Accelerator Conference*, IEEE Catalogue 93CH3279–7, pp. 3917–3921, 1993.

[72] J. Ahlbäck, J. Ikäheimo, J. Järvi, D. Leroy, L. Oberli, R. Perin, D. Perini, S. Russenchuck, J. Salminen, M. Savelainen, J. Soini, G. Spigo and T. Tortschanoff, "Electromagnetic and mechanical design of a 56 mm aperture model dipole for the LHC," *IEEE Trans. Magn.*, Vol. 30 No. 4, pp. 1746–1749, 1994.

[73] J. Ahlbäck, D. Leroy, L. Oberli, D. Perini, J. Salminen, M. Savelainen, J. Soini and G. Spigo, "Construction of a 56 mm aperture high-field twin-aperture superconducting dipole magnet," *IEEE Trans. Magn.*, Vol. 32 No. 4, pp. 2097–2100, 1996.

[74] D. Leroy, L. Oberli, D. Perini, A. Siemko and G. Spigo, "Design features and performance of a 10 T twin aperture model dipole for LHC." In L. Lianghzhen, S. Guoliao and Y. Lugang (eds.), *Proc. of Fifteenth International Conference on Magnet Technology (MT15)*, Beijing: Science Press, pp. 119–122, 1998.

[75] A. Yamamoto, T. Shintomi, N. Kimura, Y. Doi, T. Haruyama, N. Higashi, H. Hirabayashi, H. Kawamata, S.W. Kim, T.M. Kobayashi, Y. Makida, T. Ogitsu, N. Ohuchi, K. Tanaka, A. Terashima, K. Tsuchiya, H. Yamaoka, G. Brianti, D. Leroy, R. Perin, S. Mizumaki, S. Kato, K. Makishima,

T. Orikasa, T. Maeto and A. Tanaka, "Test results of a single aperture 10 Tesla dipole model magnet for the Large Hadron Collider," *IEEE Trans. Magn.*, Vol. 32 No. 4, pp. 2116–2119, 1996.

[76] N. Andreev, K. Artoos, L. Bottura, G. Kirby, D. Leroy, L. Oberli, J. Ostler, D. Perini, A. Poncet, F. Rodriguez-Mateos, S. Russenschuck, T. Siambanis, N. Siegel, A. Siemko, D. Tommasini, G. Trinquart, I. Vanenkov, L. Walckiers, and W. Weterings, "The 1m long single aperture dipole coil test program for LHC," *Proc. of the Fifth European Particle Accelerator Conference*, Bristol: Institute of Physics Publishing, pp. 2258–2260, 1996.

[77] A. Siemko, G. Kirby, J. Ostler, D. Perini, N. Siegel, D. Tommasini and L. Walckiers, "Power test results of the first LHC second generation superconducting single aperture 1m long dipole models." In T. Haruyama, T. Mitsui and K. Yamafuji (eds.), *Proc. of the 16th International Cryogenic Engineering Conference/International Cryogenic Materials Conference*, London: Elsevier, pp. 837–842, 1997.

[78] N. Andreev, K. Artoos, T. Kurtyka, D. Leroy, L. Oberli, D. Perini, S. Russenschuck, N. Siegel, A. Siemko, D. Tommasini, I. Vanenkov, L. Walckiers, and W. Weterings, "Present state of the single and twin aperture short dipole model program for the LHC." In L. Lianghzhen, S. Guoliao and Y. Luguang (eds.), *Proc. of Fifteenth International Conference on Magnet Technology (MT15)*, Beijing: Science Press, pp. 115–118, 1998.

[79] N. Andreev, K. Artoos, T. Kurtyka, L. Oberli, D. Perini, S. Russenschuck, N. Siegel, A. Siemko, D. Tommasini, I. Vanenkov and L. Walckiers, "State of the short dipole model program for the LHC." In S. Myers, L. Liljeby, Ch. Petit-Jean-Genaz, J. Poole and K.-G. Rensfelt (eds.), *Proc. of the Sixth European Particle Accelerator Conference*, Bristol: Institute of Physics Publishing, pp. 311–313, 1998.

[80] D. Dell'Orco, S. Caspi, J. O'Neill, A. Lieztke, R. Scanlan, C.E. Taylor and A. Wandesforde, "A 50 mm bore superconducting dipole with a unique iron yoke structure," *IEEE Trans. Appl. Supercond.*, Vol. 3 No. 1, pp. 637–641, 1993.

[81] S. Caspi, K. Chow, D. Dell'Orco, R. Hannaford, H. Higley, A. Lietzke, A. McInturff, M. Morrison, L. Morrison, R.M. Scanlan and H. Van Oort, "Design and construction of a hybrid –Nb3Sn, NbTi– dipole magnet," *IEEE Trans. Appl. Supercond.*, Vol. 7 No. 2, pp. 547–550, 1997.

[82] A.F. Lietzke, R. Benjegerdes, S. Caspi, D. Dell'Orco, W. Harnden, A.D. McInturff, M. Morrison, R.M. Scanlan, C.E. Taylor and H. Van Oort, "Test results for a Nb3Sn dipole magnet," *IEEE Trans. Appl. Supercond.*, Vol. 7 No. 2, pp. 739–742, 1997.

[83] D. Leroy, G. Spigo, A.P. Verweij, H. Boschman, R. Dubbeldam and J. Gonzalez Pelayo, "Design and manufacture of a large-bore 10 T superconducting dipole for the CERN cable test facility," Presented at the 16th International Conference on Magnet Technology (MT16), Ponte Verde Beach, FL, September 26–October 2, 1999.

[84] A. Verweij, private communication, December 1999.

[85] A. den Ouden, S. Wessel, E. Krooshoop, R. Dubbeldam and H.H.J. ten Kate, "An experimental 11.5 T Nb_3Sn LHC type of dipole magnet," *IEEE Trans. Magn.*, Vol. 30 No. 4, pp. 2320–2323, 1994.

[86] A. den Ouden, S. Wessel, E. Krooshoop and H ten Kate, "Application of Nb_3Sn superconductors to high-field accelerator magnets," *IEEE Trans. Appl. Supercond.*, Vol. 7 No. 2, pp. 733–738, 1997.

[87] A. den Ouden, H. ten Kate, A. Siemko, P. Sievers, and L. Walckiers, "Quench characteristics of the 11 T Nb_3Sn model dipole magnet MSUT." In L. Lianghzhen, S. Guoliao and Y. Lugang (eds.), *Proc. of Fifteenth International Conference on Magnet Technology (MT15)*, Beijing: Science Press, pp. 339–342, 1998.

[88] D. Dell'Orco, R.M. Scanlan and C.E. Taylor, "Design of the Nb_3Sn dipole D20," *IEEE Trans. Appl. Supercond.*, Vol. 3 No. 1, pp. 82–86, 1993.

[89] A.D. McInturff, R. Benjegerdes, P. Bish, S. Capsi, K. Chow, D. Dell'Orco, D. Dietderich, R. Hannaford, W. Harnden, H. Higley, A. Lietzke, L. Morrison, R. Scanlan, J. Smithwick, C. Taylor and J.M. van Oort, "Test results for a high field (13T) Nb_3Sn dipole," *Proc. of the 1997 Particle Accelerator Conference*, IEEE Catalogue 97CH36167, pp. 3212–3214, 1998.

[90] S. Caspi, K. Chow, D.R. Dietderich, A.F. Lietzke, A.D. McInturff and R.M. Scanlan, "Development of high field dipole magnets for future accelerators." In L. Lianghzhen, S. Guoliao and Y. Lugang (eds.),

Proc. of Fifteenth International Conference on Magnet Technology (MT15), Beijing: Science Press, pp. 51–54, 1998.

[91] A. Devred, L. Bacquart, P. Bredy, C.E. Bruzek, Y. Laumond, R. Otmani and T. Schild, "Interstrand resistance measurements on Nb_3Sn Rutherford-type cables," *IEEE Trans. Appl. Supercond.*, Vol. 9 No. 2, pp. 722–726, 1999.

[92] A. Devred, P. Bredy, M. Durante, C. Gourdin, J.M. Rey, and M. Reytier, "Insulation systems for Nb_3Sn accelerator magnet coils fabricated by the wind and react technique," Presented at the Cryogenic Engineering Conference (CEC/ICMC99), Montréal, Québec (Canada), July 12–16, 1999.

[93] E. Klein, O. Napoly and J.M. Rifflet, "Final focus system with superconducting magnets in the interaction region of the TESLA linear collider." IN K. Takata, Y. Yamazaki and K. Nakahara (eds.), *Proc. of the 1994 International Linac Conference*, Tsukuba, Japan: KEK, National Laboratory for High Energy Physics, pp. 68–70, 1994.

[94] G. Ambrosio, N. Andreev, T. Arkan, E. Barzi, D. Chichili, V. Kashikhin, P.J. Limon, T. Ogitsu, J. Ozelis, I. Terechkine, J.C. Tompkins, S. Yadav, R. Yamada, V. Yarba, A.V. Zlobin, S. Caspi, and M. Wake, "Conceptual design of the Fermilab Nb3Sn high field dipole magnet model," *Proc. of the 1999 Particle Accelerator Conference*, IEEE Catalogue 99CH36366, pp. 174–176, 1999.

[95] D.R. Chichili, T.T. Arkan, I. Terechkine, and J.A. Rice, "Niobium-tin magnet technology development at Fermilab," *Proc. of the 1999 Particle Accelerator Conference*, IEEE Catalogue 99CH36366, pp. 3242–3244, 1999.

[96] G. Dugan, "Very Large Hadron Collider R&D," *Proc. of the 1999 Particle Accelerator Conference*, IEEE Catalogue 99CH36366, pp. 48–52, 1999.

[97] G. Ambrosio, G. Bellomo and L. Rossi, "A 300 T/m NbSn quadrupole for the low-beta insertion of the LHC." In S. Myers, A. Pacheco, R. Pascual, Ch. Petit-Jean-Genaz and J. Poole (eds.), *Proc. of Fifth European Particle Accelerator Conference*, Bristol: Institute of Physics Publishing, pp. 2290–2292, 1996.

[98] G. Ambrosio, M. Durante, D. Pedrini, M. Pojer, L. Rossi, R. Garrè, S. Conti and S. Rossi, "Characterization of a high critical current, low cabling degradation, NbSn conductor for accelerator magnets." In L. Lianghzhen, S. Guoliao and Y. Lugang (eds.), *Proc. of Fifteenth International Conference on Magnet Technology (MT15)*, Beijing: Science Press, pp. 993–996, 1998.

[99] T. Shintomi, private communication, August 1999.

[100] M. Wake, T.S. Jaffery, T. Shintomi, K. Mimori, H. Sugawara, R.M. Scanlan, A.D. McInturff, and A.F. Lietzke, "Nb3Sn insertion coils for the magnet development," ." In L. Lianghzhen, S. Guoliao and Y. Luguang (eds.), *Proc. of Fifteenth International Conference on Magnet Technology (MT15)*, Beijing: Science Press, pp. 103–106, 1998.

[101] R.C. Gupta, "A common coil design for high field 2-in-1 accelerator magnets," *Proc. of the 1997 Particle Accelerator Conference*, IEEE catalogue 97CH36167, pp. 3344–3346, 1998.

[102] K. Chow, D.R. Dietderich, S.A. Gourlay, R. Gupta, W. Harnden, A.F. Lietzke, A.D. McInturff, G.A. Millos, L. Morrison, M. Morrisson, and R.M. Scanlan, "Fabrication and test results of a Nb_3Sn superconducting racetrack dipole magnet," *Proc. of the 1999 Particle Accelerator Conference*, IEEE Catalogue 99CH36366, pp. 171–173, 1999.

[103] R. Gupta, K. Chow, D. Dietderich, S. Gourlay, G. Millos, A. McInturff, R. Scanlan, S. Ramberger, and S. Russenschuck, "A high field magnet design for a future hadron collider," *IEEE Trans. Appl. Supercond.*, Vol. 9 No. 2, pp. 701–704, 1999.

[104] R.M. Scanlan, D.R. Dietderich and H.C. Higley, "Conductor development for high field dipole magnets," Presented at the 16th International Conference on Magnet Technology (MT16), Ponte Verde Beach, FL, September 26–October 2, 1999.

[105] P.M. McIntyre, W. Shen, and R.M. Scanlan, "Ultra-high-field magnets for future hadron colliders," *IEEE Trans. Appl. Supercond.*, Vol. 5 No. 2, pp. 1099–1102, 1995.

[106] N. Diaczenko, T. Elliott, A. Jaisle, D. Latypov, P. McIntyre, P. McJunkins, L. Richards, W. Shen, R. Soika, D. Wendt, and R. Gaedke, "Stress management in high field dipoles," *Proc. of the 1997 Particle Accelerator Conference*, IEEE Catalogue 97CH36167, pp. 3443–3445, 1998.

[107] A. Abreu, C. Battle, G. Cryer, N. Diaczenko, T. Elliott, H. Eucker, D. Gross, E. Hill, B. Henchel, A. Jaisle, D. Latypov, P. McIntyre, P. McJunkins, S. Munson, D. Sattarov, W. Shen, R. Soika, M. Spears, "Block-coil dipole for future hadron colliders," *IEEE Trans. Appl. Supercond.*, Vol. 9 No. 2, pp. 705–708, 1999.

[108] A. den Ouden, H.H.J. ten Kate, G. Kirby, and T. Taylor, "A 10 T Nb_3Sn model separator dipole magnet for the CERN LHC." In L. Lianghzhen, S. Guoliao and Y. Lugang (eds.), *Proc. of Fifteenth International Conference on Magnet Technology (MT15)*, Beijing: Science Press, pp. 137–140, 1998.

[109] E. Gregory, "Conventional wire and cable technology." In M. Month and M. Dienes (eds.), *The Physics of Particle Accelerators*, AIP Conference Proceedings, Vol. 249 No. 2, pp. 1198–1229, 1992.

[110] P.J. Lee, D.C. Larbalestier, K. Togano, K. Tachikawa, M. Suzuki, K. Hamasaki, K. Noto and K. Watanabe, "Chapter 5: Fabrications Methods." In K. Osamura (ed.), *Composite Superconductors*, New York: Marcel Dekker, Inc., pp. 237–321, 1994.

[111] M.N. Wilson, "Superconducting materials for magnets." In S. Turner (ed.), *Proc. of the CERN Accelerator School on Superconductivity in Particle Accelerators*, CERN/96–03, Geneva: CERN, pp. 47–69, 1996.

[112] E.W. Collings, *Applied Superconductivity, Metallurgy and Physics of Titanium Alloys, Volume 1: Fundamentals*, New York: Plenum Press, 1986.

[113] E.W. Collings, *Applied Superconductivity, Metallurgy and Physics of Titanium Alloys, Volume 2: Applications*, New York: Plenum Press, 1986.

[114] P.J. Lee and D.C. Larbalestier, "Development of nanometer scale structures in composites of Nb–Ti and their effect on the superconducting critical current densities," *Acta Metall.*, Vol. 35 No. 10, pp. 2523–2356, 1987.

[115] C. Meingast and D.C. Larbalestier, "Quantitative description of a very high critical current density NbTi superconductor during its final optimization strain. II. Flux pinning mechanisms," *J. Appl. Phys.*, Vol. 66 No. 12, 5971-5983, 1989.

[116] D.G. Hawksworth and D.C. Larbalestier, "Enhanced value of H_{C2} in Nb–Ti ternary and quaternary alloys," *Adv. Cryo. Eng. (Materials)*, Vol. 26, pp. 479–486, 1980.

[117] P.J. Lee and D.C. Larbalestier, "Determination of the flux pinning force of α–Ti ribbons in Nb46.5wt% Ti produces by heat treatments of varying temperature, duration and frequency," *Journal of Materials Science*, Vol. 23, pp. 3951–3957, 1988.

[118] P.J. Lee, J.C. McKinnel and D.C. Larbalestier, "Restricted, novel heat treatments for obtaining high J_C in Nb46.5wt%Ti," *Adv. Cryo. Eng. (Materials)*, Vol. 36, pp. 287–294, 1990.

[119] P.J. Lee, D.C. Larbalestier, J.C. McKinnell and A.D. McInturff, "Microstructure property relationship in Nb–Ti–Ta," *IEEE Trans. Appl. Supercond.*, Vol. 3 No. 1, pp. 1354–1357, 1993.

[120] J.W. Ekin, "Strain effects in superconducting compounds" *Adv. Cryo. Eng. (Materials)*, Vol. 30, pp. 823–836, 1984.

[121] J.W. Ekin, "Effect of transverse compressive stress on the critical current and upper critical field of Nb_3Sn," *J. Appl. Phys.*, Vol. 62 No. 12, pp. 4929–4834, 1987.

[122] D.C. Larbalestier, "The road to conductors of high temperature superconductors: 10 years do make a difference!," *IEEE Trans. Appl. Supercond.*, Vol. 7 No. 2, pp. 90–97, 1997.

[123] M.N. Wilson, *Superconducting Magnets*, Oxford: Clarendon Press, 1983.

[124] D.P. Hampshire and H. Jones, "A detailed investigation of the *E–J* characteristic and the role of defect motion within the flux-line lattice for high-current-density, high-field superconducting compounds with particular reference to data on Nb_3Sn throughout its entire field–temperature phase space," *J. Phys. C: Solid State Phys.*, Vol. 20, pp. 3533–3552, 1987.

[125] W.H. Warnes and D.C. Larbalestier, "Critical current distributions in superconducting composites," *Cryogenics*, Vol. 26, pp. 643–653, 1986.

[126] J.W. Ekin, "Irregularities in Nb–Ti filament area and electric field versus current characteristics," *Cryogenics*, Vol. 27, pp. 603–607, 1987.

[127] Courtesy of Alstom/MSA/Fil, 3 bis avenue des 3 chênes, F-90018 BELFORT CEDEX, FRANCE, 1997.

[128] M. Garber, M. Suenaga, W.B. Sampson and R.L. Sabatini, "Effect of Cu_4Ti compound formation on the characteristics of NbTi accelerator magnet wire," *IEEE Trans. Nucl. Sci.*, Vol. NS–32 No. 5, pp. 3681–3683, 1985.

[129] A.K. Ghosh, W.B. Sampson, E. Gregory and T.S. Kreilick, "Anomalous low field magnetization in fine filament NbTi conductors," *IEEE Trans. Magn.*, Vol. MAG–23, pp. 1724–1727, 1987.

[130] E.W. Collings, K.R. Marken Jr., M.D. Sumption, E. Gregory and T.S. Kreilick, "Magnetic studies of proximity-effect coupling in a very closely spaced fine-filament NbTi/CuMn composite superconductor," *Adv. Cryo. Eng. (Materials)*, Vol. 36, pp. 231–238, 1990.

[131] K.J. Faase, P.J. Lee, J.C. McKinnel and D.C. Larbalestier, "Diffusional reaction rates through the Nb wrap in SSC and other advanced multifilamentary Nb 46.5WT%Ti composites," *Adv. Cryo. Eng. (Materials)*, Vol. 38, pp. 723–730, 1992.

[132] M.S. Lubell, "Empirical scaling formulas for critical current and critical fields for commercial NbTi," *IEEE Trans. Magn.*, Vol. MAG-19 No. 3, pp. 754–757, 1983.

[133] L. Bottura, "A practical fit for the critical surface of NbTi," Presented at the 16th International Conference on Magnet Technology (MT16), Ponte Verde Beach, FL, September 26–October 2, 1999.

[134] D.C. Larbalestier and P.J. Lee, "New development in niobium titanium superconductors," *Proc. of the 1995 IEEE Particle Accelerator Conference*, IEEE catalogue 95CH35843, pp. 1276–1281, 1996.

[135] L.T. Summers, M.W. Guinan, J.R. Miller and P.A. Hahn, "A model for the prediction of Nb_3Sn critical current as a function of field, temperature, strain and radiation damage," *IEEE Trans. Magn.*, Vol. 27 No. 2, pp. 2041–2044, 1991.

[136] R. Aymar, "Overview of the ITER project." In T. Haruyama, T. Mitsui and K. Yamafuji (eds.), *Proc. of the 16th International Cryogenic Engineering Conference/ International Cryogenic Materials Conference*, London: Elsevier, pp. 53–59, 1997.

[137] P. Bruzzone, H.H.J. ten Kate, C.R. Walters and M. Spadoni, "Testing of industrial Nb_3Sn strands for high field fusion magnets," *IEEE Trans. Magn.*, Vol. 30 No. 4, pp. 1986–1989, 1994.

[138] J.M. Royet and R.M. Scanlan, "Manufacture of keystoned flat superconducting cables for use in SSC dipoles," *IEEE Trans. Magn.*, Vol. MAG-23 No. 2, pp. 480–483, 1987.

[139] M.N. Wilson and R. Wolf, "Calculation of minimum quench energies in Rutherford-type cables," *IEEE Trans. Appl. Supercond.*, Vol. 7 No. 2, pp. 950–953, 1997.

[140] A.K. Ghosh, W.B. Sampson and M.N. Wilson, "Minimum quench energies of Rutherford cables and single wires," *IEEE Trans. Appl. Supercond.*, Vol. 7 No. 2, pp. 954–957, 1997.

[141] T. Shintomi, A. Terashima, H. Hirabayashi, M. Ikeda and H Ii, "Development of large keystone angle cable for dipole magnet with ideal arch structure," *Adv. Cryo. Eng. (Materials)*, Vol. 36(A), pp. 323–328, 1990.

[142] R.M. Scanlan and J.M. Royet, "Recent improvements in superconducting cable for accelerator dipole magnets," *Conference Record of the 1991 IEEE Particle Accelerator Conference*, IEEE catalogue 91CH3038–7, pp. 2155–2157, 1991.

[143] R.M. Scanlan, "The evolution of tooling, techniques, and quality control for accelerator dipole magnet cables," *IEEE Trans. Appl. Supercond.*, Vol. 3 No. 1, pp. 842–849, 1993.

[144] D. Richter, J.D. Adam, J.M. Depond, D. Leroy and L.R. Oberli, "DC measurements of electrical contacts between strands in superconducting cables for the LHC magnets," *IEEE Trans. Appl. Supercond.*, Vol. 7 No. 2, pp. 786–792, 1997.

[145] J.M. Depond, D. Leroy, L.R. Oberly and D. Richter, "Examination of contacts between strands by electrical measurement and topographical analysis," *IEEE Trans. Appl. Supercond.*, Vol. 7 No. 2, pp. 793–796, 1997.

[146] J.D. Adam, D. Leroy, L.R. Oberly, D. Richter, M.N. Wilson, R. Wolf, H. Higley, A.D. McInturff, R.M. Scanlan, A. Nijhuis, H.H.J. ten Kate and S. Wessel, "Rutherford cables with anisotropic transverse resistance," *IEEE Trans. Appl. Supercond.*, Vol. 7 No. 2, pp. 958–961, 1997.

[147] M. Garber, W.B. Sampson and M.J. Tannenbaum, "Critical current measurements on superconducting cables," *IEEE Trans. Mag.*, Vol. MAG–19 No. 3, pp. 720–723, 1983.

[148] H. Boschman, A.P. Verweij, S. Wessel, H.H.J. ten Kate and L.J.M. van de Klundert, "The effect of transverse loads up to 300 MPa on the critical currents of Nb_3Sn cables," *IEEE Trans. Mag.*, Vol. 27 No. 2, pp. 1831–1834, 1990.

[149] H.H.J. ten Kate, H. Weijers and J.M. van Ort, Critical current degradation in Nb_3Sn cables under transverse pressure, *IEEE Trans. Appl. Supercond.*, Vol. 3 No. 1, pp. 1334–1337, 1993.

[150] R.A. Haarman and K.D. Williamson, "Jr., Electrical breakdown and tracking characteristics of pulsed high voltages in cryogenic helium and nitrogen," *Adv. Cryo. Eng.*, Vol. 21, pp. 102–108, 1975.

[151] P. Védrine, J.M. Rifflet, J. Perot, B. Gallet, C. Lyraud, P. Giovannoni, F. Le Coz, N. Siegel and T. Tortschanoff, "Mechanical tests on the prototype LHC lattice quadrupole," *IEEE Trans. Magn.*, Vol. 30 No. 4, pp. 2475–2478, 1994.

[152] M. Anerella, A.K. Ghosh, E. Kelly, J. Schmalzle, E. Willen, J. Fraivillig, J. Ochsner and D.J. Parish, "Improved cable insulation for superconducting magnets," *Proc. of the 1993 Particle Accelerator Conference*, IEEE catalogue 93CH3279–7, pp. 2790–2792, 1993.

[153] P. Bruzzone, K. Nylund, and W.J. Muster, "Electrical insulation system for superconducting magnets according to the wind and react technique," *Adv. Cryog. Eng.*, Vol. 36, pp. 999–1006, 1990.

[154] R.A. Beth, "Complex representation and computation of two-dimensional magnetic fields," *J. Appl. Phys.*, Vol. 37 No. 7, pp. 2568–2571, 1966.

[155] A.I. Markushevich, *Theory of Functions of a Complex Variable*, Englewood Cliffs, N.J.: Prentice-Hall Inc., Vol. 1, 1965.

[156] R.A. Beth, "An integral formula for two-dimensional fields," *J. Appl. Phys.*, Vol. 38 No. 12, pp. 4689–4692, 1967.

[157] K. Halbach, "Fields and first order perturbation effects in two-dimensional conductor dominated magnets," *Nuclear Instruments and Methods*, Vol. 78, pp. 185–198, 1970.

[158] R.C. Gupta, S.A. Kahn and G.H. Morgan, "SSC 50 mm dipole cross section." In J. Nonte (ed.), *Supercollider 3*, New York: Plenum Press, pp. 587–599, 1991.

[159] G.H. Morgan, "Shaping of magnetic fields in beam transport magnets." In M. Month and M. Dienes (eds.), *The Physics of Particle Accelerators*, AIP Conference Proceedings, Vol. 249 No.2, pp. 1242–1261, 1992.

[160] A. Devred and T. Ogitsu, "Ramp-rate sensitivity of SSC dipole magnet prototypes." In S.I. Kurokawa, M. Month and S. Turner (eds.), *Frontiers of Accelerator Technology*, Singapore: World Scientific, pp. 184–308, 1996.

[161] T. Tortschanoff, "Grading of the current density in coils of superconducting dipole magnets." In C. Marinucci and P. Weymuth (eds.), *Proceedings of 9th International Conference on Magnet Technology (MT9)*, Swiss Institute for Nuclear Research, pp. 68–71, 1985.

[162] J.M. Cook, "Strain energy minimization in SSC magnet winding," *IEEE Trans. Mag.*, Vol. 27 No. 2, pp. 1976–1980, 1991.

[163] J.S. Brandt, N.W. Bartlett, R.C. Bossert, J.A. Carson, J.J. Konc, G.C. Lee, J.M. Cook, S. Caspi, M.A. Gordon and F. Nobrega, "Coil end design for the SSC collider dipole magnet," *Conference Records of the 1991 IEEE Particle Accelerator Conference*, IEEE catalogue 91CH3038–7, pp. 2182–2184, 1991.

[164] A. Devred, T. Bush, R. Coombes, J. DiMarco, C. Goodzeit, J. Kuzminski, M. Puglisi, P. Radusewicz, P. Sanger, R. Schermer, G. Spigo, J. Tompkins, J. Turner, Z. Wolf, Y. Yu, H. Zheng, T. Ogitsu, M. Anerella, J. Cottingham, G. Ganetis, M. Garber, A. Ghosh, A. Greene, R. Gupta, J. Herrera, S. Kahn, E. Kelly, A. Meade, G. Morgan, J. Muratore, A. Prodell, M. Rehak, E.P. Rohrer, W. Sampson, R. Shutt, P. Thompson, P. Wanderer, E. Willen,

M. Bleadon, R. Hanft, M. Kuchnir, P. Mantsch, P.O. Mazur, D. Orris, T. Peterson, J. Strait, J. Royet, R. Scanlan and C. Taylor, "About the mechanics of SSC dipole magnet prototypes." In M. Month and. M. Dienes (eds.), *The Pysics of Particle Accelerators*, AIP Conference Proceedings Vol. 249 No.2, pp. 1309–1374, 1992.

[165] T. Ogitsu, K. Tsuchiya and A. Devred, "Investigation of wire motion in superconducting magnets," *IEEE Trans. Magn.*, Vol. 27 No. 2, pp. 2132–2135, 1991.

[166] D. Perini, N. Galante, J. Gilquin, G. Patti and R. Perin, "Measurements of the resistance to stress cycling at 4.2 K of LHC dipole collars," *IEEE Trans. Magn.*, Vol. 30 No. 4, pp. 1754–1757, 1994.

[167] D. Leroy, R. Perin, D. Perini and Y. Yamamoto, "Structural analysis of the LHC 10 T twin-aperture dipole." In T. Sekiguchi and S. Shimamoto (eds.), *Proc. of 11th International Conference on Magnet Technology (MT11)*, London: Elsevier Applied Science, pp. 59–164 (1990).

[168] E. Acerbi, M. Bona, D. Leroy, R. Perin and L. Rossi, "Development and fabrication of the first 10 m long superconducting dipole prototype for the LHC," *IEEE Trans. Magn.*, Vol. 30 No. 4, pp. 1793–1796, 1994.

[169] G. Spigo, "Preliminary assessment of the mechanical strength of a dipole with aluminum collars, vertically split yoke and aluminum bars to control the gap from room to working temperatures," 1990 (unpublished).

[170] P. Fessia, D. Perini, S. Russenschuck, C. Voellinger, R. Vuilermet and C. Wyss, "Selection of the cross-section design for the LHC main dipole," Presented at the 16th International Conference on Magnet Technology (MT16), Ponte Verde Beach, FL, September 26–October 2, 1999.

[171] K. Artoos, L. Bottura, P. Fessia, M. Bajko, M. Modena, O. Pagano, D. Perini, F. Savary, W. Scandale, A. Siemko, G. Spigo, E. Todesco, J. Vlogaert and C. Wyss, "Design, manufacturing status, first results of the LHC main dipole final prototypes and steps towards series manufacture," Presented at the 16th International Conference on Magnet Technology (MT16), Ponte Verde Beach, FL, September 26–October 2, 1999.

[172] J. Strait, B.C. Brown, R. Hanft, M. Kuchnir, M. Lamm, R. Lundy, P. Mantsch, P.O. Mazur, A. McInturff, J.R. Orr, J.G. Cottingham, P. Dahl, G. Ganetis, M. Garber, A. Ghosh, C. Goodzeit, A. Greene, J. Herrera, S. Kahn, E. Kelly, G. Morgan, A. Prodell, W. Sampson, W. Schneider, R. Shutt, P. Thompson, P. Wanderer, E. Willen, S. Caspi, W. Gilbert, R. Meuser, C. Peters, J. Rechen, R. Royer, R. Scanlan, C. Taylor, J. Zbasnik, M. Chapman, A. Devred, J. Kaugerts, J. Peoples, J. Tompkins and R. Schermer, "Tests of full scale SSC R&D dipole magnets," *IEEE Trans. Magn.*, Vol. 25 No. 2, pp. 1455–1458, 1989.

[173] A. Jain, "Basic theory of magnets." In S. Turner (ed.), *Proc. of CERN Accelerator School on Measurement and Alignment of Accelerator and Detector Magnets*, CERN 98–05, Geneva, Switzerland: CERN, pp. 1–26, 1998.

[174] A. Jain, "Harmonic coils." In S. Turner (ed.), *Proc. of CERN Accelerator School on Measurement and Alignment of Accelerator and Detector Magnets*, CERN 98–05, Geneva, Switzerland: CERN, pp. 175–217, 1998.

[175] G. Morgan, "Stationary coil for measuring the harmonics in pulsed transport magnets." In Y. Winterbottom (ed.), *Proceedings of Fourth International Conference on Magnet Technology (MT4)*, BNL CONF–720908 , Upton, NY: BNL, pp. 787–790, 1972.

[176] A.I. Markushevich, *Theory of Functions of a Complex Variable*, Englewood Cliffs, N.J.: Prentice-Hall Inc., Vol. 3, 1967.

[177] W.G. Davis, "The theory of the measurements of magnetic multipole fields with rotating coil magnetometer," *Nuclear Instruments and Methods in Physics Research*, Vol. A311, pp. 399–436, 1992.

[178] L. Walckiers, "The harmonic coil method." In S. Turner (ed.), *Proc. of the CERN Accelerator School on Magnetic Measurement and Alignment*, CERN/ 92–05, Geneva: CERN, pp. 138–166, 1992.

[179] T. Garavaglia, K. Kauffmann and R. Stiening, "Application of the SSCRTK numerical simulation program to the evaluation of the SSC magnet aperture." In M. MacAshan (ed.), *Supercollider 2*, New York: Plenum Press, pp. 59–76, 1990.

[180] H. Brück, R. Meinke, and P. Schmüser, "Methods for magnetic measurements of the superconducting HERA magnets," *Kerntechnik*, Vol. 56 No. 4, pp. 248–256, 1991.

[181] T. Ogitsu and A. Devred, "Influence of azimuthal coil size variations on magnetic field harmonics of superconducting particle accelerator magnets," *Rev. Sci. Instrum.*, Vol. 65 No. 6, pp. 1998–2005, 1994.

[182] C.P. Bean, "Magnetization of high-field superconductors," *Review of Modern Physics*, Vol. 36 No. 1, pp. 31–39, 1964.

[183] H. Brück, R. Meinke, F. Müller and P. Schmüser, "Field distortions from persistent magnetization currents in the superconducting HERA magnets," *Z. Phys. C – Particles and Fields*, Vol. 44, pp. 385–392, 1989.

[184] R.W. Hanft, B.C. Brown, D.A. Herrup, M.J. Lamm, A.D. McInturff and M.J. Syphers, "Studies of time dependent field distortions from magnetization currents in Tevatron superconducting dipole magnets," *IEEE Trans. Magn.*, Vol. 25 No. 2, pp.1647–1651, 1989.

[185] A. Devred, J. DiMarco, J. Kuzminski, R. Stiening, J. Tompkins, Y. Yu, H. Zheng, T. Ogitsu, R. Hanft, P.O. Mazur, D. Orris and T. Peterson, "Time decay measurements of the sextupole component of the magnetic field in a 4-cm aperture, 17-m-long SSC dipole magnet prototype," *Conference Record of the 1991 IEEE Particle Accelerator Conference*, IEEE catalogue 91CH3038–7, pp. 2480–2482, 1991.

[186] F. Willeke and F. Zimmermann, "The impact of persistent current field errors on the stability of the proton beam in the HERA proton ring," *Conference Record of the 1991 IEEE Particle Accelerator Conference*, IEEE catalogue 91CH3038–7, pp. 2483–2487, 1991.

[187] P. Schmüser, "Properties and Practical Performance of SC Magnets in Accelerators." In H. Henke, H. Honeger and Ch. Petit-Jean-Genaz, *Proc. of Third European Particle Accelerator Conference.*, Gif sur Yvette, France: Editions Frontières, pp. 284–288, March 24–28, 1992.

[188] L. Bottura, L. Walckiers and R. Wolf, "Field errors decay and "snap-back" in LHC model dipoles," *IEEE Trans. Appl. Supercond.*, Vol. 7 No. 2, pp. 602–605, 1997.

[189] P.W. Anderson, "Flux creep in hard superconductors," *Phys. Rev. Letters*, Vol. 9 No. 7, pp. 309–311, 1962.

[190] T. Ogitsu, A. Devred and V. Kovachev, "Influence of inter-strand coupling current on field quality of superconducting accelerator magnets," *Part. Accel.*, Vol. 57, pp. 215–235, 1997.

[191] H. Brück, D. Gall, J. Krzywinski, R. Meinke, H. Preissner, M. Halemeyer, P. Schmüser, C. Stolzenburg, R. Stiening, D. ter Avest, L.J.M. van de Klundert, "Observation of a periodic pattern in the persistent-current fields of the superconducting HERA magnets," *Conference Record of the 1991 IEEE Particle Accelerator Conference*, IEEE catalogue 91CH3038–7, pp. 2149–2151, 1991.

[192] A.K. Ghosh, K.E. Robins and W.B. Sampson, "Axial variations in the magnetic field of superconducting dipoles and quadrupoles," *Proc. of the 1993 Particle Accelerator Conference*, IEEE catalogue 93CH3279–7, pp. 2742–2743, 1993.

[193] A. Akhmetov, A. Devred, R. Schermer and R. Mints, "Current loop decay in Rutherford-type cables." In P. Hale (ed.), *Supercollider 5*, New York: Plenum Press, pp. 443–446, 1994.

[194] L. Krempanski and C. Schmidt, "Influence of a longitudinal variation of dB/dt on the magnetic field distribution of superconducting accelerator magnets," *Appl. Phys. Lett.*, Vol. 66 No. 12, pp. 1545–1547, 1995.

[195] A.P. Verweij, "Boundary-induced coupling currents in a 1.3 m Rutherford-type cable due to a locally applied field change," *IEEE Trans. Appl. Supercond.*, Vol. 7 No. 2, pp. 270–273, 1997.

[196] L. Bottura, L. Walckiers and Z. Ang, "Experimental evidence of boundary induced coupling currents in LHC prototypes," *IEEE Trans. Appl. Supercond.*, Vol. 7 No. 2, pp. 801–804, 1997.

[197] R. Stiening, A possible mechanism for enhanced persistent current sextupole decay in SSC dipoles, 1991 (unpublished).

[198] A.G. Mathewson, "Vacuum problems associated with the next generation of hadron colliders," In S.I. Kurokawa, M. Month and S. Turner (eds.), *Frontiers of Accelerator Technology*, Singapore: World Scientific, pp. 701–716, 1996.

[199] O. Gröbner, "The LHC vacuum system," *Proc. of the 1997 Particle Accelerator Conference*, IEEE Catalogue Number 97CH36167, pp. 3542–3546, 1998.

[200] C. Meuris, "Heat transport in insulation of cables cooled by superfluid helium," *Cryogenics*, Vol. 31, pp. 624–628, 1991.

[201] B.J.P. Baudouy, F.P. Juster, C. Meuris, L. Vieillard and M.X. François, "Steady-state heat transfer in He II through porous superconducting cable insulation," *Adv. Cryo. Eng.*, Vol. 41(A), pp. 289–297, 1996.

[202] S.W. Van Sciver, *Helium Cryogenics*, New York: Plenum Press, 1986.

[203] Ph. Lebrun, "Cryogenic systems for accelerators." In S.I. Kurokawa, M. Month and S. Turner (eds.), *Frontiers of Accelerator Technology*, Singapore: World Scientific, pp. 681–700, 1996.

[204] T. Peterson, private communication, November 1999.

[205] C.H. Rode, "Tevatron Cryogenic System." In F.T. Cole, R. Donaldson (eds.), *Proceedings of the 12th International Conference on High Energy Accelerators*, Batavia, IL: Fermi National Accelerator Laboratory, pp. 529–535, 1983.

[206] T.J. Peterson, "The nature of the helium flow in Fermilab's Tevatron magnets," *Cryogenics*, Vol. 37 No. 11, pp. 727–732, 1997.

[207] H.R. Barton Jr., M. Clausen, G. Horlitz, G. Knust and H. Lierl, "The refrigeration system for the superconducting proton ring of the electron proton collider HERA," *Adv. Cryo. Eng.*, Vol. 31, pp. 635–645, 1986.

[208] A.I. Ageyev, K.P. Myznikov, A.N. Shamichev, A.V. Tarasov, A.V. Zhirnov, S.I. Zinchenko, N.V. Barmin, I.K. Butkevich, S.P. Gorbachev, V.D. Kovalenko, and I.M. Morkovkin, "Development of cryogenic system for UNK." In P.F. Dahl (ed.), *Proc. of Workshop on Superconducting Magnets and Cryogenics*, BNL 52006, Upton, NY: BNL, pp. 276–279, 1986

[209] D.P. Brown, R.I. Loutitt, C. Rode and P.C. VanderArend, "The SSC cryogenic system," *Adv. Cryo. Eng.*, Vol. 31, pp. 57–62, 1986.

[210] M.S. McAshan, "SSC refrigeration system design studies." In M. McAshan (ed.), *Supercollider 1*, New York: Plenum Press, pp. 287–300, 1989.

[211] M. Iarocci, J. Sondericker, K.C. Wu, Y. Farah, C. Lac, A. Morgillo, A. Nicoletti, E. Quimby, M. Rehak, and A. Werner, "RHIC Accelerator commissioning, cryogenic tests and initial operating experience of the 25 kW refrigerator and distribution system," Presented at the Cryogenic Engineering Conference (CEC/ICMC99), Montréal, Québec (Canada), July 12–16, 1999.

[212] D.R. Tiley and J. Tilley, *Superfluidity and superconductivity*, 3rd ed., Bristol: Adam Hilger, 1990.

[213] S.W. Van Sciver, "Chapter 10: He II (superfluid helium)." In J.G. Weisend (ed.), *Handbook of Cryogenic Engineering*, Philadelphia, PA: Taylor & Francis, pp. 443–480, 1998.

[214] G. Claudet and R. Aymar, "Tore supra and He II cooling of superconducting magnets," *Adv. Cryo. Eng.*, Vol. 35(A), pp. 55–67, 1990.

[215] Ph. Lebrun, "Superfluid helium cryogenics for the large hadron collider project at CERN," *Cryogenics*, Vol. 34 ICEC Supplement, pp. 1–8, 1994.

[216] W. Frost (ed.), *Heat Transfer at Low Temperatures*, New York: Plenum Press, 1975.

[217] T.H. Nicol, "Cryostat design for the superconducting super collider." In M. Month and M. Dienes (eds.), *The Physics of Particle Accelerators*, AIP Conference Proceedings Vol. 249 No.2, pp. 1230–1241, 1992.

[218] J. Strait, M. Bleadon, B.C. Brown, R. Hanft, M. Kuchnir, M. Lamm, P. Mantsch, P.O. Mazur, D. Orris, J. Peoples, G. Tool, J.G. Cottingham, P. Dahl, G. Ganetis, M. Garber, A.K. Ghosh, C. Goodzeit, A. Greene, J. Herrera, S. Kahn, E. Kelly, G. Morgan, J. Muratore, A. Prodell, W. Sampson, R. Shutt, P. Thompson, P. Wanderer, E. Willen, M. Chapman, J. Cortella, A. Desportes, A. Devred, J. Kaugerts, T. Kirk, R. Meuser, K. Mirk, R. Schermer, J. Turner, J.C. Tompkins, S. Caspi, W. Gilbert, C. Peters, J. Rechen, J.M. Royer, R. Scanlan, C. Taylor and J. Zbasnik, "Full length SSC R&D dipole magnet test results," *Proceedings of the 1989 IEEE Particle Accelerator Conference*, IEEE catalogue 89CH2669–0, pp. 530–532, 1989.

[219] P. Wanderer, M. Anerella, G. Ganetis, M. Garber, A.K. Ghosh, A. Greene, R. Gupta, A. Jain, S. Kahn, E. Kelly, G. Morgan, J. Muratore, A. Prodell, M. Rehak, E.P. Rohrer, W. Sampson, R. Shutt, R. Thomas, P. Thompson, E. Willen, A. Akhmetov, T. Bush, W.D. Capone II, R. Coombes, A. Devred, J. DiMarco, C. Goodzeit, J. Krzywinski, J. Kuzminski, W. Nah, T. Ogitsu, P. Radusewicz, R. Schermer, R. Stiening, J.C. Tompkins, M. Wake, J. Zbasnik, Y. Zhao, H. Zheng, "Partial lifetime test of an SSC collider dipole," *IEEE Trans. Magn.*, Vol. 30 No. 4, pp. 1738–1741, 1994.

[220] T. Schneider and P. Turowski, "Critical current degradation of a NbTi-multifilament conductor due to heat treatment," *IEEE Trans. Magn.*, Vol. 30 No. 4, pp. 2391–2394, 1994.

[221] A. Devred, M. Chapman, J. Cortella, A. Desportes, J. DiMarco, J. Kaugerts, R. Schermer, J.C. Tompkins, J. Turner, J.G. Cottingham, P. Dahl, G. Ganetis, M. Garber, A. Ghosh, C. Goodzeit, A. Greene, J. Herrera, S. Kahn, E. Kelly, G. Morgan, A. Prodell, E.P. Rohrer, W. Sampson, R. Shutt, P. Thompson, P. Wanderer, E. Willen, M. Bleadon, B.C. Brown, R. Hanft, M. Kuchnir, M. Lamm, P. Mantsch, P.O. Mazur, D. Orris, J. Peoples, J. Strait, G. Tool, S. Caspi, W. Gilbert, C. Peters, J. Rechen, J. Royer, R. Scanlan, C. Taylor and J. Zbasnik, "Investigation of heater-induced quenches in a full-length SSC R&D dipole." In T. Sekiguchi and S. Shimamoto (eds.), *Proc. of 11th International Conference on Magnet Technology (MT11)*, London: Elsevier Applied Science, pp. 91–95, 1990.

[222] A. Devred, M. Chapman, J. Cortella, A. Desportes, J. DiMarco, J. Kaugerts, R. Schermer, J.C. Tompkins, J. Turner, J.G. Cottingham, P. Dahl, G. Ganetis, M. Garber, A. Ghosh, C. Goodzeit, A. Greene, J. Herrera, S. Kahn, E. Kelly, G. Morgan, A. Prodell, E.P. Rohrer, W. Sampson, R. Shutt, P. Thompson, P. Wanderer, E. Willen, M. Bleadon, B.C. Brown, R. Hanft, M. Kuchnir, M. Lamm, P. Mantsch, P.O. Mazur, D. Orris, J. Peoples, J. Strait, G. Tool, S. Caspi, W. Gilbert, C. Peters, J.Rechen, J. Royer, R. Scanlan, C. Taylor and J. Zbasnik, "Quench characteristics of full-length SSC R&D dipole magnets," *Adv. Cryo. Eng.*, Vol. 35(A), pp. 599–608, 1990.

[223] L. Coull, D. Hagedorn, V. Remondino and F. Rodriguez-Mateos, "LHC magnet quench protection system," *IEEE Trans. Magn.*, Vol. 30 No. 4, pp. 1742–1745, 1994.

[224] R. Stiening, R. Flora, R. Lauckner and G. Tool, "A superconducting synchrotron power supply and quench protection scheme," *IEEE Trans. Magn.*, Vol. MAG–15 No. 1, pp. 670–672, 1979.

[225] K. Koepke, C. Rode, G. Tool, R. Flora, J. Jölstlein, J. Saarivirta and M. Kuchnir, "Two cell doubler system test," *IEEE Trans. Magn.*, Vol. MAG–17 No. 1, pp. 713–715, 1981.

[226] W. Burgett, M. Christianson, R. Coombes, T. Dombeck, J. Gannon, D. Haenni, P. Kraushaar, M. Levin, M. McAshan, A. McInturff, G. Mulholland, D. Murray, W. Robinson, T. Savord, R. Smellie, F. Spinos, G. Tool, J. Weisend II and J. Zatopek, "Full-power test of a string of magnets comprising a half-cell of the Superconducting Super Collider," *Part. Accel.*, Vol. 43, pp. 41–75, 1993.

[227] F. Rodriguez-Mateos, L. Coull, K. Dahlerup-Petersen, D. Hagedorn, G. Krainz and A. Rijllart, "Electrical performance of a string of magnets representing a half-cell of the LHC machine," *IEEE Trans. Magn.*, Vol. 32 No. 4, pp. 2105–2108, 1996.